X-ray Diffraction by Polycrystalline Materials

René Guinebretière

ISTE

X-ray Diffraction by Polycrystalline Materials

This page intentionally left blank

X-ray Diffraction by Polycrystalline Materials

René Guinebretière

ISTE

First published in France in 2002 and 2006 by Hermès Science/Lavoisier entitled “Diffraction des rayons X sur échantillons polycristallins”
First published in Great Britain and the United States in 2007 by ISTE Ltd

ISTE Ltd
6 Fitzroy Square
London W1T 5DX
UK

ISTE USA
4308 Patrice Road
Newport Beach, CA 92663
USA

www.iste.co.uk

Library of Congress Cataloging-in-Publication Data

Guinebretière, René.
[Diffraction des rayons X sur échantillons polycristallins. English]
X-ray diffraction by polycrystalline materials/René Guinebretière.
p. cm.
Includes bibliographical references and index.
ISBN-13: 978-1-905209-21-7
1. X-rays--Diffraction. 2. Crystallography. I. Title.
QC482.D5G85 2007
548'.83--dc22

2006037726

British Library Cataloguing-in-Publication Data
A CIP record for this book is available from the British Library
ISBN 13: 978-1-905209-21-7

Printed and bound in Great Britain by Antony Rowe Ltd, Chippenham, Wiltshire.

Table of Contents

This page intentionally left blank

Preface

In 1912, when M. Laue suggested to W. Friedrich and P. Knipping the irradiation of a crystal with an X-ray beam in order to see if the interaction between this beam and the internal atomic arrangement of the crystal could lead to interferences, it was mainly meant to prove the undulatory character of this X-ray discovered by W.C. Röntgen 17 years earlier. The experiment was a success, and in 1914 M. Laue received the Nobel Prize for Physics for the discovery of X-ray diffraction by crystals. In 1916, this phenomenon was used for the first time to study the structure of polycrystalline samples. Throughout the 20th century, X-ray diffraction was, on the one hand, studied as a physical phenomenon and explained in its kinematic approximation or in the more general context of the dynamic theory, and on the other, implemented to study material that is mainly solid.

Obviously, the theoretical studies were initially conducted on single crystal diffraction, but the needs for investigation methods from physicists, chemists, material scientists and more recently from biologists have led to the development of numerous works on X-ray diffraction with polycrystalline samples. Most of the actual crystallized solid objects that we encounter every day are in fact polycrystalline; each crystal is the size of a few microns or even just a few nanometers. Polycrystalline diffraction sampling, which we will address here, is actually one of the most widely used techniques to characterize the state of the "hard" condensed matter, inorganic material, or "soft", organic material, and sometimes biological material. Polycrystalline samples can take different forms. They can be single-phased or made up of the assembling of crystals of different crystalline phases. The orientation of these crystals can be random or highly textured, and can even be unique, in the case for example of epitactic layers. The crystals can be almost perfect or on the contrary can contain a large number of defects. X-ray diffraction on polycrystalline samples enables us to comprehend and even to quantify these characteristics. However, the methods of measure must be adapted. The quality of the quantitative result obtained greatly depends on the care

taken over this measure and in particular on the right choice of equipment and of the data processing methods used.

This book is designed for graduate students, as well as engineers or active researchers studying or working in a sector related to material sciences and who are concerned with mastering the implementation of X-ray diffraction for the study of polycrystalline materials.

The introduction recounts the history of the emphasis on X-ray diffraction by crystals since the discovery of X-rays. The book is then divided into two parts. The first part focuses on the description of the basic theoretical concepts, the instrumentation and the presentation of traditional methods for data processing and the interpretation of the results. The second part is devoted to a more specific domain which is the quantitative study of the microstructure by X-ray diffraction.

The first part of the book is divided into four chapters. Chapter 1 focuses on the description of the theoretical aspects of X-ray diffraction mainly presented as a phenomenon of interference of scattered waves. The intensity diffracted by a crystal is measured in the approximations of the kinematic theory. The result obtained is then extended to polycrystalline samples. Chapter 2 is entirely dedicated to the instrumental considerations. Several types of diffractometers are presently available; they generally come from the imagined concepts from the first half of the 20^{th} century and are explained in different ways based on the development of the sources, the detectors and the different optical elements such as for example the monochromators. This chapter is particularly detailed; it takes the latest studies into account, such as the current development of large dimension plan detectors. Modern operation of the diffraction signal is done by a large use of calculation methods relying on the computer development. In Chapter 3, we will present the different methods of extracting from the signal the characteristic strength of the diffraction peaks including the position of these peaks, their integrated intensity and the shape or the width of the distribution of intensity. The traditional applications of X-ray diffraction over polycrystalline samples are described in Chapter 4. The study of the nature of the phases as well as the determination of the rate of each phase present in the multiphased samples are presented in the first sections of this chapter. The structural analysis is then addressed in a relatively condensed way as this technique is explained in several other international books.

The second part of the book focuses on the quantitative study of the microstructure. Although the studies in this area are very old, this quantitative analysis method of microstructure by X-ray diffraction has continued to develop in an important way during the last 20 years. The methods used depend on the form of the sample. We will distinguish the study of polycrystalline samples as pulverulent or massive for thin layers and in particular the thin epitactic layers. Chapter 5 is

dedicated to the theoretical description of the influence of structural flaws over the diffusion and diffraction signal. The actual crystals contain a density of varying punctual, linear, plan or three-dimensional defects. The presence of these defects modifies the diffraction line form in particular and the distribution of the diffused or diffracted intensity in general. The influence of these defects is explained in the kinematic theory. These theoretical considerations are then applied in Chapter 6 to the study of the microstructure of polycrystalline pulverulent or massive samples. The different methods based on the analysis of the integral breadth of the lines or of the Fourier series decomposition of the line profile are described in detail. Finally, Chapter 7 focuses on the study of thin layers. Following the presentation of methods of measuring the diffraction signal in random or textured polycrystalline layers, a large part is dedicated to the study of the microstructure of epitactic layers. These studies are based on bidimensional and sometimes three-dimensional, reciprocal space mapping. This consists of measuring the distribution of the diffracted intensity within the reciprocal lattice node that corresponds to the family of plans studied. The links between this intensity distribution and the microstructure of epitactic layers are presented in detail. The methods for measuring and treating data are then explained

The book contains a large number of figures and results taken from international literature. The most recent developments in the views discussed are presented. More than 400 references will enable the interested reader to find out more about the domains that concern them.

This page intentionally left blank

Acknowledgements

X-ray diffraction is a physical phenomenon as well as an experimental method for the characterization of materials. This last point is at the heart of this book and requires illustration with concrete examples from real experiments. The illustrations found throughout this book are taken from international literature and are named accordingly. Many of these examples are actually the result of studies conducted in the last 15 years in Limoges in the Laboratoire de Science des Procédés Céramiques et de Traitements de Surface. My profound thanks to the students, sometimes becoming colleagues, who by the achievement of their studies have helped make this book a reality. I would like to particularly acknowledge O. Masson and A. Boulle in Limoges for their strong contribution to the development X-ray diffraction on polycrystalline samples and epitactic layers respectively.

One of the goals of this book is to continually emphasize the link between the measuring device, the way in which it is used and the interpretation of the measures achieved. I am deeply convinced that in experimental science only a profound knowledge of the equipment used and the underlying theories of the methods implemented can result in an accurate interpretation of the experimental results obtained. We must then consider the equipment that has helped us conduct the experimental study as the centerpiece. Because of this conviction, I have put a lot of emphasis on the part of this book that describes the measuring instruments. I learned this approach from the experience of A. Dauger who has directed my thesis as well as during the years following my research studies. He is the one who introduced in Limoges the development of X-ray diffusion and diffraction instruments, and I thank him for his continued encouragement in this methodology.

Ever since the first edition written in French and published in 2002, several colleagues have commented on the book. These critiques led me to completely redo the structure of the book, in particular separating the conventional techniques from the more advanced techniques linked to the study of microstructure. I would once more like to thank A. Boulle, now a researcher at the CNRS and also M. Anne, director of the Laboratoire de Cristallographie in Grenoble, whose comments and encouragement have been very helpful.

An Historical Introduction: The Discovery of X-rays and the First Studies in X-ray Diffraction

X-rays and "cathode rays": a very close pair

On November 8th, 1895, Röntgen discovered by accident a new kind of radiation. While he was using a Crookes tube, he noticed a glow on a plate, covered with barium platinocyanide, and rather far away from the tube. Röntgen, who was working at the time on the cathode rays produced by Crookes tubes, immediately understood that the glow he was observing could not be caused by this radiation. Realizing the importance of his discovery, and before making it known to the scientific community, he tried for seven weeks to determine the nature of this new kind of radiation, which he named himself *X-Strahlen*. On December 28th, 1895, Röntgen presented his observations before the Würzburg Royal Academy of Physics and Medicine [RON 95]. His discovery was illustrated by the photographic observation of the bones in his wife's hand (see Figure 1). Röntgen inferred from his experiments that the Crookes tube produced beams that propagated in straight lines and could pass through solid matter [RON 95, RON 96a, RON 96b, RON 96c]. Very quickly, these "Röntgen rays" were used in the medical world to produce radiographies [SWI 96].

Immediately after this discovery, a large number of studies were launched to find out the nature of this radiation. Röntgen tried to find analogies between this kind of radiation and visible light, which lead him to conduct unsuccessful experiments that consisted of reflecting X-rays on quartz, or lime. He believed he was observing this reflection on platinum, lead and zinc [RON 95, RON 96b]. He noticed that X-rays, unlike electronic radiation, are not affected by magnetic fields. Röntgen even tried, to no avail, to produce interference effects in X-rays by making

the X-ray beam pass through holes [RON 95]. The analogy between X-rays and visible light prompted researchers to study how X-rays behave with regard to the well-known laws of optics. Thus, Thomson [THO 96], Imbert and Bertin-Sans [IMB 96], as well as Battelli and Garbasso [BAT 96], showed in 1896 that specular reflection was not possible with X-rays, hence confirming the studies of Röntgen. They also found, in agreement with the works of Sagnac [SAG 97a], that the deviation of X-rays by refraction is either non-existent or extremely small.

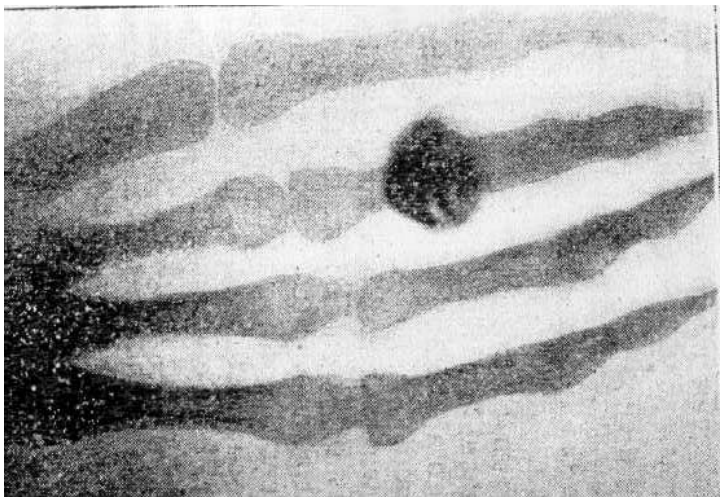

Figure 1. *The first radiographic observation*

In November 1896, Stokes gave a short presentation before the Cambridge Philosophical Society, explaining some of the fundamental properties of X-rays [STO 96]. He claimed that X-rays, like γ-rays, are polarizable. This comment, made in November, did not take into account several studies, even though they had been published in February of the same year by Thompson [THO 96a], who established the absence of polarization in X-rays by having them pass through oriented crystal plates. The polarizable nature of X-rays was conclusively demonstrated in 1905 by Barkla [BAR 05, BAR 06a]. Based on the absence of refraction for X-rays, Stokes described this radiation as vibrations propagating through solid material between the molecules of this material. Finally, by analyzing the absence of interference effects for this radiation, he concluded that either the wavelength of this propagation was too small or the phenomenon was not periodical. The author, who mistakenly believed that the latter hypothesis was the right one, assumed that each “charged

molecule[1]" that hit the anode emitted a radiation, the pulsation of which was independent of the pulsations of the radiations emitted by the other molecules.

Having demonstrated that X-rays are a secondary radiation caused by what was referred to at the time as "cathode rays", Röntgen showed that the study of the nature of X-rays had close ties with the determination of the nature of electronic radiation. After the discovery by Crookes of the existence of a radiation emitted by the cathode and attracted by the anode, the question of the nature of these cathode rays was the subject of intense activity. When X-rays were discovered, the two theories clashed. Some considered that this cathode rays was caused by a process of vibration taking place in the rarefied gas inside the tube (the "ether") [LEN 94, LEN 95], while others thought that this current was the result of the propagation of charged particles emitted by the cathode [PER 95, THO 97a].

In 1895, Perrin proved experimentally that the cathode rays carried an electric charge and that this charge was negative [PER 95]. This view was the one supported by Thomson [THO 97a, THO 97b], who published an article in 1897, considered to be the major step in the discovery of the electron [THO 97b]. He noticed that these cathode rays could be diverted by an electrical field. This observation led him to demonstrate experimentally that this radiation was caused by the motion of charged particles, for which he estimated the charge to mass ratio. He found that this ratio e/m is independent of the nature of the gas inside the tube and established the existence of "charged particles", which are the basic building blocks of atoms [THO 97b].

This is how Thomson became interested in X-rays while studying electronic radiation. In January 1896, he presented an analysis that could be described as the "theoretical discovery of X-rays". He used the Maxwell equations and included the contribution from a convection current caused by the motion of charged particles. He demonstrated analytically that these particles suddenly slowing down led to an electromagnetic wave that propagated through the medium with an extremely low wavelength [THO 96b]. The author himself noted that the properties of the radiation discovered by Röntgen were not sufficiently well known to be able to say that the electromagnetic waves he had found evidence of were, in fact, Röntgen radiation. Two years later [THO 98a], Thomson was more assertive and concluded that the radiation related to the sudden slowing down of charged particles – later referred to as braking radiation – was a kind of X-ray radiation.

By analogy with the characteristics of electron radiation, many authors imagined that X-rays also corresponded to the propagation of particles. This debate over the particle or wave-like nature of electromagnetic radiation only comes to a close with

1 The concept of electron was only definitively accepted the following year.

the advent of quantum physics. This is why, after the studies of Thomson, several authors compared the respective properties of X-rays and electrons [LEN 97, RIT 98, WAL 98]. Lenard [LEN 97] showed, on the one hand, that irradiating photographic plates with X-rays caused a much weaker effect than what was observed when the same plates were irradiated with an electron beam. On the other hand, he showed that the two kinds of radiation had significantly different electric properties. Ritter von Geitler [RIT 98] irradiated flat metal screens with X-rays in order to find evidence of a possible charge carried by these particles. He did not observe an electrical signal, but nonetheless he did not conclude that the particles were not charged. In the same issue of the *Annalen der Physik und Chemie*, Walter [WAL 98] was more assertive and considered that the particles associated with X-rays have no electric charge. Furthermore, given the high penetrating ability of X-rays, he refuted a theory, acknowledged at the time, according to which X-rays could consist of the incident electrons that had lost their charge after hitting the anode [VOS 97].

Thus, before the beginning of the 20th century, it was accepted as fact that X-rays were very different from the electronic radiation that created them. Scientists also knew that they consist of particles that are not charged, since they are not diverted in a magnetic field [STR 00]. The theoretical works of Thomson describe the propagation of X-rays as that of a wave with a very small wavelength. Furthermore, these X-rays do not seem to be reflected of refracted under conditions that would generally be used to observe these effects with visible light. While some authors were trying to discover the nature of X-rays, other authors were studying the effects of having X-rays travel through gases.

In 1896, Thomson and Rutherford [RUT 97, THO 96c] showed that irradiating a gas with an X-ray beam created an electrical current inside this gas. They showed that the intensity of this current depends, on the one hand, on the voltage applied to the two terminals of the chamber containing a gas, and on the other hand, on the nature of this gas. Rutherford [RUT 97] also observed that the decrease in the X-ray beam's intensity due to the absorption by the gas follows an exponential law which depends on a coefficient specific to each gas. From these findings, Rutherford measured the linear absorption coefficient of several gases and found a correlation between this coefficient and the intensity of the electrical current, produced by the interaction between this gas and the X-rays. In a commentary on Rutherford's article, Thomson [THO 97c] observed that his colleague's findings were evidence of a strong analogy between X-rays and visible light, and that they were likely to be electromagnetic waves or pulses. He also attributed the decrease in the intensity of the X-ray beam, observed by Rutherford, to the production of ions from the gas molecules, with each ionization leading to a small decrease in the beam's intensity.

Based on these first accomplishments, the ionization of gases was used to study the nature of the particles created from the interaction between the X-rays and the gas. By using a cloud chamber designed in 1897 by Wilson [WIL 97], Thomson [THO 98b] used the ionization of gases by X-rays to measure the electric charge of the electrons[2] created by the X-rays traveling through the gas. By measuring the electrical current produced by the ionization of various polyatomic gases, the same author showed that the electrons correspond to a modification of the atoms themselves, rather than to the simple dissociation of gas molecules [THO 98c]. This result was confirmed by Rutherford and McClung [RUT 00], who measured, in 1900, the energy required for the ionization of certain gases. This is how they showed that an electron accounts for a very small part of the mass in an atom.

We mentioned above that, at the dawn of the 20th century, the nature of X-rays was already well known. Evidence of gas ionization by X-rays quickly led to the creation of devices designed to quantitatively measure the intensity of X-ray beams. This enabled researchers at the beginning of the last century to study in detail the interaction between X-rays and solid matter, leading, naturally, to the observation and quantitative analysis of scattering, and then diffraction, of X-rays.

Scattering, fluorescence and the early days of X-ray diffraction

Scattering and fluorescence

In 1897, Sagnac [SAG 97a, SAG 97b] observed that, by irradiating a metal mirror with an X-ray beam, the mirror would produce a radiation of the same nature as the incident beam, but much less intense. This radiation propagates in every direction and therefore cannot involve specular reflection. Sagnac noted that the intensity of this scattered radiation depends on the nature of the material irradiated with the primary X-ray beam [SAG 97b, SAG 99]. These experiments were confirmed by Townsend [TOW 99], who quantitatively measured the intensity of the scattered beams by using an ionization detector. Townsend observed that if the scattered beams, before reaching the detector, pass through a sheet of aluminum, then the residual intensity significantly depends on the nature of the scattering material. Unfortunately, he did not specify the chemical nature of the anticathode he was using to produce the primary X-rays, thus making it difficult to make the connection between this observation and a selective absorption effect.

---

2 In the paper in question, Thomson and other authors use the word “ion”, but are actually writing about electrons created by the X-ray-induced ionization. In this case, the word ion is merely the present participle of the Greek verb *ienai*. Therefore, *ion* means going, and refers to particles in motion.

As we have mentioned already, Thomson showed that when a charged particle slows down, it causes the emission of electromagnetic radiation [THO 96b, THO 98a]. Based on these considerations, the same author found a simple explanation to the scattering effect observed by Sagnac. By assuming that the atoms contain charged particles, irradiating these atoms with an electromagnetic wave (the X-rays) would disturb the trajectory of these particles and modify their speed. This explained the subsequent emission of secondary X-rays [THO 98d]. Starting with this simple demonstration, Thomson calculated the intensity of the beam scattered during the interaction between an electron and an X-ray beam. This calculation led him to the now famous Thomson formula, which gives the scattering power of an electron. Once these preliminary results had been achieved, several authors, between 1900 and 1912, characterized in detail this secondary emission phenomenon, which would later come to be called scattering.

In 1906, Thomson [THO 06a, THO 06b] showed that the intensity of the scattered beam increases with the atomic mass of the scattering elements. He measured the intensity of the scattered beams by using a crude ionization detector, in which the ionized gas is the air located between the surface of the sample, consisting of a flat plate or a powder, and a metal grating placed a few millimeters away from that surface. He managed, nevertheless, to establish a direct link between the atomic mass of over 30 elements of the periodic table and the intensity scattered by these elements [THO 06b]. Also, he noticed that the scattered intensity increases with the atomic number, but this relation is not strictly linear: there are gaps in the intensity (see Figure 2). Thomson noted that the position and the amplitude of these intensity gaps directly depend on the nature (hard or soft) of the X-rays used.

These discontinuities in the emitted intensity were studied from a more general perspective by Barkla and Sadler [BAR 06b, BAR 08a, BAR 08b, BAR 08c, SAD 09]. These two authors presented a combined analysis of secondary emission and absorption of X-rays by solid matter. The characteristics of the scattered radiation were investigated by measuring their intensities after absorption by a sheet of aluminum with a known thickness. Barkla showed by this way that there are sharp discontinuities in the graphs showing the emitted intensity or the absorption coefficient plotted according to the atomic number of the irradiated material, located in the same places [BAR 08c]. The positions of these discontinuities do not depend on the intensity of the primary beam, but only on its "hardness[3]" [BAR 08a]. This author makes a distinction between two effects involving the secondary beams emitted by the irradiated substances: he observes, as Thomson did, the presence of a diffuse signal with characteristics similar to the incident beam, and also a more intense signal with characteristics specific to the nature of the irradiated element. Barkla adds that this emission of X radiation involves the ejection of electrons from

3 The words energy and wavelength were not yet used at the time.

the atoms irradiated by the primary beam. This ejection disturbs the atoms and results in the emission of an electromagnetic wave specific to the atom in question [BAR 08b]. The works of Barkla, which were quickly confirmed by the results of other authors [CHA 11, GLA 10, WHI 11], constituted the first evidence of X-ray fluorescence, whose developments in elementary analysis are still known today.

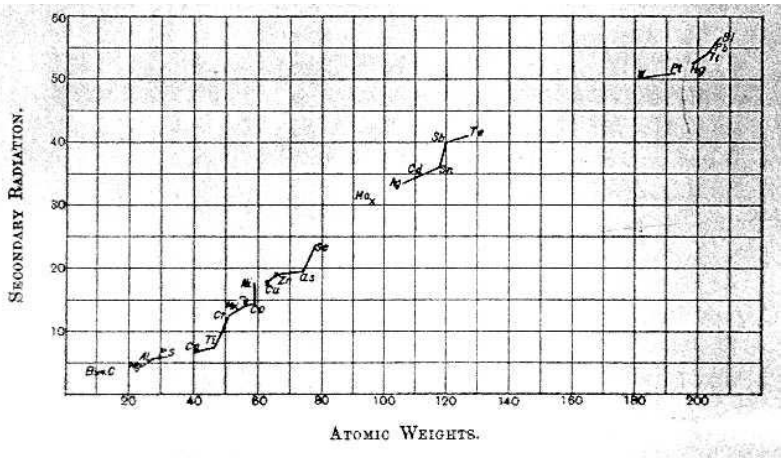

Figure 2. *Evolution of the scattered intensity according to the atomic masses of the scattering atoms (Thomson, 1906 [THO 06b])*

All of these studies led by Thomson, Barkla and Sadler, involving the secondary radiation emitted by solids irradiated with X-ray beams, were consistent with the results of Thomson described above, and tend to show that this secondary emission is the result of an interaction between the electrons of the atoms and the electromagnetic wave, associated by Thomson and Barkla with the X-rays. This wave description was disputed by Bragg [BRA 07, BRA 11], who considered that, if X-rays are "energy bundles" concentrated in extremely small volumes, as Thomson claimed, then they should be diverted when they travel through the atoms. The concept developed by Thomson leads to the assumption that the radiation scattered by the irradiated atoms is isotropic and, in particular, independent of the incident beam's direction of propagation. This is why Bragg focused on experimentally proving that the intensity distribution of secondary X-rays is not isotropic [BRA 07, BRA 09]. Barkla refuted Bragg's arguments in favor of a particle-based description of X-rays, by showing that it would be very difficult otherwise to account for the polarizable nature of X-rays [BRA 08a]. He added that wave theory can account for a certain anisotropy in the distribution of the scattered intensity, since the intensity would be higher in the incident beam's direction of

propagation than it would in the perpendicular direction. This argument did not convince Bragg and Glasson, who showed that the intensity of radiation that has traveled through a thin plate of scattering material is greater than that measured on the side of the incident beam [BRA 09].

Crowther presented a series of articles on how to experimentally determine the shape of the intensity distributions for the secondary X-rays emitted by thin plates irradiated with primary X-rays [CRO 10, CRO 11a, CRO 11b, CRO 12a, CRO 12b]. This way, and in agreement with Bragg, he showed that the intensity of the secondary radiation is much greater on the side opposite to the surface irradiated by the incident beam. Crowther notes [CRO 12a], however, that this is not enough to settle on the nature of X-rays with regard to the wave theory or the particle theory. This led him to think that a second phenomenon occurs on top of classical scattering, corresponding, for example, to the emission of X-rays, associated with the emission of electrons inside the materials irradiated by the primary X-ray beam. This interpretation was in perfect agreement with the works of Barkla and Sadler [BAR 08b] who, as we have mentioned before, were the first to observe X-ray fluorescence. Therefore, in the end, the anisotropic shape of the secondary X radiation's intensity distribution was interpreted as the result of a combination of two different types of emission: scattering and fluorescence [BAR 11].

X-ray diffraction by a slit

While some were studying the nature of secondary X-ray emission, other authors, Germans mostly, conducted experiments in order to observe X-ray diffraction by very thin slits. Given the fact that X-rays are similar to visible light, and due to their high penetrating ability, which means that their wavelengths must be very small, these authors surmised that they would be able to observe Fresnel diffraction by placing a slit as thin as possible on the path of an X-ray beam as punctual as possible. There were two goals to these studies, which were initiated by Fomm [FOM 96]. They consisted, on the one hand, of demonstrating that X-rays are waves and, on the other hand, of measuring their wavelength.

Wind and Haga [HAG 99, HAG 03, WIN 99, WIN 01] thus presented their first observations of Fresnel fringes obtained with X-rays. By measuring the space between these fringes, they were able to quantitatively estimate the wavelength of X-rays. The value they found was in the range of one angström. The results of these studies were disputed by Walter and Pohl [WAL 02, WAL 08, WAL 09]. They examined the works of their colleagues and conducted new experiments, by using slits a few micrometers wide placed, roughly one meter away from the photographic plate. They did not observe any fringes in the photographs they obtained and concluded that the diffraction effect did not occur. By considering, however, that the

propagation of X-rays is the same as for waves, they inferred that the associated wavelength had to be extremely small and suggested the value of 0.1 angström. Furthermore, Walter and Pohl considered that the photographs taken by Wind and Haga simply corresponded to an increase in width of the direct beam, and that the fringes obtained could be caused, for example, by an effect related to overexposure.

Convinced that X-rays are waves, Sommerfeld suggested a mathematical analysis of X-ray diffraction in several articles [SOM 00a, SOM 00b, SOM 01]. Based on these works, he was able to use the images observed by Haga and Wind to confirm that X-rays have a very small wavelength. In March 1912, shortly before Friedrich, Knipping and Laue's breakthrough experiment (see below), he published [SOM 12] which is a combined analysis of the works of Wind and Haga on the one hand, and of Walter and Pohl on the other hand. This study was based on a quantitative measurement of the darkening of the photographs taken by various authors. This measurement was performed by Koch [KOC 12], who was Röntgen's assistant at the time. Koch concluded, in contradiction with Walter and Pohl, that their photographs could display regular fluctuations in the way they darkened. From this analysis and by calculating the intensity profiles of fringe patterns according to the wavelength, the opening of the slit and the slit-photographic plate distance, Sommerfeld established the existence of a diffraction effect and approximately confirmed the wavelength announced by Haga and Wind.

This debate over X-ray diffraction by slits was temporarily interrupted, probably because of the discovery of X-ray diffraction by crystals and also because of World War I. In 1924, Walter resumed his work. After having shown as early 1909 [WAL 09] that the slit's opening had to be extremely small, he used a V-shaped slit with an opening 40 μm wide at the top and with a length of 18 mm. Walter irradiated this slit with X-ray radiation produced by a copper anticathode and actually observed interference fringes [WAL 24a, WAL 24b] which made it possible to find values for the K_α and K_β wavelengths of this compound that were in agreement with those obtained with diffraction by crystals. Immediately, these studies were independently confirmed by Rabinov [RAB 25], who conducted the same kind of experiment with a V-shaped slit. This author placed, between the molybdenum X-ray source and the slit, a crystal that made it possible to select a single wavelength by diffraction and therefore to improve the quality of the interference images.

The first studies of diffraction by crystals

In 1910, Ewald began his thesis in Munich under the supervision of Sommerfeld, the director of the theoretical physics laboratory, and defended it on February 16th, 1912 [EWA 12]. The subject, suggested by Sommerfeld, consisted of studying the interaction between an incident electromagnetic wave and a periodic

lattice of dipoles. Laue, who had been a member of the same laboratory since 1909, worked on wave physics at the time. By considering, according to the works of Barlow [BAR 97], that crystals were likely to be a periodic three-dimensional packing of atoms, he discussed with Ewald the consequences of his results on the interactions between these crystals and X-rays, which were known at the time to have a very small wavelength [HAG 99, HAG 03, KOC 12, SOM 00a, SOM 00b, SOM 01, SOM 12, WAL 02, WAL 08, WAL 09, WIN 99, WIN 01], probably in the same range as the interatomic distances inside crystals.

Laue suggested to Friedrich, who was Sommerfeld's assistant, and to Knipping, who was Röntgen's assistant, to conduct experiments that would consist of observing the interference of X-rays scattered by atoms in a single crystal. In order to do this, Friedrich and Knipping constructed a device comprised of an X-ray source (a Crookes tube), a sample holder making it possible to place the single crystal on the trajectory defined by this tube and a slit and, finally, a photographic film located behind the single crystal (see Figure 3). The crucial experiment was conducted on April 21st, 1912. Laue and his colleagues irradiated a sphalerite crystal with a polychromatic X-ray beam and observed on the photographic plate the first ever X-ray diffraction pattern with crystals [FRI 12] (see Figure 4). This discovery led to a new field in experimental physics: radiocrystallography. Two new applications appeared: on the one hand, measuring the wavelength of X-rays and, on the other hand, determining the structure of crystals. Shortly thereafter, Laue published several articles [FRI 12, LAU 13a, LAU 13b] in which he laid out the "Laue relations" and showed that the diffraction spots are distributed along conic curves.

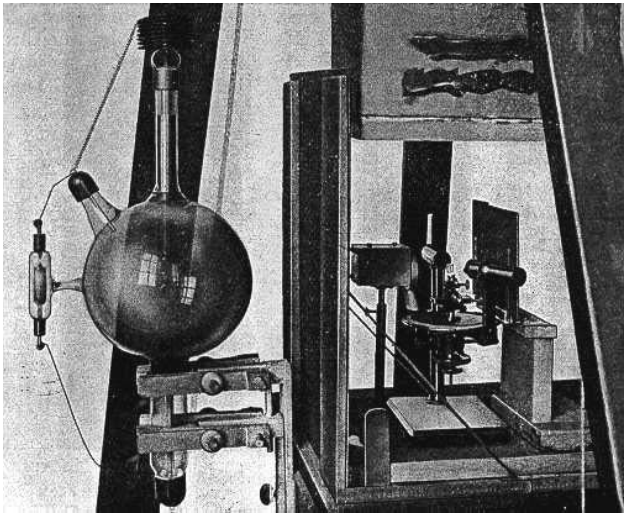

Figure 3. *Friedrich, Knipping and Laue's diffractometer*

Very quickly, the importance of these findings was given proper recognition [BRA 12a, LOD 12, TUT 12]. Bragg immediately understood that these results and their interpretations made by Laue were perfectly consistent with the wave approach to X-rays and would be difficult to explain by describing X-rays as particles, which was the theory he stood by. This led Bragg, in October 1912, to publish a short commentary on the results obtained by Laue and his colleagues [BRA 12a]. He suggested that the spots observed on Laue's photographs could be the result of beams traveling through "paths" laid out between the "molecules" that comprise the crystal. This idea was disputed by Tutton [TUT 12] who, while staying in Munich, produced several additional photographs with a sphalerite crystal by varying the angle between the direction of the incident beam and the sides of the crystal sample. He observed that a slight angular shift simply caused the spots on the film to move, thus resulting in a pattern that was no longer symmetrical with respect to the trace of the direct beam. Tutton inferred from this result that the crystal lattice was, in fact, responsible for the observed patterns. Two weeks later, Bragg [BRA 12b] answered Tutton. He admitted that the phenomenon of X-ray diffraction by crystals tends to show that X-rays, like light, are waves, but he noted that certain properties of X-rays and light can be explained by considering them as particles. Thus, Bragg concluded by pointing out that what matters is not to determine whether light and X-rays are particles or waves, but instead to find a theory that could combine the two representations.

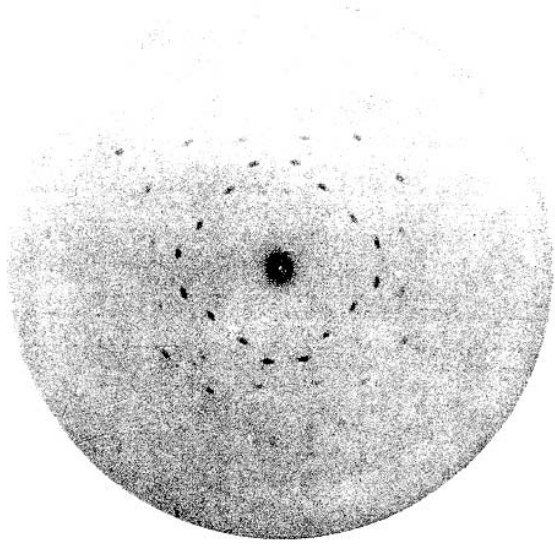

Figure 4. *Diffraction photography of a zinc sulfate single crystal. Courtesy of Friedrich and Knipping [FRI 12]*

In November 1912, W.L. Bragg, the son of W.H. Bragg, gave before the Cambridge Philosophical Society a detailed analysis of Laue's results. He showed that Laue's photographs can only be explained by assuming that the incident beams has a continuous wavelength spectrum. He noted that, if the crystal is considered a stacking of families of planes comprised of atoms, then, since each family is a series of planes parallel with each other and a distance d apart, the interference phenomenon observed by Laue can be interpreted as caused by the reflection of X-ray beams with a given wavelength on the crystal planes. The reflected waves can only interfere if the wavelength and the angle between the incident beam and the normal to the family of planes in question are such that $\lambda = 2d \cos \theta$[4]. Bragg established the second fundamental law of X-ray diffraction, following the conditions laid out by Laue. The concept of reflections[5] on crystal planes, which was theoretical at first, led W.L. Bragg to design a diffractometer [BRA 12d] that was different from Laue's. Following the advice of Wilson, he created a device, in order to prove his theory, where the incident X-ray beam hits a cleaved crystal at an incidence angle equal to what will quickly come to be named as the "Bragg angle". A photographic plate, replaced shortly by an ionization detector [BRA 13a], made it possible to measure the intensity of beams that are "reflected" at an angle equal to the incidence angle. This configuration, referred to as the *Bragg configuration*, enabled the user to measure the diffracted beams on the side of the sample where the source is located, whereas in the Laue configuration, the measurement was made after the transmission of the X-ray beam though the crystal.

4 The expression $\lambda = 2d \cos \theta$, where θ is the angle between the normal to the diffracting planes and the incident beam, was gradually replaced with $\lambda = 2d \sin \theta$, where θ is the angle between the incident beam and the diffracting angles.

5 The use of the word "reflection" has been, and is still, a source of confusion between X-ray diffraction and reflection as described the Snell-Descartes laws.

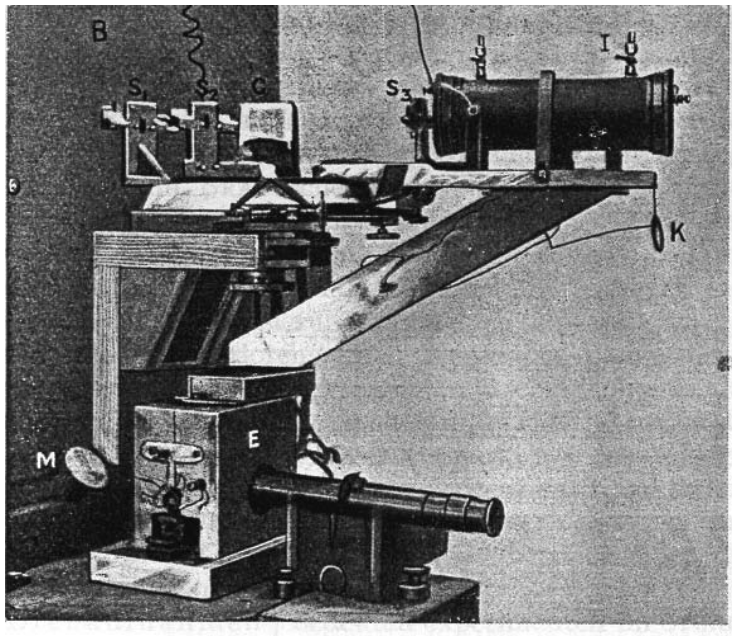

Figure 5. *W.H. and W.L. Bragg's diffractometer*

A photograph of this system is shown in Figure 5. In December 1912, only eight months after Friedrich, Knipping and Laue's discovery, W.L. Bragg conducted another X-ray diffraction experiment [BRA 12d]. He irradiated the surface of a cleaved mica crystal with a thin X-ray beam and observed intense spots on a photographic film. The author noticed that when the incidence angle is modified, the diffraction angle also changes. He hastily concluded from this that the effect he was observing follows the same reflection law as visible light. W.L. Bragg mentioned specular reflection because the experiments were always being conducted in such a way that the incidence angle was equal to the diffraction angle. In a short time, many authors [BAR 13, BRO 13, HUP 13, KEE 13, TER 13] conducted experiments using the same method as W.H. and W.L. Bragg. They concluded, in agreement with the Braggs and from experiments conducted with sodium chloride [BRO 13, HUP 13, TER 13], mica [HUP 13, KEE 13] and fluorite [BRO 13, TER 13], that the spots observed on film or on a fluorescent screen [BRO 13] were caused by the reflection on crystal planes that contained many atoms.

In April 1913, W.H. and W.L. Bragg [BRA 13b] went before the Royal Society of London to present the first quantitative measurements of diffraction by a single crystal. These measurements were achieved with the diffractometer shown in Figure

5. A cleaved crystal was placed on a rotating platform so as to have the rotation axis inside the cleavage plane. The beam's incidence angle on the cleavage plane was maintained constant, whereas the diffracted intensity was measured by using the ionization chamber rotating around the same axis. The authors noted that an intensity maximum is observed when the angle that gives the detector's position is equal to twice the incidence angle. Based on this observation, they produced diffractograms by simultaneously rotating the crystal and the ionization chamber, so that the angle between the transmitted beam and the detector would always be equal to twice the incidence angle of the beam with the cleavage plane. This will come to be referred to as the Bragg-Brentano configuration. Such a diffractogram is shown in Figure 6.

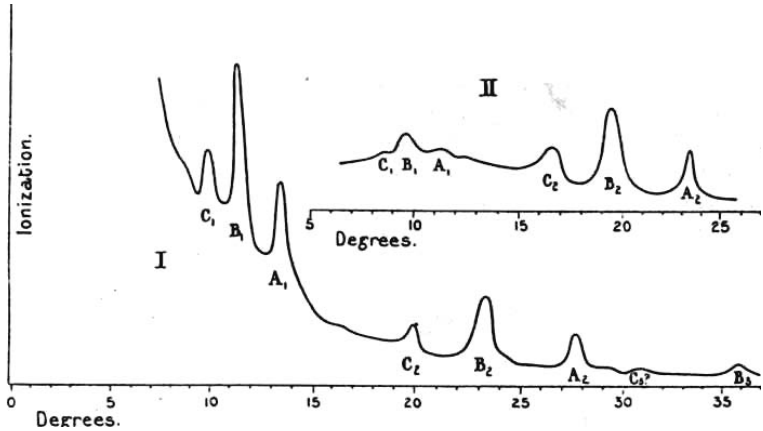

Figure 6. *Diffractograms produced by W.H. and W.L. Bragg with sodium chloride crystals. I: diffractogram obtained with a crystal cleaved along the (100) planes, II: diffractogram obtained with a crystal cleaved along the (111) planes*

This is how the authors observed the first two orders of reflection for the (h00) planes in example I and for the (hhh) planes in example II. They found three maxima for each reflection. Since the presence of these three peaks has nothing to do with the choice of the crystal, but is related to the nature of the anticathode, the Braggs concluded that these three peaks were related to the presence of three different radiations, each one of them having a specific wavelength. Therefore, the experimental method they suggested made it possible to determine the wavelength of these radiations by measuring the diffraction angles for several families of planes (h00), (hhh), etc. [BRA 13c].

These results were used by Moseley and Darwin [MOS 13], who studied the intensity reflected by various cleaved crystals. These authors, by using a diffractometer similar to that used by the Braggs, measured the reflected intensity according to the incidence angle. The studies were always conducted in symmetrical reflection conditions. When the incidence angle is relatively small, a significant intensity is measured continuously, whereas for higher incidence angles, in addition to this first signal, intensity peaks located at specific angles are obtained. Moseley and Darwin inferred from this result that the X-ray beam emitted by the tube contains two types of radiation: a continuous wavelength spectrum combined with peaks at specific wavelengths.

At the same time, it quickly became clear that X-ray diffraction by crystals should make it possible to explore the internal structure of crystals [TUT 13a, TUT 13b]. Studies of crystals that were made before the discovery of X-ray diffraction, which served as the basis for Laue's breakthrough experiment, attributed the presence of very flat surfaces and the existence of well defined cleavage planes, to a very regular arrangement of elementary units that comprise the crystals. It was known that crystals were the result of the infinite repetition in three dimensions of an elementary cell, containing one or more molecules of the substance in question. The works of Fedorov [FED 12], among others, had led to the definition of 230 space groups with which any crystal could be described. X-ray diffraction by crystals became an experimental method for studying crystal symmetry, but also the internal structure of the crystal cell, which was still uncharted territory at the time.

Measurements of the diffraction angles with the Bragg diffractometer, as well as the interpretation of Laue's photographs by using stereographic projections [BRA 13d] led to determining the Bravais lattice and the dimensions of the crystal cell. The study of relative values of diffracted intensity made it possible to suggest a structural arrangement [BAR 14, BRA 13d, BRA 13, BRA 14a, BRA 14b]. These studies were spearheaded by W.H. and W.L. Bragg who very early on, in 1913, discovered the structure of potassium chloride, potassium bromide, sphalerite, cooking salt, fluorite, calcite, pyrite [BRA 13d] and diamond [BRA 13e]. Note that these studies are largely based on the interpretation of Laue's photographs. In November 1912 [BRA 12c], W.L. Bragg had already shown that the geometric shapes shown in those photographs could easily be interpreted by assuming that the incident X-ray beam was polychromatic. The Braggs simultaneously used photographs from Laue that were obtained with a polychromatic beam (the braking radiation) and diagrams obtained in reflection with their diffractometer by using a radiation as monochromatic as possible, produced by an anticathode made out of platinum or rhodium. By comparing the intensities diffracted by crystals of potassium bromide or chloride on the one hand, and diamond and sphalerite on the other, Bragg showed that the diffracted intensity was strongly dependent on the mass of the atoms comprising the crystals [BRA 14a].

In 1915, Bragg spoke before the London Philosophical society [BRA 15] outlining his concepts. He showed that the crystal planes "reflecting" the X-rays are in fact a simplified way of representing the crystal's actual structure, which can be described as a continuous medium in which the electron density varies periodically. Based on this idea, Bragg showed, in agreement with his experiments, that the diffracted intensity decreases like the square of the order of reflection. Additionally, he noted that X-ray diffraction, in this regard, must make it possible to determine the electron density associated with each atom.

These experimental results and their interpretations clearly showed that the study of the diffracted intensity makes it possible to accurately determine the nature and the positions of the atoms inside the crystal cell. Nevertheless, the link between structural arrangement and the value of the total diffracted intensity was not proven. This aspect will be studied in detail by Darwin, who showed in two famous articles [DAR 14a, DAR 14b] that, on the one hand, the intensity is not concentrated in one point (defined by the Laue relations), but that there is a certain intensity distribution around this maximum (referred to as the Darwin width) and, on the other hand, that real crystals show a certain mosaicity that can account for the values of the diffracted intensity measured experimentally. These considerations were based on a description similar to that used for visible light in optics and constituted a preamble to the dynamic theory of X-ray diffraction, the core ideas of which were later established by Ewald [EWA 16a, EWA 16b].

While these experimental and theoretical studies of X-ray diffraction by single crystals were being developed, other authors thought about studying diffraction figures obtained when the analyzed sample is comprised of a large number of small crystals. Debye and Scherrer [DEB 16] in 1916, in Germany, followed by Hull [HUL 17a, HUL 17b] in 1917, in the USA, irradiated a cylindrical polycrystalline sample with an X-ray beam, and observed diffraction arcs on a cylindrical film placed around the sample. By measuring the angular position of these arcs, they were able to estimate, by using the Bragg relation, the characteristic interplanar distances of the diffracting planes, whereas the intensities were measured from the darkening of the film. These studies significantly widened the range of studies for X-ray diffraction, since this technique could be used on samples that were much more common than single crystals.

PART 1

Basic Theoretical Elements, Instrumentation and Classical Interpretations of the Results

This page intentionally left blank

Chapter 1

Kinematic and Geometric Theories of X-Ray Diffraction

When matter is irradiated with a beam of X photons, it emits an X-ray beam with a wavelength equal or very close to that of the incident beam, which is an effect referred to as scattering. The scattered energy is very small, but in the case where scattering occurs without a modification of the wavelength (coherent scattering) and when the scattering centers are located at non-random distances from one another, we will see how the scattered waves interfere to give rise to diffracted waves with higher intensities. The analysis of the diffraction figure, that is, the analysis of the distribution in space of the diffracted intensity, makes it possible to characterize the structure of the material being studied. This constitutes the core elements of X-ray diffraction. Before we discuss diffraction itself, we will first describe the elementary scattering phenomenon.

1.1. Scattering by an atom

1.1.1. *Scattering by a free electron*

1.1.1.1. *Coherent scattering: the Thomson formula*

The scattering of X-radiation by matter was first observed by Sagnac [SAG 97b] in 1897. The basic relation expressing the intensity scattered by an electron was laid down the following year by Thomson [THO 98d].

Consider a free electron located inside a parallel X-ray beam with intensity I_0. This beam constitutes a plane wave traveling along the x-axis, encountering a free electron located in O. The electron, subjected to the acceleration:

$$\vec{\gamma} = \frac{\vec{E}_0 e}{m} \qquad [1.1]$$

starts vibrating and emits an electromagnetic wave whose electrical field vector is written, in P, as:

$$\vec{E} = \vec{\gamma} \frac{m r_e}{e} \frac{\sin\varphi}{r} \qquad [1.2]$$

where e is the charge of the electron, m is the mass of the electron, r_e is the radius of the electron, φ is the angle between $\vec{OP}$ and $\vec{\gamma}$, and r is the distance between O and P.

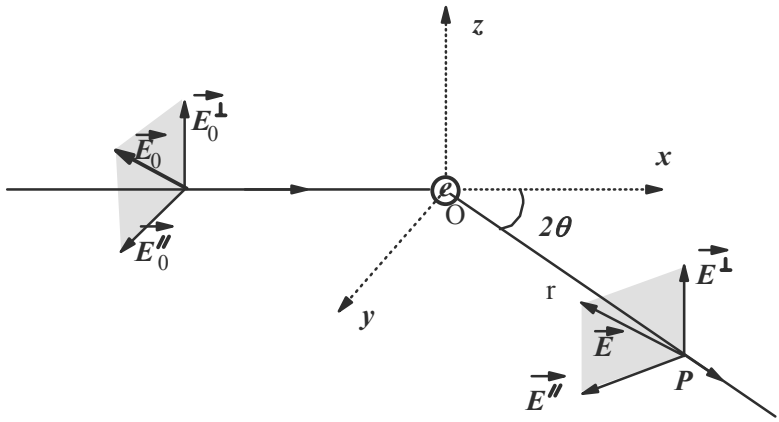

Figure 1.1. *Coherent scattering by a free electron*

Therefore, we obtain a wave traveling through P with the same frequency as the incident wave and with amplitude:

$$E = E_0 r_e \frac{\sin\varphi}{r} \qquad [1.3]$$

The vector $\vec{E}_0$ can be decomposed in two independent vectors $\vec{E}_0^{\perp}$ and $\vec{E}_0^{//}$. The expression for the amplitude of vector $\vec{E}^{\perp}$ is:

$$E^{\perp} = E_0 \frac{r_e}{r} \qquad [1.4]$$

$I^{\perp}$, which is the corresponding intensity in P, is defined as the flow of energy traveling through a unit surface located in P over 1 second. The ratio of the incident and scattered waves in P is equal to the squared ratio of the amplitudes of the electrical fields; therefore we have:

$$I^{\perp} = I_0 \frac{r_e^2}{r^2} \qquad [1.5]$$

The unit surface located in P is observed from O with a solid angle equal to $1/r^2$. Therefore, the intensity in question, with respect to the unit of solid angle is $I^{\perp} = I_0 r_e^2$. Likewise, the intensity along the Oy-axis is given by $I^{//} = I_0 r_e^2 \cos^2 2\theta$.

Any incident beam will be scattered with the proportions x and (1 – x) along the directions Oz and Oy and thus the total intensity in P can be written as:

$$I = I_0 r_e^2 [x + (1 - x) \cos^2 2\theta]$$

If the beam is not polarized, then x = 0.5 and therefore:

$$I = I_0 r_e^2 \left(\frac{1 + \cos^2 2\theta}{2} \right) \qquad [1.6]$$

From now on, we will refer to this intensity as I_e and therefore we have:

$$I_e = I_0 r_e^2 \left(\frac{1 + \cos^2 2\theta}{2} \right) \qquad [1.7]$$

This relation is called the Thomson formula [THO 98d]. It has a specific use: the scattering power of a given object can be defined as the number of free and independent electrons this object would have to be replaced with, in order to obtain the same scattered intensity.

1.1.1.2. *Incoherent scattering: Compton scattering [COM 23]*

In addition to the coherent scattering just discussed, X photons can scattered incoherently, that is, with a change in wavelength. This effect can be described with classical mechanics by considering the incident photons and the electrons as particles and by describing their interactions as collisions, as shown in Figure 1.2.

$\vec{S}_0$ and $\vec{S}$ are the unit vectors of the incident and scattered beams, 2θ being the scattering angle, m the mass of the electron and V the electron's recoil velocity once it is struck by the photon. If the vibration frequencies of the incident photon and the scattered photon are denoted by ν and ν', respectively, the energy conservation principle leads to the relation:

$$h\nu = h\nu' + \frac{1}{2}mV^2 \qquad [1.8]$$

By applying the momentum conservation principle, we get:

$$\frac{h\nu}{c}\vec{S}_0 = \frac{h\nu'}{c}\vec{S} + m\vec{V} \qquad [1.9]$$

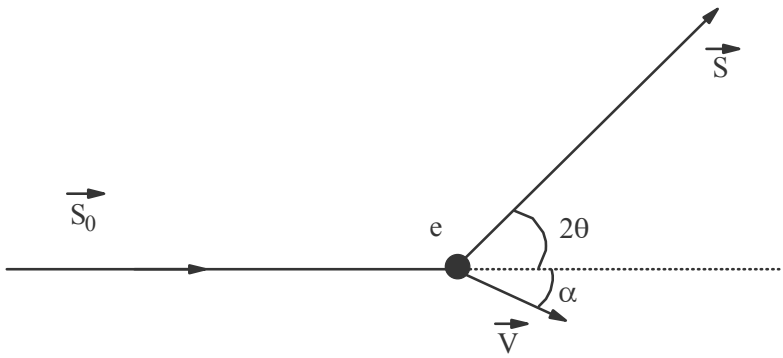

Figure 1.2. *Incoherent scattering by a free electron*

Calculation of the difference in wavelength between the incident wave and the scattered wave

By using the two principles just applied, we will be able to calculate this difference δλ, since we have:

$$\begin{cases} h\nu = h\nu' + \dfrac{1}{2}mV^2 \\ \dfrac{h}{c}\left(\nu\vec{S}_0 - \nu'\vec{S}\right) = m\vec{V} \end{cases} \Rightarrow \begin{cases} hc\left(\dfrac{1}{\lambda} - \dfrac{1}{\lambda+\delta\lambda}\right) = \dfrac{1}{2}mV^2 \\ \dfrac{h}{\lambda}\left(\vec{S}_0 - \vec{S}\right) - \dfrac{h}{c}\delta\nu\vec{S} = m\vec{V} \end{cases} \Rightarrow \begin{cases} hc\left(\dfrac{\delta\lambda}{\lambda(\lambda+\delta\lambda)}\right) = \dfrac{1}{2}mV^2 \\ -h\vec{s} - \dfrac{h}{\delta\lambda}\vec{S} = m\vec{V} \end{cases}$$

with:

$$\vec{s} = \frac{\vec{S} - \vec{S}_0}{\lambda} \quad \text{and} \quad \left\|\vec{s}\right\| = \frac{2\sin\theta}{\lambda}$$

$$\Rightarrow \begin{cases} hc\dfrac{\delta\lambda}{\lambda^2} \approx \dfrac{1}{2}mV^2 \\ -h\sin 2\theta\left\|\vec{s}\right\| - \dfrac{h}{\delta\lambda}\cos 2\theta\left\|\vec{S}\right\| = mV\cos\alpha \\ h\cos 2\theta\left\|\vec{s}\right\| - \dfrac{h}{\delta\lambda}\sin 2\theta\left\|\vec{S}\right\| = mV\sin\alpha \end{cases} \Rightarrow \begin{cases} hc\dfrac{\delta\lambda}{\lambda^2} \approx \dfrac{1}{2}mV^2 \\ -h\sin 2\theta\dfrac{2\sin\theta}{\lambda} - \dfrac{h}{\delta\lambda}\cos 2\theta = mV\cos\alpha \\ h\cos 2\theta\dfrac{2\sin\theta}{\lambda} - \dfrac{h}{\delta\lambda}\sin 2\theta = mV\sin\alpha \end{cases}$$

because $\vec{S}$ is a unit vector.

$$\Rightarrow \begin{cases} V^2 \approx \dfrac{2hc}{m\lambda^2}\delta\lambda \\ h^2\left(\dfrac{2\sin 2\theta\sin\theta}{\lambda} + \dfrac{\cos 2\theta}{\delta\lambda}\right)^2 = m^2V^2\cos^2\alpha \\ h^2\left(\dfrac{2\cos 2\theta\sin\theta}{\lambda} - \dfrac{\sin 2\theta}{\delta\lambda}\right)^2 = m^2V^2\sin^2\alpha \end{cases}$$

$$\Rightarrow \begin{cases} V^2 \approx \dfrac{2hc}{m\lambda^2}\delta\lambda \\ m^2V^2\cos^2\alpha \approx h^2\dfrac{4\sin^2 2\theta\sin^2\theta}{\lambda^2} \\ m^2V^2\sin^2\alpha \approx h^2\dfrac{4\cos^2 2\theta\sin^2\theta}{\lambda^2} \end{cases}$$

$$\Rightarrow \begin{cases} V^2 \approx \dfrac{2hc}{m\lambda^2}\delta\lambda \\ m^2V^2\left(\cos^2\alpha + \sin^2\alpha\right) \approx 4h^2\dfrac{\sin^2\theta}{\lambda^2}\left(\sin^2 2\theta + \cos^2 2\theta\right) \end{cases}$$

$$\Rightarrow 4h^2 \frac{\sin^2 \theta}{\lambda^2} \approx m^2 \frac{2hc}{m\lambda^2} \delta\lambda$$

and finally:

$$\delta\lambda \approx \frac{2h}{mc} \sin^2 \theta \approx 0{,}048 \sin^2 \theta \qquad [1.10]$$

Therefore, the variation in wavelength is independent of the initial wavelength and increases with θ.

In the case of a free electron, nothing prevents it from moving, since it is subjected to no outside force. Hence, the predominant effect is Compton scattering. However, it can be shown that the intensity of this scattering effect is accurately described by Thomson's relation. When considering a set of free electrons, the different waves scattered by these electrons have different wavelengths and therefore do not lead to interference effects. What we observe is merely the sum of the scattered intensities.

1.1.2. *Scattering by a bound electron*

In an atom, an electron can assume different energy states. If, during the interaction with the X photon, the state of the electron does not change, then the photon emitted by the atom has the same energy as the incident photon. Hence, the resulting scattering is coherent (Thomson scattering). On the other hand, if the electron's energy level changes, the scattered photon has a different energy and therefore a different wavelength from those of the incident photon: this is incoherent scattering. It means that by irradiating an atom with an X-ray beam whose energy is insufficient to cause electronic transitions, what we will observe is, for the most part, coherent scattering. Throughout this book, we will assume that this is the case.

Generally speaking, it can be shown that the total intensity scattered by a bound electron is equal to the coherent intensity scattered by a free electron, as given by the Thomson formula. This result can be expressed by the relation:

$$I_{\text{bound electron}}^{\text{Total}} = I_e = I_{\text{bound electron}}^{\text{Coherent}} + I_{\text{bound electron}}^{\text{incoherent}} \qquad [1.11]$$

Calculating the intensity of coherent scattering

Each electron moves about in an orbital and, if $\rho(\vec{r})$ denotes the charge density of the bound electron in any elementary volume dV of this orbital, vector $\vec{r}$ being the one shown in Figure 1.3, then $\rho(\vec{r})$ is expressed as $\rho(\vec{r}) = |\Psi(\vec{r})|^2$, where $|\Psi(\vec{r})|$ is a wave function which is a solution to the Schrödinger equation.

Since the volume dV contains the charge ρdV, it scatters an amplitude equal to the one scattered by one electron multiplied by ρdV. If we consider coherent scattering, the waves scattered by each elementary volume dV interfere, because they have the same wavelength. The coherent amplitude scattered by the bound electron is therefore given by the sum of the amplitudes scattered by each volume element dV and hence:

$$A^{\text{Coherent}}_{\text{bound electron}} = A^{\text{Free electron}} \iiint \rho(\vec{r}) e^{\phi} dV \qquad [1.12]$$

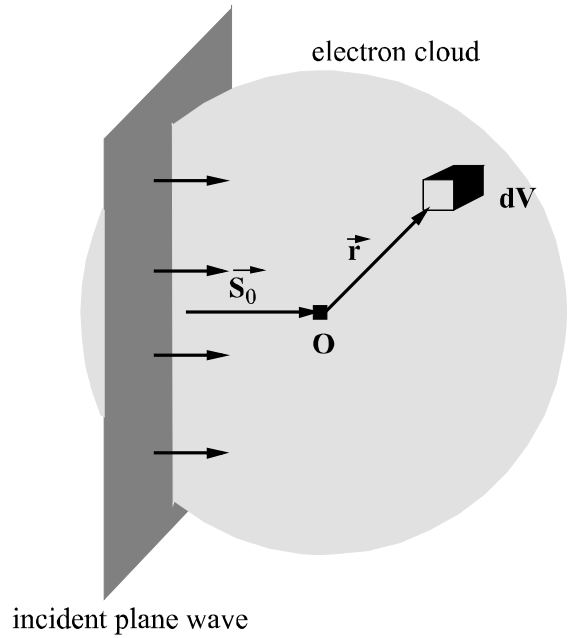

Figure 1.3. *Diagram showing the scattering electron cloud*

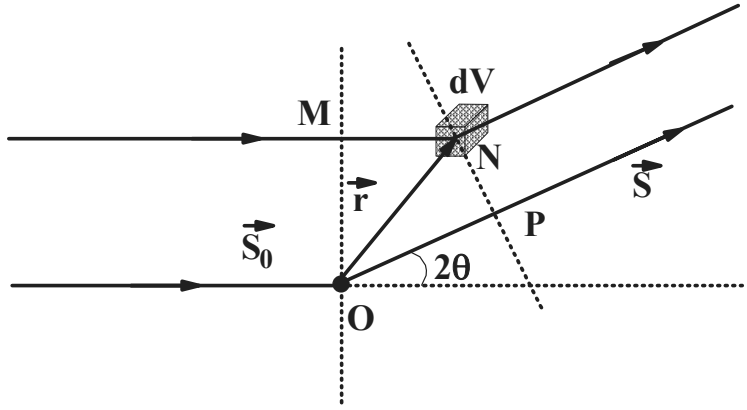

Figure 1.4. *Sum of the waves scattered by the entire electron cloud*

The path length between point O and the volume element dV is equal to $\delta = \vec{r}.(\vec{S} - \vec{S}_0)$ and the phase difference ϕ is expressed as:

$$\phi = -\frac{2\pi i\delta}{\lambda} \qquad [1.13]$$

We have already mentioned that the vector $\left(\vec{S} - \vec{S}_0\right)/\lambda$ is the scattering vector $\vec{s}$ and that $\left\|\vec{s}\right\| = 2\sin\theta/\lambda$; hence:

$$A_{\text{bound electron}}^{\text{Coherent}} = A^{\text{Free electron}} \iiint \rho(\vec{r}) e^{-2\pi i \vec{s}.\vec{r}} dV \qquad [1.14]$$

The following term is referred to as the electron cloud's scattering factor:

$$f = \iiint \rho(\vec{r}) e^{-2\pi i \vec{s}.\vec{r}} dV \qquad [1.15]$$

The scattered coherent intensity is equal to the product of the amplitude and the conjugate of the amplitude; therefore:

$$I_{\text{bound electron}}^{\text{Coherent}} = |f|^2 I_e \qquad [1.16]$$

We know that the total intensity scattered by the bound electron is equal to the coherent intensity scattered by the free electron, therefore the incoherent intensity is given by the following relation:

$$I_{\text{bound electron}}^{\text{Incoherent}} = \left(1 - |f|^2\right) I_e \qquad [1.17]$$

The scattering factor f depends on the vector $\vec{s}$ and, hence, on $\sin\theta/\lambda$, therefore, a variation in wavelength causes a variation in the scattering angle.

The scattering factor reaches its maximum for $\theta = 0$ and decreases with θ, meaning that the contributions to the total scattering from coherent scattering and Compton scattering behave as shown in Figure 1.5.

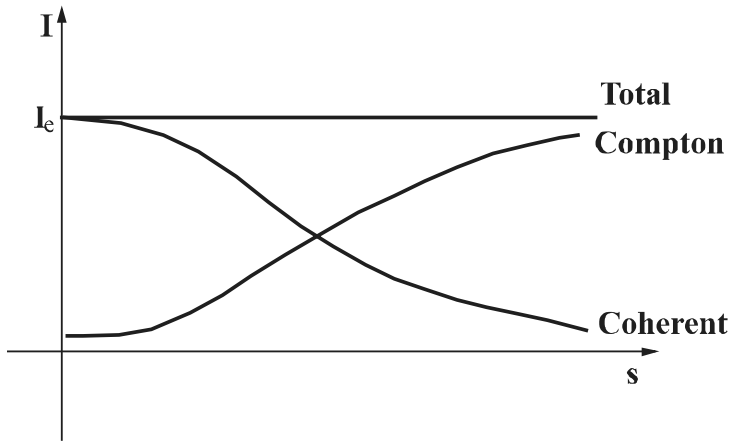

Figure 1.5. *Simplified representation of the coherent and incoherent intensities as a function of the scattering vector*

1.1.3. *Scattering by a multi-electron atom*

An atom with the atomic number Z contains Z electrons. The waves scattered by these Z electrons will contribute in different ways to the overall scattering by the atom, depending on which orbital they belong to.

The waves scattered coherently by each of the electrons all have the same wavelength. Therefore, they will interfere. Hence, the total scattered amplitude is the sum of the amplitudes scattered by each electron. The electron scattering factor, which is the amplitude scattered by an electron, was denoted earlier by f. For a given electron it depends on how far its orbital extends (see equation [1.15]). Therefore, the coherent intensity can be written as:

$$I_{atom}^{Coherent} = \left(\sum_{1}^{Z} f_j \right)^2 I_e \qquad [1.18]$$

and the atom's scattering factor is defined as:

$$f = \sum_{1}^{Z} f_j \qquad [1.19]$$

By knowing the radial distribution of the electronic densities for the different shells of a given atom, it becomes possible to calculate the corresponding scattering factors, the total scattering factor being equal to the sum of all of these terms. Generally speaking, the outer shells correspond to a very broad distribution of the electronic density, but since coherent scattering is low when the scattering angle is high, these shells contribute only slightly to the coherent scattering of the atom. The electrons most involved in coherent scattering are the electrons in the inner shells. This important aspect is illustrated in Figure 1.6. Figure 1.6a shows a centered cross-section of various orbitals for the potassium ion K^+. Note, of course, that the electron density functions for the orbitals 1s, 2s and 2p have a maximum located at small distances from the center of the ion, unlike orbitals 3p and 3s, which are further away from the nucleus. Figure 1.6b shows the electron scattering factors associated with each of these orbitals. The evolution of these factors is plotted according to the norm of the scattering vector $\vec{s}$. Note that, as soon as the values of $\|\vec{s}\|$ increase, the contributions to the overall scattering factor from orbitals 3p and 3s rapidly drop. On the other hand, the contribution from orbital 1s decreases very slowly with the value of $\|\vec{s}\|$, to the point that the contributions from the surface orbitals become negligible. These results tell us that the scattering effect is not much affected by the degree of ionization of the atoms in question.

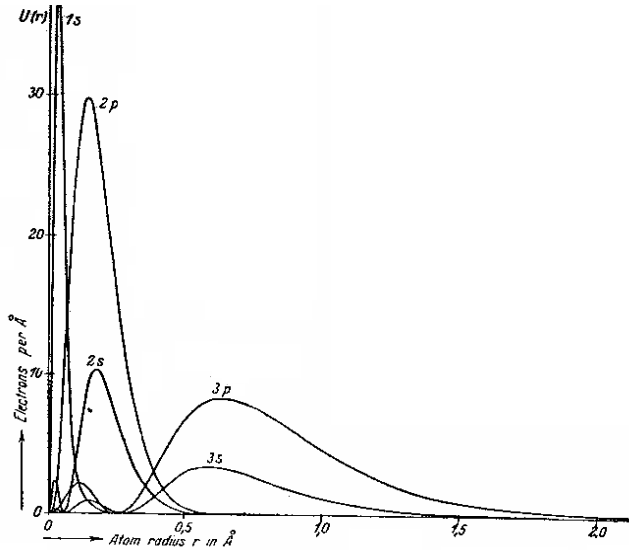

(a) radial distribution of the electron density in a potassium ion

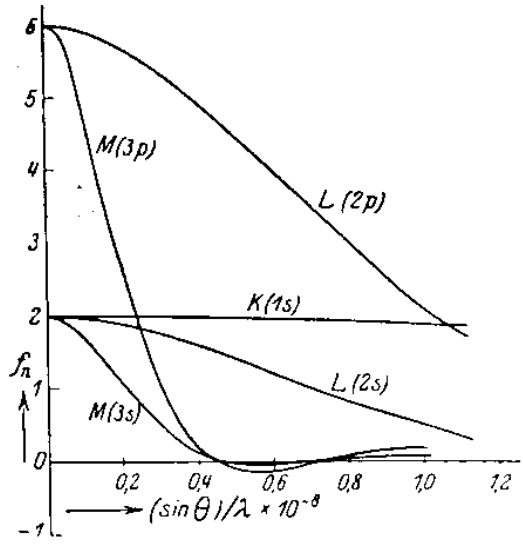

(b) scattering factors associated with each orbital

Figure 1.6. *Evolution of the scattering factors associated with each atomic orbital according to that orbital's electron density*

The values of the scattering factors for the various atoms are compiled in the *International Tables for Crystallography*.

In the case of incoherent radiation, which would then indicate inelastic scattering or also Compton scattering, the wavelengths of the radiations emitted by the various electrons are different, depending on what orbital is considered. Therefore, there is no interference. The intensity scattered by the entire atom is the sum of the intensities scattered by each of the electrons and it is written:

$$I_{atom}^{incohorent} = \left(\sum_{1}^{Z} \left(1 - f_j^2 \right) \right) I_e \qquad [1.20]$$

1.2. Diffraction by an ideal crystal

1.2.1. *A few elements of crystallography*[1]

1.2.1.1. *Direct lattice*

A crystal is a given atomic pattern repeated in three dimensions. The unit cell is defined as constituting a basis for the crystal lattice. This basis, which generally is not orthonormal, is defined by the triplet $\left(\vec{a}, \vec{b}, \vec{c}\right)$ and the angles between these different vectors are: $\alpha = \left(\vec{b}, \vec{c}\right)$; $\beta = \left(\vec{a}, \vec{c}\right)$; $\gamma = \left(\vec{a}, \vec{b}\right)$. Inside this cell, the position of each atom in the crystal pattern is specified by the vector $\vec{r}$. The position of each cell is specified by the vector $\vec{R} = u\vec{a} + v\vec{b} + w\vec{c}$. The crystal is completely described by the translations along the cell's three vectors $\left(\vec{a}, \vec{b}, \vec{c}\right)$.

The lattice points can be arranged in atomic rows. If we go from the point (u,v,w) to the origin of the lattice, the line we draw will go through the points (0,0,0), (u,v,w), (2u,2v,2w), (3u,3v,3w), etc. For each lattice point there is another line, parallel to the first, and containing the same number of points. Thus, the lattice is decomposed in a series of regularly arranged, parallel rows. They are referred to as rows with indices [u,v,w].

---

1 The intent in this section is not to discuss crystallography extensively, but instead to simply point out in a few lines the elements that are essential to understanding the diffraction effect. It goes without saying that knowledge of crystallography is a prerequisite to understand X-ray diffraction. Many books give a detailed presentation of crystallography (see, for example, [GIA 96], published with support from the International Union of Crystallography).

Likewise, it is possible to define crystal planes where the lattice points are now arranged in parallel planes at equal distances from one another, forming a family of planes characterized by an interplanar distance. These families of planes are characterized by three integers (h,k,l), referred to as the Miller indices. If we consider the plane that passes through the origin of the lattice for a given family (h,k,l), then, by definition, the next plane intersects the axis $\vec{a}$ of the crystal cell in a/h, the axis $\vec{b}$ in b/k and the axis $\vec{c}$ in c/l (to make this simpler, we will denote $\|\vec{a}\|$ by "a", here and throughout this book, and likewise for "b" and "c"). The plane with indices (3,2,1) is shown in Figure 2.8. When one of the Miller indices is equal to zero, the intersection of this plane with the axis is pushed back to infinity and therefore the plane is parallel to this axis.

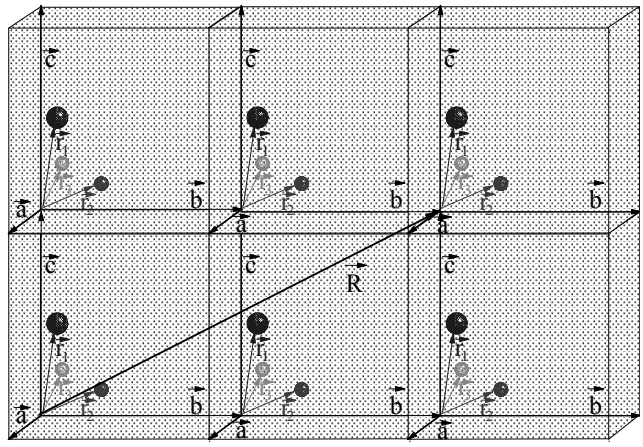

Figure 1.7. *Representation of an arbitrary crystal*

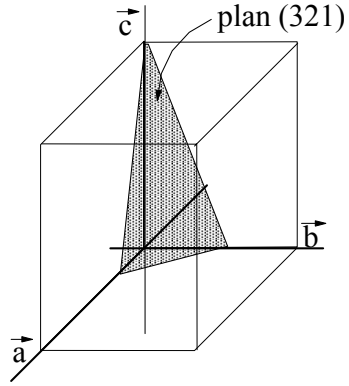

Figure 1.8. *The concept of the Miller indices*

1.2.1.2. *Reciprocal lattice*

The reciprocal lattice, which from a mathematical standpoint is equivalent to the dual space of the direct space, is very often used in X-ray diffraction, since it makes it possible to associate each family of planes with its normal.

The triplet $(\vec{a}^*, \vec{b}^*, \vec{c}^*)$ constitutes a basis of this space if the vectors in question are such that they verify the following relations:

$$\begin{aligned} &\vec{a}^*.\vec{a} = 1 \quad \vec{b}^*.\vec{a} = 0 \quad \vec{c}^*.\vec{a} = 0 \\ &\vec{a}^*.\vec{b} = 0 \quad \mathbf{b}^*.\vec{b} = 1 \quad \vec{c}^*.\vec{b} = 0 \\ &\vec{a}^*.\vec{c} = 0 \quad \vec{b}^*.\vec{c} = 0 \quad \vec{c}^*.\vec{c} = 1 \end{aligned} \qquad [1.21]$$

The volume V of the direct lattice's primitive cell is given by $V = \vec{a}.(\vec{b} \wedge \vec{c})$, and likewise $V^* = \vec{a}^*.(\vec{b}^* \wedge \vec{c}^*)$. These relations can be used to express the vectors of the reciprocal lattice according to those of the direct lattice, resulting in the following equations:

$$\vec{a}^* = \frac{1}{V}\left(\vec{b} \wedge \vec{c}\right) \quad \vec{b}^* = \frac{1}{V}\left(\vec{c} \wedge \vec{a}\right) \quad \vec{c}^* = \frac{1}{V}\left(\vec{a} \wedge \vec{b}\right) \quad V^* = \frac{1}{V} \qquad [1.22]$$

Consider any vector of the reciprocal lattice $\vec{r}^* = h\vec{a}^* + k\vec{b}^* + l\vec{c}^*$ where h, k and l are any integers. Note in Figure 1.8 that the vectors $\vec{p} = (1/h)\vec{a} - (1/k)\vec{b}$ and $\vec{q} = (1/h)\vec{a} - (1/l)\vec{c}$ belong to the plane of the direct lattice with (h,k,l) as its Miller indices. The product $\vec{r}^*.\vec{p}$ is written:

$$\vec{r}^*.\vec{p} = \left(h\vec{a}^* + k\vec{b}^* + l\vec{c}^*\right).\left(((1/h)\vec{a} - (1/k)\vec{b}\right)$$

and is therefore based on the vector relations above, $\vec{r}^*.\vec{p} = 1 - 1 = 0$. Likewise, $\vec{r}^*.\vec{q} = 0$. Vector $\vec{r}^*$, with coordinates (h,k,l) in the reciprocal lattice is therefore normal to the plane in the direct lattice with indices (h,k,l).

Moreover, if $d_{(hkl)}$ is the interplanar distance between two planes of the (h,k,l) family, then it can be shown that:

$$d_{hkl} = \frac{1}{\left\|\vec{r}^*_{hkl}\right\|} \qquad [1.23]$$

The interplanar distance is equal to the inverse of the norm of the corresponding vector in the reciprocal lattice.

1.2.2. *Kinematic theory of diffraction*

We know that each atom scatters the incident radiation and that the amplitude of the scattered wave, called the atomic scattering factor, depends on the number of electrons in the atom in question. We are now going to make two assumptions:

– the amplitude of the incident wave is constant;

– a wave scattered by an atom is not scattered again: there is no multiple scattering.

These two approximations are what characterizes the kinematic approach to diffraction and make it possible to describe the effect in a relatively simple way. The dynamic theory [AUT 05] takes both of these effects into account. The implementation of this dynamic theory is necessary when studying diffraction by very high quality single crystals, or also in the field of homoepitxial thin film characterization. These two subjects are beyond the scope of this book and therefore from here on, we will apply the kinematic theory of X-ray diffraction.

1.2.2.1. *Diffracted amplitude: structure factor and form factor*

First of all, consider a crystal cell, the origin of which is located at an arbitrary point M of the crystal lattice. Inside this cell, an arbitrary point N can be defined by the vector $\vec{r} = \overrightarrow{MN}$ and we have $\vec{r} = x\vec{a} + y\vec{b} + z\vec{c}$, where $\vec{a}, \vec{b}$ and $\vec{c}$ are the basic vectors of the crystal cell.

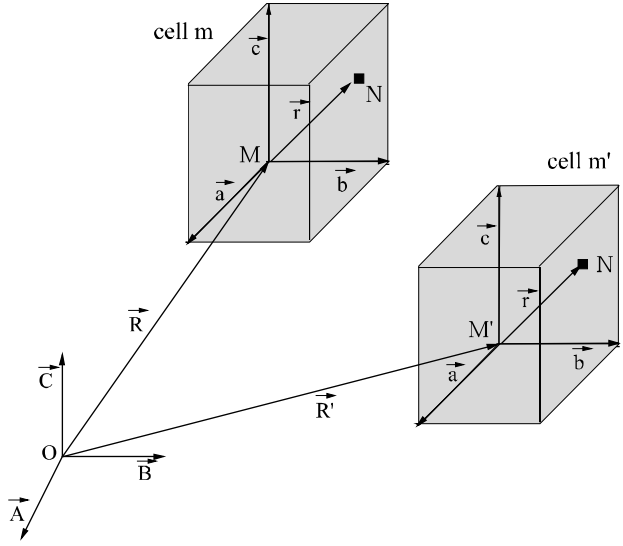

Figure 1.9. *Amplitude diffracted by one cell and by the entire crystal*

If this cell is irradiated with a parallel beam of X-rays traveling along the direction of the vector $\vec{S}_0$, then by applying the same process as before, it is possible to calculate the amplitude scattered by this cell. This amplitude is written:

$$F\left(\vec{S}\right) = \iiint_{\text{cell}} f\left(\vec{r}\right) e^{-2\pi i \vec{s}.\vec{r}} dV \qquad [1.24]$$

The factor F, which is called the structure factor, depends only on the nature of the atoms in the cell (scattering factor f_j) and on the relative positions $\left(\vec{s}.\vec{r}\right)$ of these atoms, the vector $\vec{s}$ being defined as before.

The amplitude diffracted by all of the crystal's cells is the sum of all the amplitudes scattered by each cell and, furthermore, each cell scatters the same amplitude. If we denote by $\vec{R} = X\vec{A} + Y\vec{B} + Z\vec{C}$ the vector indicating the relative position of each cell, then we can write that the amplitude diffracted by the entire crystal is given by the following relation:

$$A\left(\vec{S}\right) = F\left(\vec{S}\right) \sum_X \sum_Y \sum_Z e^{-2\pi i \vec{s}.\vec{R}} \qquad [1.25]$$

The structure factor $F(\vec{S})$ is taken out of the sum since it is the same, regardless of the cell. The form factor is defined as the term:

$$L\left(\vec{S}\right) = \sum_X \sum_Y \sum_Z e^{-2\pi i \vec{s}.\vec{R}} \qquad [1.26]$$

1.2.2.2. *Diffracted intensity*

The intensity, which is the flow of energy that travels through a unit surface over one second is, as we have already seen, equal to the product of the amplitude with its conjugate (denoted by A*). Hence, we have:

$$I\left(\vec{S}\right) = I_e F\left(\vec{S}\right) F^*\left(\vec{S}\right) L\left(\vec{S}\right) L^*\left(\vec{S}\right) = I_e \left|F\left(\vec{S}\right)\right|^2 \left|L\left(\vec{S}\right)\right|^2 \qquad [1.27]$$

The calculation of the product of the form factor with its conjugate calls for a few additional comments. We will now consider a prismatic crystal, the faces of which are parallel to the axes of the primitive cell. In that case, the dimensions of the crystal are N_1a, N_2b and N_3c if a, b and c are its cell parameters. The vectors

$\vec{A}, \vec{B}$ and $\vec{C}$ defined above then become multiples of the crystal cell's basic vectors and the vectors $\vec{R}$ can be expressed as a linear combination of these basic vectors. If we define $\vec{R} = u\vec{a} + v\vec{b} + w\vec{c}$, then we can write:

$$L(\vec{S}) = \sum_{u=0}^{N_1-1} e^{-2\pi i \vec{s}.u\vec{a}} \sum_{v=0}^{N_2-1} e^{-2\pi i \vec{s}.v\vec{b}} \sum_{w=0}^{N_3-1} e^{-2\pi i \vec{s}.w\vec{c}} \qquad [1.28]$$

These different terms are the sums of geometric series with common ratio ρ, with ρ such that:

$$\rho = e^{-2\pi i \vec{s}.\vec{a}}$$

If we consider a geometric series with t as its first term, q as its last and ρ as its common ratio, then the sum of this series is given by:

$$\sigma = t + t\rho + t\rho^2 + ... + q = \frac{\rho q - t}{\rho - 1}$$

therefore:

$$\sum_{u=0}^{N_1-1} e^{-2\pi i \vec{s}.u\vec{a}} = \frac{e^{-2\pi i \vec{s}.N_1\vec{a}} - 1}{e^{-2\pi i \vec{s}.\vec{a}} - 1}$$

If we multiply this term with its conjugate and if we define $x = 2\pi \vec{s}.\vec{a}$, we get the products of the form:

$$\left(\frac{e^{-iNx} - 1}{e^{-ix} - 1}\right)\left(\frac{e^{iNx} - 1}{e^{ix} - 1}\right)$$

$$(e^{-ix} - 1)(e^{ix} - 1) = e^{-ix + ix} - (e^{-ix} + e^{ix}) + 1$$

and additionally:

$$\sin x = \frac{e^{ix} - e^{-ix}}{2i} \text{ and } \cos x = \frac{e^{ix} + e^{-ix}}{2}$$

hence:

$$(e^{-ix} - 1)(e^{ix} - 1) = 1 - 2\cos x + 1 = 4\sin^2\frac{x}{2}$$

and therefore:

$$\left(\frac{e^{-iNx} - 1}{e^{-ix} - 1}\right)\left(\frac{e^{iNx} - 1}{e^{ix} - 1}\right) = \frac{\sin^2 N\,x/2}{\sin^2 x/2}$$

In the end, the diffracted intensity can be expressed:

$$I(\vec{S}) = I_e \left|F(\vec{S})\right|^2 \frac{\sin^2 \pi\vec{s}.N_1\vec{a}}{\sin^2 \pi\vec{s}.\vec{a}} \frac{\sin^2 \pi\vec{s}.N_2\vec{b}}{\sin^2 \pi\vec{s}.\vec{b}} \frac{\sin^2 \pi\vec{s}.N_3\vec{c}}{\sin^2 \pi\vec{s}.\vec{c}} \qquad [1.29]$$

The behavior of the form factor's square modulus is shown in Figure 1.10, for a direction in space parallel to one of the cell's axes. As the number of cells taken into account increases, the intensity distribution becomes thinner and we obtain maxima when the product $\vec{s}.\vec{a}$ is an integer.

Expression [1.29], first established for X-ray diffraction by Laue [FRI 12], is not specific to this filed of application. It represents the intensity distribution of any basic wave interference effect. However, in the diffraction of X-rays, in most cases, the number of atoms or of crystal cells can be considered to be infinite. The diffraction signal then corresponds to a series of Dirac peaks (a result described as a "Dirac comb").

In order to illustrate this fundamental result of X-ray diffraction, which gives for any crystal the expression of the diffracted intensity, we have calculated the intensity diffracted by an imaginary crystal with a cubic symmetry and a cell parameter equal to 5 Å. The atoms that comprise it, which are all of the same kind, are located at the vertices of the crystal cell. The wavelength of the incident beam was chosen equal to the wavelength of copper's $K\alpha_1$ radiation (1.540598 Å). The evolution of the diffracted intensity according to the scattering vector's norm is shown in Figure 1.10a for a crystal comprised 50 crystal cells. We note that the diffracted intensity shows up as a series of peaks with decreasing intensities when $\vec{s}$ increases. This decrease is directly related to the decrease of the scattering factor's value when $\vec{s}$ increases.

Figure 1.10b shows the intensity distribution's behavior depending on the number of cells contained in the crystal. We see that when this number N decreases

the intensity distribution grows wider. Thus, when the diffracting crystal or crystals are nanometric in size, the corresponding diffraction signal shows a certain distribution about the Bragg angle. We will show later on that the width of this distribution is directly related to the size of the diffracting crystals. This observation, first made by Scherrer [SCH 18] in 1918, is at the core of microstructural analysis by X-ray diffraction, which constitutes the theme of Part 2 of this book.

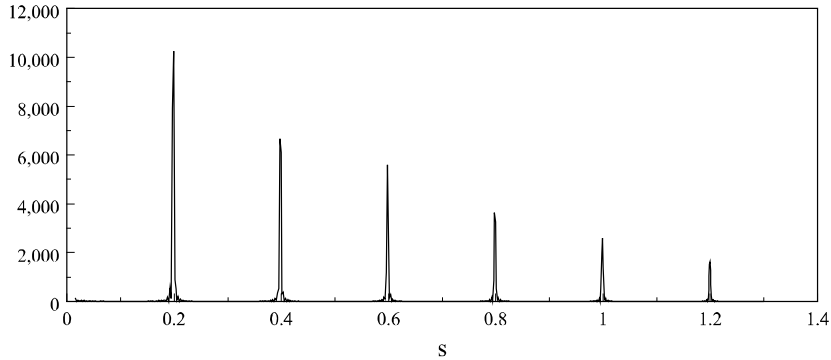

(a) distribution of the intensity diffracted by a crystal containing 50 cells

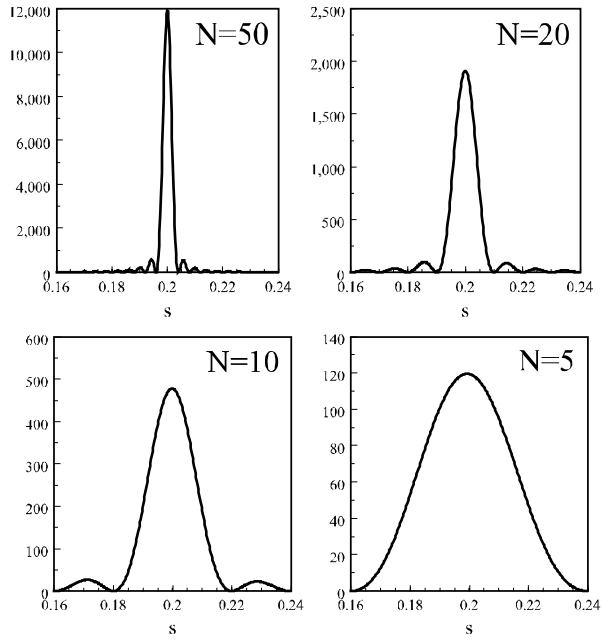

(b) influence of the number of cells on the intensity distribution

Figure 1.10. *Influence of the number of scattering cells on the intensity distribution*

1.2.2.3. *Laue conditions [FRI 12]*

We saw that the form factor's square modulus, and therefore the diffracted intensity, reach their maxima when $\vec{s}.\vec{a} = \text{integer}$ (the same goes for axes $\vec{b}$ and $\vec{c}$). If we consider three integers (h,k,l) and if we assume that we are dealing with an infinite crystal, we can write that the diffracted intensity is not equal to zero if:

$$\begin{cases} \vec{s}.\vec{a} = h \\ \vec{s}.\vec{b} = k \\ \vec{s}.\vec{c} = l \end{cases} \qquad [1.30]$$

These three equations are the Laue conditions, which can be expressed in the reciprocal lattice. Consider an arbitrary vector $\vec{r}^*$ in the reciprocal lattice with coordinates (h,k,l). The dot product $\vec{r}^*.\vec{a} = h\vec{a}^*.\vec{a} + k\vec{b}^*.\vec{a} + l\vec{c}^*.\vec{a}$ is equal to h. The same relation can be written for each of the vectors $\vec{b}$ and $\vec{c}$, and therefore the Laue conditions impose that the scattering vector $\vec{s}$ must be a vector of the reciprocal lattice .

With this result, we can express the structure factor, which was previously defined differently. The vector $\vec{s}$ is now written $\vec{s} = h\vec{a}^* + k\vec{b}^* + l\vec{c}^*$ and therefore $\vec{s}.\vec{r} = \left(h\vec{a}^* + k\vec{b}^* + l\vec{c}^*\right).\left(x\vec{a} + y\vec{b} + z\vec{c}\right) \Rightarrow \vec{s}.\vec{r} = hx + ky + lz$.

We have seen that each family of planes with indices (hkl) is defined by its normal vector, the coordinates of which are the triplet (h,k,l) in the reciprocal lattice. Hence, it is possible to associate each of the families of planes with a structure factor which is expressed as:

$$F_{hkl} = \iiint_{cell} f_{xyz} e^{2\pi i(hx+ky+lz)} dV \qquad [1.31]$$

where the factor $f_{(xyz)}$ is the scattering factor of the atom located at the crystallographic site with coordinates (x,y,z). Note that, according to the expression we have just given, the structure factor is the scattering factor's Fourier transform and therefore by the inverse Fourier transform:

$$f_{xyz} = \sum_h \sum_k \sum_l F_{hkl} e^{-2\pi i(hx+ky+lz)} \qquad [1.32]$$

Determining all of the structure factors of a given crystal makes it possible to determine *a priori* the value taken by the diffusion factor in any point of the crystal cell and therefore it is possible by comparison to determine the nature of the scattering atoms.

However, this type of study, commonly referred to as structural analysis, poses two problems:

– the intensity diffracted by the family of plane with indices (hkl) is proportional to the square modulus of the structure factor;

– only a certain number of reflections (hkl) can be measured and therefore the Fourier series is limited.

We will see in detail in the last chapter of this first part how it is possible, nonetheless, to determine the average structure of the diffracting crystals from the integrated intensity measurements.

1.2.3. *Geometric theory of diffraction*

1.2.3.1. *Laue conditions*

This section will enable us to return to the Laue conditions which we showed with the help of the kinematic theory of diffraction. These conditions express the fact that the waves scattered by each of the points on a row have to be in phase.

The crystal lattice can be defined entirely based on the three rows [100], [010] and [001], which means that if the waves scattered by the points of each of these rows are in phase, then all of the lattice points scatter in phase.

Figure 1.11 shows a schematic representation of the scattering by the row [100] of a crystal lattice with cell parameters a, b and c. The incident X-ray beam is characterized by vector $\vec{S}_0$ and wavelength λ. This beam is scattered in the direction defined by vector $\vec{S}$.

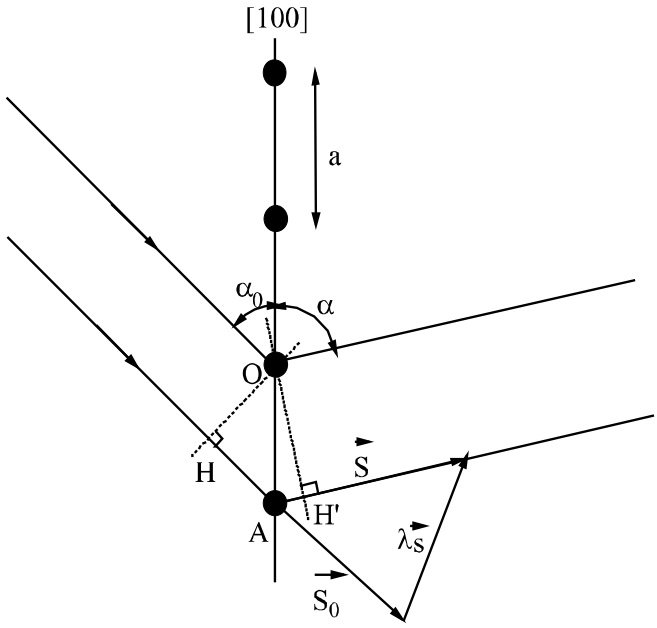

Figure 1.11. *Geometrical evidence of the Laue conditions*

As we have already seen, the diffraction condition states that the path difference between the waves scattered by each of the lattice points is a multiple of the wavelength. Let δ be this path difference:

$$\delta = \overline{HA} + \overline{AH'}$$

hence:

$$\delta = a(\cos\alpha_0 + \cos\alpha) \text{ or } \delta = -\vec{a}.\vec{S}_0 + \vec{a}.\vec{S} = \vec{a}.\lambda\vec{s}$$

$\vec{s}$ being defined as it was previously. In addition to this, we know that δ must be equal to $h\lambda$ for diffraction to occur; therefore, $h\lambda = \vec{a}.\lambda\vec{s}$ and in the end, we again find $\vec{s}.\vec{a} = h$.

1.2.3.2. *Bragg's law [BRA 13b, BRA 15]*

We are going to show this fundamental relation of X-ray diffraction using the schema shown in Figure 1.12, drawn in the direct lattice.

Consider an arbitrary family of planes (hkl) characterized by the interplanar distance d_{hkl} and irradiated at an angle θ with a monochromatic beam of X-rays. If the crystal is relatively small, each atom of this crystal is placed inside a beam with constant intensity and coherently scatters a wave, whose amplitude and intensity were calculated above. If all of these scattered waves are in phase on a wave plane π perpendicular to the scattering direction, they interfere and give rise to a scattered wave with a strong intensity in that direction. If we consider the wave plane π_0 of the incident wave, the necessary condition to diffraction is therefore to have the path difference between the planes π_0 and π equal to a multiple of the wavelength.

First of all, consider an atomic plane. The paths between the two wave planes π' and π of the waves scattered by the atoms located in A and A_1 are equal if the angle between the atomic plane and the incident beam is equal to the angle between this plane and the scattered beam.

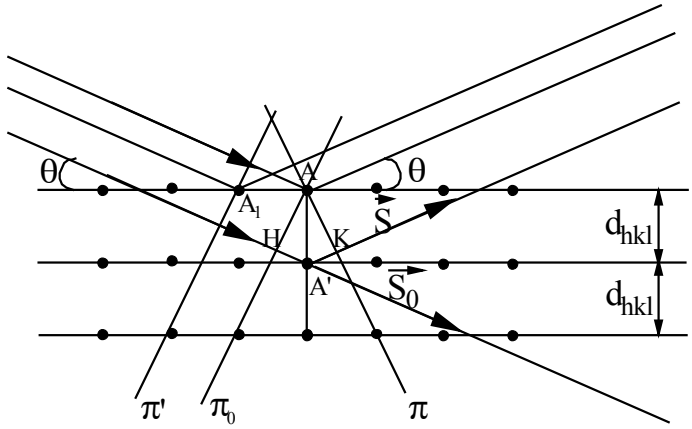

Figure 1.12. *Interference of waves scattered by atoms inside the crystal. Geometrical illustration of Bragg's law*

In addition to this first condition, the waves scattered by each plane of the considered family have to be in phase. As we have just seen, the waves scattered by each of the planes have the phase of the wave scattered by an arbitrary atom in these planes. The path difference between the wave scattered by the atom located in A' and the wave scattered by the atom located in A is written $\delta = \overline{HA'} + \overline{A'K}$. If d is the interplanar distance that characterizes this family of planes, then $\delta = 2d \sin\theta$, but this path difference has to be a multiple of the wavelength, hence:

$$n\lambda = 2d_{hkl} \sin\theta \qquad [1.33]$$

This relation is called Bragg's law and it constitutes, along with the equation that leads to the scattered intensity, the core of radiocrystallography. It shows how the interplanar distances in a given crystal can be calculated from the measurements of the diffraction angles. Note that if we consider a family of plane with indices (hkl), for a given wavelength λ, the diffraction angle (Bragg angle) is given and therefore we will observe a wave diffracted by this family of planes if and only if the angle between this family and the incident wave is equal to the one given by Bragg's law.

In order for diffraction to occur with an X-ray beam with a given wavelength λ, Bragg's law has to be verified and therefore we must have:

$$\frac{n\lambda}{2d} \leq 1 \Rightarrow d \geq \frac{\lambda}{2} \qquad [1.34]$$

For a given interplanar distance, this relation gives us the maximum useable wavelength and therefore limits the families of planes that can be characterized by using a beam with a given wavelength. Likewise, note that if the wavelength were very small compared to the interplanar distances, the ratio $\lambda/2d$ would be very small and therefore, the value of the diffraction angle θ would also be very small and difficult to observe. These two conditions show that the beam's wavelength should be in the same range as the values of the interplanar distances.

1.2.3.3. *The Ewald sphere*

Ewald [EWA 17] suggested a geometric representation in the reciprocal lattice of the results we have just shown. The Ewald sphere is defined as a sphere centered in O, the origin of the direct and diffracted wave vectors, and with radius $1/\lambda$. Vectors $\vec{k}_0$ and $\vec{k}$ are co-linear to vectors $\vec{S}_0$ and $\vec{S}$, respectively.

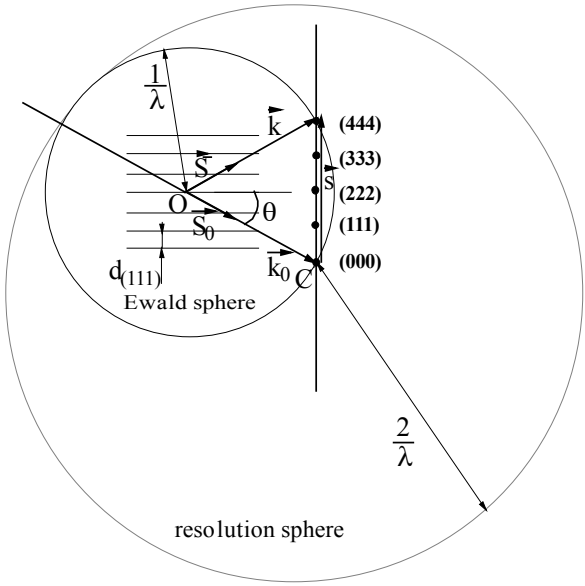

Figure 1.13. *The Ewald sphere*

Ewald's condition can be expressed as follows: in order for n^{th} order diffraction to occur on a family of planes with index (hkl), the n^{th} node of the reciprocal lattice's row [hkl]* has to be on the Ewald sphere, the corresponding diffracted beam then passes through that point.

When the crystal is in a random position, the point of the reciprocal lattice that corresponds to a given family of planes is not on the Ewald sphere, and additionally, it is generally possible that no point is on that sphere, in which case there is no diffracted beam. In order for a given family of planes to be able to diffract, the corresponding point has to be inside a sphere with radius $2/\lambda$, centered in C, the tip of the vector $\vec{k}_0$. This sphere is called the resolution sphere. This can also be written:

$$\left\|\vec{s}\right\| \leq \frac{2}{\lambda} \qquad [1.35]$$

We know that:

$$\left\|\vec{s}\right\| = \frac{1}{d} \qquad [1.36]$$

and therefore we find the same condition as the one established before:

$$d \geq \frac{\lambda}{2} \qquad [1.37]$$

1.3. Diffraction by an ideally imperfect crystal

We showed in section 1.2.2.2 that the intensity diffracted by a crystal is expressed as:

$$I = I_e \left|F_{hkl}\right|^2 \left|L_{hkl}\right|^2$$

However, this relation is not exactly true. The crystals are not comprised of perfect crystal planes: they show domains slightly misoriented with respect to one another. These crystal domains usually extend over a few tens of cells and their misorientation are characteristic of the crystal in question, something referred to as the crystal's mosaicity. A qualitative illustration of this mosaicity is shown in Figure 1.14.

Figure 1.15 shows the evolution of the intensity diffracted by the (110) planes of an aluminum oxide single crystal according to the beam's angle of incidence on these planes. The X-ray beam used is almost parallel (the equatorial divergence is equal to 12 arcseconds) and monochromatic ($\Delta\lambda/\lambda = 1.4 \times 10^{-4}$) [MAR 00].

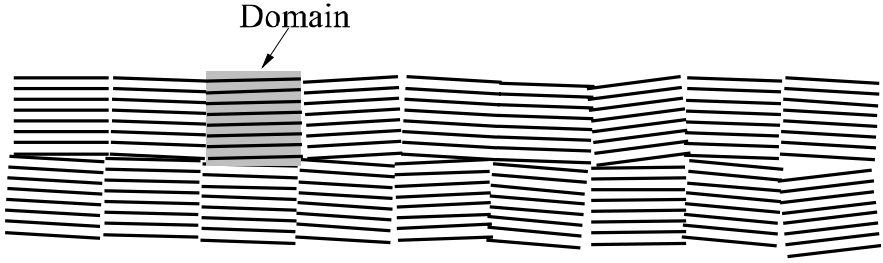

Figure 1.14. *Mosaicity of a real crystal*

A certain diffracted intensity is observed when the angle of incidence is close to the Bragg angle of the chosen family of planes. The angular range for which this

intensity is significant is small, but not null, and clearly greater than the beam's divergence. For each angle of incidence, a certain diffracted intensity is observed, corresponding to the integral of the measured peak. If the evolution of this integrated intensity is plotted according to the difference between the Bragg angle and the angle of incidence of the beam on the crystal planes in question, the width of the resulting graph is a direct measurement of the crystal's mosaicity. This type of graph is called a rocking curve and the widths of these curves are typically of a few thousandths of a degree for single crystals free of any particular defects.

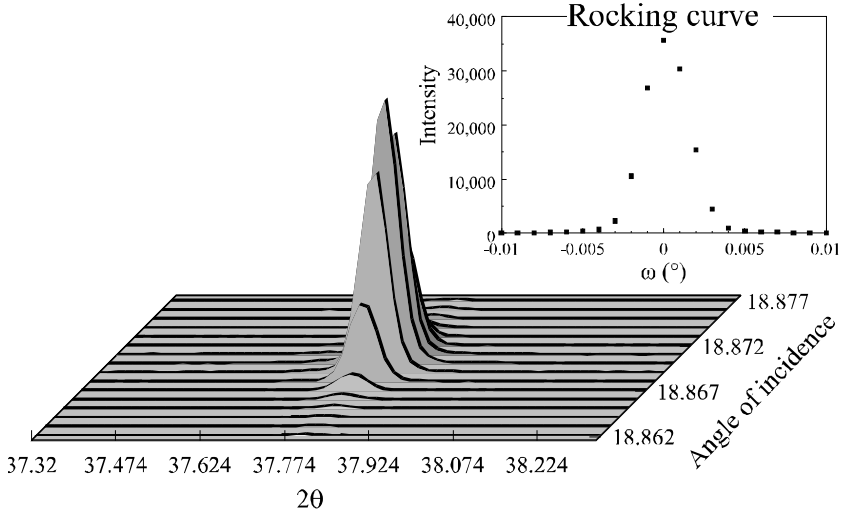

Figure 1.15. *Measurement of the mosaicity of an aluminum oxide single crystal*

These are very general considerations and they show that the total intensity diffracted by a crystal is the sum of the elementary contributions, each one of them obtained for a given angle of incidence. The domains diffract independently from one another. The total intensity will therefore be obtained by adding the elementary intensities diffracted for each value of the angle of incidence. This result was discovered in the first studies involving X-ray diffraction conducted by Bragg [BRA 13b], who suggested a method, discussed in detail by Warren [WAR 69], that makes it possible to calculate the actual intensity diffracted by a single crystal, which we will refer to as the integrated intensity, denoted by P_{hkl}.

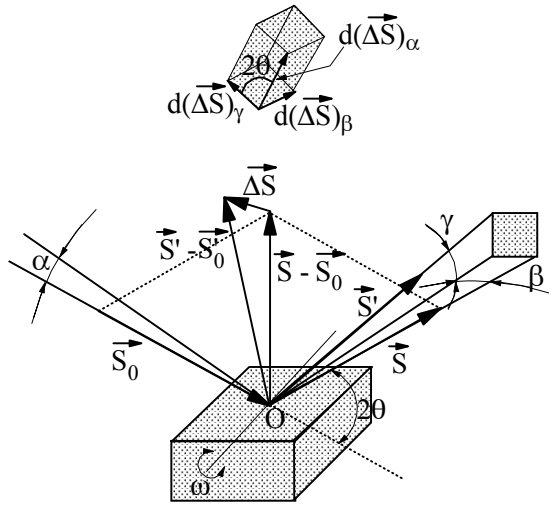

Figure 1.16. *Diffracting power of an ideal crystal*

Consider a beam with intensity I_0 irradiating a small single crystal in the Bragg position. This crystal is rotating at a constant angular speed ω around an axis parallel to the planes (hkl) and perpendicular to the incident beam, so as to have the angle of incidence vary from $\theta - \alpha$ to $\theta + \alpha$. A detector is placed on a sphere with unit radius with the objective of measuring the overall energy diffracted during the crystal's rotation. Let E be that energy. The total intensity diffracted by this crystal is given by the relation:

$$P_{hkl} = \frac{E\omega}{I_0} \qquad [1.38]$$

The total energy E going through the detector's surface is obtained by integrating the intensity I_{hkl} over the receiving surface, given by the product $d\beta \cdot d\gamma$, and over the time t:

$$E = \iiint I_{hkl} dt d\beta d\gamma \qquad [1.39]$$

we can write:

$$\omega = \frac{d\alpha}{dt} \qquad [1.40]$$

and if we substitute the value of I_{hkl}, E can be expressed as:

$$E = I_e \frac{|F_{hkl}|^2}{\omega} \iiint |L_{hkl}|^2 d\alpha d\beta d\gamma \qquad [1.41]$$

In this section, the scattering vector is assumed to have coordinates (h_1,h_2,h_3) which are variables of the reciprocal lattice. In fact, the crystal's orientation for which a diffraction signal is observed varies in the vicinity of the Bragg angle (see Figure 1.15). Therefore, vector $\vec{s}$, which is normal to the diffracting planes, varies.

$$\vec{s} = h_1\vec{a}^* + h_2\vec{b}^* + h_3\vec{c}^* \qquad [1.42]$$

The triplet (hkl) corresponds to particular values of these variables. The variations of vector $\vec{S}_0 - \vec{S}$ are described by vector $\Delta\vec{S}$ such that:

$$\Delta\vec{S} = \lambda\left(\varepsilon_1\vec{a}^* + \varepsilon_2\vec{b}^* + \varepsilon_3\vec{c}^*\right) \qquad [1.43]$$

The volume generated by these variations is the mixed product of the vectors $d\left(\Delta\vec{S}\right)_\alpha$, $d\left(\Delta\vec{S}\right)_\beta$ and $d\left(\Delta\vec{S}\right)_\gamma$; therefore:

$$dV = d\left(\Delta\vec{S}\right)_\beta \cdot \left(d\left(\Delta\vec{S}\right)_\alpha \wedge d\left(\Delta\vec{S}\right)_\gamma\right)$$

or also:

$$dV = \sin 2\theta \left\|d(\Delta\vec{S})_\beta\right\| \left\|d(\Delta\vec{S})_\alpha\right\| \left\|d(\Delta\vec{S})_\gamma\right\|$$

Additionally:

$$\left\|d\left(\Delta\vec{S}\right)_\alpha\right\| = d\alpha \; ; \; \left\|d\left(\Delta\vec{S}\right)_\beta\right\| = d\beta \; ; \; \left\|d\left(\Delta\vec{S}\right)_\gamma\right\| = d\gamma$$

since vectors $\vec{S}$ and $\vec{S}_0$ are unit vectors, hence:

$$dV = \sin 2\theta \, d\alpha \, d\beta \, d\gamma$$

Therefore, we can write:

$$E = I_e \frac{|F_{hkl}|^2}{\omega} \frac{1}{\sin 2\theta} \iiint |L_{hkl}|^2 dV \qquad [1.44]$$

dV can be expressed using the coordinates of vector $\Delta\vec{S}$. We then get: $dV = \lambda d\varepsilon_1 \vec{a}^* . \left(\lambda d\varepsilon_2 \vec{b}^* \wedge \lambda d\varepsilon_3 \vec{c}^*\right)$ or also $dV = \lambda^3 d\varepsilon_1 d\varepsilon_2 d\varepsilon_3 \vec{a}^* . \left(\vec{b}^* \wedge \vec{c}^*\right)$, and therefore:

$$dV = \frac{\lambda^3}{V_c} d\varepsilon_1 d\varepsilon_2 d\varepsilon_3 \qquad [1.45]$$

where V_c is the cell volume. Hence:

$$E = I_e \frac{|F_{hkl}|^2}{\omega} \frac{1}{\sin 2\theta} \frac{\lambda^3}{V_c} \iiint |L_{hkl}|^2 \, d\varepsilon_1 d\varepsilon_2 d\varepsilon_3 \qquad [1.46]$$

The expression of $|L_{hkl}|^2$ is a product of terms of the form:

$$\frac{\sin^2 \pi \vec{s}.N_1\vec{a}}{\sin^2 \pi \vec{s}.\vec{a}}$$

In this case, $\vec{s}$ has to be replaced with $\vec{s} + \frac{\Delta\vec{S}}{\lambda}$. Now:

$$\sin^2 \pi \left(\vec{s} + \frac{\Delta\vec{S}}{\lambda}\right).N_1\vec{a} = \sin^2 \pi \left(hN_1 + \frac{\Delta\vec{S}.N_1\vec{a}}{\lambda}\right)$$

and hN_1 is an integer. Therefore the expression becomes:

$$\sin^2 \left(\frac{\pi}{\lambda} \Delta\vec{S}.N_1\vec{a}\right)$$

and in the end:

$$\sin^2 (\pi N_1 \varepsilon_1)$$

therefore:

$$\left|L_{hkl}\right|^2 = \frac{\sin^2 \pi N_1 \varepsilon_1}{\sin^2 \pi \varepsilon_1} \frac{\sin^2 \pi N_2 \varepsilon_2}{\sin^2 \pi \varepsilon_2} \frac{\sin^2 \pi N_3 \varepsilon_3}{\sin^2 \pi \varepsilon_3} \quad [1.47]$$

Hence, we get:

$$E = I_e \frac{\left|F_{hkl}\right|^2}{\omega} \frac{1}{\sin 2\theta} \frac{\lambda^3}{V_c} \int \frac{\sin^2 \pi N_1 \varepsilon_1}{\sin^2 \pi \varepsilon_1} d\varepsilon_1 \int \frac{\sin^2 \pi N_2 \varepsilon_2}{\sin^2 \pi \varepsilon_2} d\varepsilon_2 \int \frac{\sin^2 \pi N_3 \varepsilon_3}{\sin^2 \pi \varepsilon_3} d\varepsilon_3 \quad [1.48]$$

By noting that the values of ε_1, ε_2 and ε_3 are very small, we can say that $\sin \pi\varepsilon_1 \approx \pi\varepsilon_1$ and thus show that the three integrals are equal to N_1, N_2 and N_3, respectively, the product of these three terms being equal to N, which is the total number of cells in the crystal. The expression of E then becomes:

$$E = I_e \frac{\left|F_{hkl}\right|^2}{\omega} \frac{1}{\sin 2\theta} \frac{\lambda^3}{V_c} N \quad [1.49]$$

The number N is equal to the ratio of the crystal's volume δV to the volume of a cell V_c. If we replace I_e by its value we get the final expression of E:

$$E = \frac{I_0}{\omega} r_e^2 \left(\frac{1 + \cos^2 2\theta}{2} \right) \left(\frac{\lambda^3 \left|F_{hkl}\right|^2}{V_c^2} \right) \frac{1}{\sin 2\theta} \delta V \quad [1.50]$$

We showed that the intensity diffracted by a crystal, denoted by P_{hkl}, was given by the relation $P_{hkl} = E\omega/I_0$ and therefore we can write:

$$P_{hkl} = r_e^2 \left(\frac{1 + \cos^2 2\theta}{2} \right) \left(\frac{\lambda^3 \left|F_{hkl}\right|^2}{V_c^2} \right) \frac{1}{\sin 2\theta} \delta V \quad [1.51]$$

1.4. Diffraction by a polycrystalline sample

The general principles of X-ray diffraction were established in the case of a single crystal. This situation led to a great number of studies that made it possible in

particular to describe the structure of crystals. However, other studies, which constitute the focus of this book, are conducted on polycrystalline samples.

The sizes of the elementary crystals are very small, of the order of micrometers and cannot be singled out to be characterized in the same way as single crystals. We will see how, nonetheless, they can be studied, using certain experimental techniques. In other works, these techniques are often called "powder techniques", the word powder simply referring to polycrystals in this case. The microcrystals in question should not be confused with the more general term *grain of powder*, since a grain of powder can be either poly- or monocrystalline.

Consider a polycrystalline sample irradiated by a monochromatic X-ray beam. This sample contains a very high number of grains and if these crystals are randomly oriented, then for each family of planes (hkl) a large number of grains are in the Bragg position and therefore diffract. As we have seen, the diffracted beams are at an angle equal to 2θ with the direction of the incident beam.

Therefore, the locus of all the beams diffracted by the entire set of crystals in the Bragg position is a cone with a half opening angle 2θ. If we take into account diffraction by several families of planes, the result is a series of diffraction cones sharing the same apex (see Figure 1.17).

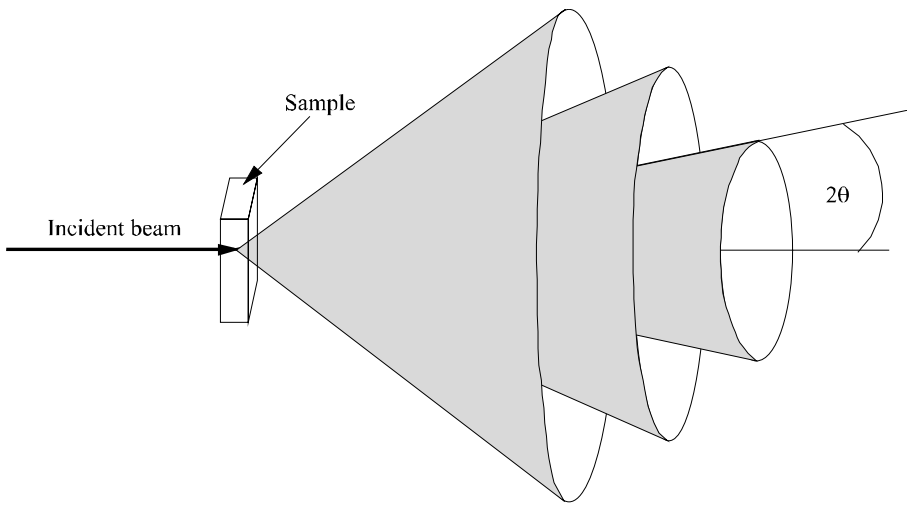

Figure 1.17. *Diffraction cones of a polycrystalline sample irradiated with a monochromatic beam*

Let M be the number of elementary crystals contained in the sample and let δV be the average elementary volume of each of these crystals. We are going to calculate the expression of the intensity diffracted by m crystals in the Bragg position for a given family of planes (hkl).

These m crystals have to be oriented in such a way that the family of planes (hkl) creates an angle contained between $\theta + \alpha$ and $\theta + \alpha + d\alpha$ with the direction of the incident beam.

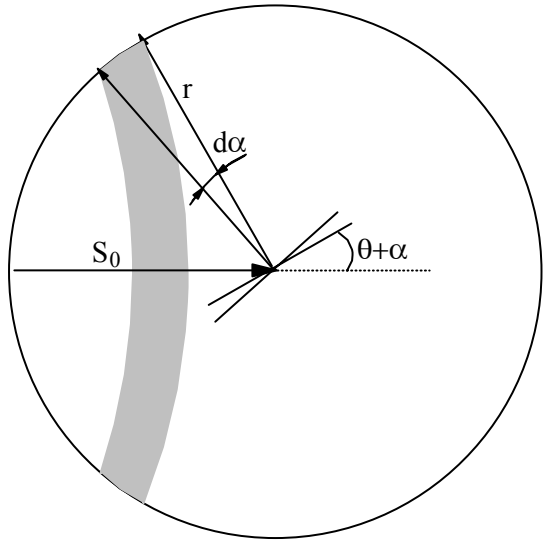

Figure 1.18. *Calculation of the number of grains in the Bragg position for a given family of planes*

In a crystal, there are several families of planes with different orientations but with the same interplanar distance and the same structure factor modulus. In the case of a polycrystalline sample, these different families will diffract simultaneously and, will therefore contribute to the overall intensity of the peak in question. n_{hkl} denotes the number of equivalent families of planes for a given triplet (hkl) and n is the multiplicity factor of the diffraction peak being studied. If we wish to calculate the number of families of planes (hkl) in the Bragg position, we will have to multiply the resulting value by n_{hkl}.

The normals to each family of planes for each of the crystals in the sample are defined by the vector $\vec{r}_{hkl}^{\,*}$ of the reciprocal lattice. In the case of a polycrystalline sample, the total number of these vectors is Mn_{hkl}. The tips of these vectors form

the entire surface of the sphere with radius $\|\vec{r}_{hkl}^*\|$. On the other hand, the tips of the vectors $\vec{r}_{hkl}^*$ associated with the diffracting planes inside the crystals that are in the Bragg position form a portion of the sphere, shown in Figure 1.18. The number of crystals in the Bragg position is therefore given by the ratio between the surface of this portion of sphere and the surface of the sphere. So, in the end, the number of crystals in the Bragg position is equal to:

$$m = \frac{Mn_{hkl}}{4\pi r^2} 2\pi r^2 \cos(\theta + \alpha) d\alpha \qquad [1.52]$$

$$\Rightarrow m = \frac{Mn_{hkl}}{2} \cos\theta d\alpha \qquad [1.53]$$

The intensity of a peak (hkl) is equal to the number of crystals in the Bragg position multiplied by the intensity diffracted by an elementary crystal. If the total volume of the sample is equal to dV, then $dV = M\delta V$ and the total volume of the crystals in the Bragg position is equal to the number of grains multiplied by the volume of each grain. Hence the volume is expressed as follows:

$$\left(\frac{Mn_{hkl}}{2} \cos\theta d\alpha\right) \delta V = \frac{n_{hkl} dV}{2} \cos\theta d\alpha \qquad [1.54]$$

If $I(\alpha)$ is the intensity diffracted by the family of planes (hkl) with the incidence α, the total intensity diffracted by the sample with volume dV, for the cone that corresponds to the family of planes (hkl), is given by:

$$\Phi = \frac{n_{hkl} dV}{2} \cos\theta \int I(\alpha) d\alpha \qquad [1.55]$$

This intensity corresponds to the intensity diffracted by a single crystal with volume: $\frac{n_{hkl} dV}{2} \cos\theta$ and therefore is given by the value of P_{hkl} for a crystal of that volume.

However, this intensity is distributed over a cone with a half opening angle 2θ. If a detector is placed at a distance R from the crystal, the intensity we measure will be the diffracted intensity expressed with the circle's perimeter $2\pi R \sin 2\theta$ as the unit

of length. Hence, the measured intensity will be described by the following expression:

$$I_{hkl} = r_e^2\left(\frac{1+\cos^2 2\theta}{2}\right)\left(\frac{\lambda^3|F_{hkl}|^2}{V_c^2}\right)\left(\frac{1}{\sin 2\theta}\right)\frac{n_{hkl}\,dV}{2}\cos\theta I_0\,\frac{1}{2\pi R\sin 2\theta} \quad [1.56]$$

therefore:

$$I_{hkl} = I_0 r_e^2\left(\frac{1+\cos^2 2\theta}{16\pi R\sin\theta\sin 2\theta}\right)\left(\frac{\lambda^3 n_{hkl}|F_{hkl}|^2}{V_c^2}\right)dV \quad [1.57]$$

where the term $\frac{1+\cos^2 2\theta}{2}$ is called the polarization factor.

The relation given here is only valid in the case of an unpolarized incident beam. In practice, the beam used to irradiate the sample is sometimes diffracted beforehand by a single crystal acting as a monochromator, in which case the polarization factor's expression is more complex and depends in particular on the diffraction angle of the monochromator single crystal.

The term $\lambda^3/\sin 2\theta$ is referred to as the Lorentz factor; the Lorentz-polarization factor, which is the product of the two previous expressions, is also commonly used.

The expression of the intensity that was transferred in [1.57] does not account for two effects that we have neglected throughout this chapter.

First, a polycrystalline sample usually has a size that ranges in millimeters and the beam irradiating this sample is partially absorbed. This means that a crystal located in a given area of the sample sees an incident intensity I that is different from the initial beam's intensity I_0. Furthermore, the diffracted beams are also partially absorbed. As a result, the actual intensity that is measured is attenuated by an absorption factor which we will denote by A. The form of this factor depends on the geometric characteristics of the diffractometer used for the experiment. This point will be detailed later on, in particular when describing the diffractometers designed for the study of thin films.

The second effect involves thermal agitation. It is well known that atoms, although located in atomic sites inside the crystal, are subjected to a certain agitation that increases with the temperature. When we calculated the expression of the

structure factor, we assumed that the atoms had a certain position defined by the vector $\vec{r}$. We now see that the positions of these atoms are constantly changing. As a result, the diffracted amplitude is modified. This modification depends in theory on what family of planes considered because each atom is moving inside a potential well with an anisotropic shape, since it depends on the crystallographic direction. The complete description of this effect will not be given here. We will simply point out that the diffracted intensity is attenuated by a factor, called the Debye or Debye-Waller factor, smaller than 1, and whose value usually depends on which family of planes is being considered. This factor will be denoted by D. Finally, the intensity diffracted by a polycrystalline sample is therefore written:

$$I_{hkl} = I_0 r_e^2 \left(\frac{1+\cos^2 2\theta}{16\pi R \sin\theta \sin 2\theta} \right) \left(\frac{\lambda^3 n_{hkl} |F_{hkl}|^2}{V_c^2} \right) ADdV \qquad [1.58]$$

Chapter 2

Instrumentation used for X-ray Diffraction

2.1. The different elements of a diffractometer

2.1.1. *X-ray sources*

Aside from synchrotron radiation sources, which will be mentioned later on, whatever the type of source used, the process of X-ray production results from bombarding a metallic target with electrons. The electrons, accelerated by an electrical field, are suddenly slowed down when they come into contact with the target and lose some of their energy which is dispersed in the form of radiation, a process called braking radiation (or *Bremsstrahlung*). The resulting X-rays do not have a specific wavelength, the emission spectrum is continuous and its intensity increases with the electron acceleration voltage (see Figure 2.1a).

The electron bombardment generates a second type of emission. The electrons transmit their energy to the atoms of the target and cause electronic transitions, meaning that the atoms reach an excited state. They return to a more stable energy level through a series of electronic transitions and the emission of X photons with non-random energies $E = h\nu$, equivalent to the energy gaps between the different electron shells of the atom in question. Therefore, this radiation is comprised of several wavelengths, but the emission spectrum is totally discontinuous. Figure 2.1b shows an illustration of this type of emission. Note that, in this case, the emission spectrum still includes a contribution from the braking radiation which causes the continuous background emission.

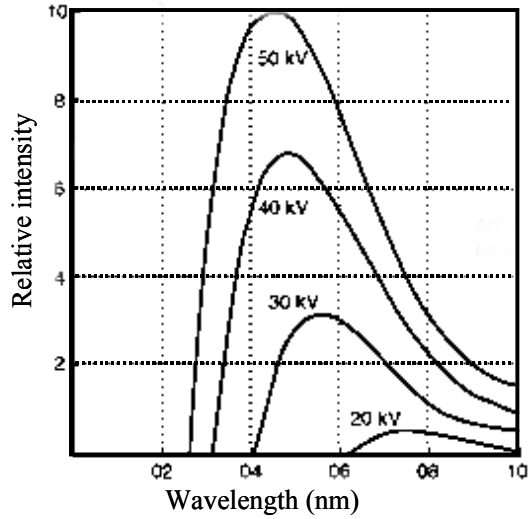

(a) Braking radiation

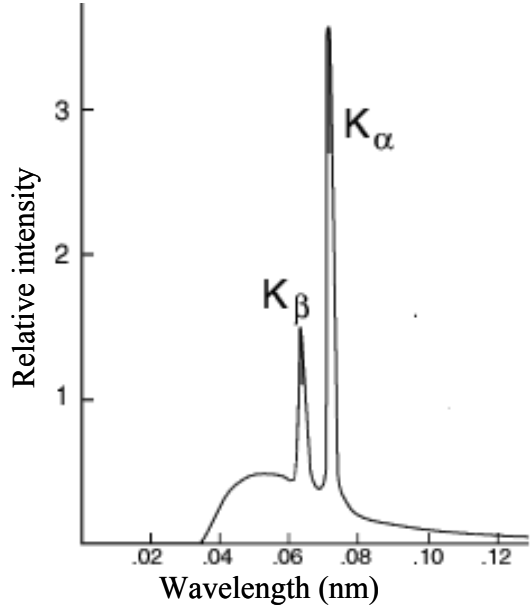

(b) Characteristic radiation

Figure 2.1. *Emission spectrum of a molybdenum anode bombarded with an electron beam*

Table 2.1 lists the emission wavelengths of a few materials commonly used in X-ray diffraction. Only the K radiations, which are the ones used, are shown.

Element	Wavelength (Å)			Excitation threshold (Kev)
	$K_{\alpha 1}$	$K_{\alpha 2}$	K_{β}	
Ag	0.55941	0.5638	0.49707	25.52
Mo	0.7093	0.71359	0.63229	20
Cu	1.540598	1.54439	1.39222	8.98
Ni	1.65791	1.66175	1.50014	8.33
Co	1.78897	1.79285	1.62079	7.71
Fe	1.93604	1.93998	1.75661	7.11
Cr	2.2897	2.29361	2.08487	5.99

Table 2.1. *Emission wavelength and excitation threshold of a few elements*

2.1.1.1. *Crookes tubes*

This type of tube was the one used by Röntgen, who discovered the existence of X-rays in 1895.

It consists of a tube, connected to a pumping unit, which contains a gas at a very low pressure (0.01 Torr). An electrical discharge is applied between the two electrodes placed inside the tube. The impact of the positive ions against the cathode causes it to emit electrons. These electrons then bombard the anode (also called the anticathode) which itself emits de-excitation X-rays. A schematic view of this device is shown in Figure 2.2.

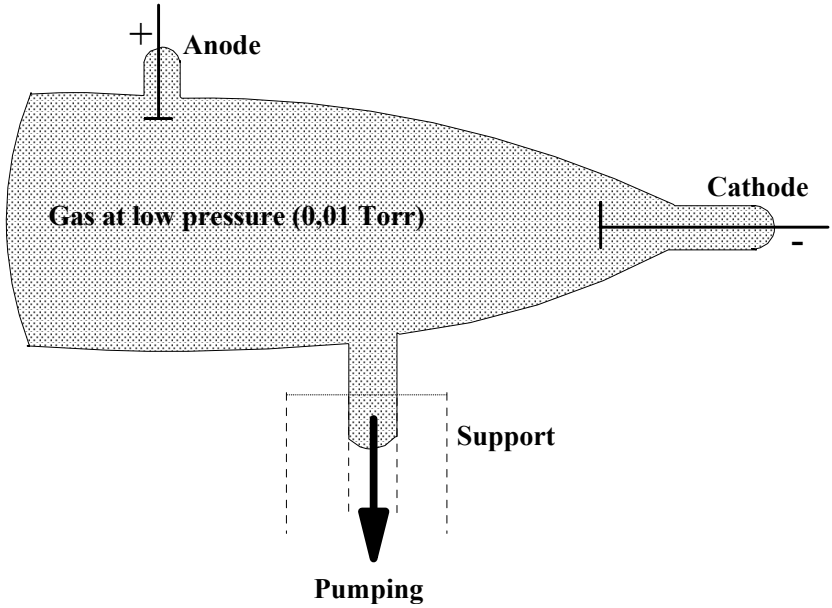

Figure 2.2. *Schematic view of a Crookes tube*

The intensity of the discharge current in a tube of this kind is highly dependent on the gas pressure, hence the need to be able to control it precisely and maintain it a constant level. This feature constitutes the main weakness of this kind of tube. The anticathode's lifetime is short (roughly 100 hours) but, on the other hand, its surface is not polluted, unlike in Coolidge tubes, and therefore the X-rays emitted are pure. Currently these tubes are in practice no longer used.

2.1.1.2. *Coolidge tubes*

In 1913, Coolidge [COO 13] imagined another kind of X-ray source. The cathode is comprised of a tungsten filament heated by the Joule effect. According to the Edison effect, this filament emits electrons that are accelerated by an electrical field and bombard the anticathode which then emits X-rays. The entire device is placed in a sealed tube inside which the pressure must be as low as possible. A schematic view of such a tube is shown in Figure 2.3.

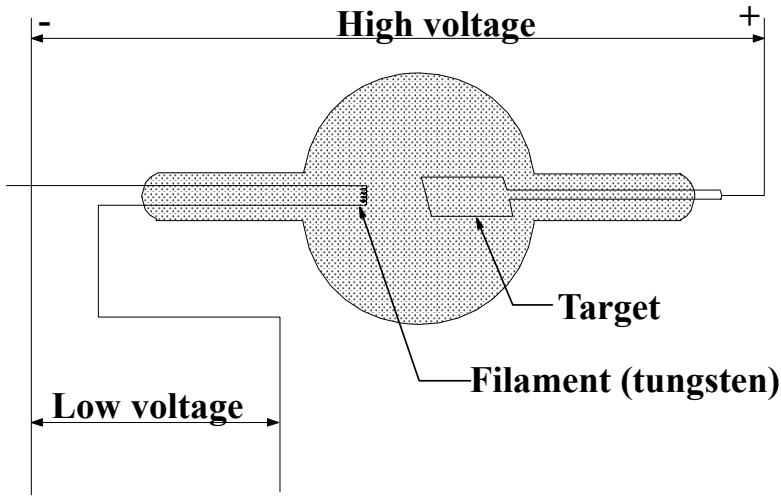

Figure 2.3. *Schematic view of a Coolidge tube*

2.1.1.2.1. Energy efficiency – intensity of the emitted X-rays

The intensity of an X-ray beam emitted by the anticathode is directly proportional to the current inside the tube and to the square of the applied voltage. However, the efficiency of the emission process is very low, and even in the best conditions, with a voltage of 100 kV, only 2% of the energy provided is transmitted to the X-rays.

Roughly 98% of the electron beam's energy is consumed by the Joule effect and heats up the anticathode, which is why it is important to set up a system to evacuate heat. A cooling system by water circulation is used.

Despite this cooling system, the heat evacuation is limited by the anticathode's thermal conduction and partial melting of the target is sometimes observed. The target's surface gradually gets rougher, something which is called "craterization" of the target. This roughness causes local variations in intensity for the emitted X-rays. The intensity distribution in the beam's right section becomes irregular and the tube can no longer be used. This effect is one of the normal causes for wear in Coolidge tubes. The typical lifetime of these tubes ranges from 8,000 to 10,000 hours.

2.1.1.2.2. Focusing of the electron beam: use of a Wehnelt or electromagnetic lenses

The "Wehnelt" is a piece of metal that surrounds the cathode and to which a voltage is applied, negative with respect to the filament. This part is therefore repulsive for electrons. This device, which makes it possible to focus the beam, is

commonly implemented in Coolidge tubes. In the most common tubes, the shape of this part is designed in order to obtain an almost rectangular electron beam.

The method that would seem the most efficient for producing an electron beam with a specific shape and with an electron flow per unit of surface as high as possible consists of focusing this electron beam by using an electromagnetic lens similar to that found in electron microscopes. Although this approach, described by Guinier [GUI 64], is rather old [COS 53], it was only rarely used during the second half of the 20th century. In the past few years, this type of tube has found renewed interest. Several companies have recently designed new X-ray tubes based on this method [ARN 98]. The X-ray beams produced this way have square or circular sections a few tenths of a micrometer wide. In order to limit the effects of craterization, which were described above, the anode is set into motion either as an alternative translation in the plane of its surface if it is flat or as a rotation if it is cylindrical. This last case of the rotating anode will be discussed in greater detail in the next section.

2.1.1.2.3. Shape and size of the focal spot

Typically, a rectangular electron beam is used, with a size of 1 mm by 10 mm. This rectangular beam hits the anticathode, which, as a result, emits another beam of X-rays. The surface of the anode irradiated by the electron beam constitutes the actual focal spot, also referred to as the thermal focal spot, not to be confused with the apparent focal spot, which depends in which we see the angle of the X-ray beam. The diagram in Figure 2.4 makes it possible to visualize this effect.

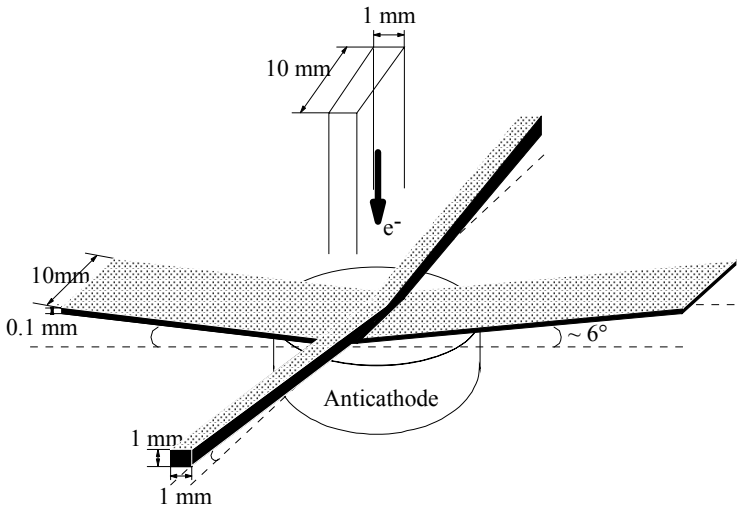

Figure 2.4. *Shapes and sizes of the X focal spots in a Coolidge tube*

The resulting dimensions for the apparent focal spot are as follows:

– linear focal spot: 10×0.1 mm;

– punctual focal spot: 1×1 mm.

Tubes sold on the market are built with four windows at 90° angles, thus allowing the user to choose between linear[1] or punctual X-ray beams.

2.1.1.2.4. Absorption by the windows

The X-ray beam produced exits the tube through the windows which must, on the one hand, be able to resist the difference in pressure between the inside of the tube and the atmosphere, and, on the other hand, be as transparent as possible to X-rays.

The ability to let X-rays pass through is related to the absorption factor, which increases with the atomic number. This is why the windows are manufactured using elements with a low atomic number. They were at first made out of glass, particularly "Lindemann glass", which is composed of boron oxide or lithium oxide. However, this glass still absorbs a large portion of X-rays and it is unstable in a humid atmosphere.

Very thin mica windows (≈ 10μm) were later designed. Since these strips of mica are sensitive to electron bombardment, they are protected with sheets of beryllium. The tubes used today are equipped with beryllium windows. Figure 3.5 shows the absorption curves according to the wavelength for these different windows.

1 Beams are often described as being linear because, as shown in the diagram in Figure 2.4, the beam's length can be roughly 100 times greater than its width.

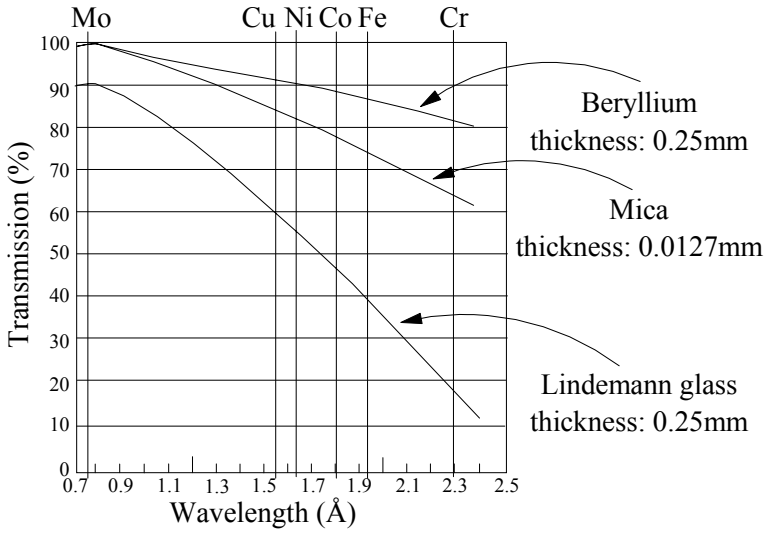

Figure 2.5. *Absorption graphs of different materials used for making windows*

2.1.1.2.5. Target contamination and aging

The heating of the tungsten filament, though necessary to produce electrons, causes the emission of metal vapors that can condense, particularly on the anode or on the walls of the tube, forming a thin layer of tungsten. The tungsten deposit on the anode leads, on the one hand, to the absorption of some of the emitted X-rays (up to 50% of the beam's intensity for a deposit of 2 μm thick), and second, to the presence of parasitic X-ray peaks.

The walls of the traditional X-ray tubes are made of glass. The deposit on these tube's glass walls causes the glass to gradually recrystallize, leading to the formation of tiny cracks that render the tube unusable. These effects, caused by the very principle of X-ray production, cannot be completely eliminated, but they can be minimized, for example, by increasing the cathode-anode distance. Most manufacturers have been selling tubes with ceramic walls for a few years. This problem is then solved. The lifetime of these "ceramic tubes" would therefore seem to be longer; however, this aspect is not clearly established.

Modern tubes used in practice take into account all of these details and can be described by the diagram in Figure 2.6.

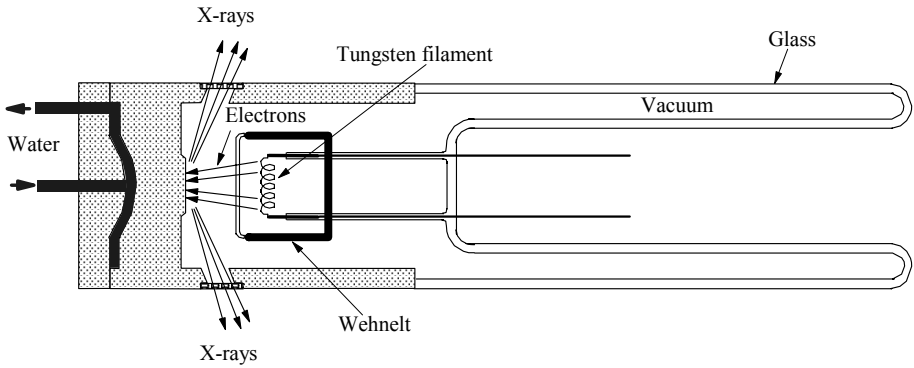

Figure 2.6. *Diagram of a Coolidge tube*

2.1.1.3. *High intensity tubes*

Conventional sealed tubes are used at powers of about a few hundred Watts per square millimeter. In such conditions, the necessary exposure times, although highly dependent on the type of detector used and on the geometric configuration of the system, are commonly from a few tens of minutes up to several hours long (sometimes several days). It is important to reduce these exposure times, particularly when the samples are not stable or when conducting kinetic studies of structural evolution. It then becomes necessary to use a source of high intensity X-ray beams.

The method commonly used consists of using a rotating anode tube. This rotation, which is done at high speeds (2,000 to 6,000 rpm), makes it possible to work at powers of several thousand Watts per square millimeter.

We can show that the performances of such a tube are proportional to $a\sqrt{bv}$, where a and b are the dimensions of the electron spot and v is the anode's surface speed. The increase in power therefore implies an increase either of the diameter or of the anticathode's rotation speed.

Most of the time, the rotating anode tubes are open tubes and can be described by the diagram shown in Figure 2.7.

The anode is a hollow cylinder, typically about 10 cm in diameter, rotating at several thousand revolutions per minute in a vacuum of roughly 10^{-7} Torr with a steady circulation of water at a typical flow rate of 20 liters per minute. Usually, a turbomolecular pump is used for maintaining the very low pressure inside the tube.

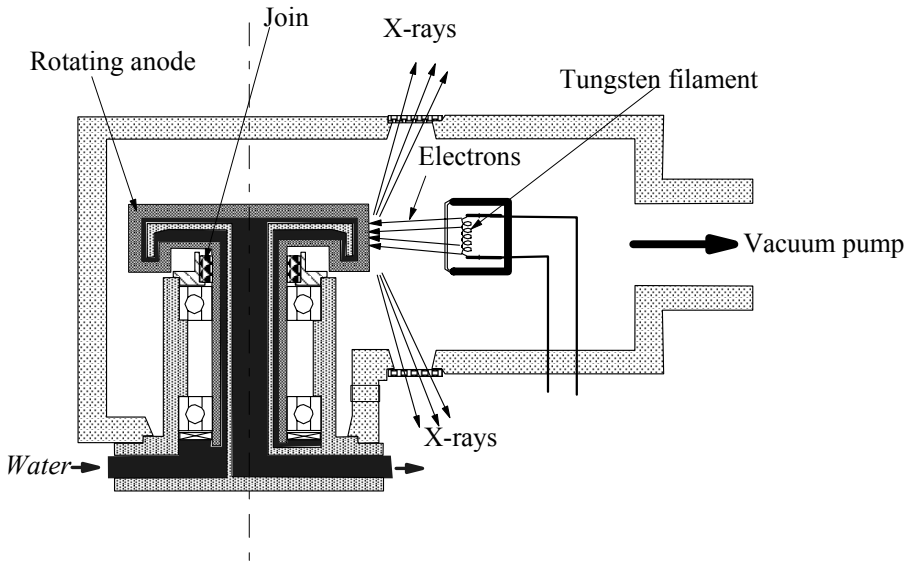

Figure 2.7. *Diagram of a rotating anode tube*

As the diagram in Figure 2.7 shows, the electron beam strikes the generatrixes of the cylinder that constitutes the anode. Therefore, the position of these generatrixes must not change so as not to cause the X-ray beam to move. This condition is particularly severe, since it means that, despite the high flow of water, the anode's rotation must remain stable.

Technically achieving this type of rotating anode open tube is still quite difficult. These tubes first appeared in the 1960s; however, up to now, only two companies in the world sell X-ray generators equipped with a rotating anode open tube. Note, however, that there are rotating anode sealed tubes. These tubes are simple to produce, but they were not designed to be used in X-ray scattering or diffraction experiments. Their field of application is the X-ray based medical imaging by radiography. Their description goes beyond the scope of this book.

2.1.1.4. *Synchrotron radiation*[2]

The X-ray sources we have just described in the previous sections emit X photons by de-excitation of atoms that underwent electronic transitions. The origin of synchrotron radiation is different.

As we have already mentioned, a charged particle in motion with a decreasing speed emits an electromagnetic radiation called braking radiation. On the contrary, when a charged particle is accelerated, the electromagnetic radiation that is emitted is called synchrotron radiation [SCH 49].

The power radiated by a particle moving along a circular trajectory with radius ρ is given by the relation:

$$P = \frac{2}{3}\frac{e^2 c \beta^4 \gamma^4}{\rho^2} \qquad [2.1]$$

with:

– e: electric charge of the particle;

– c: speed of light; $\beta = v/c$, v being the speed of the particle;

– γ: acceleration;

– $\gamma = \frac{E}{m c^2} = \frac{1}{\sqrt{1-\beta^2}}$ where E is the energy of the particle;

– $\rho = \frac{m\gamma c}{eB}$.

This general relation enables us to emphasize two essential features of synchrotron radiation:

– the lighter a particle is, the more radiation it emits. Therefore, we will be using electrons or positrons rather than protons;

– only particles moving at relativistic speeds ($\beta \approx 1; \gamma >> 1$) radiate with significant power.

2 Synchrotron radiation has been used in X-ray diffraction for over 50 years [HEL 98]. Over the past 20 years, the use of this type of source has become more and more widespread. However, the apparatus created for synchrotron radiation sources are specific prototypes. We will not go into the details of these instrumental developments in this book. This section on synchrotron radiation is intentionally brief and those readers interested in knowing more can refer to specialized works (see, for example, [WIE 03]).

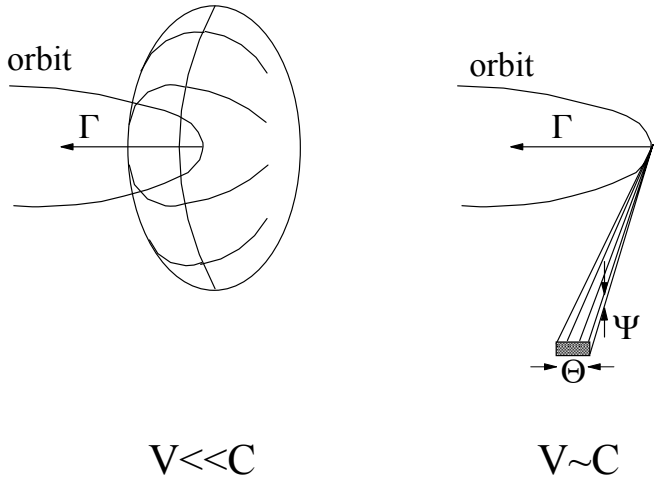

Figure 2.8. *Shape of the X-ray beam emitted by a particle in motion according to the speed of that particle*

The shape of the beams emitted by a particle is represented in Figure 2.8. When the particle is moving at a small speed, the emission is equivalent in every direction of space. On the contrary, if its speed is close to the speed of light, most of the emitted radiation is located in a cone characterized by a vertical opening $\Psi = 1/\gamma$. This very small divergence is characteristic of synchrotron radiation.

The main advantage of synchrotron radiation sources lies in the very high intensity of the X-ray beams they produce [FIN 89, HAS 84]. Synchrotron radiation sources can be divided into three different generations. The second and third generation sources were designed explicitly to provide very intense X-ray beams, whereas first generation sources were machines created to study the behavior of accelerated charges. There are currently 50 2^{nd} and 3^{rd} generation machines worldwide. Figure 2.9 shows the evolution of the brightness of X-ray sources over the course of the 20^{th} century. Brightness is defined as the number of photons emitted per second by square millimeter and by unit of solid angle for a wavelength in bandwidth $\Delta\lambda/\lambda = 0.01$. The synchrotron sources located in France are mentioned. This diagram shows that the beams produced by third generation synchrotrons are roughly 10^{12} times brighter than the ones emitted by rotating anode generators.

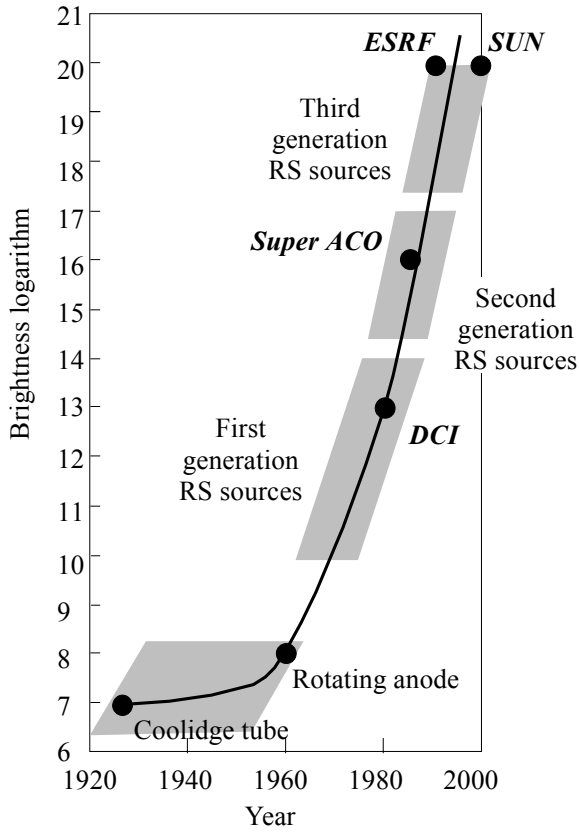

Figure 2.9. *Brightness of the different X-ray sources*

Also, as we have already mentioned, the beams produced by synchrotrons are only slightly divergent. This divergence, characterized by angle Ψ, is usually in the range of 0.1 to 1 mrad.

Finally, one of the essential characteristics of synchrotrons is that they emit in a wide range of wavelengths, which is why the beams are described as "white". Therefore, with the appropriate equipment, the user can choose the wavelength he wishes to use. This feature of synchrotron radiation is used more and more to conduct studies where the wavelength varies, particularly in order to choose a wavelength close to a characteristic absorption threshold of a given chemical element, which is referred to as anomalous scattering or diffraction [ISH 99, IWA 99, SCH 97]. This approach makes it possible to exacerbate the intensity of the signal scattered by an atom. Hence, these experiments in anomalous scattering or

diffraction are performed in order to distinguish the contribution from cations corresponding to neighboring atomic numbers.

2.1.2. *Filters and monochromator crystals*

Generally speaking, X-ray beams produced with a tube are polychromatic, in other words, they contain characteristic emission peaks in addition to a continuous spectrum over a wide range of wavelengths. In order to characterize the material to be studied, it is important to have a monochromatic beam which makes it possible to associate a single diffraction peak with each family of crystal planes. Therefore, it is necessary to select one peak among all of those emitted by the tube. Naturally, the most intense one is chosen.

There are two common techniques used to solve this problem:

– the filter: this consists of a thin sheet of a material that absorbs all of the radiations emitted with wavelengths below the one we wish to select;

– the monochromator crystal (or monochromator): this consists of a single crystal cut with respect to a specific family of planes. This single crystal is oriented so as to have the chosen family of planes in the Bragg position for the wavelength we wish to select, which means that only the X photons with that wavelength are diffracted. The result is a monochromatic beam.

2.1.2.1. *Filters*

The idea behind filters functioning lies in the absorption characteristics of the materials used. The absorption varies as $e^{-\mu\rho x}$, where μ is the linear absorption coefficient, ρ is the density and x is the length traveled. Naturally, the absorption coefficient varies with the wavelength.

Filters have to meet two conditions: first, to absorb as much as possible of the unwanted peaks, and so be thick enough, and second, to be as transparent as possible to the wavelength we wish to select (the Kα peak in practice), and so be thin enough.

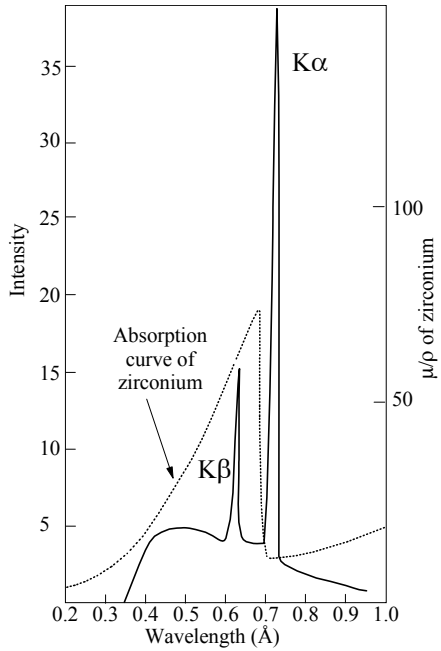

Figure 2.10. *Choosing a material for a filter which makes it possible to select the Kα radiation of molybdenum*

Therefore, it is important to choose a material whose absorption spectrum according to the wavelength shows a sharp decrease at a value very close to the wavelength of the anode's K_α peak. In practice, the appropriate material is an element very close in Mendeleyev's table to the one used in the anode. Figure 2.10 shows the example of a zirconium filter used for a molybdenum anode.

Based on information on the linear absorption coefficients (found in the *International Tables for Crystallography*), the optimal thickness of the filter can be calculated. Table 2.2 shows this data in the case of a molybdenum anode and a zirconium filter.

	Wavelength (Å)	**μ/ρ**	**ρ**	**μ = (μ/ρ)ρ**
Kβ	0.63	79	6.4	506
Kα	0.71	15.9	6.4	1,021

Table 2.2. *Absorption by a zirconium filter of the radiation emitted by a molybdenum source*

The result, for a thickness of 5μm, are the following transmissions:

– for the K_β radiation:

$$\frac{I}{I_0} = e^{-(506\times0.005)} = e^{-2.53} = 0.08 = 8\%$$

– for the K_α radiation

$$\frac{I}{I_0} = e^{-(102\times0.005)} = e^{-0.51} = 0.60 = 60\%$$

In the absence of filters, the intensity ratio of Kβ/Kα is 18.5/100; hence we obtain a ratio of about 2.5/100 with this zirconium filter. This data is listed in Table 2.3 for a few commonly used anticathodes.

Anticathode	**λ of Kα**	**Filter**	**Thickness (mm)**	**Absorption of Kβ (%)**
Ag	0.561	Pd	0.0461	96
		Rh	0.48	96.4
Mo	0.711	Nb	0.0481	96.5
		Zr	0.0678	96.8
Cu	1.542	Ni	0.017	98.4
Ni	1.659	Co	0.0158	98.7
Co	1.79	Fe	0.0166	98.9
Fe	1.937	Mn	0.0168	99.2
Cr	2.291	V	0.0169	99.4

Table 2.3. *Absorption factors obtained with filters adapted to the radiation emitted by a few commonly used sources*

The complete description of the different radiations that comprise the Kα emission is complex. In the case of copper, for example, at least 6 different peaks are observed [DEU 95; DEU 96; DIA 00]. However, the K_α emission spectrum can be considered in a first approximation to be comprised of 2 main peaks, $K_{\alpha 1}$ and $K_{\alpha 2}$. These two contributions cannot be separated by an absorption filter, which is why the resulting beam remains bichromatic. The two peaks can only be separated with the use of a monochromator crystal, under certain conditions.

2.1.2.2. *Monochromator crystals*

As we have already mentioned, the underlying idea of such an instrument lies in the selective diffraction of a polychromatic beam by a single crystal. It can be described by the diagram in Figure 2.11a.

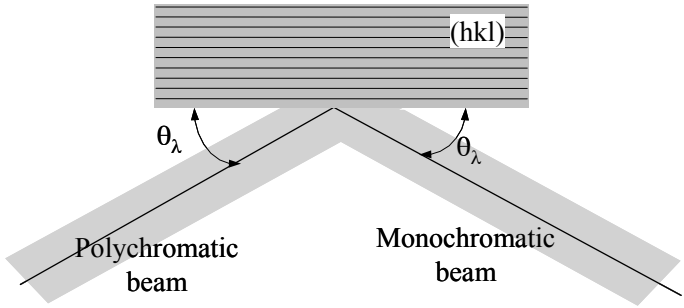

(a) Selective diffraction by a single crystal of a polychromatic X-ray beam

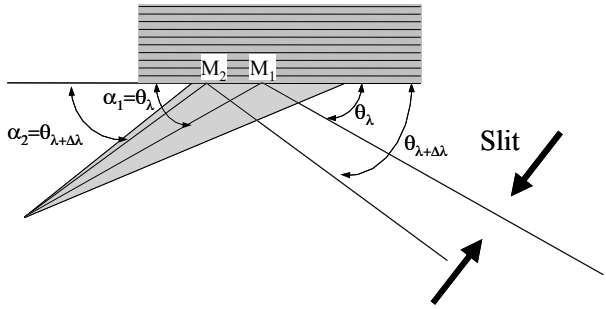

(b) Detail of figure (a)

Figure 2.11. *Diagram showing how a plane crystal monochromator works*

The polychromatic beam produced by the X-ray source irradiates a plane crystal cut parallel to a family of crystal planes. This single crystal is oriented around a rotation axis parallel to the reference family of planes. For the chosen wavelength λ, when the incidence angle of the X-ray beam is equal to the Bragg angle θ_λ, a diffracted beam with wavelength λ is observed.

It is clear that the wavelength selectivity of this method directly depends on the angular range inside which the crystal diffracts, for a given wavelength. We saw in the previous chapter that all crystals show a certain mosaicity. The selectivity of a monochromator single crystal increases when its mosaicity decreases. However, if we imagine a single crystal with an infinitely small mosaicity, then for a given position of the crystal only the photons arriving exactly at the Bragg angle θ_λ would be diffracted. We know that the traditional X-ray sources produce divergent beams, so the intensity of the beam originating from the monochromator should be very small. In practice, the objective is to achieve a compromise and to produce crystals with such a mosaicity that the diffracted beam is as monochromatic as possible, while still remaining relatively intense.

The diagram in Figure 2.11a does not explicitly take into account the divergence of the X-ray beam originating from the source. The situation is described in greater detail in Figure 2.11b. Consider a divergent beam irradiating a plane single crystal. Let us assume that the photons arrive at a point M_1 of the crystal at an incidence $\alpha_1 = \theta_\lambda$. They arrive at M_2 at an angle $\alpha_1 \neq \alpha_2$. If diffraction occurs, the diffracted beam has a wavelength $\lambda + \Delta\lambda$ and the diffraction angle is $\theta_{\lambda+\Delta\lambda}$. We can see that the two beams diffracted in M_1 and M_2 are divergent. Wavelength λ is selected by adding a slit F on the path of the diffracted beams, in order to let the diffracted beam at the angle θ_λ pass and to stop the one at the angle $\theta_{\lambda+\Delta\lambda}$. The intensity of the beam originating from this kind of plane monochromator associated with a divergent source is, in fact, after the considerations we have just made, small. This constitutes the main drawback of this kind of monochromator.

In order to avoid this problem, it is possible to create curved crystal monochromators. The diagram showed in Figure 2.12 shows how a Johann monochromator [JOH 31] works.

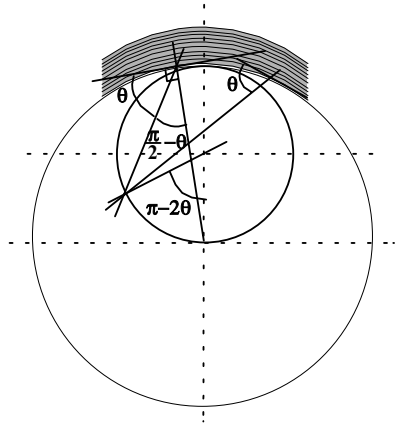

(a) Geometric construction

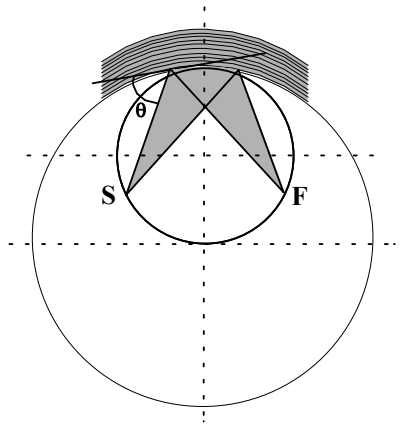

(b) Path of the X-ray beams

Figure 2.12. *Diagram showing how a curved crystal monochromator works*

The single crystal is a strip cut parallel to a family of crystal planes. This strip is then curved with a radius 2R. The divergent X-ray source is placed at point S, which is on the circle with radius R, tangent to the previous circle, and defined so as to have the angle (SOC) equal to $\pi - 2\theta$. The X-rays with wavelength λ are at a constant angle $\pi/2 - \theta$ with the normals to the reticular planes and hence at an angle θ_λ with the crystal planes. The diffracted beams form a beam that converges to the focal point F. Note that the crystal planes do not exactly fit the circle with radius R and therefore the convergence of the diffracted beams is only approximate.

Other experimenters, such as Johansson [JOH 33], designed monochromators with a rigorous focusing. The technique consists of cutting a cylinder with radius 2R inside a plane single crystal strip with its faces parallel to a family of planes. The strip is then curved on a circle with radius R which is the focusing circle. A diagram of such a monochromator is shown in Figure 2.13.

In any point of the crystal tangent to the circle with center C, the normal to the curved crystal planes passes through O, which is the center of curvature of these planes. Let S be a point of the circle such that the angle (SCO) = $\pi - 2\theta_\lambda$ with θ_λ as the corresponding Bragg angle. For any point M of the single crystal, we then have:

$$(SMO) = (SCO)/2 = \pi/2 - \theta_\lambda$$

Finally, if S represents a punctual X-ray source, all of the beams originating from this source and with a wavelength K_λ will be at an angle θ_λ with the (hkl) planes of the single crystal (since they are at an angle $\pi/2 - \theta$ with the normal to these planes) and therefore will be diffracted by these planes. The diffracted beams will all converge to a point F called the focusing point. If the source is linear and perfectly parallel to the generatrixes of the cylinder defined by the monochromator, the diffracted beam will be focused on a line that passes through F. If the source S is thin enough, and if the single crystal's orientation is perfectly controlled, it is possible, in the case of copper for example, to single out the $K_{\alpha 1}$ radiation, leading to a monochromatic beam.

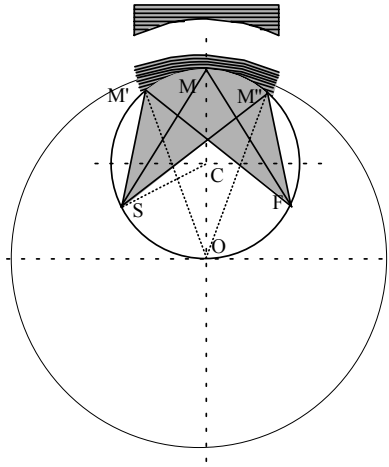

Figure 2.13. *Diagram showing how a Johansson curved crystal monochromator works*

The Johansson monochromator is symmetric, since the distances SM and MF are identical. It is often an advantage from an experimental point of view to have the length MF greater than the length SM. Guinier [GUI 37] created an asymmetric monochromator by tilting the diffracting crystal planes at an angle α in relation to the single crystal's surface (see Figure 2.14).

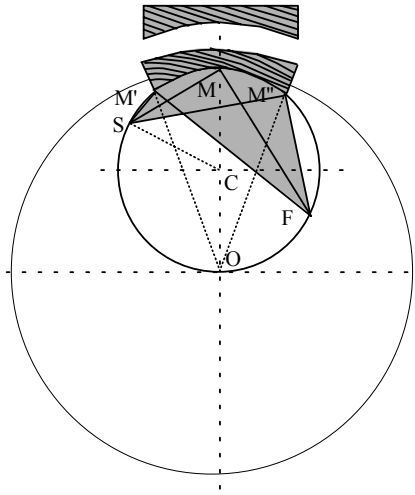

Figure 2.14. *Diagram showing how a Guinier crystal monochromator works*

2.1.2.3. *Multi-layered monochromators or mirrors*

In the early 1990s, a new type of monochromator elements appeared. These devices were made of stacks of alternate metal layers a few nanometers thick. The first layer is the same as the third, the fifth, the seventh, etc., whereas the even layers are different from the odd layers but all identical [ARN 90, SCH 88]. The resulting multi-layered object can be considered an artificial crystal with an interplanar distance equal to the distance between two layers of the same kind. The intensity diffracted by these artificial crystals will be all the greater if the deposited layers show a strong electronic contrast. The most common elements are made of an alternate stacking of tungsten and silicon layers [SCH 95]. More recently, some authors have designed similar multi-layered monochromators out of refractory materials. Stacks of aluminum oxide and tungsten layers were produced to create monochromators that could withstand high temperatures [MOR 96].

These artificial crystals are designed so as to have the thickness of the layers vary continuously from one end of the substrate to the other (see Figure 2.15a). Two types of configuration have been imagined. In the first case, the substrate has a

parabolic curve and the thickness of the layers varies along the substrate's length according to the same parabolic law. When a divergent incident beam originating from a source placed in the parabola's focus is diffracted by this type of layering, the beam originating from the monochromator is parallel (see Figure 2.15b). In the second case, the substrate is elliptical and the beam diffracted by the monochromator is then convergent (see Figure 2.15c).

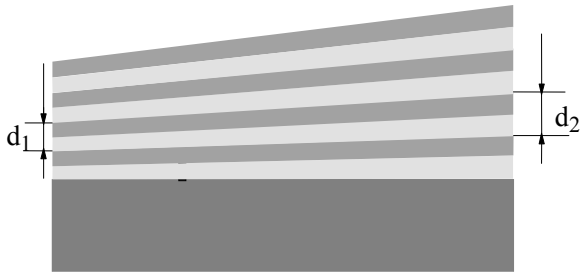

(a) Structure diagram

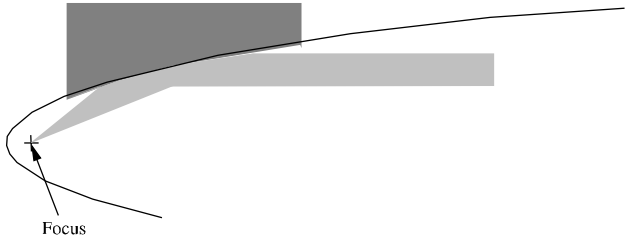

(b) Path of the X-ray beams for a parabolic element

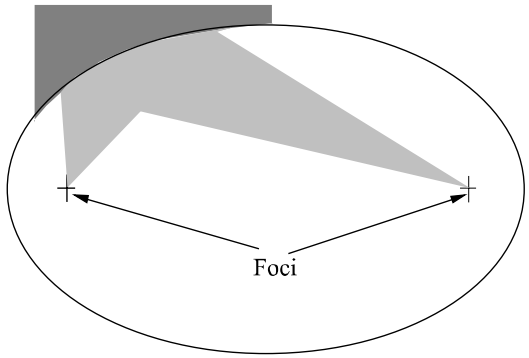

(c) Path of the X-ray beams for an elliptical element

Figure 2.15. *Multi-layered monochromator*

Therefore, these monochromators make it possible, depending on the substrate's initial curvature, to produce parallel or converging beams. The intensity of the beams diffracted by these elements is much higher than the output of traditional monochromators based on quartz or germanium crystal. This is because the curvature of these "artificial crystals" ensures that all of the incident beams are diffracted, and since their characteristic interplanar distances are typically ten times greater than those of natural crystals, their selectivity is much smaller.

Therefore, the diffracted beams are more intense, but the wavelength selectivity is not as good. Generally speaking, these artificial monochromators are unable to separate the $K_{\alpha 1}$ and $K_{\alpha 2}$ wavelengths [TOR 00].

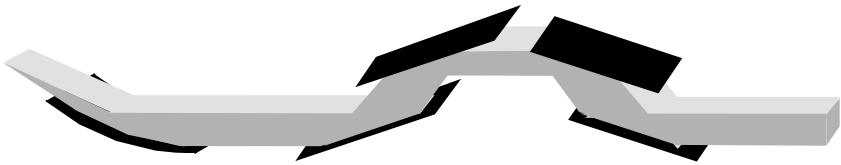

(a) Hybrid monochromator. The result is a wide and intense monochromatic beam

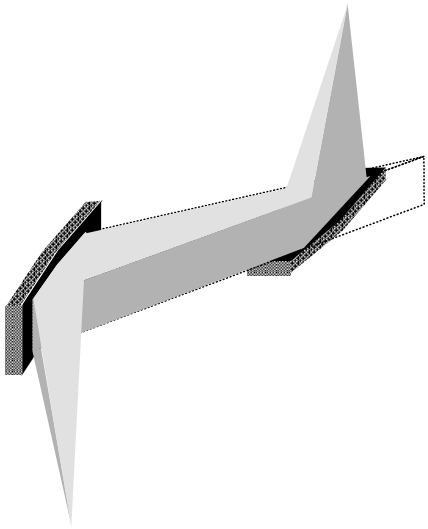

(b) Production of punctual monochromatic beams.
Use of two crossed elliptical "artificial crystals"

Figure 2.16. *Association of several types of monochromators*

For some specific applications, they can be associated with traditional monochromators. An illustration of a typical configuration of this kind is shown in Figure 2.16a. A parabolic artificial crystal is irradiated by a divergent source, and the beam diffracted by this element is then diffracted by a monochromator comprised of two or four plane crystals [SCH 95]. The beam resulting from this system, sometimes referred to as a hybrid monochromator, is perfectly monochromatic and much more intense than in the absence of a parabolic artificial crystal. Note, however, that this beam is much wider than the initial beam produced by the source. Therefore, this monochromator is only used for particular types of configurations and these hybrid monochromators are essentially used for certain studies of epitaxial thin films [STO 97].

Another typical configuration based on these artificial crystals is shown in Figure 2.16b [ARN 98]. It consists of the association of two elliptical crystals. A punctual beam originating from a traditional source irradiates the first elliptical crystal and then the resulting beam converges to a plane defined by the position of this first crystal. A second crystal is placed in a plane normal to the first and the beam produced by this system then converges to one point.

2.1.3. *Detectors*

2.1.3.1. *Photographic film*

X-rays reduce silver halides the same way light does and therefore can produce images on photographic film. These films were the first X-ray detectors, first used by Röntgen to show the existence of X radiation [RON 95].

The darkening of the film is related to the intensity of the X-ray beam and, additionally, there is no illumination threshold. Therefore, even very low intensities can be detected, simply by lengthening the exposure time. The plotted curve in Figure 2.17 shows the evolution the film's optical density according to the radiation intensity and the exposure time.

In the linear area of this graph, it is possible to measure the intensity of the various peaks that left an image on the film. For this purpose, an optical microdensitometer is used, in order to convert into an electrical signal the intensity of a light beam passing through the film. This technique enables the user to make a semi-quantitative measurement of the diffracted intensity.

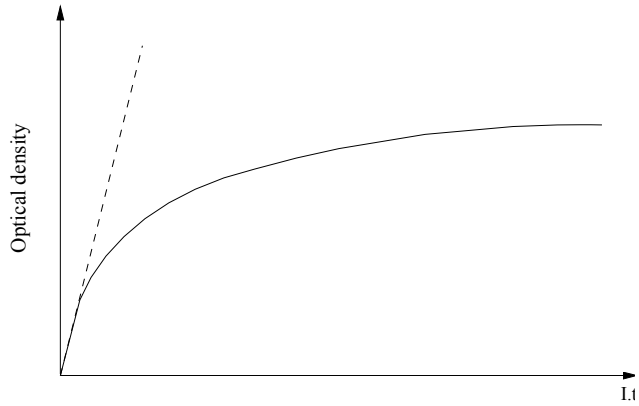

Figure 2.17. *Darkening of film according to the intensity of the beam that irradiates it*

Throughout the 20th century, film was an important element in the design of diffraction apparatus. However, the resulting signal is not directly digital and therefore requires a transformation in order to be analyzed quantitatively. This intrinsic characteristic is the cause for the gradual disappearance of the use of photographic film. There are currently no manufacturers selling film-based diffractometers.

2.1.3.2. *Gas detectors*

2.1.3.2.1. Mechanism

The way these detectors work relies on the measurement of electrical currents produced by the ionization of the atoms in a gas irradiated by an X-ray beam. This effect was observed by Thomson shortly after X-rays were discovered [THO 98b], so these detectors were used in the earliest studies of X-ray scattering and diffraction; in fact, the diffractometer built by the Braggs was equipped with a gas detector [BRA 13a] (see Figure 5 in the introduction of this book).

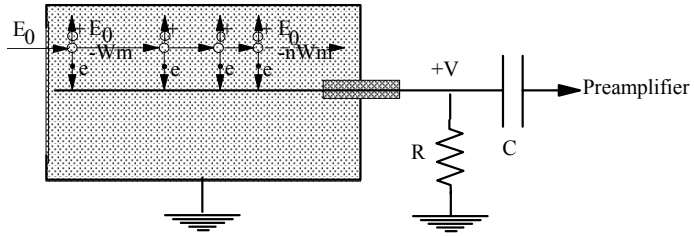

Figure 2.18. *How a gas detector works*

Here is how the measurement is done: the X photons, with energy $E = h\nu$, ionize the atoms of a gas placed inside a chamber and the current resulting from this ionization process is measured. The X-rays reach the chamber filled with gas through the window. Voltage is applied between the chamber, which constitutes the cathode, and a wire, working as the anode, located in the center of the chamber. The electrons are attracted towards the anode and the resulting electrical current is measured. A diagram explaining how this type of detector works is shown in Figure 2.18.

The detection threshold is set by the first ionization energy W_1. An incident photon, with energy E_0, gradually loses its energy and therefore ionizes $n_0 = E_0/W_1$ atoms. However, some atoms are ionized several times and an average of $n_m = E_0/W_m$ electrons is obtained, where W_m is the average detection threshold. As an example, argon, which has the atomic number $Z = 18$, has an average ionization energy $W_m = 26.4$ eV, the X photons of copper's K_α peak, which have an energy $E_0 = 8{,}040$ eV, can produce $nm = E_0/W_m = 304$ ion-electron pairs.

The electrical behavior of this type of detector depends on what voltage is applied. Several operating areas related to the applied voltage can be defined. The difference between these areas is the amplification coefficient, which expresses the behavior of electrons produced during the ionization (Figure 2.19).

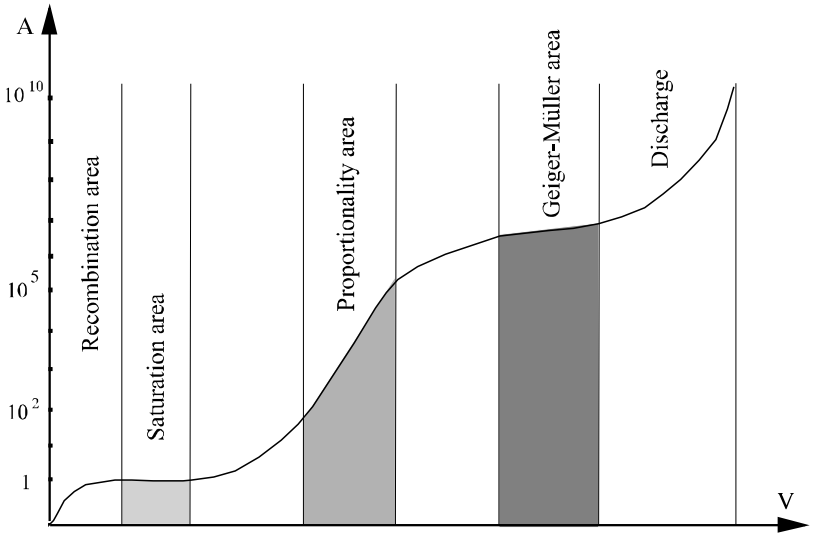

Figure 2.19. *The different operating conditions of gas detectors*

In the first area, when the voltage is low, the ion-electron pairs recombine to form atoms again; this is the "recombination area".

In the next area, the voltage applied is just enough to ensure that the electrons are collected without recombination; this is the “saturation area”.

Beyond a threshold value of a few hundred volts, the electrons produced by the ionization induced by the X-rays have an energy high enough to ionize other atoms, producing new electrons that also lead to more ionizations, causing an avalanche process. However, the applied voltage is relatively small and the electrons only acquire enough energy to trigger the avalanche in the vicinity of the anode. Also, the ions move much more slowly than the electrons, forming a positively charged zone with the same center as the anode. The electrons produced by the X-rays are held back by this charge, damping the avalanche effect. In the end, each X photon only produces one avalanche. The number of electrons produced is proportional to the intensity of the X radiation received. This is the “proportionality area”.

When the voltage is increased some more, a single photon is enough to trigger an avalanche process that becomes widespread. The intensity of the produced current is no longer proportional to the intensity of the X-ray beam. This is the “Geiger-Müller counter area”.

For higher voltages, a spontaneous and permanent discharge is observed. This is the discharge area.

Based on these various operating conditions, three types of detectors are traditionally defined.

2.1.3.2.2. The different types of gas detectors

Ionization chambers

The use of the phrase “ionization chamber” is cause for some confusion since, literally speaking, all gas detectors are ionization chambers. However, this terminology is the one used to refer to gas detectors designed to work at voltages that place them in the saturation area.

The saturation voltage depends on the intensity of the radiation we wish to measure; if this intensity is relatively low, a voltage of a few hundred volts is enough, whereas for more intense beams, the saturation voltage can go up to 800 volts.

The chamber’s sensitivity increases with the fraction of absorbed radiation, so a heavy gas is generally used. Argon at atmospheric pressure absorbs the X photons of copper’s K_α peak almost completely. The sensitivity depends on the wavelength and therefore the intensities of two beams with different wavelengths can be compared.

Geiger-Müller counters

As we have said, these systems only need one photon to trigger an avalanche process, which makes them highly sensitive. Since each photon causes a discharge, an electronic device is used to count the number of discharges, leading to the number of photons absorbed over a given period of time.

This system is relatively simple and is used as a mobile detector. However, it has a high dead time (≈ 200 μS), hence a low maximum counting rate[3]. This type of device cannot be used for quantitative intensity measurements.

Proportional counters

This last type of gas detector is currently the most used in X-ray diffraction. It has several advantages compared to the Geiger-Müller counter:

– the dead time is very short (≈ 1 μS) so the counting rate is high (up to 10^7 count/s), while maintaining a linear response;

– the amplitude of the signal is proportional to the energy of the photons, which enables an energy discrimination, and therefore wavelength discrimination as well. If the bandwidth is centered in the energy $E_{K\alpha}$, only the diffracted peaks with that wavelength are selected, thus significantly reducing the continuous background by limiting the contribution of fluorescence radiation;

– due to the absence of a discharge, the lifetime of these detectors is much longer than that of Geiger-Müller counters.

2.1.3.2.3. Position sensitive gas detectors

This type of detector enables the user to measure the number of X photons and also to know where the ionization center of the gas molecules is along the anode [CHA 70]. This makes it a one-dimensional (or two-dimensional) detector [GAB 78, SUL 94] that can measure the function $I = f(x)$ (or $I = f(x,y)$), where x is the position. The position is determined by measuring the time difference for the signal to travel along the anode between the impact point and one of its ends. A multi-channel analyzer memorizes the number of hits per channel.

Two different kinds of one-dimensional detectors like these are currently sold. On the one hand, there are linear detectors with windows that have an opening of a few centimeters [GAB 77]. And on the other hand, curved detectors shaped like a part of torus with a 120° opening [WOL 83]. We will see later on how both of these detectors can be used. Note, however, that they provide a considerable time gain, since the acquisition is made simultaneously over an entire angular area.

3 The maximum counting rate is defined as the maximum number of photons that can be counted per second.

The position sensitivity of this type of detector is set by the minimum distance between the impact points of two photons below which the system considers that they hit the detector in the same spot. This sensitivity is equal to roughly 150 μm for current models.

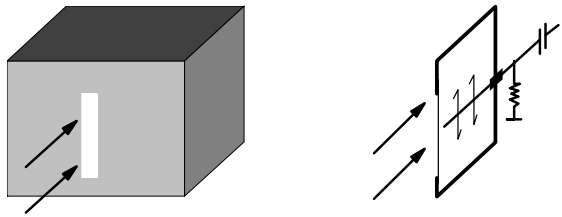

(a) Traditional punctual detector

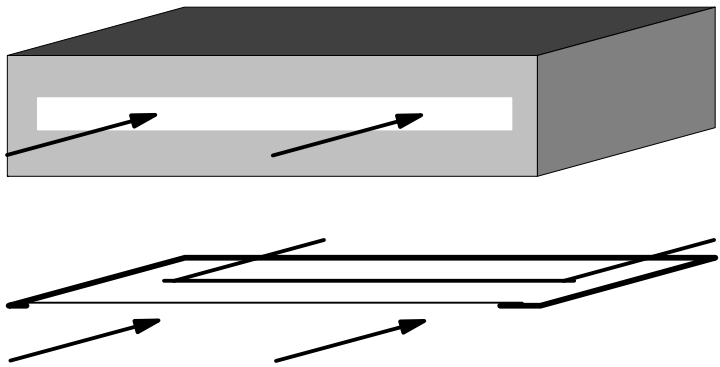

(b) Linear position sensitive detector

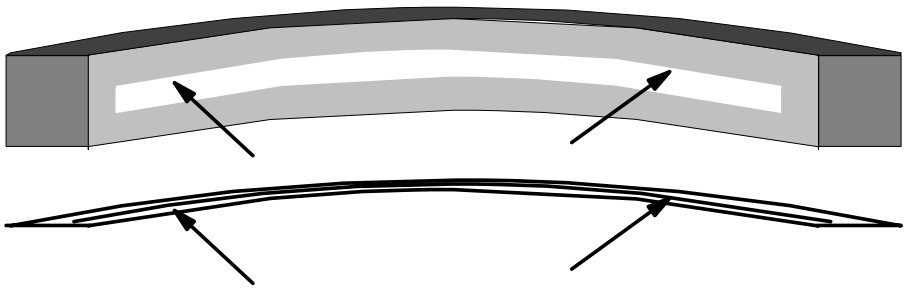

(c) Curved position sensitive detector

Figure 2.20. *One-dimensional position sensitive detector*

2.1.3.3. *Solid detectors*

2.1.3.3.1. Detectors that use fluorescence in the visible spectrum

Luminescence is the emission of visible (or infrared or ultraviolet) electromagnetic radiation with an origin that is not thermal. Some bodies can emit light radiation when they are irradiated with X-rays or electrons. The word fluorescence is used to refer to an emission that occurs immediately after the irradiation, while phosphorescence refers to an emission that persists for a certain time after the excitation. Generally speaking, the emission process takes place as follows: a radiation bombarding the atoms induces electronic transitions in these atoms. The subsequent return of the electrons to more stable energy levels induces an emission of energy in the form of photons. The details of this process will not be described here, however we can point out that for a crystal to be luminescent, it must have intermediate energy levels between the valence band and the conduction band. These intermediate levels are caused by the presence of crystal defects (vacancies, interstitial atoms, etc.) which are voluntarily created by adding dopants.

In the case of X radiation induced luminescence (referred to as radioluminescence), the process is a little more complicated. The X-ray irradiation induces the production of electrons with a high energy, which bombard the neighboring atoms, causing electronic transitions and the emission of visible photons by excitation. This physical phenomenon has been known for a long time and is used in several types of X-ray detectors.

Direct observation of light photons

i) Fluorescent screens

With this type of detector, fluorescence is observed directly. Barium platinocianide, willemite and zinc sulfur are examples of materials used. It is possible to produce screens coated with these products. Zinc sulfur is currently the most used.

In X-ray diffraction, such screens are not used to detect diffracted beams, since their intensity is much too small to yield visible spots. These screens are used to visualize the primary beam while geometric adjustments are made to diffraction apparatus.

ii) Detectors that use CCD cameras

A new application of the fluorescence effect in the visible spectrum has appeared in the past few years. It consists of recording on a digital camera the image created by the light photons emitted by a fluorescent screen. These are CCD (charge coupled device) cameras. The principle of such detectors will not be described in detail in this book.

These cameras have been known for some time, but their use in X-ray diffraction is recent [STA 92]. They are used to create plane detectors, the main problem being the uniformity in space of the intensity measurement.

Detectors with a functional surface of over 10 cm in diameter are currently available on the market. Since the end of the 1990s, they are custom-made on diffractometers designed for structural studies of single crystals. This maximum size, a technical feat for the manufacturers that justifies a very high price, is a significant limitation to the use of these detectors for diffraction on polycrystalline samples. As we will see later on, prototypes of diffractometers designed for the study of polycrystalline samples and equipped with this type of detector have recently been produced.

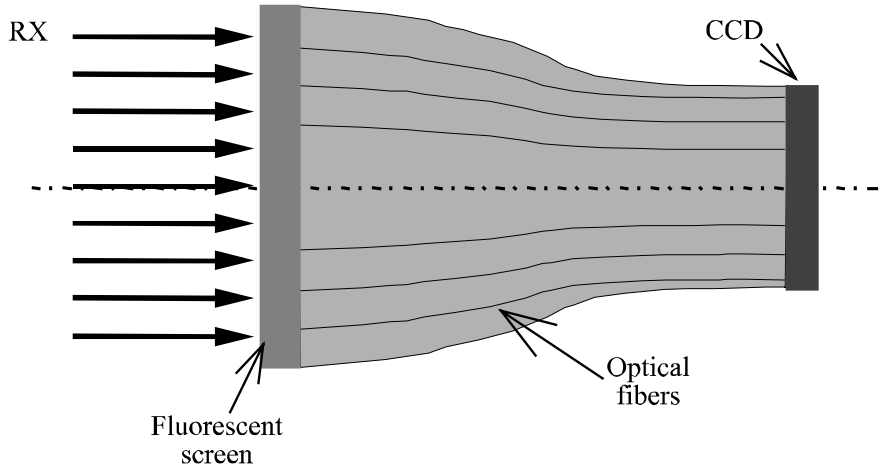

Figure 2.21. *Diagram of a CCD detector*

Scintillation detectors [ARN 66]

In these detectors, as for the previous ones, the X photons are transformed into light photons. However, the measurement is then achieved by transforming these light photons into electrons and into an electrical signal by way of a photocathode. A diagram explaining how such a device works is shown in Figure 2.22.

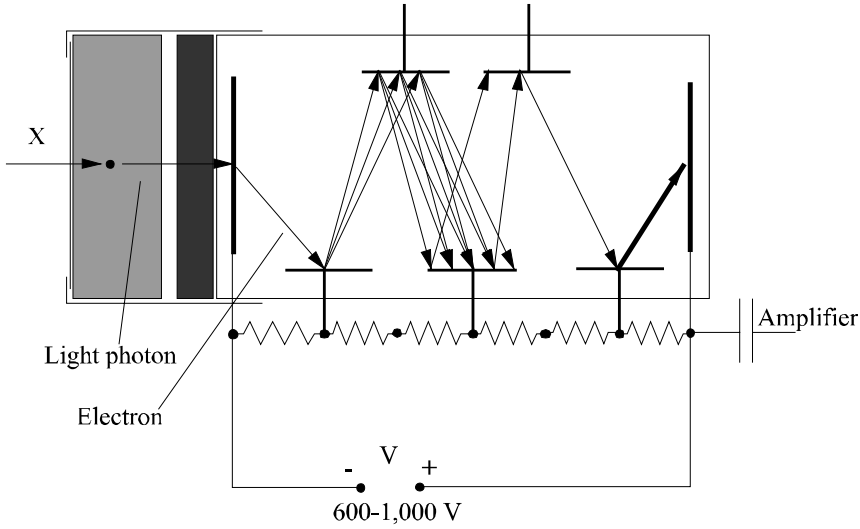

Figure 2.22. *Diagram of a scintillation detector*

The scintillator that transforms X photons into light photons is made of crystals, most often NaI doped with thallium, CsI doped with thallium, CaI_2 doped with europium and ZnS doped with silver.

Due to the photoelectric effect, light photons, when in contact with the cathode, create electrons that are accelerated toward the dynode, themselves creating secondary electrons that are accelerated toward another dynode, the process repeating itself about ten times, after which the electrons are collected by an anode. This constitutes a photomultiplier with an amplification factor of about 10^6 to 10^8, whose exact value depends on the voltage applied to the dynodes. After amplification, the current that was created is measured.

This type of detector is one of the oldest and most often used in X-ray diffraction. Its response time is extremely low (≈ 0.2 μS). This feature is its main advantage compared to proportional gas detectors. It is sensitive to the energy of X-rays but has a poor energy resolution. Its efficiency is almost 100%. Compared to proportional gas counters, the background noise is more significant and scintillating crystals deteriorate in a humid atmosphere.

Indirect method: the imaging plate

Measurements made by using those solid detectors are conducted in three distinct phases: recording, reading and erasing. This separation in different

sequences gives these devices, which first appeared in the early 1990s, their own category. The different steps are shown in Figure 2.23. The active part of the detector is comprised of a film made of phosphorescent material: BaBrF doped with europium. Irradiating this film induces electronic transitions and a certain number of electrons end up at high energy levels. Together, these excited sites form a latent image, read by a controlled scanning of the impressed film with a lazer beam. The lazer radiation induces the atoms to return to lower energy levels and the emission of photons in the visible spectrum. These light photons are detected in the same way as in a scintillation detector. A two-dimensional image is thus created point by point. After this reading sequence, the measurement is erased by using a sodium lamp which irradiates all the atoms on the detection film back to a state of equilibrium.

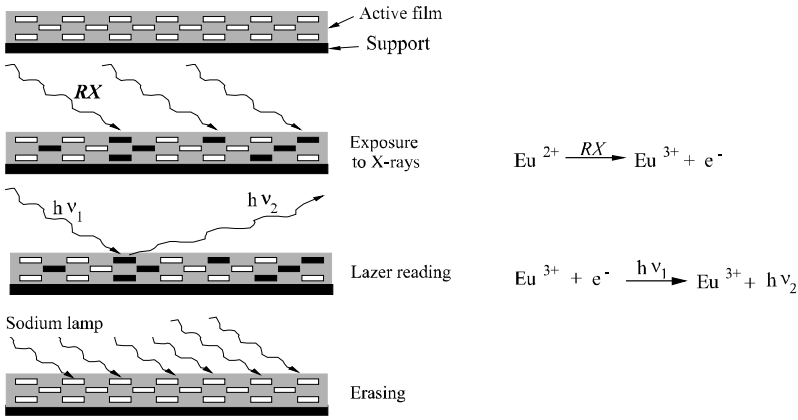

Figure 2.23. *Diagram of how an imaging plate detector works*

This mechanism was used to produce plane detectors in large sizes (up to 25 cm in diameter) and with a resolution of up to 100 μm^2. Because of their size, these detectors are used for diffraction by polycrystalline samples in order to directly measure all of the diffraction rings. They have been implemented for this purpose since the early 1990s, for example, on synchrotron radiation sources [GUA 96, NOB 97]. The main drawback is a certain remanence of the image after it has been erased.

2.1.3.3.2. Semiconductor detectors

X-rays are absorbed by a diode made from a semiconductor single crystal of silicon or germanium doped with lithium. The X photons produce electrons that induce electronic transitions in the valence and conduction bands of the silicon atoms.

A voltage applied between the two faces of the semiconductor enables the user to measure the electric charge, which is proportional to the energy of the incident X photons. A diagram of such a device is shown in Figure 2.24.

The main advantage of this type of detector is its energy resolution. This resolution is set by the energy required for creating an electron-hole pair and, in this case, is close to 3.5 eV. Therefore, it is used for studies in energy dispersion which are rarely applied in diffraction and that will not be described here. We will simply point out that this type of detector is showing interesting developments in the field of X-ray diffraction, but these are still nothing more than prospects [HON 92, OTT 97].

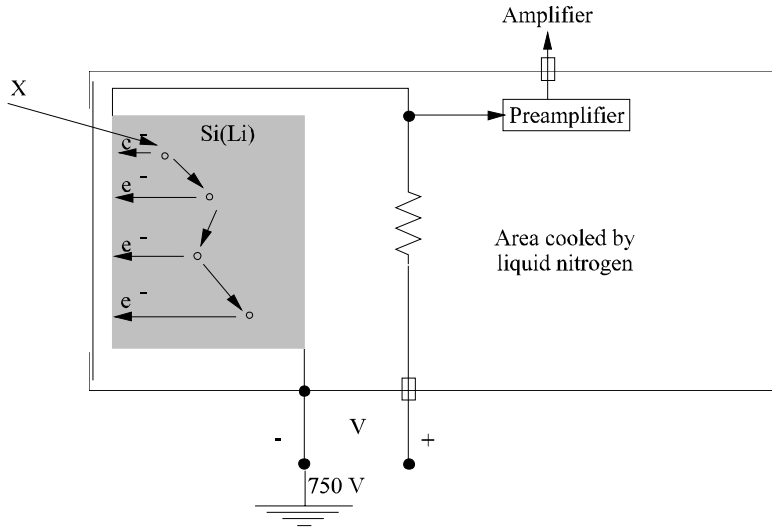

Figure 2.24. *Diagram of how a semiconductor detector works*

2.2. Diffractometers designed for the study of powdered or bulk polycrystalline samples

Nowadays, most diffractometers are modern versions of devices designed during the first quarter of the 20th century. We saw in the introduction of this book that the first diffraction measurements on polycrystalline samples were conducted in 1916, only four years after the discovery of diffraction by single crystals. The first three devices which we will describe in this part of the book were designed between 1916 and 1920, whereas the other two date back to only 10 years ago for the first and two or three years for the second.

Aside from their field of application, the essential difference between these diffractometers is their geometric layout [GUI 05]. In particular, the relative positions of the source, of the sample-holder and of the detector are different. Therefore, the description of these devices will rely essentially on geometric considerations. One of the most significant consequences of choosing a particular geometric configuration is the angular resolution of the device. Therefore, the description of these devices will be illustrated by measurements which make it possible to evaluate this essential feature.

Generally speaking, the objective of the following detailed descriptions is to enable researchers or engineers who are implementing X-ray diffraction for the characterization of polycrystalline samples to choose the device best adapted to their needs. It goes without saying that no device is able to make every type of measurement, hence the need to know their advantages and drawbacks.

2.2.1. *The Debye-Scherrer and Hull diffractometer*

This was the device used in 1916 by Debye and Scherrer [DEB 16] in Germany, and later in 1917 by Hull [HUL 17a, HUL 17b] in the USA, to conduct the first diffraction experiments on polycrystalline samples. A schematic view of the geometrical arrangement of this device is shown in Figure 2.25. The sample is irradiated with an X-ray beam produced by a Coolidge tube. The diffracted beams are collected by using a cylindrical detector placed so as to have the sample on its axis.

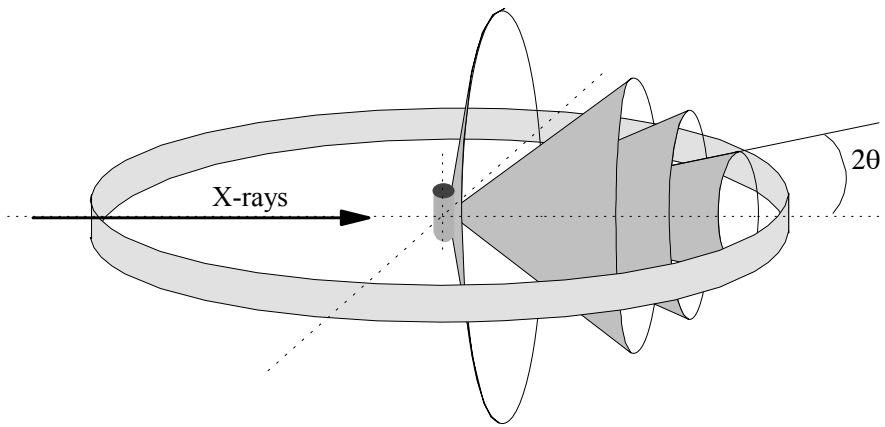

Figure 2.25. *Geometric arrangement of the Debye-Scherrer and Hull diffractometer*

2.2.1.1. *The traditional Debye-Scherrer and Hull diffractometer*

The X-rays emitted by the Coolidge tube penetrate the cylindrical chamber on the axis of which is placed the sample. An imprint of the diffracted beams is produced using a film placed on the inside of the chamber. The intersection of the diffraction cones and the cylinder gives diffraction arcs with a curvature that depends on the angle. These arcs become lines when $2\theta = 180°$ and their curvature is reversed beyond that.

In order to obtain a relatively fine beam, to limit the width of the arcs, a collimator is added to define the beam's geometry. However, the beam has to remain wide enough to ensure a high enough intensity. After going through the sample, the transmitted (non-diffracted) beam is still very intense and widely scattered by the air present inside the chamber. This effect significantly darkens the film in the vicinity of the direct beam and can prevent certain arcs with low diffraction angles from being seen. This effect can be virtually eliminated by adding a beam stop as close as possible to the sample, which absorbs most of the transmitted beam immediately after it exits the sample, thus significantly containing the effects of this scattering.

Two sample holders can be considered, but they must always be made of glass so as not to diffract the X-rays.

Fiberglass

In this case, the sample holder is made of fiberglass, which is as thin as possible, on which the powder we wish to study is deposited and glued using a thin layer of grease.

This method, while relatively simple, has a drawback. The powder located on the edges of the fiber cannot be placed in exactly the center of the device, which widens the diffraction arcs.

Capillary

This time, the powder sample is placed inside a glass tube with very thin sides. The major problem of this sample holder is absorption, since the X-ray beam must go through the tube's walls and therefore be partially absorbed. Therefore, the capillary is made out of low absorbing material, in practice Lindemann glass or silica.

Regardless of whether the sample holder is a fiber or a capillary, it has to be placed in the center of the chamber. Therefore, the stand made for the sample holder is built on a moving axis that can be adjusted using a system of screws and springs. This adjustment must imperatively be made before each experiment.

In both cases, the quantity of material used is very small, since the analysis is transmission-based, making it important to limit the absorption by the sample. In order to prevent effects caused by too small a number of grains, the stand for the sample holder can rotate, so that each grain can be, in turn, placed in the Bragg position for different families of planes.

The beam originating from the X-ray tube is polychromatic. In order to select the appropriate wavelength, the Debye-Scherrer and Hull devices are usually equipped with filters. The use of monochromators is a possibility, but the intensity of the diffracted beams would be too low and the exposure times too long. The $K_{\alpha 1}$-$K_{\alpha 2}$ doublet cannot be separated with filters, which constitutes one of the limitations of this type of device. A schematic view of a traditional Debye-Scherrer and Hull diffractometer is shown in Figure 2.26.

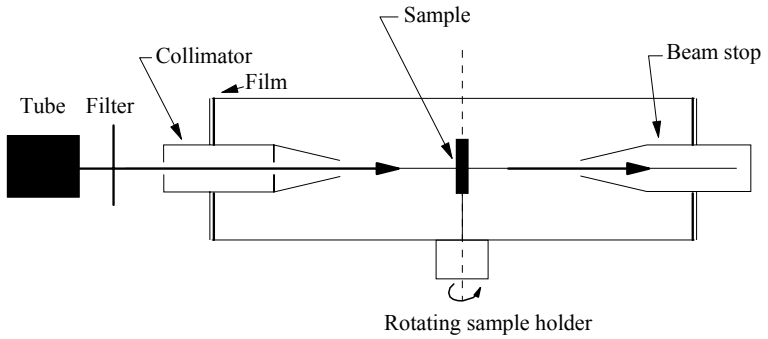

Figure 2.26. *Traditional Debye-Scherrer and Hull diffractometer*

Figure 2.27 shows a film obtained for a sample of magnesium oxide.

Each of the arcs corresponds to a family of crystal planes with an interplanar distance that can be inferred from Bragg's law and a measurement of the diffraction angle. In order to make the interpretation simpler, the radius of the chamber is such that a length of 180 mm on the film is equivalent to an angle of 180° (the radius has to be equal to 57.3 mm).

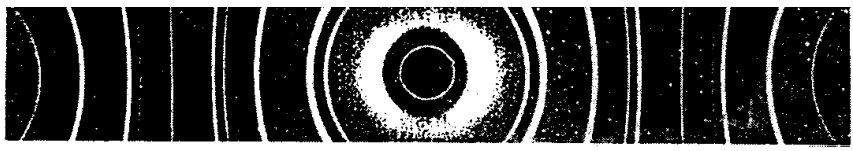

Figure 2.27. *Film recorded in a Debye-Scherer and Hull diffractometer with a sample of zinc oxide*

Each diffraction cone leads to two arcs with symmetric positions with respect to the center of the film, which is defined by the direct beam. We saw that the half opening angles of the cones is equal to 2θ and, since the distance between two arcs corresponds to a single cone, a direct reading gives the angle 4θ.

These traditional Debye-Scherrer diffractometers are no longer used today. Their geometry is such that the beams diffracted by the sample are divergent, or at least do not converge on the detector film. This intrinsic situation causes the diffraction arcs that are detected to widen, hence causing a poor angular resolution. We will see later on that other configurations make it possible to detect diffracted beams where they converge, thus increasing the angular resolution. Furthermore, the detection of diffracted beams in these systems was achieved with photographic film. This makes it more difficult to process the data with a computer. These two elements caused these systems to gradually disappear. However, at the beginning of the 1980s, the arrival of position sensitive gas detectors led to a renewed interest in this type of system. New devices were designed and even though they are distant relatives of the ones used in the early 20th century by Debye, Scherrer and Hull, they are of the same kind in the sense that the sample is in the center of the detection circle [SHI 86].

2.2.1.2. *The modern Debye-Scherrer and Hill diffractometer: use of position sensitive detectors*

Strictly speaking, photographic film is a position sensitive detector but, as we have already mentioned, the resulting signal is not directly digital. This is why modern Debye-Scherrer and Hull diffractometers combine a beam originating from a plane or curved monochromator with a one-dimensional position sensitive detector, giving the user a direct reading of the diffraction signal and with the sample placed in its center. In the first part of this chapter, we described the different types of detectors, and saw that, today, there are position sensitive gas or solid detectors that use an imaging plate. The latter are of much more recent design than the former, so the modern Debye-Scherrer and Hull systems were developed by implementing the concept of curved position sensitive gas detectors. Additionally, this type of gas detector requires the sample to be placed in the center of the detector[4], since the beams diffracted by the sample have to travel the same distance inside the detector regardless of what diffraction angle is considered. Variations of this distance would modify the measurements of the diffracted intensity. Hence the use of curved position sensitive gas detector requires a Debye-Scherrer and Hull geometry. As we have already said, the use of one-dimensional imaging plate

4 Some authors [ORT 78; WOL 81; WOL 83] thought of placing the sample on the detection circle, i.e. on the circle defined by the curved detector. This configuration was tested with a detector with a small radius; however, the intensity measurements were not accurate and it would be necessary to include corrections in this case. It would seem that no one until now has suggested a satisfactory method.

detectors is much more recent. We will give a few details about this at the end of this section.

2.2.1.2.1. The traditional modern Debye-Scherrer and Hull diffractometer: cylindrical sample

Figure 2.28 shows a schematic drawing of a Debye-Scherrer device equipped with a curved position sensitive detector.

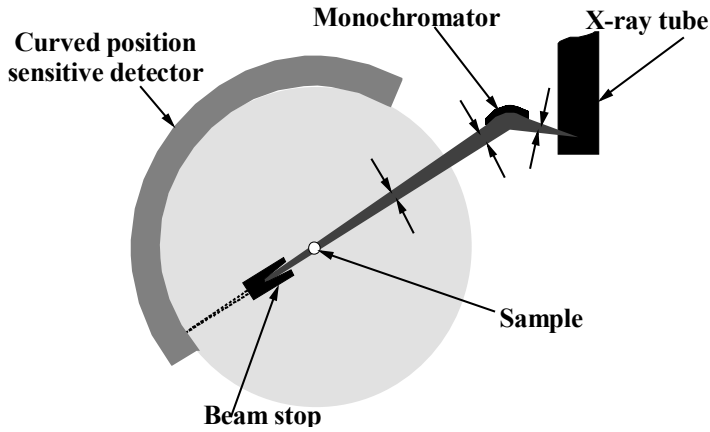

Figure 2.28. *Debye-Scherrer diffractometer equipped with a position sensitive detector*

The sample is irradiated with an incident monochromatic beam originating from a Guinier type, curved crystal monochromator. Due to the crystal's curvature being set, the front and rear focal distances are fixed and the beam's section is defined by the slit located between the tube and the monochromator. The two slits placed beyond the monochromator are oriented in the direction defined by the monochromator's diffraction angle, making it possible to actually select the source's $K_{\alpha 1}$ radiation. This matter will be discussed in great detail later on when we discuss the Bragg-Brentano diffractometers.

The sample is a fine cylinder usually comprised of a capillary filled with the powder we wish to study. It can also be made of a thin wire, particularly when the material we wish to study is a metal. In any case, this sample is placed in the center of a curved, position sensitive gas detector used to simultaneously detect all of the diffracted beams. We saw before that when these gas detectors are irradiated with X photons, the gas is ionized and a local avalanche effect takes place which leads to the ionization of the neighboring atoms. The size of this ionized zone depends on

the operating conditions of the detector. Some detectors operate in proportional conditions, others in intermediate conditions between the proportional conditions and the Geiger-Müller and they are referred to as the "streamer conditions" [ALE 80; ATA 82; BAL 83]. At any rate, the linear dimension of the ionized zone can be considered to be in the order of 150 μm. The detector's[5] angular resolution is directly related to its radius and can therefore be estimated from this value of 150 μm. It would seem that the radius must be as large as possible. However, we should point out that this increases the length of the delay line, and thus significantly complicates the design of such a detector. The detectors currently available have radii between 250 and 500 mm. Due to the absorption by the air surrounding the sample, the increase in the sample-detector distance causes a significant decrease in the measured intensity. We could of course consider designing systems where the sample is placed in the center of a chamber with a crude vacuum, but this considerably complicates the design of the equipment and increases its cost.

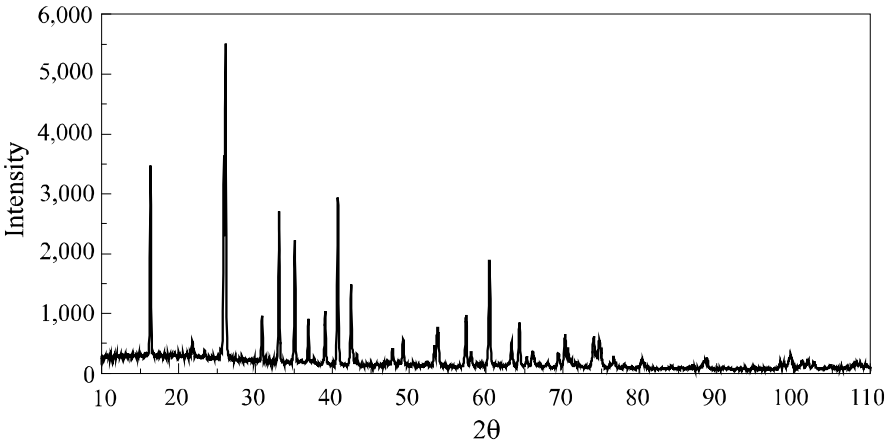

Figure 2.29. *Diffraction pattern obtained using a Debye-Scherrer and Hull device equipped with a curved position sensitive gas detector*

5 A diffractometer's angular resolution is one of its essential features. However, it depends not only on the resolution of each of the elements that comprise it, but also on the device's general configuration, in particular on the relative positions of its various elements. What we are discussing here is the detector's resolution, not to be confused with the device's global resolution. For example, it is quite odd to say [PEC 03] that the angular resolution of those diffractometers including such position sensitive detectors is not good since that resolution depends on the configuration. We will show later on that high resolution devices can be produced with this type of detector, for example by optimizing the incident beam's geometry.

The detected signal is then plotted in a diagram showing the evolution of the diffracted intensity according to the diffraction angle (see Figure 2.29). The main advantage of this type of system is very clear. All of the diffracted beams are collected simultaneously. We will see other systems later on, in particular the Bragg-Brentano diffractometer, where the detection must be intrinsically punctual. The acquisition time of a diagram is in that case longer. In practice, these Debye-Scherrer and Hull diffractometers make it possible to produce diffraction patterns in a few minutes or sometimes a few seconds [YAM 92].

The arrival on the market of these curved position sensitive gas detectors stirred new enthusiasm for this configuration. Several laboratories, among them the Nantes Institute for Materials [DEN 93, EVA 93], have dedicated their research to study the characteristics and the quality of diffraction patterns produced using this kind of device. With these diffractometers designed for fine cylindrical samples (capillaries), the equipment's angular resolution directly depends on the diameter of the sample, since that is the dimension that determines the incident beam's useful part. In the conventional configuration, which is the one studied by Evain [EVA 93], the detector's radius is 250 mm. In this case, if we use a capillary that is 0.5 mm in diameter, the peak widths vary between 0.08° and 0.16° when the diffraction angle changes from 10° to 120°. This study shows that the angular resolution of these devices is high, but not as good as the one obtained with a Bragg-Brentano device in its high resolution configuration, which will be described later on.

These position sensitive gas detectors are divided into different channels and each intensity is specified with its channel number. Therefore, the pattern obtained after the acquisition gives the diffracted intensity according to the channel number. The relation between the channel number and the angle is not strictly linear, straying from the straight line by about a tenth of a degree (see Figure 2.30). These significant differences constitute one of the major weaknesses of these detectors. We will see, however, that angular calibration can help solve this problem. However, we should point out that the quality of this calibration, which is obtained experimentally, determines the accuracy of the diffraction angle measurements. Since the early 1980s, three methods have been found to perform the angular calibration on these systems.

The first method consists of placing in front of the detector window a sheet of metal pierced at regular intervals with very thin holes. The detector is then irradiated using an isotropic radiation source (a radioactive source, or fluorescent radiation). In each point corresponding to the holes, a peak is observed. Since the holes are regularly spaced out, it is possible to draw the link between the channel and angle numbers [STA 92]. This method assumes that the sheet is perfectly cylindrical and that it has the same center as the detector, a condition that is difficult to meet.

The second method consists of recording a diffraction diagram for a perfectly well-known sample [EVA 93, MAS 96a]. The positions of the diffraction peaks, along with the corresponding channels, are matched with the values of the diffraction angles associated with the characteristic interplanar distances of the control sample. The result is the relation between the channel and the angle number.

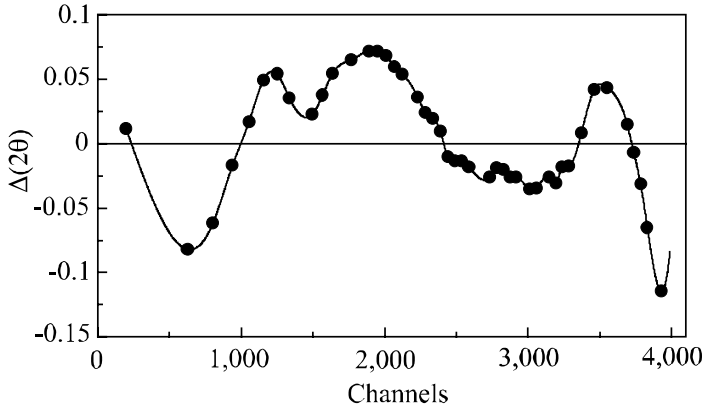

(a) Illustration of the straying from linearity. The dots correspond to the measurements conducted on a sample of $Na_2Ca_3Al_2F_{14}$ [COU 88]

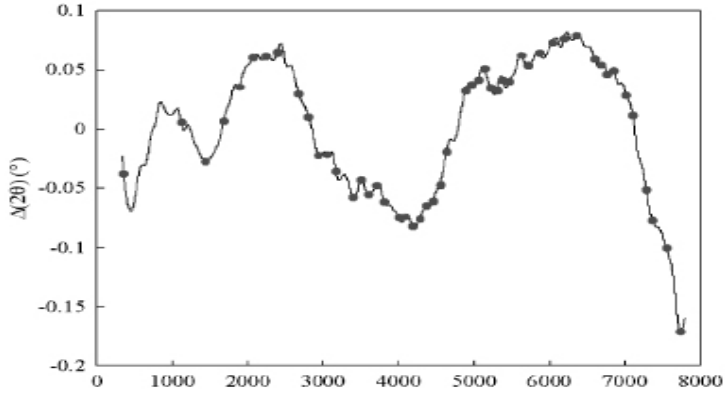

(b) Comparison of several calibration methods [MAS 05]. The black dots correspond to measurements conducted on a standard sample of $Na_2Ca_3Al_2F_{14}$. The full line is obtained by calibrating the detector with a rotation in front of the direct beam, with measurements conducted every 0.5°

Figure 2.30. *Angular calibration of a curved position sensitive detector*

A third method consists of turning the detector step by step in front of the direct beam by recording the direct beam at each step [STA 94, MAS 98a , MAS 05]. Since the increment is known, the angular calibration is directly obtained. As Figure 2.30b shows, this last method is the most effective, but it requires to be able to turn the detector with an accuracy in the range of a thousandth of a degree. The system can be equipped with a motorized rotation, and the calibration according to this method can then be performed automatically.

Generally speaking, the most commonly used method is the second one. When this calibration is properly done, it enables the user to perform measurements of diffraction diagrams with a high angular accuracy [DEN 93, MAS 96a].

As we have already said, systems equipped with position sensitive gas detectors can produce diagrams with very short acquisition times. In addition to this, the measurement of the diffracted intensity is achieved in every point of the diagram simultaneously and therefore if the sample changes due to the effect of an outside solicitation, the entire diagram is modified. This characteristic feature of systems using position sensitive detectors makes Debye-Scherre and Hull systems very good candidates to follow the *in situ* evolution of materials according to one or several outside constraints.

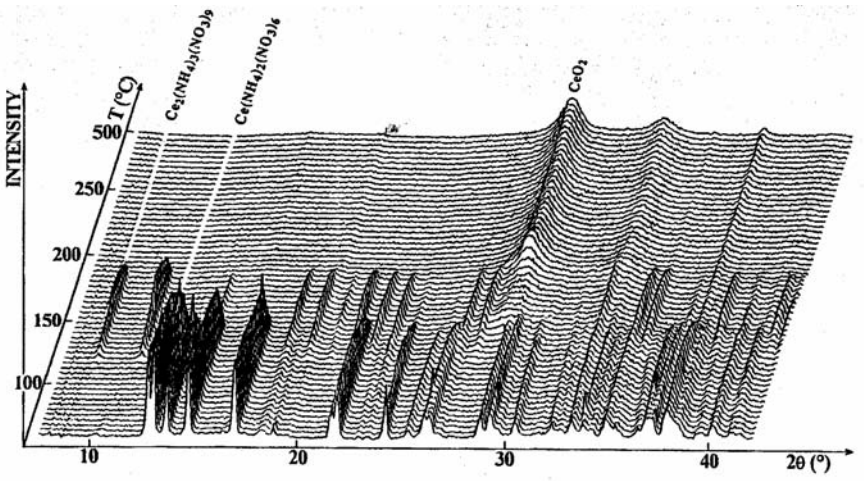

Figure 2.31. *Study of the crystallization of cerium oxide using a thermodiffraction system equipped with a curved position sensitive detector [BEN 96]*

This characteristic was used, for example, to produce diffractometers designed to track the evolution of a sample according to the temperature. Louër and his colleagues studied the structural transformations of oxide precursors using a system equipped with an oven in which the sample was placed [AUF 90, BEN 93, GUI 95, BEN 96]. An example of this type of study is shown in Figure 2.31 where the evolution of a cerium oxide precursor can be observed, showing in particular the presence of an intermediate phase. The same approach was used by other authors to study, for example, the dehydration of zeolites [STA 92, STA 94] or also to simultaneously measure, according to the temperature, the evolution of X absorption spectra (EXAFS) and of diffraction patterns [SAN 93, DEN 95].

The maximum number of photons that a gas detector can measure per unit of time depends on the operating conditions of this detector, but is nonetheless relatively limited compared with the possibilities offered by solid detectors. This limitation can be bothersome when the incident intensity is very high, such as when using a synchrotron radiation source or when it is important to precisely measure the diffracted intensity over a large number of orders of magnitude[6]. In the past few years, several authors have suggested creating Debye-Scherrer and Hull diffractometers which use one-dimensional "image plate" detectors [SAB 95, BAR 92, O'CO 97, NIS 01, TAK 02, KNA 04]. These systems were designed to be used with synchrotron sources and there are currently no manufacturers selling this type of equipment to laboratories. We will see later on that this type of detector can be used to create Seemann-Bohlin systems, where the sample is placed on the detection circle. This configuration, which uses a convergent X-ray beam, makes it possible to obtain patterns with a high angular resolution. Therefore, it would seem more favorable for laboratory experiments than the Debye-Scherrer and Hull configuration. Naturally, this question does not come into consideration for synchrotron radiation sources, since in that case the incident beam is parallel.

The use of a sample holder requires the sample to be reduced to a fine powder. This condition is not a problem when determining, for example, the structure of a new phase that has just been synthesized and this type of equipment is used for that purpose by solid state chemists. However, it is sometimes necessary to directly study bulk samples for which grinding could cause phase transitions. In those cases, the sample is a plane object that can be studied with the same diffractometer. Different configurations are then possible, with different paths for diffracted beams and different angular resolutions depending on the relative positions of the various elements included in the apparatus.

6 This last case occurs, for example, when studying epitaxial thin films. This matter will be discussed in Part 2 of this book.

2.2.1.2.2. Use of plane samples: configuration of the device and angular resolution

Figure 2.32 shows a schematic drawing of a Debye-Scherrer and Hull device devoted to the study of flat plate samples.

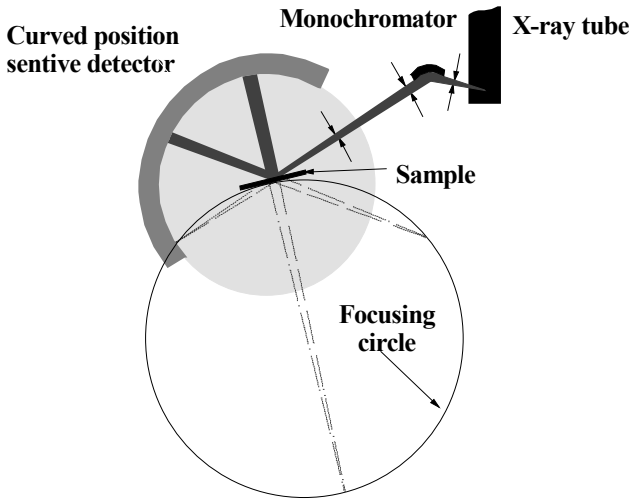

Figure 2.32. *Debye-Scherrer diffractometer with a flat plate sample. Study in reflection*

Each diffraction peak that is observed in the direction 2θ results from all of the X photons diffracted by all of the grains in the Bragg position, for the family of reticular planes corresponding to the distance d, such that $\lambda = 2d \sin \theta$. These X photons are diffracted by all of the grains along the angle θ with respect to the family of planes in question, but the X-ray beam originating from the curved monochromator is convergent (and non-parallel). Therefore, the diffracted X-ray beams are not parallel; in the situation shown in Figure 2.32, the beams that reach the detector are divergent (see Figure 2.33). The locus of convergence of these beams is virtual in this case, since it is located behind the sample. It consists of a circle (the focusing circle) that is tangent to the sample and that passes through the convergence point of the beam originating from the monochromator (see Figure 2.32).

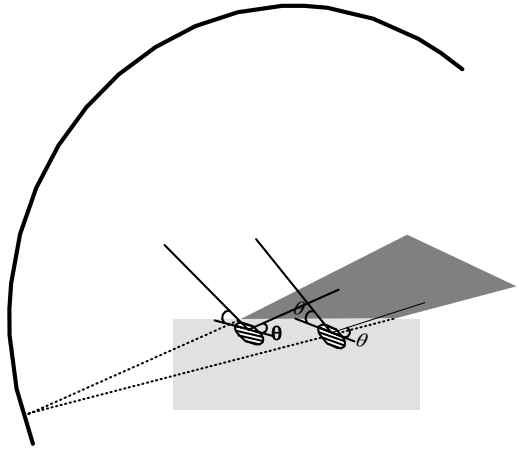

Figure 2.33. *In the configuration shown in Figure 3.31, the beams diffracted for a same angle by different crystals inside the sample are divergent*

Therefore, the configuration shown in Figure 2.32 seems to be unfavorable, since the diffraction peaks are in that case relatively wide. On the other hand, if the convergence point is located in front of the sample, the diffracted beams converge toward the detector (see Figure 2.34).

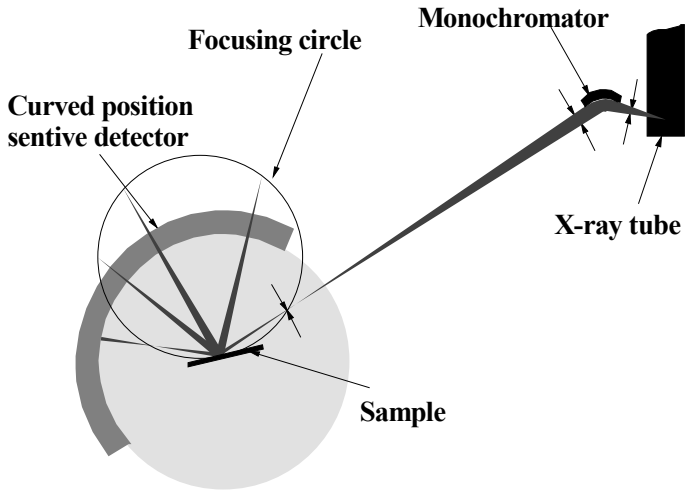

Figure 2.34. *Debye-Scherrer diffractometer with a flat plate sample. Study in reflection with the convergence point of the incident beam in front of the sample*

The reverse situation is observed when the sample is studied in transmission: the diffracted beams are convergent if the focusing point of the direct beam is placed in front of the sample (see Figure 2.35) and otherwise divergent.

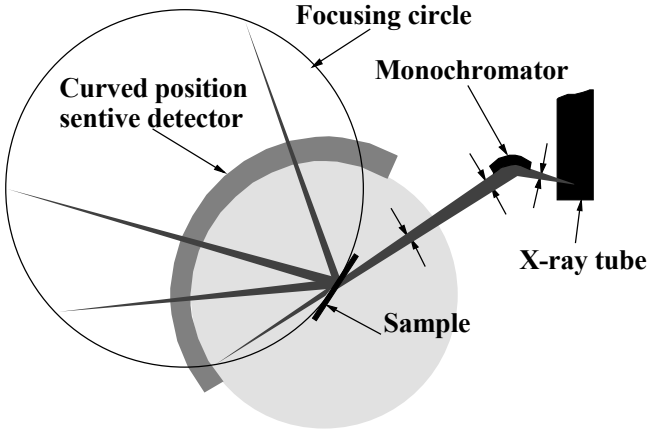

Figure 2.35. *Debye-Scherrer diffractometer with a flat plate sample. Study in transmission with the convergence point of the incident beam behind the sample*

Regardless of which configuration is chosen, the curved position sensitive gas detector cannot be placed on the focusing circle, since in that case, as we mentioned above, the detector's attack angle would vary and therefore the distance traveled by the photons in the gas would depend on the Bragg peak is considered; the intensity measurements would then be inaccurate. The diffracted beams could possibly be convergent, but the observed peaks would remain relatively wide, since the detector is not placed on the focusing circle. Note, however, that if we increase the focal distance behind the monochromator, the beam becomes more and more parallel, which causes the diameter of the focusing circle to increase. Thus, if this focal distance is high enough, the influence of this defocusing effect is small. In practice, these devices are equipped with a monochromator comprising of a quartz or germanium crystal that is curved, so that the back focal distance is close to 1 meter, making the influence of the defocusing effect rather small. Another approach enabling the user to modify the diameter of the focusing circle consists of modifying the incidence angle of the X-ray beam on the sample. We may choose a situation where the incidence angle is equal to the Bragg angle of certain diffraction peaks deemed interesting; this is referred to as diffraction by symmetric reflection, something we will discuss in greater detail later on. The focusing circle is then tangential to the detection circle and as a result, locally, and for a certain angular range, we obtain a high resolution.

The optimum use of a curved detector with a plane sample probably requires a thin parallel incident beam in order to prevent any convergence or divergence effects. Such a beam could be obtained with a plane monochromator comprised of several reflections. This led Dumont [DUM 37], followed by Bartels [BAR 83], to design a monochromator with four reflections on single crystals of germanium. The beam originating from this monochromator is strictly monochromatic and shows an extremely low divergence. We can mention, as an example, the values obtained for a monochromator using four reflections on the planes (220) of the germanium crystal. The resulting spectral dispersion is $\Delta\lambda/\lambda = 1.4 \times 10^{-4}$ and the divergence is $\Delta\theta = 12$ arcseconds. The diagram of a system including such a monochromator associated with a curved detector is shown in Figure 2.36 [GUI 96, MAS 98a, BOU 02a]. Naturally, this type of monochromator greatly reduces the intensity of the beam hitting the sample, but causes a very high increase in resolution.

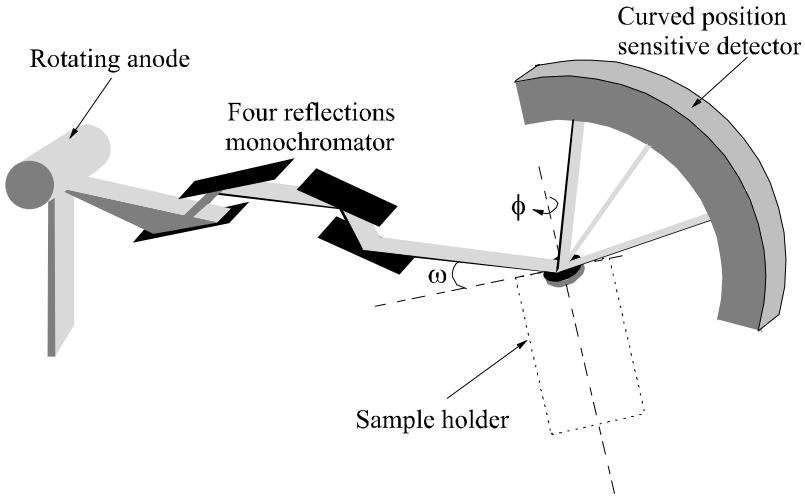

Figure 2.36. *Diffractometer associating a position sensitive detector with a flat plate sample and a parallel beam*

In order to illustrate this result, we realized two diffraction patterns using a sample with a low crystal symmetry, hence the large number of peaks. One of the patterns was recorded with a diffractometer using a convergent beam and corresponding to the setup described in Figure 2.32. The other pattern was obtained using the diffractometer shown in Figure 2.36. The sample that was chosen is a monoclinic zirconia powder used in an international structure refinement test [HIL 94] performed under the authority of the International Union of Crystallography.

The results of these measurements are shown in Figure 2.37. Note how the use of a strictly parallel beam can greatly improve the diffractometer's angular resolution. As we will see later on, the resolution of this diffractometer is equivalent to that obtained with Bragg-Brentano diffractometers in the high resolution configuration.

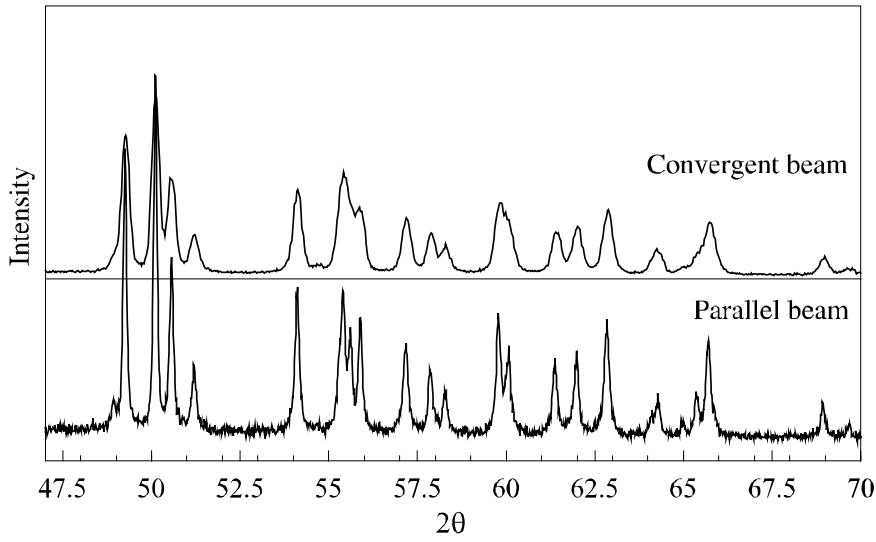

Figure 2.37. *Influence of the diffractometer's geometry on the angular resolution, illustrated by diffraction patterns of monoclinic zirconia*

2.2.2. *Focusing diffractometers: Seeman and Bohlin diffractometers*

2.2.2.1. *Principle*

A few years after the first experiments led by Debye, Scherrer and Hull, Seemann [SEE 19] and Bohlin [BOH 20] thought of an X-ray diffraction apparatus for polycrystalline samples that would detect where they converge the beams diffracted by the crystals in the Bragg position. The corresponding configuration is shown in Figure 2.38.

The X-rays produced by the source, placed in S, are divergent. They hit a curved sample and, for given family of planes corresponding to a certain diffraction angle, all of the beams diffracted by the crystals for which that family of planes is in the Bragg position converge to a point F, located on the circle that passes through S and to which the sample is tangent.

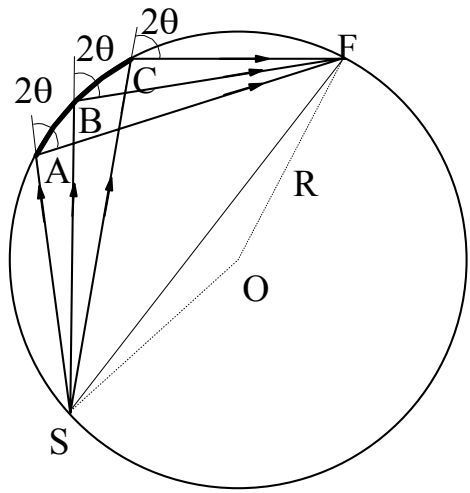

Figure 2.38. *Geometric arrangement of a Seemann-Bohlin diffractometer*

This description corresponds to a plane projection of the apparatus. In a three-dimensional perspective, all of the diffracted beams converge to F if and only if the sample is placed on a section of the torus generated by the rotation of the arc AC around the line SF and, of course, if the source is punctual.

In practice, this condition is not met, that is, the source is linear and is equivalent to a line segment perpendicular to the projection, essentially so as to have a strong enough intensity. The sample is then comprised of a portion of a cylinder and the focusing locus is a line segment parallel to the source.

2.2.2.2. *The different configurations*

2.2.2.2.1. Use of a curved monochromator (Guinier chamber) [GUI 37, GUI 39, WOL 48]

Following the works of Seemann and Bohlin, these systems were improved by several authors [GUI 37, GUI 39, WOL 48, HAG 69], the first among them being Guinier, who suggested including a curved monochromator crystal [GUI 37]. The beam's optical path then corresponds to the one shown in Figure 2.39. This is sometimes referred to as the "Guinier chamber" (or also Guinier-de Wolf or Guinier-Hägg). The word "chamber", i.e. to describe a diffractometer, comes from the fact that the detector used was a piece of photographic film. Of course, this feature is not specific to the geometric configuration in question. We will see in the following sections that there are Seemann-Bohlin diffractometers which use other

kinds of detectors. Therefore, we will be using the word “diffractometer” rather than “chamber”.

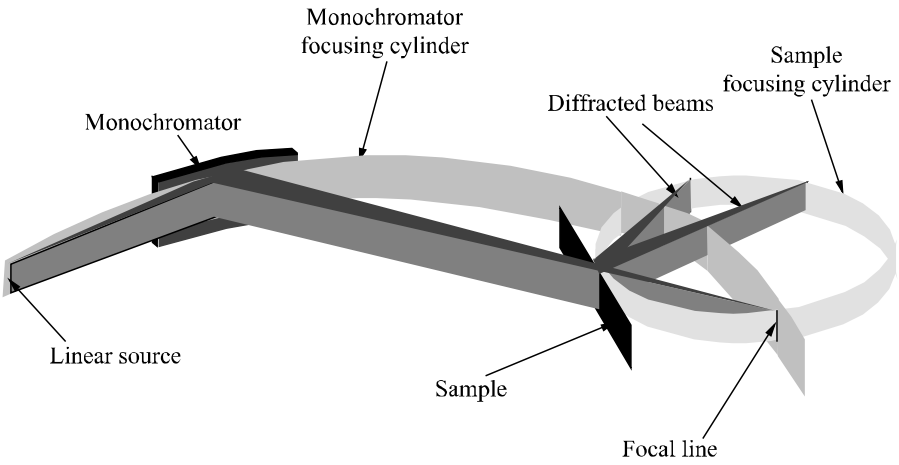

Figure 2.39. *The Guinier diffractometer*

A Guinier monochromator can separate the $K_{\alpha 1}$-$K_{\alpha 2}$ doublet. However, there are two possible configurations. Consider a beam with a certain wavelength dispersion headed for the monochromator. In order for a beam with wavelength λ arriving toward the monochromator to be diffracted, it has to be at an angle θ_λ with crystal planes parallel to which the monochromator is cut. If we consider photons with wavelength $\lambda + \Delta\lambda$, they will be diffracted by the monochromator only if they reach it at an angle $\theta_{\lambda+\Delta\lambda}$. Therefore, it is necessary that they originate from a slightly different area of the source (see Figure 2.40a). On this condition, these photons with wavelength $\lambda + \Delta\lambda$ are diffracted in a direction defined by the angle $\theta_{\lambda+\Delta\lambda}$. This means that the diffracted photons with wavelengths λ or $\lambda + \Delta\lambda$ will take different directions. The sample has the same effect as the monochromator and a given family of planes will diffract these two beams in slightly different directions. The two possible configurations are shown in Figure 2.40.

S configuration (subtraction)

The two effects are subtracted and the diffraction on the sample tends to bring the two beams closer together.

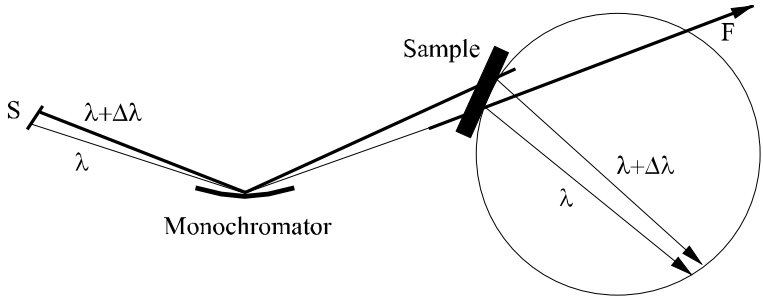

Figure 2.40a. *S configuration of a Seemann-Bohlin diffractometer*

O configuration (addition)

The beams diffracted by the sample are more separated than they were before the diffraction.

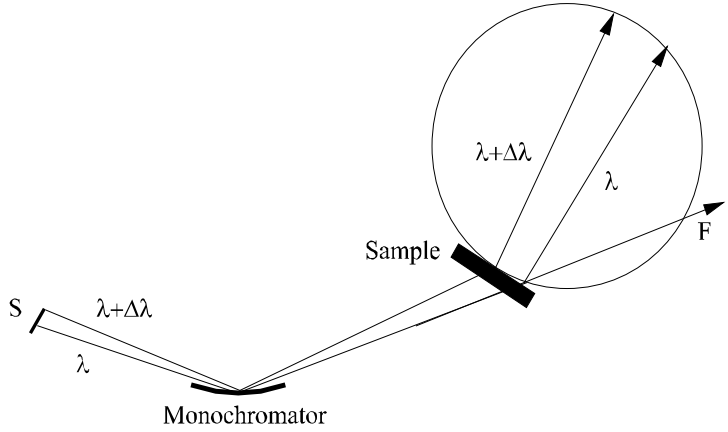

Figure 2.40b. *O configuration of Seemann-Bohlin diffractometer*

Current Seemann-Bohlin diffractometers can be used in either configuration. The S configuration has a better angular resolution.

2.2.2.2.2. Transmission, reflection; symmetric, dissymmetric

These diffractometers can be used in various configurations. All of the possibilities are shown in Figure 2.41.

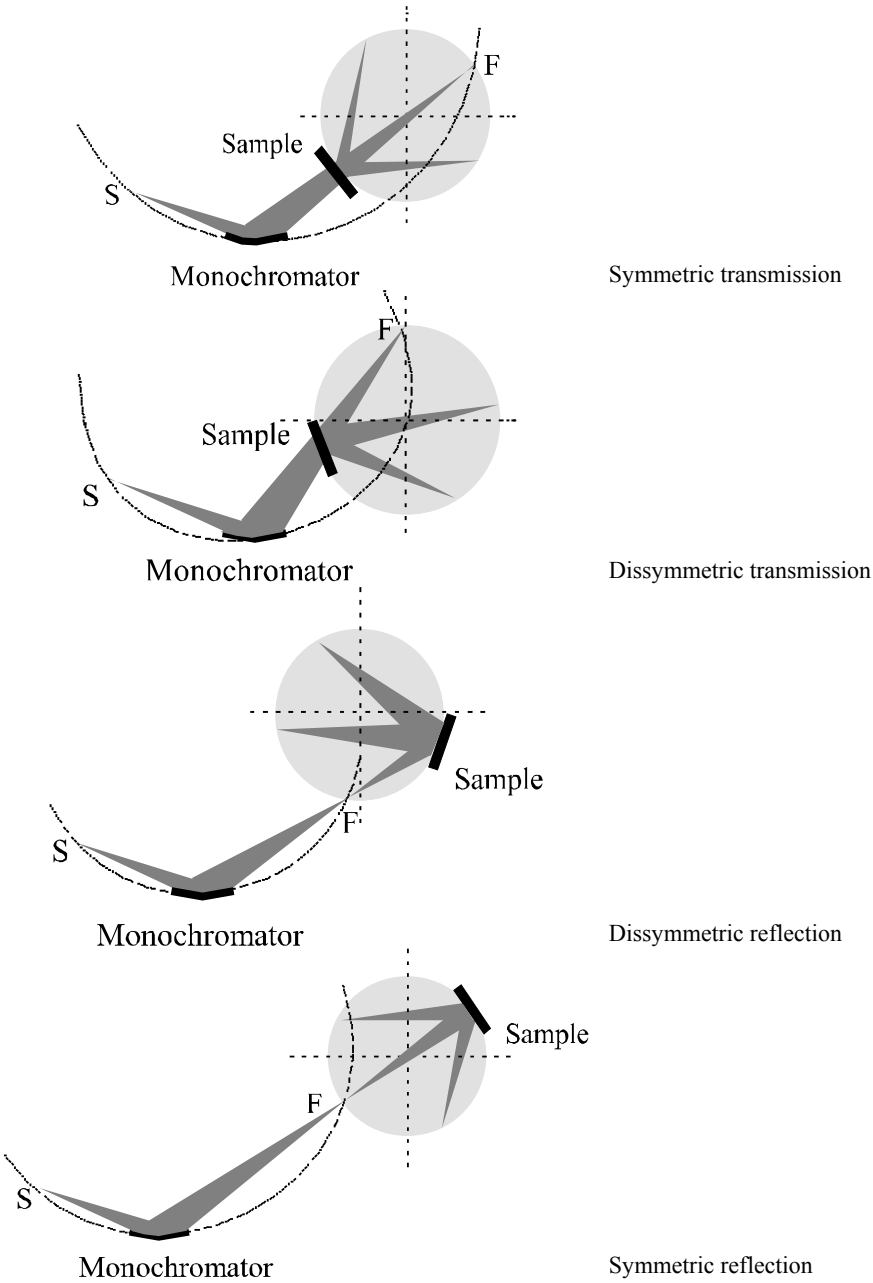

Figure 2.41. *Use in transmission or in reflection*

Note, however, that the choice of one configuration or another imposes an angular area on the measurement. Generally speaking, the use of the system in reflection makes it impossible to measure peaks at low angles, the angle θ must be higher than 37°. Due to this very restrictive condition, Seemann-Bohlin diffractometers are used in transmission most of the time. The reflection configuration is only used when the measurements involve peaks with high angles. This can occur for very precise measurements of cell parameters for purposes of evaluating the rate of homogenous strains.

Hofmann and Jagodzinski [HOF 55] designed a double chamber system, one used in transmission and the other in reflection. The angular range covered by this design is of 0 to 45° for the first chamber and 45 to 90° for the second. The two combined enable the user to make measurements from 0 to 90°. This configuration, however, is rarely used.

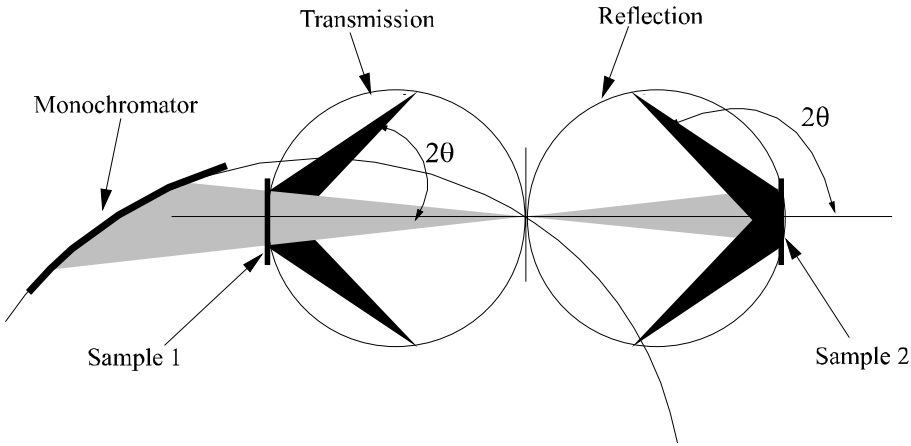

Figure 2.42. *Double Guinier chamber*

2.2.2.2.3. Simultaneous observation of several samples

Some devices [WOL 48] enable the user to study several samples simultaneously. The different powders are placed on top of each other and diffract different portions of the beam. The resulting film looks like the one shown in Figure 2.43 [KLU 74].

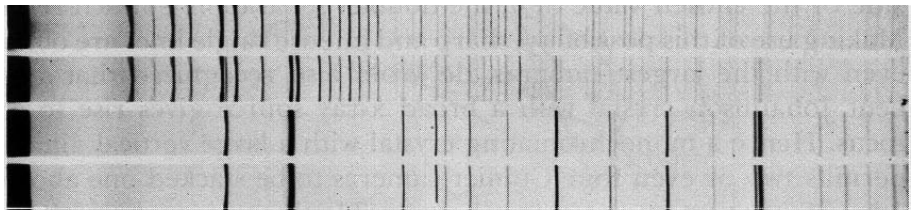

Figure 2.43. *Film obtained from the simultaneous study of several samples*

Guinier devices are diffractometers with a very good angular resolution. However, the use of photographic films as detectors greatly lessens their appeal, since most modern studies require a digital signal that can directly be processed by a computer. There are two different methods for solving this problem.

2.2.2.2.4. Use of an imaging plate detector

Guinier chambers with imaging plate detectors started appearing in the late 1990s [STA 00]. The active material is deposited on a flexible polymer holder, producing a detector, which is simply placed where the photographic film would have been. The signal can be read very quickly because of a lazer source integrated in the diffractometer. This type of device, sold by the Huber company, is still very recent. It seems quite efficient and can produce diffractograms which have a good angular resolution with very short exposure times (a few minutes). However, as we have mentioned before, these detectors show a certain remanence that lessens their appeal.

2.2.2.2.5. Use of a punctual detector: goniometric setup

For many years, another method has been used to directly produce a digital signal using a Seemann-Bohlin diffractometer. Traditional film is replaced with a punctual detector moving along the focusing circle [WAS 53]. Usually, scintillation detectors or proportional gas detectors are used. The detector's movement can be either continuous or incremental.

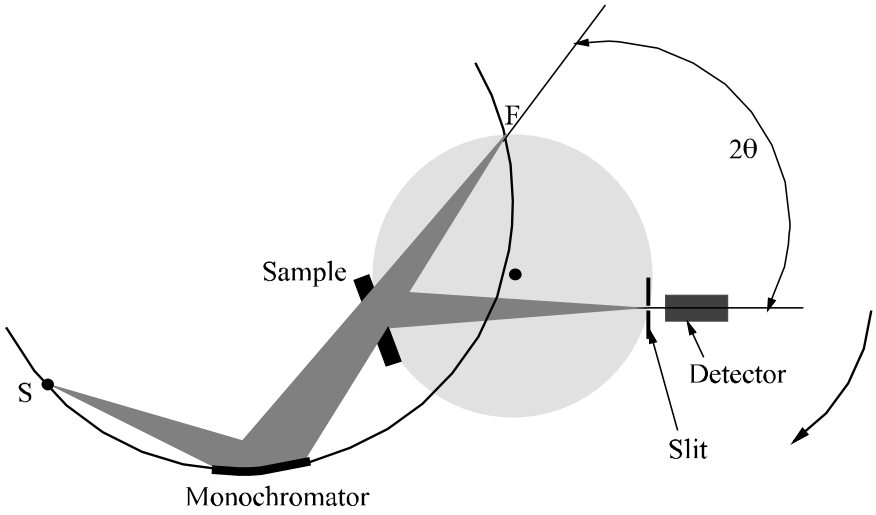

Figure 2.44. *Seemann-Bohlin device equipped with a punctual detector*

These diffractometers were described in detail by Parrish and Mack [PAR 67, MAC 67], and even though they have been available on the market for 40 years, they are only rarely used. They show a high angular resolution but are particularly difficult to adjust. The value of the diffraction angle 2θ is directly given by the detector's position on the focusing circle. Therefore, precisely determining this angle requires the focusing point of the incident beam originating from the monochromator to exactly coincide with the angular zero. In addition, other authors [MAC 67, SPE 95] have noted that any movement of the sample along the radius has a strong influence on the measured position of the diffraction peaks. Hence, it is important that the sample is exactly tangent to the focusing circle.

2.2.3. *Bragg-Brentano diffractometers*

2.2.3.1. *Principle*

Seemann-Bohlin devices which have already been described (see Figure 2.38) are such that the diffracted beams converge to the focusing circle, the diameter of which is constant, thus causing the sample-detector distance to vary with the diffraction angle.

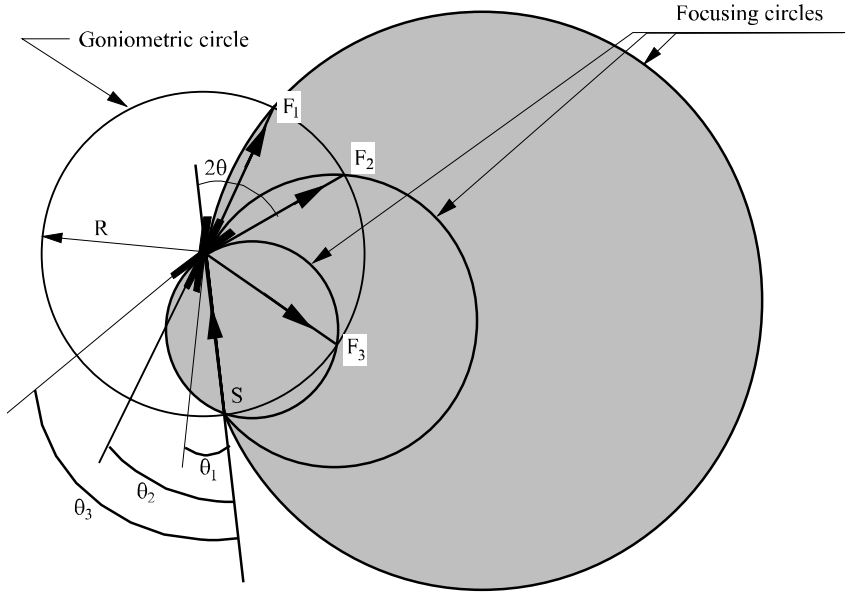

Figure 2.45. *Schematic drawing of the principle of the Bragg-Brentano diffractometer*

Bragg-Brentano diffractometers [BRA 21, BRE 17a, BRE 17b, BRE 46] are approximate focusing systems for which the sample-detector distance is constant for any angle θ. This condition means that the locus of the focusing points is a circle with its center on the sample and passing through S, but it implies that the diameter of the focusing circle changes for each θ. The focusing circles pass through the point S and are always tangent to the sample, which must therefore turn around its center so as to maintain an angle θ with the X-ray beam. Figure 2.45 displays this configuration.

Two types of devices can function this way.

2.2.3.1.1. θ-2θ diffractometers

With this type of device the source does not move, the sample rotates around its axis at a speed ω, whereas the detector is moving at a speed 2ω along the circle, centered on the sample, and referred to as the goniometric circle. The detector, placed in 2θ, measures at every instant the diffraction peaks corresponding to the angle θ.

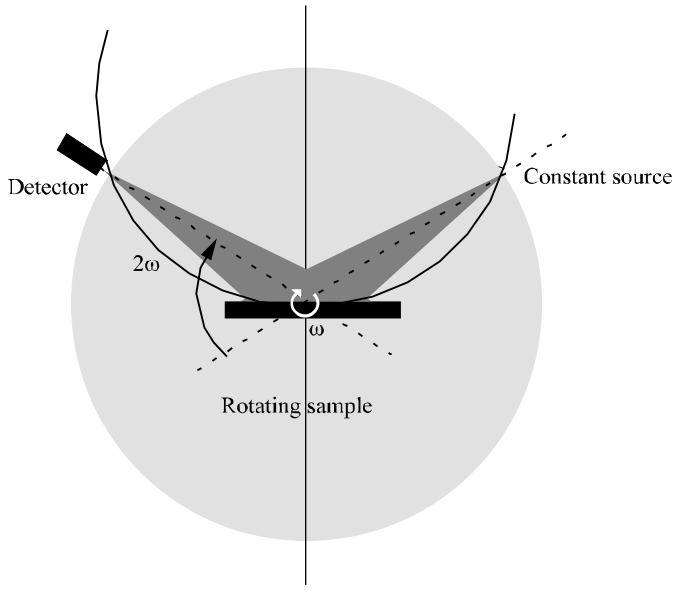

Figure 2.46. *θ-2θ Bragg-Brentano diffractometers*

This is the most common system. However, it has a major drawback: since the sample is rotating, it can sometimes fall, if it is in powder form, when the angle of rotation is too high. The use of this kind of device with a heating sample holder is difficult for the same reason.

It is possible to create a diffractometer based on the same idea, but with a sample that does not move.

2.2.3.1.2. θ-θ diffractometers

With this type of device, the sample does not move. The source and the detector simultaneously move in opposite directions along the goniometric circle at a speed ω.

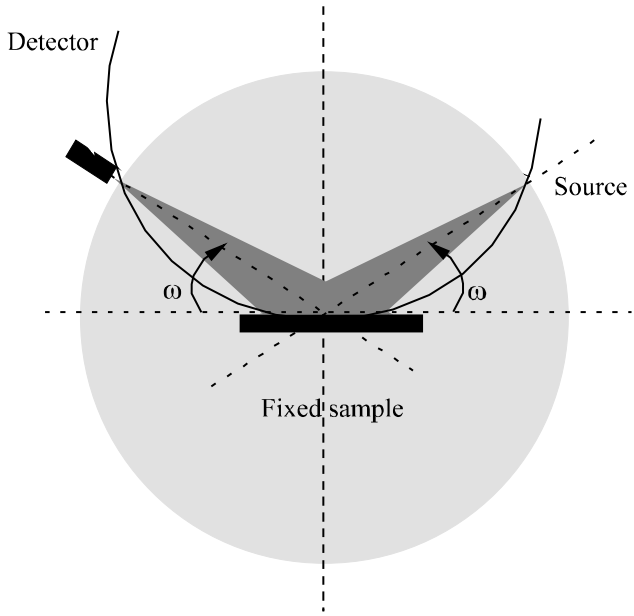

Figure 2.47. *θ-θ Bragg-Brentano diffractometer*

These diffractometers are generally more expensive than the previous ones, since it is difficult to achieve a perfectly controlled movement of the X-ray tube, which is quite heavy.

For both of these two systems, the movements of the different elements can be either continuous or incremental.

2.2.3.2. *Description of the diffractometer; path of the X-ray beams*

A diagram of the X-ray beam's path and of the different elements of the device is shown in Figure 2.47.

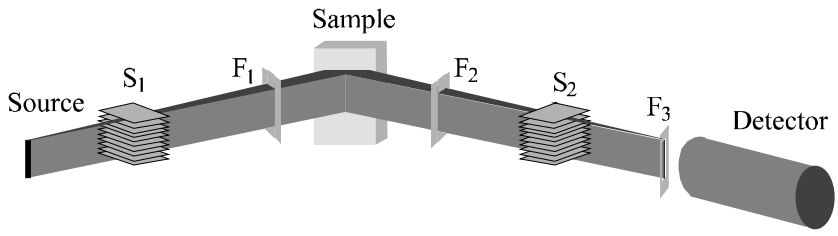

Figure 2.48. *Path of the X-ray beams in a Bragg-Brentano diffractometer*

The focal line emits a divergent X-ray beam. A first slit, F_1, makes it possible to limit the incident beam's opening, since it is important, at any diffraction angle, for the area irradiated by the incident beam to be smaller than the sample. Otherwise, the irradiated volume would vary with the angle θ and the relative intensity values would not be specific to the material used. Aside from this particular case, which must be avoided, the volume studied in this type of system is constant for any θ. Note, finally, that the irradiated surface increases when θ decreases. Therefore, when conducting experiments at low diffraction angles, the width of the slit can be decreased. Some devices are equipped with a slit that automatically varies in width with the angle θ. This configuration has its advantages, but the irradiated volume is then no longer constant.

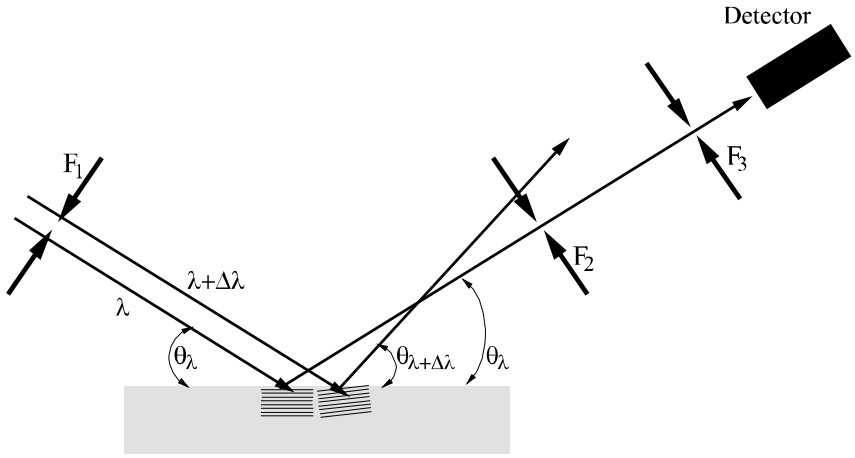

Figure 2.49. *Illustration of how the slits work*

The slits located after the sample (F_2 and F_3) enable the user to select what the detector picks up. As we have already mentioned, in this type of device, the detector is moving along the goniometric circle on which the source is placed and in the center of which the sample is placed. Therefore, the source-sample and sample-detector distances are set and equal to the radius of the circle. This means that the solid angle seen by the detector is entirely determined by the slit F_1, and slits F_2 and F_3 are not necessary in defining the width of the beam as seen by the detector. However, as we have already mentioned, in the case of diffraction by a polycrystalline sample, the incident beam has to be monochromatic. Including a filter or a monochromator associated with slits F_2 and F_3 ensures that only the beams with the chosen wavelength are seen by the detector. The role of these slits is explained in Figure 2.49. In order to make the diagram simpler, the incident beam was assumed to be parallel. In reality it is divergent in Bragg-Brentano systems, but

this does not change the concept. Consider a chosen beam originating from the source and characterized by a wavelength $\lambda + \Delta\lambda$ different from the wavelength λ and a family of planes (hkl) associated with an interplanar distance d_{hkl}. When the sample is irradiated at an angle θ_λ, the crystals for which the family of planes (hkl) is parallel to the surface diffract in a direction defined by the angle θ_λ and the resulting beams hit the detector. The radiation with wavelength $\lambda + \Delta\lambda$ is not diffracted by these crystals, but is diffracted by crystals for which the family of planes (hkl) is slightly disoriented with respect to the sample's surface. The diffraction direction is given by the angle $\theta_{\lambda + \Delta\lambda}$. If slits F_2 and F_3 are positioned in the direction defined by the angle θ_λ, the beams diffracted at an angle $\theta_{\lambda + \Delta\lambda}$ are stopped and not picked up by the detector.

The vertical divergence is limited by two series of slits placed before and after the sample. These slits, referred to as Soller slits [SOL 24], are comprised of parallel plates, regularly spaced out, that divide the beam into several, very slightly divergent beams.

Generally speaking, whatever type of slit is used, they must be made out of highly absorbing materials, and hence of heavy chemical elements. Most of the time, tantalum or molybdenum slits are used.

We have seen that combining different slits can limit the spectral dispersion of the beams picked up by the detector. However, this is only efficient if the incident beams are somewhat monochromatic. Bragg-Brentano systems can be equipped with filters or monochromator crystals. The measurements conducted with the diffractometers are, by nature, sequential, meaning that the acquisition times are directly related to the angular range that is explored, but these times are always longer than those corresponding to overall measurements of the diffraction signal. This characteristic implies that the incident beam that hits the sample has to be as intense as possible. This is why many Bragg-Brentano diffractometers are equipped with filters that make it possible to maintain a significant incident intensity. Figure 2.50 shows a diffraction diagram produced with this type of system equipped with a copper anode source and a nickel filter.

As we have already mentioned, copper's $K_{\alpha 1}$ peak cannot be selected with a filter. Each peak is actually split in two and the angular gap between two peaks corresponding to the same family of planes increases as a function of the diffraction angle.

Adding a monochromator between the source and the sample makes it possible to avoid this problem. However, since the incident intensity is then smaller, the total acquisition time will be longer, often a few days or even up to a week for high resolution patterns.

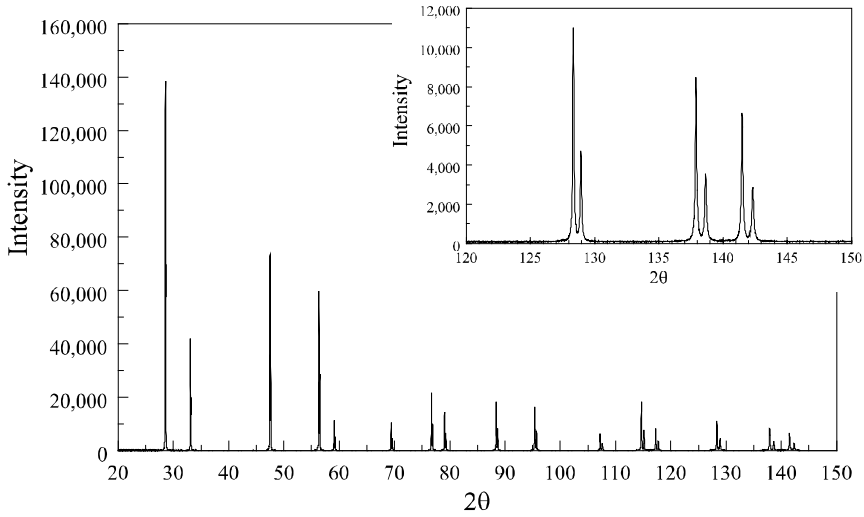

Figure 2.50. *Diffraction pattern of a sample of cerium oxide powder obtained with a Bragg-Brentano diffractometer equipped with a copper anode source and a nickel filter [BAL 04]*

The monochromators must make it possible to irradiate the sample with a divergent beam, which is why, most of the time, curved Guinier monochromators are used. They are made out of quartz or, out of germanium. A diagram of the corresponding set-up is shown in Figure 2.51. The pattern obtained with this device using the same sample as in Figure 2.50 is shown in Figure 2.52.

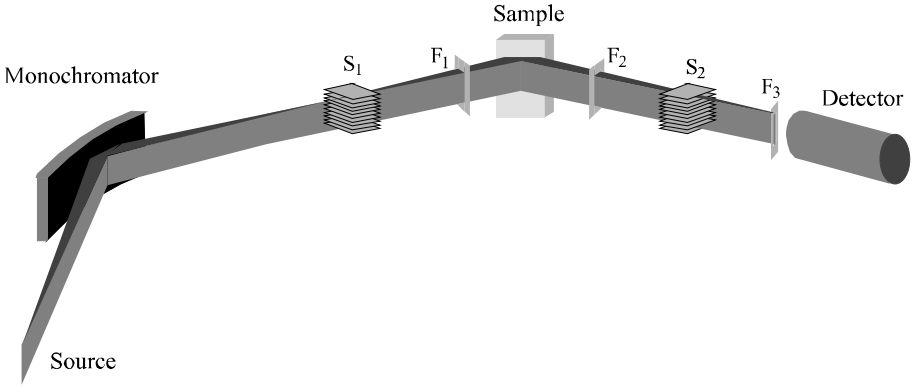

Figure 2.51. *Path of the X-ray beams in a Bragg-Brentano diffractometer equipped with a front monochromator*

Another possibility consists of placing the monochromator on the path of the beams diffracted by the sample, a configuration referred to as a back monochromator. It helps prevent parasite radiation, such as that caused by the sample's fluorescence hitting the detector.

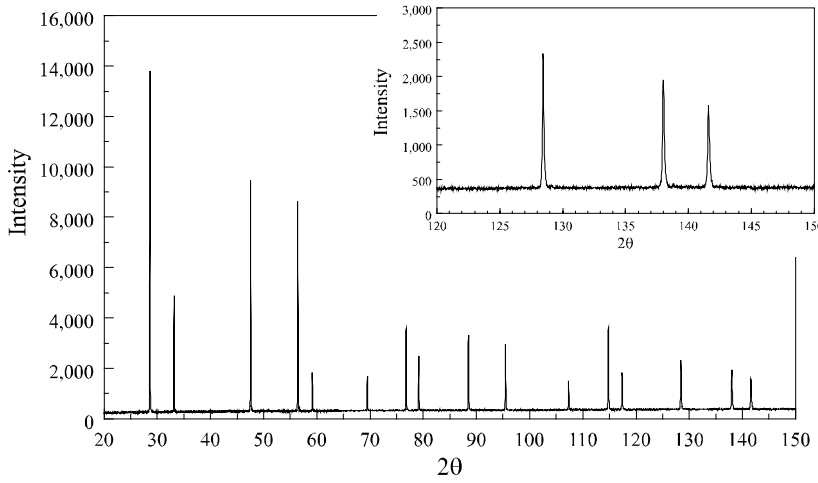

Figure 2.52. *Diffraction pattern of a sample of cerium oxide powder obtained by using a Bragg-Brentano diffractometer equipped with a copper anode and front quartz monochromator [BAL 04]*

In Brentano's original configuration, the direct beam directly irradiates the sample, as shown in Figure 2.48. We saw that these set-ups systematically produce diagrams with peaks split in two due to the presence of the $K_{\alpha 1}$-$K_{\alpha 2}$ doublet. We also mentioned that the main advantage of Bragg-Brentano diffractometers is the possibility to have a high angular resolution, because the diffracted beams are detected where they converge. The angular resolution functions of these systems are sometimes determined by only taking into account the width of the diffraction peaks' $K_{\alpha 1}$ components but, as discussed by Langford and Louër [LAN 96], this approach is not entirely correct. The presence of the component due to the $K_{\alpha 2}$ radiation causes a significant increase in the partial overlap of the peaks, which complicates the processing of the diffraction diagrams a great deal. The usual approach [RAC 48] for processing the results of diagrams comprising split peaks is to set the intensity ratio between the peak caused by the $K_{\alpha 1}$ radiation and the peak caused by the $K_{\alpha 2}$ radiation. We have already mentioned in the first part of this chapter [DEU 95, DEU 96, DIA 00] that a description of the $K\alpha$ radiation's actual form is much more complex. Therefore, this approach is just an approximation, and it is particularly difficult to find a precise model to predict the shapes of the

diffraction peaks obtained with devices not equipped with a monochromator. This does not constitute an actual problem if the purpose of processing the pattern is to determine the integrated intensities, but it makes the analysis of the peak profiles very difficult. Therefore, even though the use of a monochromatic beam is always the better option [OET 99], structural studies that are led from the measurements of the integrated intensities can be conducted based on the pattern obtained using diffractometers equipped with absorption filters [LOU 88, HIL 92, HIL 94, CUS 99]. On the other hand, in the case of microstructural studies, the information sought is related to the shape of the diffraction peaks, requiring an analysis of the peak profiles, which means that in those cases, a system equipped with a front monochromator is necessary [LAN 96, SYN 99].

As we have shown, the Bragg-Brentano diffractometer imposes, by definition, the use of a punctual detector. Under these conditions, and aside from improving the efficiency of detectors, reducing the acquisition time can only be done by increasing the intensity of the incident beam, that is, either by using a high intensity source (rotating anode generator or synchrotron source), or by increasing the ratio between the intensity of the beam originating from the monochromator and that of the beam produced by the source. The increase of this ratio can be achieved by increasing the mosaicity of the monochromator crystal. Note, however, that this increase in mosaicity causes at the same time a decrease in wavelength selectivity. Thus, the use of an elliptical artificial crystal causes a significant increase in the flow of X-rays irradiating the sample, but at the same time causes a strong decrease in the device's angular resolution, since these monochromators are unable to separate the $K_{\alpha 1}$-$K_{\alpha 2}$ doublet.

A few authors have suggested replacing the punctual detector by a position sensitive linear detector [GOB 79]. This reduces the acquisition time, meaning that these systems can be used to study the *in situ* structural transformations associated, for example, with temperature variations. However, the diffracted beams are detected outside of their focusing points, thus greatly deteriorating the angular resolution [STO 01, CHE 04]. Most of the time, position sensitive detectors are linear gas detectors placed so that they are tangent to the goniometric circle and present an angular opening of several degrees. Generally speaking, this configuration results in a poor angular resolution, with acquisition times that remain longer than those obtained with Debye-Scherrer and Hull systems, which use curved position sensitive detectors. An interesting compromise between acquisition speed and angular resolution was recently suggested [REI 02]. This author used a real-time multiple strip, solid, position sensitive detector which makes it possible to choose an angular opening adapted to the beam's imperfections. We know that the focusing in a Bragg-Brentano system is approximate (the sample is tangent to the focusing circle and also, the size of the source is not infinitely small), which led to the idea of choosing an angular opening that generally corresponds to the actual size of the diffracted beam when it reaches the detection circle (goniometric circle). When the Bragg-Brentano diffractometer is used in low

resolution configurations, in other words, with an absorption filter and relatively open windows, the detector's entrance slits can have a size of 2°, thus reducing the acquisition time by a factor of up to 100! [REI 02]. In the high resolution mode, this opening has to be significantly reduced. Nonetheless, by choosing an opening in the range of a quarter of a degree, the resolution function's quality is not diminished, whereas the acquisition time is reduced by a factor 10.

2.2.3.3. *Depth and irradiated volume*

We will determine later on, when describing systems designed for the study of thin layers, the general expressions of the irradiated volume and of the penetration depth according to the incidence angle and the diffraction angle. However, it is rather easy to note in the case of Bragg-Brentano diffractometers, for which the incidence angle is always equal to the Bragg angle, that the irradiated volume is unaffected by variations of θ. However, as the diagram in Figure 2.53 shows, the penetration depth varies with the angle θ. These two characteristics of the acquisition conditions for patterns produced using these systems has a considerable effect on how they are used. Since the irradiated volume is constant for any diffraction angle, the intensities diffracted for the different peaks can be directly compared. On the other hand, because the depth of the analysis varies with the diffraction angle, the sample has to be perfectly homogenous with respect to its thickness. If this condition is not met, the resulting pattern is difficult to use, because the various peaks do not correspond to identical areas in the sample. In practice, this happens fairly often, particularly with bulky samples that have undergone a thermal process. This characteristic prohibits the use of these systems in cases where the sample is a layer thin enough for the X-ray beam to go through it (≈ μm).

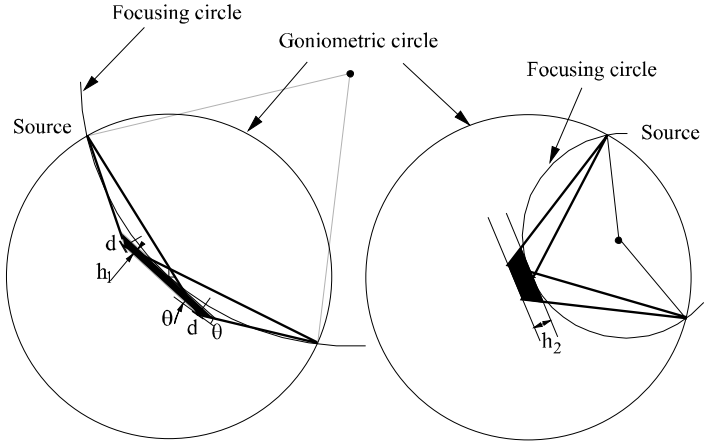

Figure 2.53. *Variations of the irradiated depth and surface with the Bragg angle*

2.2.4. *Parallel geometry diffractometers*

The three types of diffractometers we have just described use divergent X-ray sources. As we have seen, this leads to the problem of detecting the beams diffracted by the sample as close as possible to where they converge. These diffractometers were designed in the first part of the 20th century, at a time when all of the available X-ray sources provided divergent beams. The advent of synchrotron radiation sources, which produce practically parallel beams, led to the design of diffractometers based on these sources, created for the study of polycrystalline samples with parallel beams [FIT 95, HAS 84]. Since the beginning of the 1990s, experimental laboratory set-ups based on this geometry have started to appear.

We will not describe here in detail the diffractometers installed on synchrotron sources, since they almost always consist of prototypes adapted to a particular type of study and measurement. We can point out, however, that since the source directly produces a parallel beam, the diffracted beams will be non-divergent regardless of the sample's shape (capillary, plane, transmission, reflection, etc.).

Generally speaking, in these systems, the beam originating from the storage ring is diffracted by a double crystal, often made out of silicon. This beam then irradiates the sample (plane or capillary) and the beams diffracted by the sample are again diffracted by a plane crystal[7], before being picked up by the detector (see Figure 2.54a). This analyzer crystal can be replaced with a set of slits comprised of relatively long, parallel plates. The spaces between these plates and their lengths define the angular opening and therefore the diffractometer's angular resolution (see Figure 2.54b).

7 This crystal makes it possible to select a specific wavelength bandwidth. By analogy with spectroscopic methods, it is referred to as an analyzer crystal.

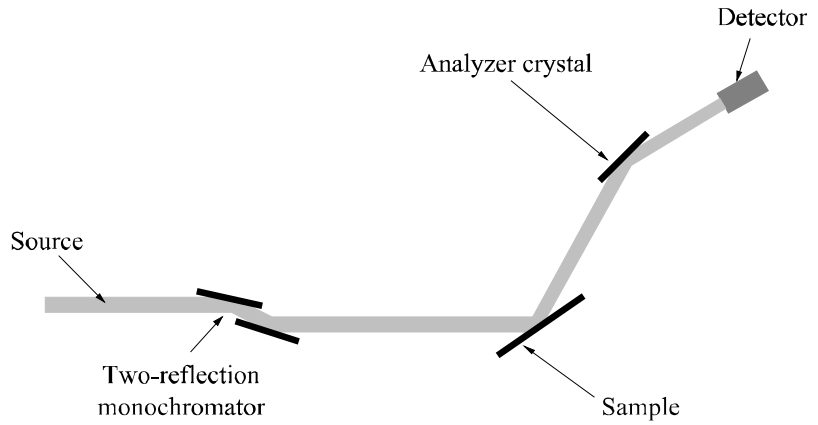

(a) Use of an analyzer crystal

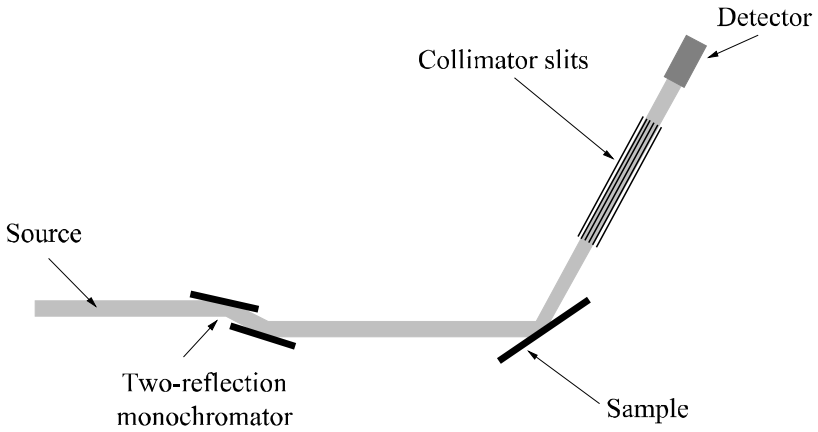

(b) Use of back collimator slits

Figure 2.54. *Geometrical arrangement of diffractometers for polycrystalline samples using a synchrotron source*

Since the middle of the 1990s, some authors [SCH 96, FUG 99, GRO 98a] have suggested creating parallel geometry devices in laboratories designed by using the same idea as diffractometers installed on synchrotron sources. Naturally, the main problem in this case is the intensity of the incident beam. This is why, in most cases, the multi-reflection, front monochromator is replaced with a parabolic multi-layer

monochromator. The beam produced by the source is diffracted by the multi-layer monochromator and then by the sample. The divergence of the beam originating from this type of monochromator is typically in the range of a few hundredths of a degree[8] [JIA 02]. Usually, collimator slits are placed in the back (see Figure 2.55). This configuration makes it possible to obtain diffraction patterns with very short exposure times. The main advantage of these diffractometers is that, because of the analyzer crystal (or of the back collimator slits), the position of the sample has little influence on the measurements [SCH 96], thus making it possible to produce diffraction patterns with samples that have irregular surfaces. However, as we have already mentioned, these multi-layer monochromators cannot select the $K_{\alpha 1}$ peak, resulting in split peaks. The use of an analyzer crystal instead of collimator slits can sometimes help solve this problem.

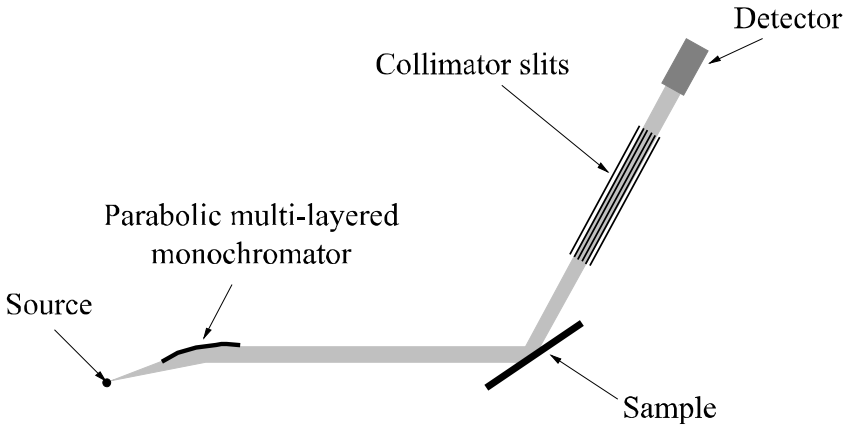

Figure 2.55. *Parallel geometry configuration in the laboratory*

We saw that the parallel beam originating from the parabolic, multi-layered monochromator is wider than the initial X-ray focusing spot. Therefore, the resulting diffraction peaks should be wider. The device's actual resolution increases when the space between the plates comprising the collimator slits decreases. The decrease of this opening, however, will of course cause the intensity to decrease. Shown in Figure 2.56 are three diffraction patterns produced by using a standard sample of lanthanum hexaboride provided by National Institute of Standards and Technology. The first was obtained on a device equipped with a

8 The divergence of a beam originating from a Bartels four-reflection monochromator is typically 12 arcseconds, or 2.7 thousandths of a degree. Note that, in the case of parabolic multi-layer monochromator, the divergence is 10 times that.

parabolic, multi-layered monochromator and collimator slits, and the second was produced with an analyzer crystal and a front hybrid monochromator, comprised of a multi-layered parabolic monochromator and two plane germanium crystals. The third, finally, was obtained with a Bragg-Brentano device equipped with a front monochromator made out of quartz.

Quite clearly, the Bragg-Brentano diffractometer leads to the best angular resolution. The peaks which are split in two, specific to the $K_{\alpha 1}$ and $K_{\alpha 2}$ emission peaks, are plainly visible in the first pattern . The peaks in the second pattern are not split, but they are clearly wider than those obtained with the Bragg-Brentano diffractometer.

These laboratory parallel geometry configurations lead to average angular resolutions, but have the advantage of requiring limited acquisition times. Therefore, they are used for applications where the acquisition speed is a key factor. From this point of view, they constitute an alternative to the Debye-Scherrer and Hull systems with a curved position sensitive detector, for example, when conducting thermodiffraction measurements.

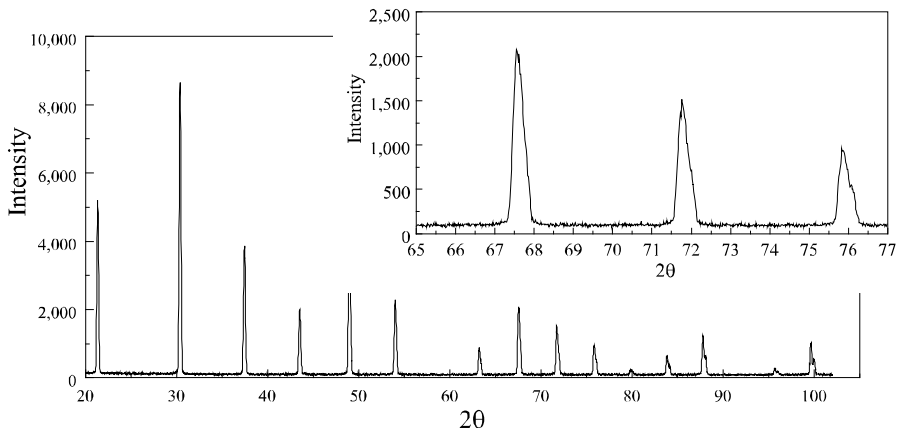

(a) X-ray diffraction pattern of an LaB_6 sample obtained by using a parallel geometry device with a parabolic multi-layered monochromator and collimator slits

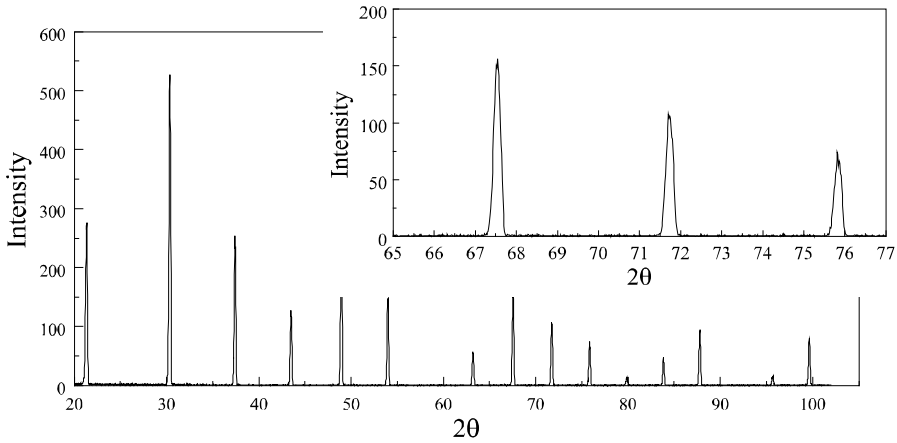

(b) X-ray diffraction pattern of an LaB_6 sample obtained by using a parallel geometry device with a hybrid monochromator and an analyzer crystal

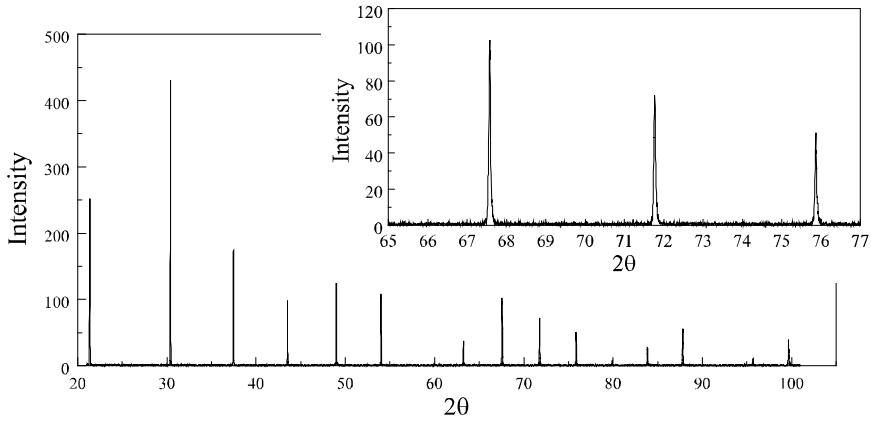

(c) X-ray diffraction pattern of an LaB_6 sample obtained by using a Bragg-Brentano device with a front monochromator made out of quartz

Figure 2.56. *Comparison of patterns obtained with laboratory systems working in parallel geometry or in the Bragg-Brentano configuration. These patterns were realized by Vermulen from the PANAlytical company*

2.2.5. *Diffractometers equipped with plane detectors*

It is a well-known fact that the diffraction figure of a monochromatic X-ray beam with a polycrystalline sample comprised of crystals with random orientations is a set of diffraction cones that all have the same apices. The intersection of these cones with a plane orthogonal to their axis corresponds to the Debye-Scherrer rings. In all of the diffractometers we have described in this book, the diffracted intensity is measured for a specific radius of these rings, meaning that most of this diffracted intensity is lost. In the case of samples that have a certain texture, the rings are discontinuous and this information does not appear, or appears only indirectly when the measurements are performed with the devices we have just described. The use of plane detectors can simultaneously solve these two problems, and usually leads in particular to excellent measurement statistics. Strictly speaking, traditional photographic plates are plane detectors, but the information obtained is not directly digital. It is only very recently, with the arrival of plane gas or solid detectors (CCD or imaging plate detectors), that two-dimensional diffraction measurements on polycrystalline samples have started to appear. The main problem remains the detector's size since, for a given wavelength, the device's angular resolution increases proportionally to the distance between the detector and the sample, but the detector's size quickly becomes very large. In practice, this is certainly the feature that limits the most the development of this type of device.

The first studies led with these systems used synchrotron radiation [GUA 96, NOR 97]. These authors used a plane, imaging plate detector and showed that the patterns produced by integrating the intensity along the Debye-Scherrer rings can lead to data with a quality suitable for structural analysis. One of the problems is that the distance between the sample and different points of the detector is variable; in other words, a parallax effect is observed. This effect has to be corrected digitally. A slightly different approach consists of using curved two-dimensional detectors. The optimal situation would consist of designing spherical detectors. It would seem that such detectors are not currently technologically feasible. However, other authors have suggested using cylindrical imaging plate detectors [ROB 98, TAK 98].

Recently, these studies have led to the production of laboratory diffractometers. Stachs and his collaborators [STA 00], for example, built a device equipped with a rotating anode generator and a cylindrical two-dimensional imaging plate detector. The maximum size of these detectors, currently the largest on the market, is close to 30 cm in diameter. Despite this size, the measurement of diffraction peaks corresponding to relatively small interplanar distances can only be achieved, with this type of device, if the incident beam's wavelength is small. These authors used the Kα radiation of a silver anode tube. However, this choice leads to a significant overlap of the peaks. Other authors performed the same type of measurements with

a two-dimensional gas detector [HE 02, DIC 02]. Since the size of these detectors is limited to about 10 cm, they are unable to completely measure Debye-Scherrer rings. Today, this type of device is essentially used for texture measurements. One of the big advantages of these diffraction systems with two-dimensional detection is that they do not require any movement on the part of the detector. This feature can prove to be crucial in extreme conditions. Such a diffractometer was built, for example, with a plane CCD detector in order to perform measurements on Mars [SAR 05a, SAR 05b].

These studies, which have been led since the beginning of this new century, show that it is now possible to obtain two-dimensional measurements of the intensity diffracted by a polycrystalline sample. However, several questions involving the optics and the angular resolution remain unanswered. For example, the angular resolution of such devices is directly related to the size of the beam, which usually has a square or circular cross-section and has to be as small as possible. The development of micro-sources could help to meet this condition [STA 00], but the number of crystals in the Bragg position is then quite low, resulting in poor measurement statistics. A possible solution would be to have the sample continuously oscillate during the measurement [SAR 05a]. The main problem remains the limited size of the detectors. This aspect could be gradually solved and these devices might see important developments in the years to come.

We have described in detail the features of the different types of diffractometers used for diffraction on polycrystalline samples. The analyzed samples take various forms, can be powdery or bulky, and can be analyzed in transmission or in reflection. Virtually all existing diffractometers can be described based one or the other of these typical configurations. We should point out, however, that samples in the form of thin films are a different matter and diffractometers designed for the study of these samples have to be adapted. We will detail in the following sections the characteristics of these diffraction systems.

2.3. Diffractometers designed for the study of thin films

2.3.1. *Fundamental problem*

2.3.1.1. *Introduction*

The energy of the X-ray beams used in radiocrystallography, while rather high, is small enough for the penetration depth of this radiation to be no greater than a few micrometers. If the devices used are adapted accordingly, X-ray diffraction should then make it possible to characterize thin films. For about 20 years, researchers in

radiocrystallography have been working on developing instruments and experimental and theoretical tools which would enable them to study these films.

We will assume that a film is an object thin enough for an X-ray beam with a normal incidence to pass through it. In this regard, a deposit of several hundreds or many tens of micrometers of ceramic or metallic materials is not a film. On the other hand, a film is not necessarily a deposit. It can simply be a structural modification caused by any process that alters the superficial area of the object over a thickness of 10 or 20 nanometers with respect to the core. Generally speaking, we can say that the methods described here all involve films with a thickness between 10 micrometers and a few nanometers.

2.3.1.2. *Penetration depth and diffracted intensity*

2.3.1.2.1. Penetration depth

Let us consider a sample irradiated at an incidence angle α and for which we measure the beams diffracted at variable angles 2θ. The sample's useful thickness is determined by its absorption properties. If I_0 is the incident intensity and I is the intensity after absorption, ratio I/I_0 can be written:

$$\frac{I}{I_0} = e^{-\mu\rho l} \qquad [2.2]$$

with:

– l: length traveled inside the sample;

– ρ: density;

– μ: mass absorption coefficient.

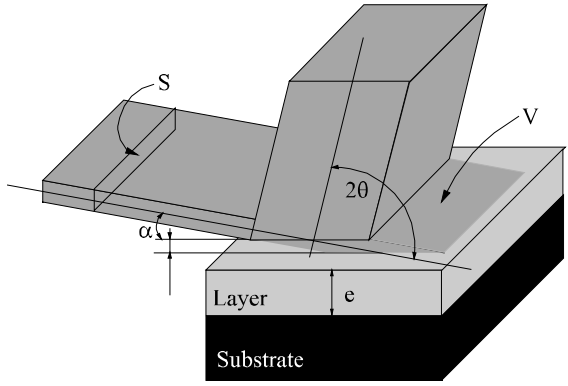

Figure 2.57. *Penetration depth and irradiated volume in asymmetric geometry*

The irradiated depth can easily be inferred from Figure 2.57; we then get:

$$p = -\frac{1}{\mu\rho}\left[\ln\left(\frac{I}{I_0}\right)\right]\left[\frac{\sin\alpha\sin(2\theta-\alpha)}{\sin\alpha+\sin(2\theta-\alpha)}\right] \qquad [2.3]$$

For traditional inorganic materials, the factor $\mu\rho$ (linear absorption coefficient) varies from a few hundred to a few thousand cm^{-1}. Of course, from a theoretical point of view, the irradiated depth is always infinitely long, but it is common to assume that when the intensity is equal to a tenth of the incident intensity, it becomes negligible. From such a hypothesis, it is possible to plot the penetration depth according to the incidence angle. This type of curve, obtained for a dense sample of zirconia (ZrO_2), is shown in Figure 2.58. We can clearly see that the penetration depth increases when the incidence angle changes from a few tenths of a degree to a few degrees[9]. Therefore, when studying a film of zirconia roughly 100 nanometers thick, the incidence angle should be in the range of 0.5°. We can also point out that at a high incidence, the irradiated depth is no greater than a few micrometers.

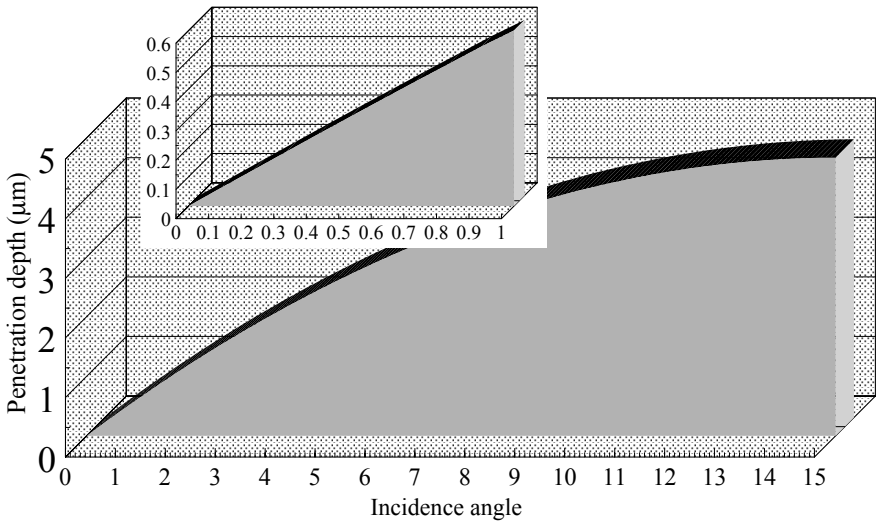

Figure 2.58. *Evolution of the X-ray penetration depth plotted according to the diffraction angle for several incidence angles of the beam*

9 When the incidence angle becomes very small, typically a few tenths of a degree, the X-ray beam is reflected by the film's surface and refracted toward the inside. Throughout this section, this effect is neglected.

Therefore, when producing a diffraction pattern for a film, the beam's incidence angle is set and, of course, the diffraction angle is variable. Naturally, this means that for a given diffraction diagram, the irradiated area will not be the same at the beginning and at the end of the pattern.

Figure 2.59 shows the evolution of the irradiated depth for a zirconia sample according to the diffraction angle 2θ, for several values of the incidence angle α. The resulting curves clearly show that if the incidence angle is significantly smaller than the angle 2θ, then the irradiated depth shows little variation with θ. This important result shows that all of the crystals that diffract during the acquisition of a diagram produced at a set incidence are located in the same area in the sample. Thus, if the sample is heterogenous with respect to its thickness, this heterogenity can be characterized by producing several patterns at different incidence angles, and each pattern will be specific to a layer of the sample.

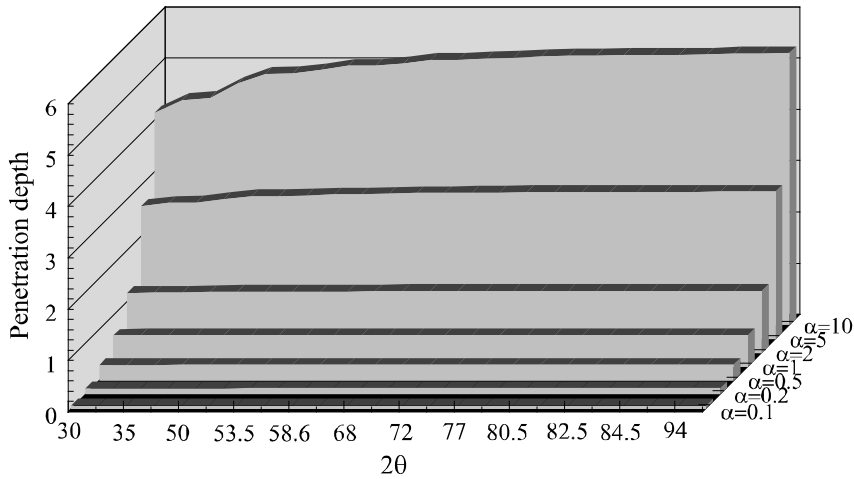

Figure 2.59. *Evolution of the X-ray penetration depth according to the beam's incidence angle with a film of zirconia*

2.3.1.2.2. Irradiated volume and diffracted intensity

The diffracted intensity is directly related to the irradiated volume[10]. When a bulky sample is studied in reflection, its thickness is infinite with respect to X-ray penetration and, as we have already mentioned, if the study is conducted in symmetric diffraction (Bragg-Brentano configuration), then the volume remains the

10 Throughout this section, we will be dealing with a polycrystalline film comprised of randomly oriented crystals.

same regardless of the diffraction angle. When studying a film, we saw that the sample had to be irradiated at a constant incidence, causing the irradiated volume to take on a more complex expression and to become dependent on the diffraction angle. Based on Figure 2.57, the following equation can be laid out:

$$V = p\left(\frac{S}{\sin\alpha}\right) \qquad [2.4]$$

with:

– S: area of the beam's cross-section;

– p: penetration depth;

– α: incidence angle.

Hence, the expression of volume V is:

$$V = \frac{S}{\mu\rho}\left[\ln\left(\frac{I}{I_0}\right)\right]\left[\frac{\sin(2\theta-\alpha)}{\sin(2\theta-\alpha)+\sin\alpha}\right] \qquad [2.5]$$

However, this expression of the irradiated volume does not apply if the irradiated depth, p, remains smaller than the overall thickness, e, of the film. If the penetration depth reaches the value of the film's thickness, then the irradiated volume is written:

$$V = e\left(\frac{S}{\sin\alpha}\right) \qquad [2.6]$$

If we consider a film with a specific thickness, the relative diffracted intensity measured for each characteristic peak is equal to the one found in the JCPDS file, multiplied by the ratio between the actual diffracting volume and the volume that would have been irradiated had the sample been infinite. If the beam passes through the film, this ratio is given by the ratio between the last two equations. With these relations, the actual values of the measured intensities can be established; in the case where the film is studied in symmetric diffraction, the corresponding relation is obtained by considering that $\alpha = \theta$.

Figure 2.60 shows the compared intensities for a film of zirconia studied in symmetric and asymmetric diffractions. The resulting histograms clearly show the advantage of asymmetric diffraction since, when the film is 100 nanometers thick, the intensity measured in the symmetric configuration is about 100 times smaller than in asymmetric geometry. Naturally, this effect is not as strong if the film is 1 μm thick.

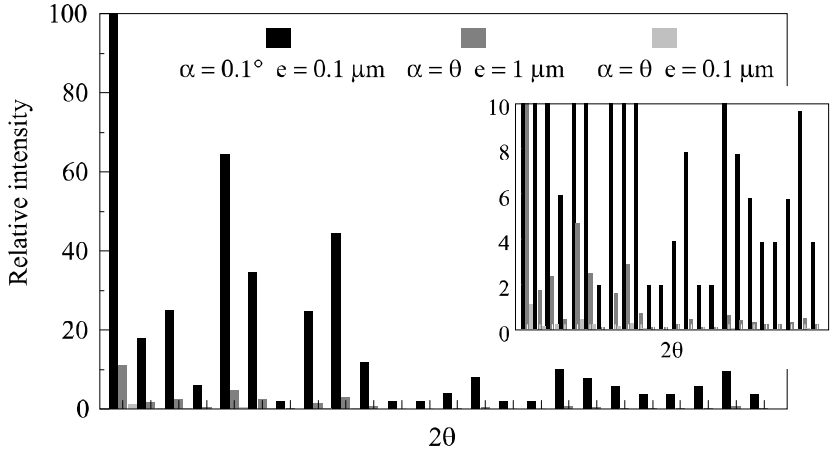

Figure 2.60. *Measured intensities diffracted in asymmetric and symmetric geometries*

We continued this analysis, this time by comparing, in Figure 2.61, the relative intensities with those provided by the JCPDS file for the phase in question. In both cases, symmetric diffraction and asymmetric diffraction, at an incidence angle of 0.1°, are compared for a film of zirconia which is 100 nm thick. In asymmetric diffraction, the resulting relative intensities, although not exactly the same, are close to the ones given in the file. On the other hand, in the case of symmetric diffraction, very significant discrepancies are observed.

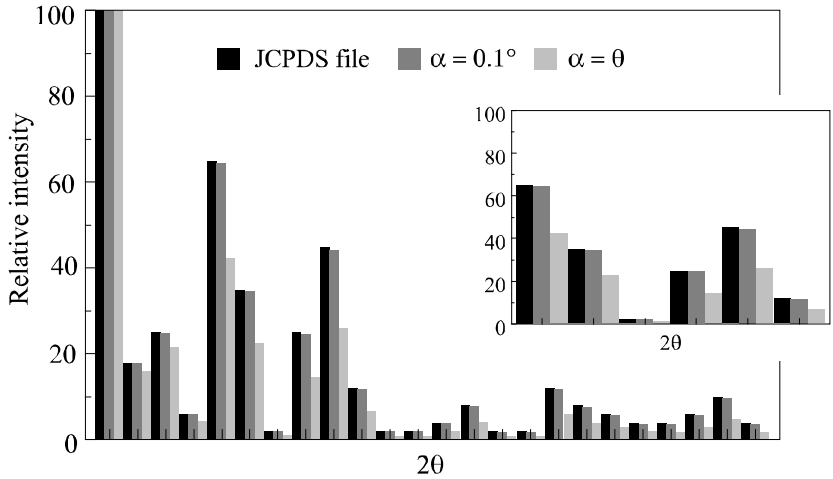

Figure 2.61. *Comparison of the relative intensities measured in asymmetric diffraction and in symmetric diffraction. The example chosen is a 100 nm thick film of zirconia*

2.3.2. *Conventional diffractometers designed for the study of polycrystalline films*

One of the main problems with X-ray diffraction on film is collecting in a reasonable amount of time, a significant number of diffracted photons for each peak. The minimum number of hits needed for a quantitative study of a pattern is in the range of several thousands for the intense peaks. For the study of peak profiles, tens or even hundreds of thousands of hits are need.

This requirement led researchers to think of a system with an intense, hence only slightly collimated, incident beam. A general diagram of such a device is shown in Figure 2.62 [ACK 94, HUA 90].

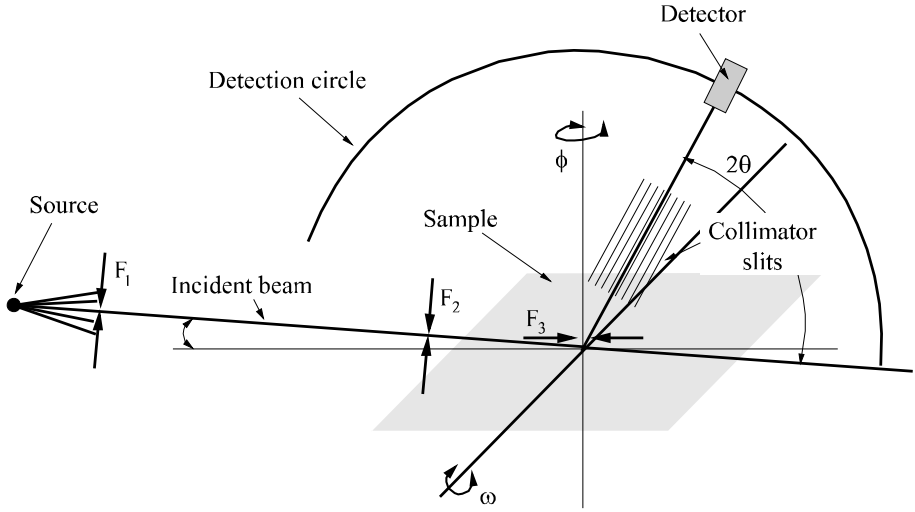

Figure 2.62. *Geometric arrangement of a low incidence diffraction device*

The X-ray source is usually a conventional sealed tube, with or without a curved monochromator, or a parabolic multi-layer monochromator. The source-sample distance is relatively high in order for the incident beam, whose opening is limited by two slits (F_1 and F_2), to be considered parallel. An additional slit is placed directly above the sample, which is irradiated at a low incidence angle. This slit, F_3, limits the angular opening seen at each moment by the detector, which is either a gas or a scintillation detector. It is also common to find analyzer slits placed on the path of the diffracted beams. By limiting the divergence, these slits make it possible reduce the peak widths.

With this system, diagrams can be produced in a few hours if the film has a reasonable thickness. However, the peak profile usually turns out to be dissymmetric.

Seemann-Bohlin diffractometers

As we saw previously, the system designed at the beginning of the century by Seemann and Bohlin to study powdery samples is one of the three traditional diffraction systems for polycrystalline samples. We saw in section 2.2.2.2 that this diffractometer enables the user to study the sample either in transmission or in reflection. When the sample is analyzed in reflection, it is possible to arrange the elements of the system in a way, so as to have a low incidence angle between the beam and the sample. In this case, the system will make it possible to characterize thin films [HAA 85, VAL 90, FIS 96, LIG 94]. This configuration is shown in Figure 2.63.

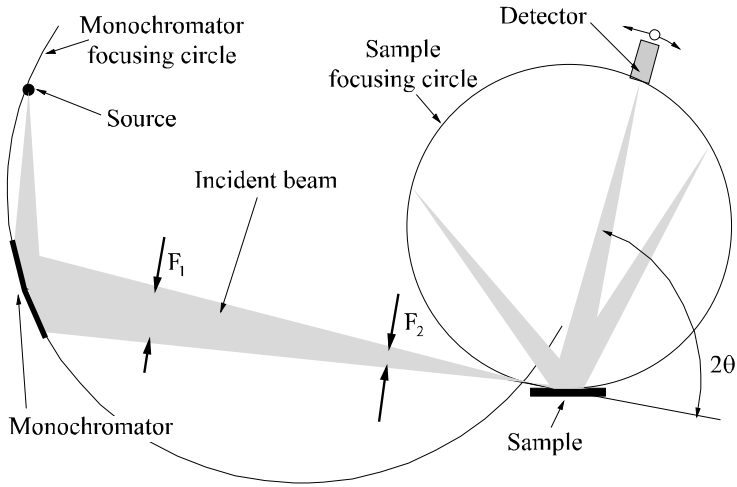

Figure 2.63. *Seemann-Bohlin diffractometer designed for the study of thin layers*

The diameter of the focusing circle is defined, on the one hand, by the distance between the convergence point of the incident beam and the sample, and on the other hand, by the incidence angle. The lower this incidence angle, the greater the diameter of the focusing circle. In practice, very low incidence angles cannot be used, meaning that this method is limited to films a few micrometers thick.

The main drawback of this geometry is that the incidence angle cannot be adjusted, since it is necessarily set for a given configuration, to the extent that it determines the diameter of the focusing circle.

2.3.3. *Systems designed for the study of textured layers*

Determining the orientation density function requires a large number of measurements conducted by varying the orientation of the sample. The machines used today are automatic diffractometers that can perform incremental measurements in reasonable amounts of time. Texture systems were initially developed to characterize bulky samples with generally high thickness. Both transmission and reflection configurations were designed, but in the case of films, studies clearly have to be done in reflection and, if possible, at low incidence angles. Figure 2.64 explains how these systems work.

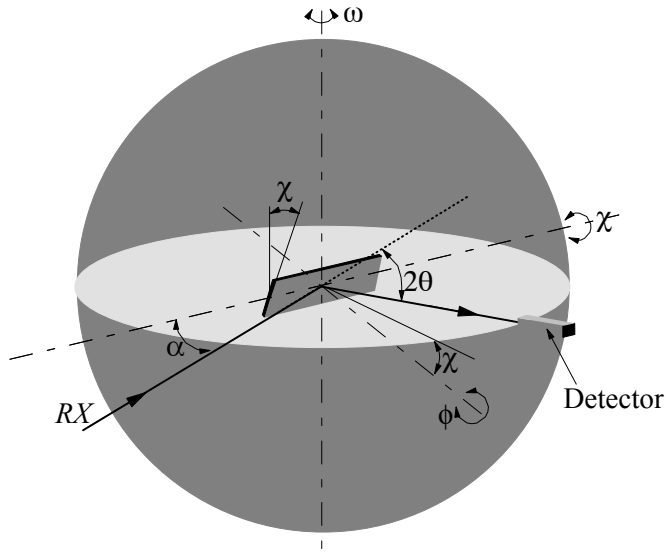

Figure 2.64. *Experimental configuration of a texture diffractometer*

The sample is mounted on a support that can move around three rotation axes: an axis ω makes it possible to choose the incidence angle α of the beam with the film, an axis ϕ, normal to the irradiated surface, makes it possible to rotate the sample in its plane, and finally an axis χ, normal to the two others and belonging to the sample's plane, makes it possible to tilt the sample. The diffracted beams are measured in the π plane, since the detector can rotate around the axis ω shared by the sample and the part holding the detector. The incidence angle α can either be coupled or not to the detector's position; if these two rotations are coupled, the measurement is performed in the Bragg-Brentano conditions, which should make it possible to have a constant irradiated volume if the sample is assumed to be infinite.

For the characterization of the layers, it is better to conduct the study at a set incidence angle, but quantitative studies will then be needed to correct the intensity measurements performed by the actual irradiated volume [TIZ 96].

The measurement of the diffracted intensities, which is necessary for a complete study of a film's texture, is done by recording the variations of the intensity diffracted at the angle 2θ that corresponds to this family of planes during the rotation of axes ϕ and χ. Therefore, most of the time, a grid along ϕ and χ is defined, and the intensity distribution is measured incrementally, with each increment equal to a fraction of a degree.

Despite the fact that these systems are automated, completely determining the orientation density function requires a long measurement time. One method can significantly reduce it [HEI 86], by using the same principle of the diagram shown in Figure 2.64, but replacing the punctual detector with a curved position sensitive detector. This method enables the user to simultaneously measure several diffraction peaks; however, it requires to precisely take into account the irradiated volume for each of the considered peaks. The corresponding scheme is shown in Figure 2.65.

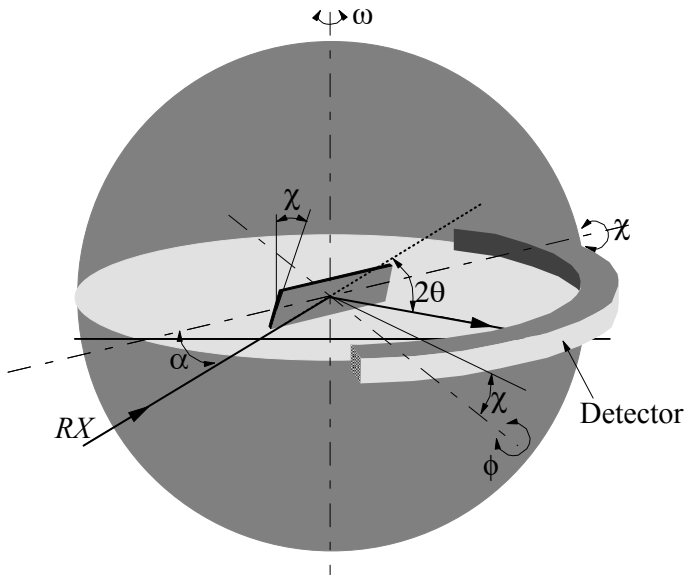

Figure 2.65. *Texture diffractometer equipped with a curved position sensitive detector*

2.3.4. *High resolution diffractometers designed for the study of epitaxial films*

The study by X-ray diffraction of epitaxial films is a field of its own. Because they are comprised of a set of crystals all of which have practically the same crystallographic orientation, epitaxial thin films are close to being single crystals. However, they are polycrystalline samples, so they deserve their own section in this book. Note, however, that the development of instruments designed for the study of these films owe a lot to the diffractometers intended for single crystals, and particularly those that focus on the study of defects in single crystals.

The production of epitaxial thin films was developed particularly by the microelectronics industry, based on semi-conductor materials [FEW 01]. The continuous decrease in the thickness of films, combined with the miniaturization of the systems, has led to the development of epitaxial films which are sometimes only a few nanometers thick. Furthermore, the development of new devices with magnetic, optical or electronic properties has encouraged the introduction of oxide crystals in active components. The structure of these oxides and the microstructures of the films produced are often complex, and improving the properties requires adequate characterization capabilities. X-ray diffraction, probably along with electronic or scanning probe microscopes, is one of the key techniques in the study and constant improvement of the characteristics of epitaxial films.

In this context, diffractometers designed for the study of epitaxial films first became available on the market about 20 years ago. The enthusiasm for nanotechnologies has led to very significant developments in this field. Several books specific to X-ray diffraction on epitaxial films have been published over the past few years [BOW 98, PIE 04]. In the second part of this book, we will describe in detail the methods for quantitative analysis of the microstructure of epitaxial films. The objective in the following sections is to give a description of the basic systems that make it possible, beyond the simple determination of the crystallographic orientation, to achieve this type of analysis.

Generally speaking, diffractometers designed for the study of epitaxial thin films need to present two essential features. First, the incident beam on the sample and the beams detected after diffraction by the sample have to be as parallel and as monochromatic as possible. Second, it has to be possible to orient the sample very precisely with respect to the incident beam, meaning that the diffractometer has to be equipped with a multi-axis sample holder able to move with an angular precision in the range of a thousandth of a degree.

We have already said that traditional sources produce divergent beams. Therefore, the production of parallel beams requires the use of adequate optical elements which will simultaneously modify the trajectory of the X photons and

reduce the beam's spectral dispersion. Even though synchrotron radiation is an obvious way of directly producing an almost parallel beam, diffractometers for epitaxial films were also developed from traditional sealed tube sources [BAR 78, FEW 01, BOW 98, PIE 04] or rotating anode generators [GUI 99, BOU 02].

A typical system of this type is shown in Figure 2.66.

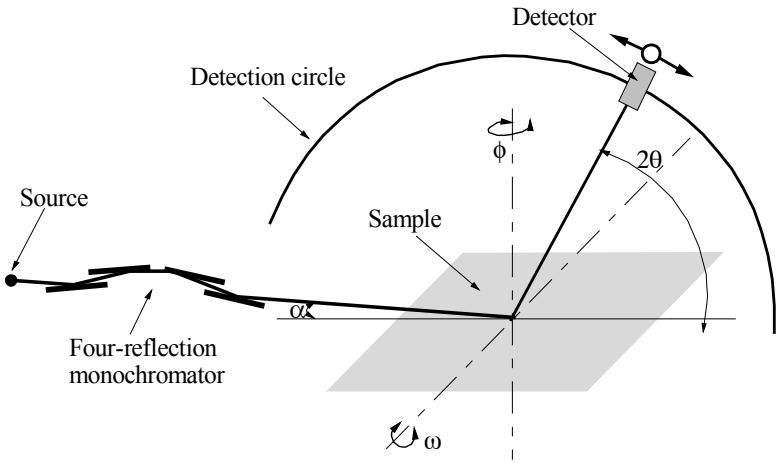

Figure 2.66. *Schematic drawing of a diffractometer designed for the study of epitaxial thin films*

A four-reflection monochromator comprised of plane single crystals is placed between the source and the sample (see Figure 2.36). The beam irradiates the sample, which is placed on a three axes sample holder. The sample holder makes it possible to orient the normal to any family of crystal planes in the diffraction plane defined by the axis of the incident beam and the directions of the diffracted beams. Since the beam is strictly parallel, it is not necessary to include a slit between the sample and the monochromator. The intensity of the diffracted beams is measured by using a detector which moves along a circle, centered on the sample or with a curved position sensitive detector. This last feature makes this system a distant relative of the Debye-Scherrer diffractometers, for which the sample is, by definition, the center of the detection circle.

In some cases, when attempting to improve the monochromaticity of the diffracted beams, a plane back monochromator is included on which the beams diffracted by the film are diffracted once more [FEW 91]. These analyzer crystals are usually made out of silicon or germanium. A back monochromator like this is comprised of one, two or three crystals. For a specific position of the sample,

defined by the rotation ω, only the beams diffracted by the sample that arrive at precisely the Bragg angle of this analyzer device will be diffracted and therefore picked up by the detector. This is referred to as the parallel configuration or "geometry". Of course, this configuration should significantly reduce the intensity of the beams picked up by the detector. However, the presence of analyzer crystals makes it possible to increase the width of the incident beam since, for each position θ, the angular opening seen by the detector is set by the mosaicity of the analyzer crystals (and not by the beam's width), which is typically in the range of a few thousandths of a degree. It is therefore very common for this type of diffractometer to use a hybrid monochromator comprised of a parabolic artificial crystal and four plane crystals. The beam's width is typically ten times greater than in the absence of the parabolic artificial crystal. It is then necessary for the sample to be homogenous over the entire irradiated surface, which can be in the range of a square centimeter. This means that the measured diffracted intensity is higher, without any decrease in the angular resolution. Note, however, that the presence of analyzer crystals prohibits the use of a position sensitive detector and therefore the measurements will be conducted point by point. The models of this type that are available to the public are equipped with punctual detectors, most of the time, or linear detectors. The choice of one or the other configuration depends on what movements are allowed by the sample holder. If we want to be able to rotate the sample around the rotation axis χ, a punctual beam is *a priori* necessary. Figure 2.67 shows a diagram of this type of system in a very high resolution configuration.

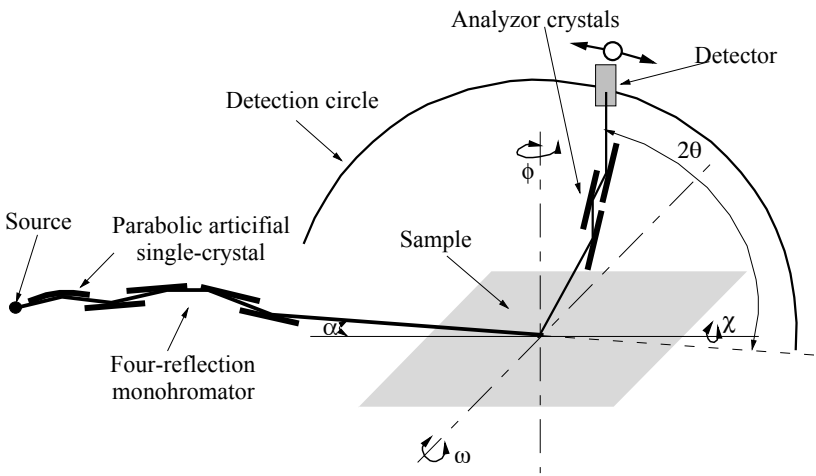

Figure 2.67. *Schematic drawing of a diffractometer that uses a parallel incident beam associated with analyzer crystals*

2.3.5. *Sample holder*

Every system designed for the study of thin films includes a sample holder which makes it possible to precisely orient the sample with respect to the incident beam. If the film is polycrystalline, the user should be able to choose the value of the angle between the incident beam and the surface of the sample. Most of the time, the sample has to rotate around the axis ϕ during the diagram acquisition. Therefore, the normal to the surface has to be parallel to the axis ϕ. If the film is textured or epitaxial, it is likewise necessary to be able to completely specify the position of a given family of planes with respect to a fixed, three-dimensional frame of reference.

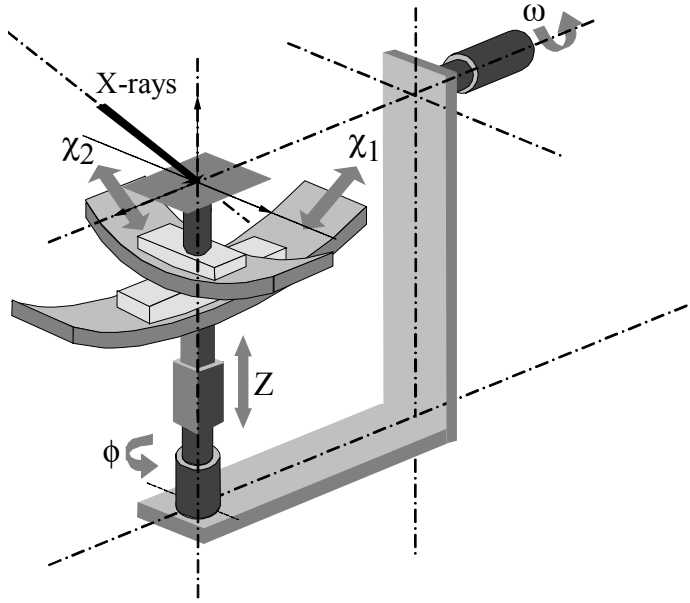

Figure 2.68. *Five-axis sample holder*

These conditions impose the use of a sample holder that includes four rotation axes and one translation axis [BOU 01a, GUI 99]. A rotation sets the beam's incidence angle with the sample (ω rotation) and another one sets the orientation in the plane (ϕ rotation). The two others, which we have named χ_1 and χ_2, are there to orient the normal to a given family of planes, or the surface of the sample, until it is parallel to the axis of rotation ϕ. The translation, finally, is there to bring the surface of the sample to the intersection point of the axis of rotation ω with the incident

beam's direction. A schematic view of such a sample holder is shown in Figure 2.68.

This sample holder corresponds to the ideal scenario, since any family of planes can be placed in the Bragg position[11]. In practice, sample holders often only include one of the two cradles χ_1 and χ_2. As a result, the adjustment of the orientation of the family of planes is approximate.

As the scheme in Figure 2.68 and its explanation show, this sample holder, for a given position around the axis ϕ, makes it possible to measure the distribution of the diffracted intensity when the position of the sample is constant with respect to the axis ω, or when the sample is rotating around this axis. The two cradles χ_1 and χ_2 are there to maintain the normal to the diffracting planes in the plane defined by the direction of the incident beam and the detector's plane of movement during the rotation around ω. When studying polycrystalline films, the sample usually does not move (it can sometimes rotate around ϕ), but for studies involving the analysis of epitaxial films, it can be useful to measure the evolution of the diffracted intensity distribution when the sample rotates about ω. We will see in the second part of this book that this type of measurement, referred to as two-dimensional reciprocal space mapping, makes it possible to quantitatively evaluate the microstructural characteristics of the epitaxial films. The sample holder shown in Figure 2.68, as we have just said, makes it possible to produce a two-dimensional mapping using the variables ω and 2θ. Generally speaking, the distribution of the diffracted intensity is equivalent to a volume in the reciprocal space and therefore these two-dimensional mappings are particular sections of these reciprocal lattice nodes . It is also possible to produce complete three-dimensional measurements of these intensity distributions, which is called three-dimensional mapping. An additional axis of rotation is then needed, which most of the time is the axis χ shown[12] in Figure 2.68. A schematic drawing of the corresponding sample holder is shown in Figure 2.69. The same type of sample holder is used for the analysis of textured films, although in this latter case, the two cradles χ_1 and χ_2 are not really necessary.

11 We will see later on that there is, in fact, a geometric relation imposed between the Bragg angle of the family of planes and the angle between that family of planes and the sample's surface.

12 It is important not to confuse this rotation χ, which is a movement used during the measurement, with the axes we have called χ_1 and χ_2, which are used for adjusting the sample's reference position.

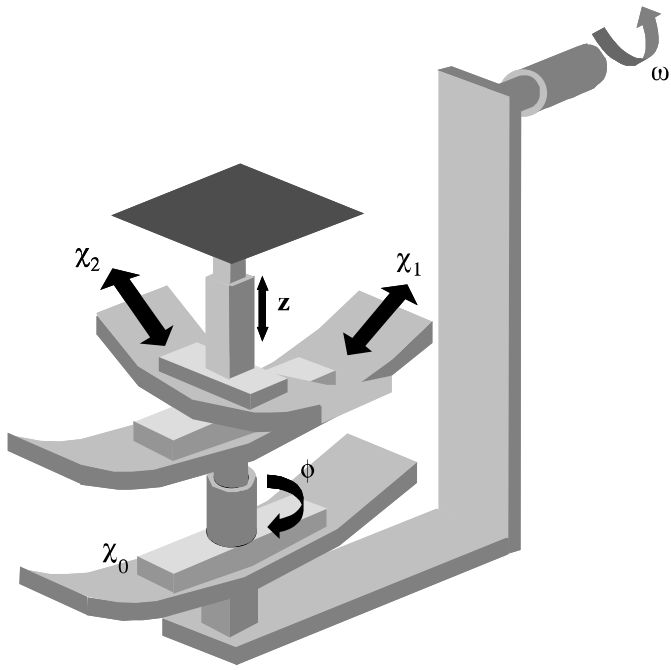

Figure 2.69. *Schematic drawing of a complete sample holder designed for the study of epitaxial films, which enables the user to make a three-dimensional measurement of the intensity distribution*

2.4. An introduction to surface diffractometry

For most solids, the surface constitutes the main defect, equivalent to a sudden break in the periodic arrangement of atoms. From a structural point of view, the surface of a solid is the layer of atoms that ends this solid. Some authors have shown that it is possible, in specific conditions, to study the structure of these surfaces, that is, the nature of the atoms that comprise the solid's limit and how they are arranged. The experimental techniques used rely on X-ray diffraction, but these methods are very specific and the structural study of surfaces, even though it started about 20 years ago, remains a field reserved to a few specialists. Most studies involve the surface of semiconductors or metals. We should point out, however, that over the past few years, the surface structure of a few simple oxides have been studied [REN 98].

The underlying idea behind these measurements is to irradiate the single crystal we wish to study at a very low angle, below the critical angle of total reflection. As

we have already mentioned, this is an angle of only a few tenths of a degree. The incident beam is totally reflected on the surface of the single crystal and therefore, the X photons do not penetrate the crystal. The resulting surface wave is diffracted by normal planes on the surface and at an angle with the incident beam equal to the Bragg angle. The diffraction signal is measured, usually with a position sensitive detector, in a plane perpendicular to the surface. The sudden break in atomic periodicity causes the diffraction spot to spread out along a direction perpendicular to the surface. The intensity of the diffraction signal is very small, which is why these diffractometers are used, most of the time, on synchrotron radiation sources. A diagram explaining how such a device works is shown in Figure 2.70.

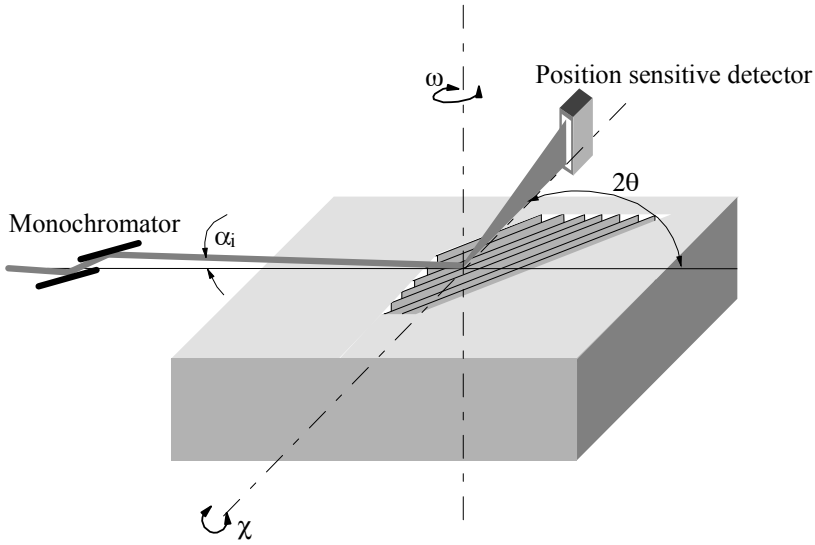

Figure 2.70. *Geometrical arrangement of a diffractometer designed for the study of surface structures*

Chapter 3

Data Processing, Extracting Information

Regardless of the diffractometer geometry and which type of detector is used, the diagrams obtained are necessarily discontinuous, that is, the space between two consecutive points is equivalent to the increment chosen for the measurement. This comment extends far beyond the field of X-ray diffraction, since it can be generalized to fit any physical measurement. The interpretation of these measurements is usually achieved by fitting[1] the measured signal with a continuous function, the parameters of which are refined so as to have this function's profile as close as possible to the experimental profile. More explicitly, the position of a diffracted peak, or the integrated intensity of that peak, are most often given, respectively, by the centroid and the integral of the continuous function that best fits the experimental peak.

Figure 3.1 describes how the fitting of diffraction patterns works. Usually, in diffraction patterns produced with a polycrystalline sample, the peaks that correspond to the diffraction associated with different families of planes overlap. Therefore, the resulting experimental signal is the sum of the different contributions, in addition to a continuous background, caused, among other things, by the

1 Many words can be found in literature to refer to this type of experimental data processing. "Fitting" and "modeling" are often used. These two terms are very close in meaning, but can have a slightly different connotation. Fitting is used when the line that passes through the experimental points has no particular meaning, physically speaking, but simply describes the observed reality correctly. On the other hand, modeling is used when the calculated line is obtained from the description of the influence of the device or the sample's specific physical parameters. In any case, however, the experimental points and the calculated line are adjusted by varying either the parameters that mathematically define the calculated line, or the values of the physical parameters specific to the device and the sample.

scattering of the incident and diffracted beams by the air surrounding the sample. The characteristics (position, integrated intensity, profile) of each diffraction peak are determined by the adjustment of this curve to the experimental data.

This process, which greatly relies on digital calculations and computing, has been going through very significant developments over the past years [BIS 89, JEN 96, LAN 96]. Today, diffraction equipment is systematically sold with fitting software of various levels of quality and performance. Many programs, usually developed by researchers, are available at no cost on international networks. The objective in the following sections is not to review these softwares, but rather to explain the different possible methods of fitting diffraction patterns. Clearly, one of the essential parameters in any fitting is the adequacy between the experimental profile that was measured and the shape of the fitting function that was chosen. We will first discuss in detail the concept of peak profiles by describing in particular the main effects that modify these profiles.

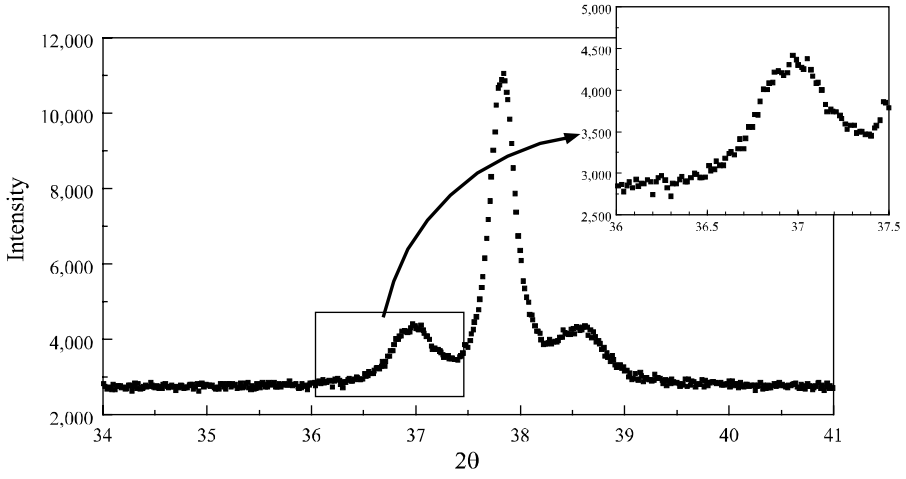

(a) Experimental patterns are discontinuous

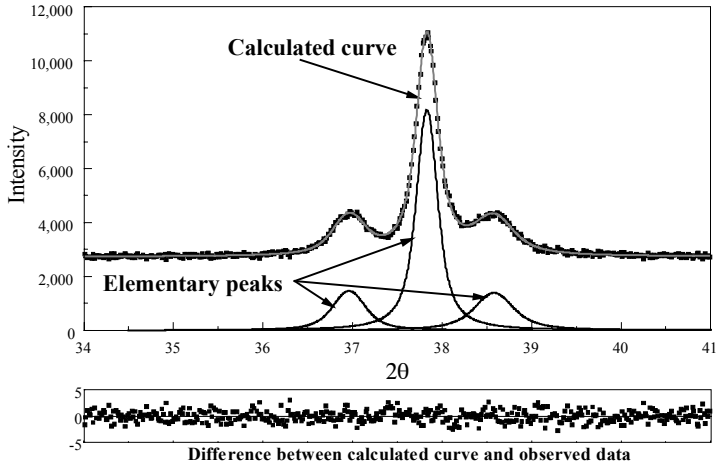

(b) An example of simulation

Figure 3.1. *The basics of diffraction pattern processing by peak fitting*

3.1. Peak profile: instrumental aberrations

Regardless of the quality of the adjustments, the geometry of the diffractometer leads to a few aberrations, resulting in peaks that are not quite symmetrical, generally wide and shifted with respect to the expected diffraction angle. We will discuss each of the aberrations caused by the device's various elements. The function obtained from the convolution of the different elementary functions associated with each aberration is called the instrumental function.

The profile of diffraction peaks depends on two types of contributions: first, the instrumental function and, second, the structural defects that also lead to changes in the intensity distribution. This last comment is at the core of microstructural analysis, which will be the subject of the second part of this book and will not be discussed here. Peak profiles can be described by a function h(ε), where the ε variable corresponds in every point to the difference with respect to the theoretical diffraction angle. The function h(ε) can be expressed as the convolution product of f(ε), which represents the pure profile associated with the sample's specific effects, and g(ε), which constitutes the instrumental function. The function h can then be expressed as:

$$h(\varepsilon) = \int_{-\infty}^{+\infty} g(\eta) f(\eta - \varepsilon) d\eta \qquad [3.1]$$

The profile observed is actually more complex because the measurement noise $\delta(\varepsilon)$, on the one hand, and the continuous background $b(\varepsilon)$, on the other hand, which have already been mentioned, must be taken into account. Hence, the expression of the peak profile:

$$h(\varepsilon) = \left(\int_{-\infty}^{+\infty} g(\eta) f(\eta - \varepsilon) d\eta \right) + b(\varepsilon) + \delta(\varepsilon) \qquad [3.2]$$

Microstructural studies require the pure profile, meaning the function f, to be determined. Solving equation [3.2] is a complex problem, dealt with later on. In this chapter, we will simply describe the different components of the instrumental function. The expressions and the relative importance of the different functions $g_i(\varepsilon)$ depend on the device. Clearly, the complete description of a given diffractometer's experimental profile requires taking into account all of its elements. We will now describe the main effects observed in virtually every case.

3.1.1. *X-ray source: $g_1(\varepsilon)$*

Generally speaking, the profile of a beam produced by a tube approximately corresponds to a Gaussian function and therefore the function $g_1(\varepsilon)$ is expressed as:

$$g_1(\varepsilon) = \frac{1}{H} e^{-\frac{1}{H^2}\varepsilon^2} \qquad [3.3]$$

H being the Gaussian's full width at half maximum.

The importance of this effect greatly depends on the width of the tube's focusing spot.

3.1.2. *Slit: $g_2(\varepsilon)$*

Naturally, this function corresponds to a rectangular profile centered on the beam's axis, the width of this rectangle being equal to the angle subtended between the slit and the goniometer's center. We saw that diffractometers generally include several slits, placed before or after the sample.

The presence of these slits causes the diffraction peaks to widen, and particularly their tails to spread out. This effect was studied in detail, for example, by Louër and

Weigel for the entrance slits of detectors [LOU 69b]. The increase in the slit's width results in an increase in the widths of the peaks.

The influence of the slits essentially depends on the respective sizes of the angular openings with respect to the size of the beam. If the slit's opening is about the same size as the beam, its influence on the peak profile will be small.

3.1.3. *Spectral width: $g_3(\varepsilon)$*

Regardless of the wavelength used, a peak always has a certain spectral width. When the beam is comprised of only one peak[2], $K_{\alpha 1}$ for example, this function approximately corresponds to a Lorentzian [JAU 22, COM 35], hence its expression:

$$g_3(\varepsilon) = \frac{1}{1 + k^2\varepsilon^2} \qquad [3.4]$$

Generally speaking, this contribution is very small compared to the ones described above. Recent studies [FRE 87, HAR 93] have established that the width of copper's $K\alpha_1$ peak is equal to 0.518×10^{-3} Å.

3.1.4. *Axial divergence: $g_4(\varepsilon)$*

Divergence referred to as axial is the divergence of beams in a plane normal to the diffraction plane, which is defined by the directions of the incident beam and of the diffracted beams. The diagram in Figure 3.2a shows the effects of axial and equatorial (in the diffraction plane) divergence on the path of the X photons. The parameters that characterize axial divergence are explained in Figure 3.2b. A complete description of this effect is complex, particularly since, as you can see, the influences of the axial and equatorial divergence are coupled [MAS 01]. Some authors [LAA 84, FIN 94] have suggested relatively simple expressions, but which only account for the divergence of the diffracted beams and not for the axial divergence of the incident beam. Recently, more complex descriptions have been suggested [CHE 98, CHE 04, MAS 01].

2 If the incident beam corresponds to several radiations with different mean wavelengths, the beam's wavelength dispersion is then described as the sum of all the Lorentzian functions associated with each radiation.

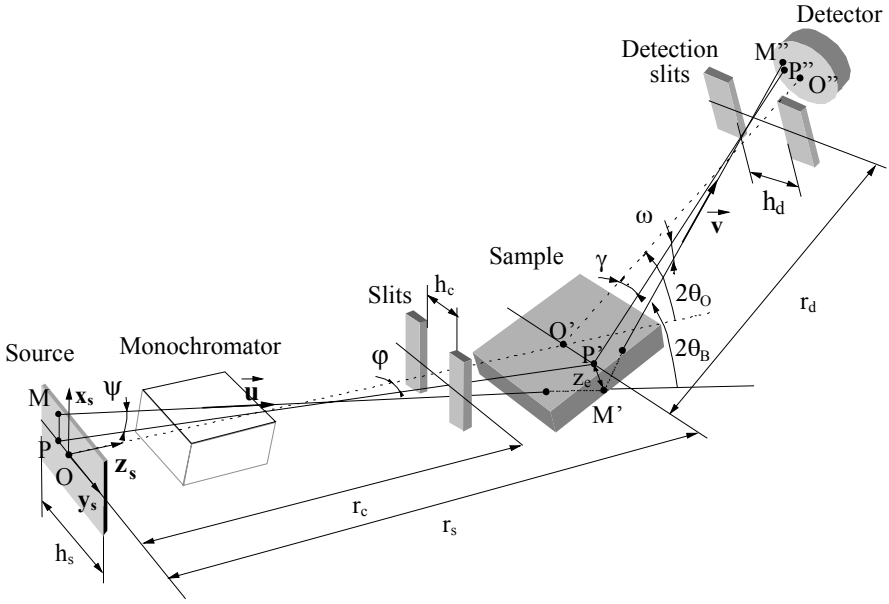

(a) Three-dimensional representation of the path of the photons

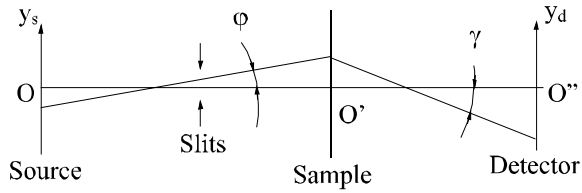

(b) Representation in the axial plane of the axial divergence before and after diffraction of the beam by the sample

Figure 3.2. *Description of the path of the X photons after taking into account the axial and equatorial divergences of the incident and diffracted beams [MAS 01]*

Although the dissymmetric function, $g_4(\varepsilon)$, is different depending on what configuration is used and particularly on whether or not it includes Soller slits, we should point out (see Figure 3.3) that, in any case, the deformation due to this effect is very significant for very low angles; then it decreases when θ increases and is practically non-existent for $90° < \theta < 120°$, before it starts increasing again. Below 90°, the profile is deformed at low angles, and beyond that, the deformation caused by this effect occurs in the other direction.

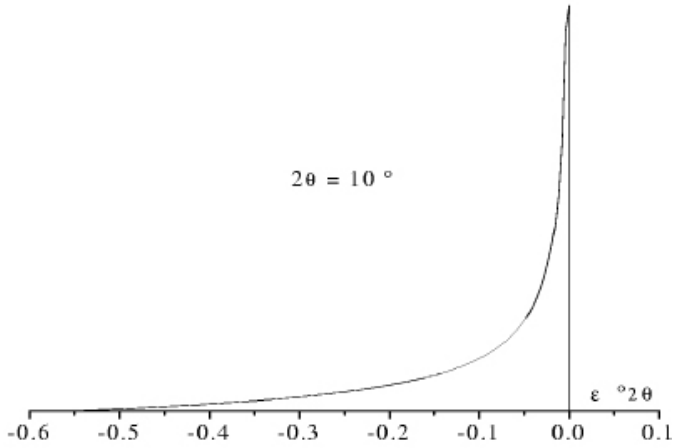

(a) asymmetrical deformation caused by the axial divergence for a peak situated at a low diffraction angle (2θ = 10°)

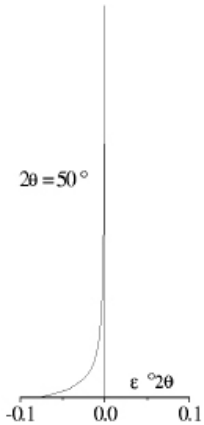

(b) asymmetrical deformation caused by the axial divergence for a peak situated at a relatively high diffraction angle (2θ = 50°)

Figure 3.3. *Shape of the intensity distribution resulting from an axial divergence of the beam. Influence of the value of the diffraction angle [CHE 04]*

3.1.5. *Transparency of the sample: $g_5(\varepsilon)$*

The X-rays penetrate the sample, whose absorption coefficient is not infinite, up to a certain depth. Therefore, the diffracted beams picked up by the detector

correspond, for each Bragg angle, to a sum of diffracted beams with variable depths, thus modifying the shape of the peaks. The function $g_5(\varepsilon)$ is written:

$$g_5(\varepsilon) = e^{k\varepsilon} \qquad [3.5]$$

The expression of k depends on which configuration is chosen. The term μ mentioned in Figure 3.4 is the sample's linear absorption coefficient, R is the radius of the goniometric circle and ε varies between 0 and $-\infty$.

In reflection, the influence of this dissymmetric function increases when the material's absorption coefficient decreases. Figure 3.4 illustrates this contribution in the case of the dissymmetric reflection configuration [MAS 98b].

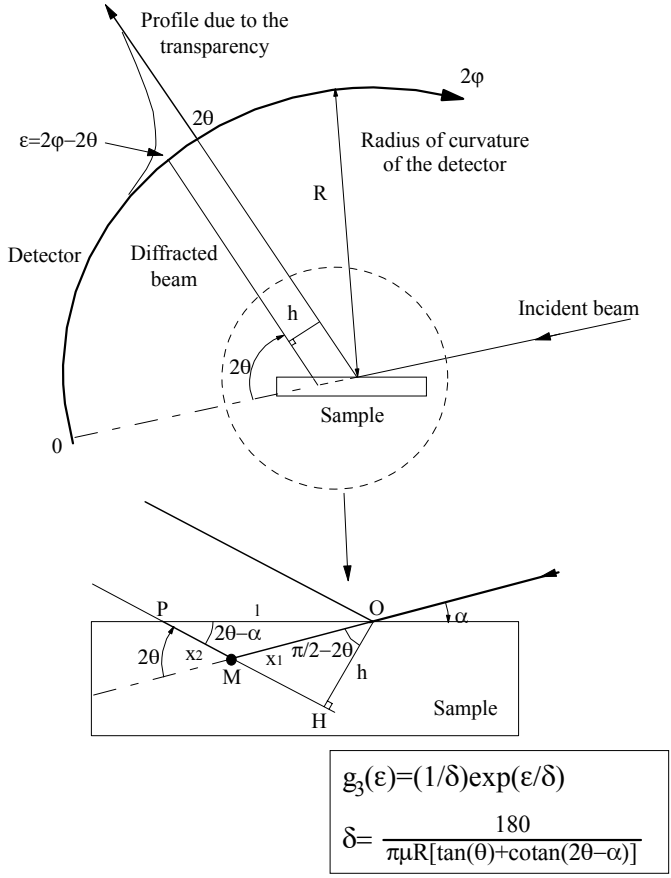

Figure 3.4. *Transparency effect*

The lower the diffraction angle is, the greater the influence of axial divergence and transparency. In practice, these two effects are only noticeable for the peaks observed at the beginning of the diffraction pattern. Figure 3.5 is an experimental illustration of the asymmetrical deformation of the peak caused by these two effects. The sample is silver behenate ($CH_3(CH_2)_{20}COOAg$), which shows a strong transparency to X-rays. The diffraction diagram was produced in asymmetrical diffraction at an incidence angle $\alpha = 4°$ [MAS 98b, MAS 01].

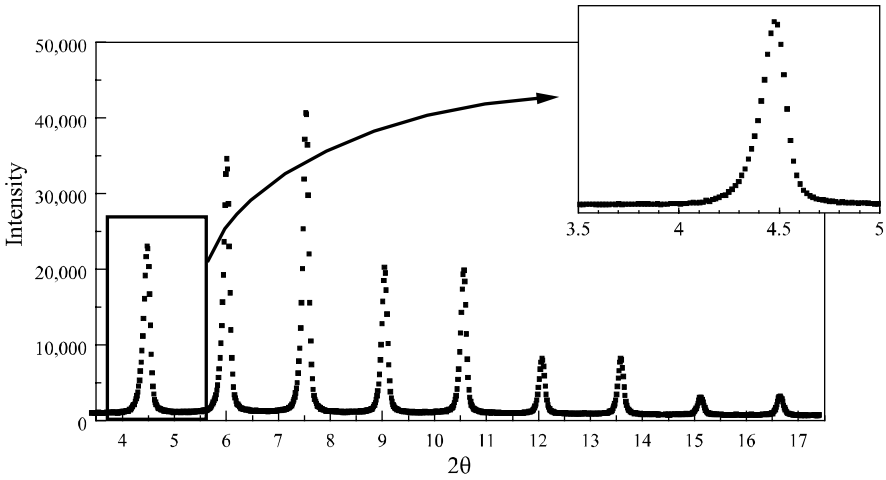

Figure 3.5. *Diffraction pattern showing the influence of divergence and transparency. Study performed in asymmetrical diffraction on silver behenate*

3.2. Instrumental resolution function

As we have just seen, the peak profile is the result of the convolution of a certain number of elementary contributions with various degrees of complexity. These functions usually depend on the diffraction angle, which means that the shape of the diffraction peaks varies with θ. With the exception of microstructural effects (see Part 2 of this book), the width of the peaks is directly determined by the various elements that comprise the diffractometer. The description of the evolution of this width according to the Bragg angle characterizes the device used. This is referred to as the instrumental resolution function.

This function usually increases with the diffraction angle and can often be approximated by a second degree polynomial in tangent θ. This equation is known as the Caglioti polynomial [CAG 58] and is written:

$$H^2 = U \tan^2 \theta + V \tan \theta + W \qquad [3.6]$$

The parameters U, V and W are specific to the diffractometer in question. This function was established almost 50 years ago on a neutron diffractometer. It actually has no theoretical background and its expression is essentially empirical, so for some diffractometers, the angular resolution function can stray significantly from this second degree polynomial. However, the expression established by Caglioti and his colleagues is still commonly used.

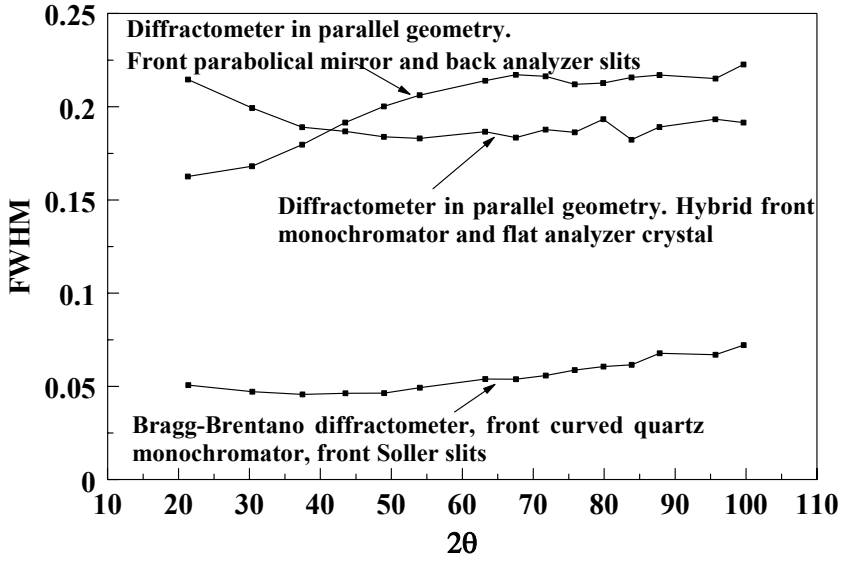

Figure 3.6. *Instrumental resolution function of several diffractometers*

With conventional laboratory diffractometers, the width of the peaks is commonly in the range of a tenth of a degree. It can go down to a few thousandths of a degree for high resolution diffractometers using a synchrotron radiation source [MAS 03]. With a laboratory Bragg-Brentano diffractometer, equipped with a front monochromator and thin slits, the resolution can go down to 0.05° or 0.06° at low angles. For high angles, the contribution from the spectral dispersion causes a significant widening and the peak widths will be in the range of 0.2° at around $2\theta = 150°$. These values are obtained for conventional equipment of excellent quality and the actual resolution will often be poorer. Figure 3.6 shows the resolution functions of several diffractometers described in the previous chapter (see Figure 2.55). These graphs were experimentally plotted by measuring the diffraction pattern of a sample assumed to be perfect, which therefore does not widen the peaks. There is currently only one sample that serves at international level as reference for this type of study: it is a powder of lanthanum hexaboride (LaB_6)

available from the National Institute of Standards (NIST) in the USA. Note in Figure 3.6 that the angular resolution of the Bragg-Brentano system used in high resolution is much better than that of parallel geometry diffractometers.

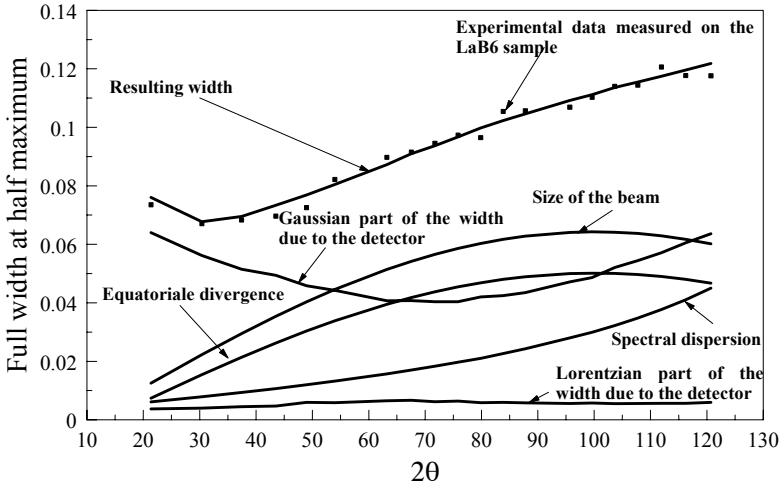

Figure 3.7. *Calculation of the instrumental resolution function of a diffractometer equipped with a four-reflection monochromator and a curved position sensitive detector*

If all the elements of a diffractometer are known, it should be possible to completely calculate *a priori* the instrumental function by using successive convolutions, among other things. It is then possible to directly calculate the instrumental resolution function. However, this process is only applicable if the number of contributions to the widening of the peaks is small. Figure 3.7 shows the result of such a study achieved for the system shown in Figure 2.35. It works in an asymmetrical diffraction configuration and is equipped with a four-reflection monochromator and a curved position sensitive detector. The calculated width values were compared to the widths measured with the lanthanum hexaboride sample sold by the NIST. The good agreement between the two confirms the validity of the method used.

3.3. Fitting diffraction patterns

3.3.1. *Fitting functions*

3.3.1.1. *Functions chosen a priori*

The first functions used were Gaussian. We have previously seen the various aberrations that can modify the shape of the diffraction peaks. It is understood that the resulting profile cannot be described by a Gaussian function. However, these functions were often used for neutron diffraction. Generally speaking, the resolution of neutron diffractometers is much smaller than the resolution of X-ray diffractometers and the shape of the peaks is accurately described by Gaussian functions. The users of neutron diffraction were the first to suggest, as early as the 1950s, the fitting of diffraction peaks and therefore the Gaussian functions were the first tools used in X-ray diffraction [BIS 89].

These functions of the Bragg angle are expressed as follows:

$$G(2\theta) = \frac{2}{H}\left(\frac{\ln 2}{\pi}\right)^{\frac{1}{2}} \exp\left(\frac{-4\ln 2}{H^2}(2\theta - 2\theta_h)^2\right) \qquad [3.7]$$

H being the full width at half maximum.

As we have already mentioned, the development of high resolution X-ray diffraction devices made it possible to show that Gaussians did not fit the experimental profiles well. Generally speaking, when instrumental aberrations lead to symmetrical increases in peak width, the peaks can usually be approximated as Gaussian or Lorentzian functions[3]. The latter are expressed as follows:

$$L(2\theta) = \frac{2}{\pi H}\left[1 + \frac{4\left(\sqrt{2}-1\right)}{H^2}(2\theta - 2\theta_h)^2\right]^{-1} \qquad [3.8]$$

3 The terms Lorentzian function and Cauchy function refer to the same mathematical object.

Therefore, the resulting profiles are bounded by these two Gaussian and Lorentzian limits. They can be described by a Pearson VII function which is expressed as [ELD 69, HAL 77]:

$$P_{VII}(2\theta) = \frac{2\sqrt{m}\Gamma(2^{\frac{1}{m}}-1)}{\pi\Gamma(m-0{,}5)H}\left[1+\frac{4(2^{\frac{1}{m}}-1)}{H^2}(2\theta-2\theta_h)^2\right]^{-m} \qquad [3.9]$$

m being a shape parameter that varies continuously. When m = 1, the function is equivalent to a Lorentzian and we get a function that tends to a Gaussian when m tends to infinity. When m is smaller than 1, the function is referred to as super-Lorentzian. The evolution of the Pearson VII function's shape according to m is shown in Figure 3.8. All the plots have the same area.

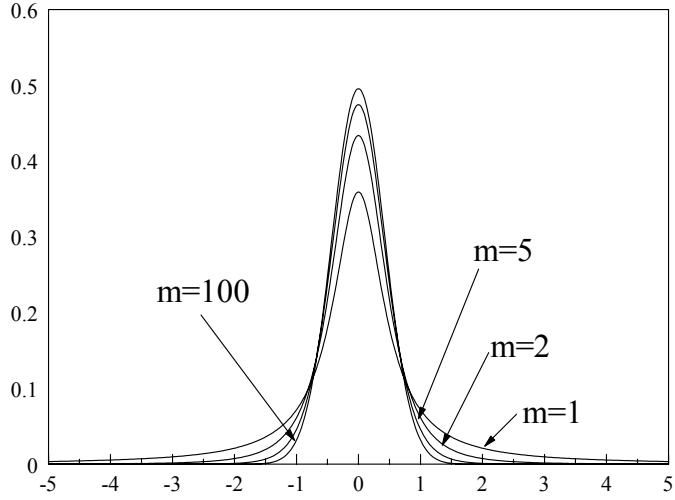

Figure 3.8. *The Pearson VII function. Influence of the shape parameter's value*

Radiocrystallographers thought many years ago describing peak profiles as convolution products of Gaussian and Lorentzian functions. These products are Voigt functions [VOI 12], the expression of which is given below. Note that the convolution product of several Voigt functions is a Voigt function and therefore the experimental profile can be accurately described by this type of function.

$$V(2\theta) = \beta_G^{-1}\,\mathrm{Re}\left[\mathrm{erfc}\left(\frac{\sqrt{\pi}}{\beta_G}|2\theta - 2\theta_h| + i\frac{\beta_L}{\beta_G\sqrt{\pi}}\right)\right] \qquad [3.10]$$

where:

– Re: real part of a complex function;

– erfc: complex error function;

– β_G and β_L: integral breadths of the Gaussian and Lorentzian components.

The Voigt function is known to be a very good description of the diffraction peaks, however, it is a difficult function to program and pseudo-Voigt functions are often used [WER 74]; these are linear combinations of Gaussian and Lorentzian functions:

$$pV(2\theta) = \eta L(2\theta,H) + (1 - \eta)G(2\theta,H) \qquad [3.11]$$

where L and G are the Gaussian and Lorentzian components and H is the full width at half maximum.

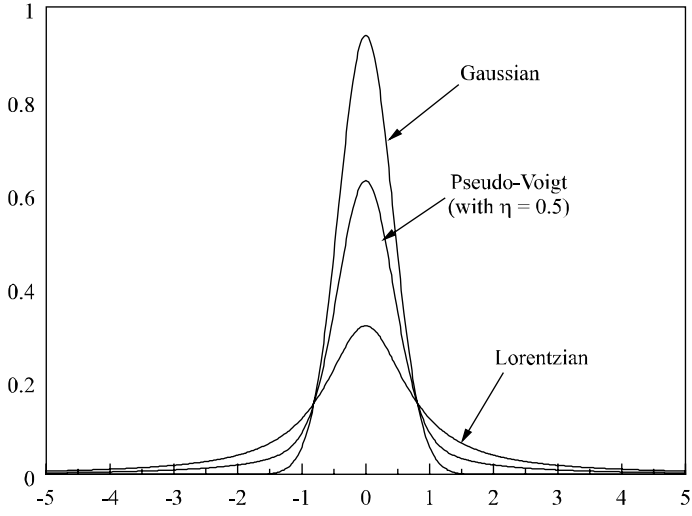

Figure 3.9. *Gaussian, Lorentzian and pseudo-Voigt functions*

An illustration of the shapes of these different profiles is shown in Figure 3.9. When the parameter η of the pseudo-Voigt function varies, we change continuously from a Lorentzian function to a Gaussian function. The relative contributions from the various instrumental aberrations change with the diffraction angle, so the peak profiles change in a given diffraction diagram. They will often be strongly Gaussian at low angles and more Lorentzian at high angles. In practice, if the value of η varies depending on the value of θ, this evolution can be accounted for. This implies that they can also be accounted for with Voigt functions.

Langford [LAN 78] introduced a parameter that described rather well the shape of the peaks. This parameter is the ratio between the full width at half maximum and the integral breadth or:

$$\phi = \frac{H}{\beta} \qquad [3.12]$$

When the experimental peaks are fitted with Voigt functions, the evolution of ϕ characterizes the shape of the peaks as more or less Gaussian (or Lorentzian).

If the profile is completely Gaussian, we have:

$$\phi = 2(\log 2/\pi)^{1/2} \approx 0.9394 \qquad [3.13]$$

If the profile is completely Lorentzian, we have:

$$\phi = 2/\pi \approx 0.6366 \qquad [3.14]$$

The case of dissymmetric functions

Some of the peak deformations caused by the device correspond to dissymmetric profiles. Therefore, the diffraction peaks are theoretically always dissymmetric. Although this effect can sometimes be neglected, some authors have come up with fitting functions that have a dissymmetric shape.

The method most commonly used consists of considering that each diffraction peak corresponds to two half-Pearson VIIs or two half pseudo-Voigts; each one defined on one of the two sides of the peak's maximum. This is called a "split-Pearson VII" or a "split pseudo-Voigt". The parameters that characterize each of the parts of the profile are independent and the resulting overall function is dissymmetric.

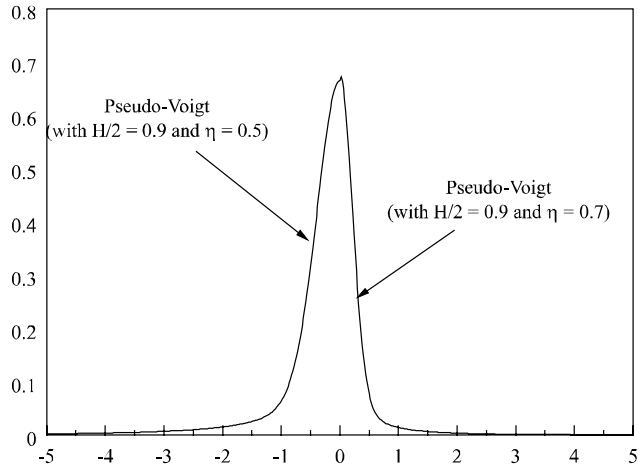

Figure 3.10. *Dissymmetric fitting profile, use of a split pseudo-Voigt*

Another possibility consists of truncating an initial function on both sides of its maximum and describing the profile in the two additional domains thus created by a function with another expression. An example of such a profile is shown in Figure 3.11. A Gaussian function is truncated on the left and on the right of its center, with its extreme portions defined by exponential expressions.

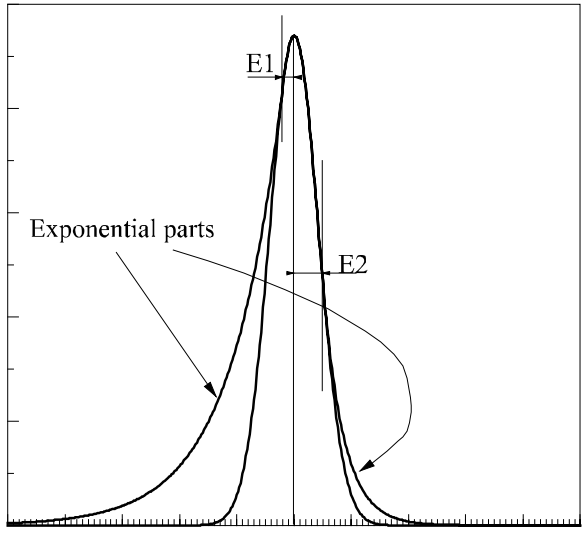

Figure 3.11. *Dissymmetric fitting profile, use of a truncated Gaussian function*

3.3.1.2. *Functions calculated from the physical characteristics of the diffractometer*

A new approach to diffraction peak fitting appeared few years ago. It still consists of trying to make a calculated graph and an experimental peak coincide as best as possible but, this time, the calculated graph is defined according to the physical characteristics of the device used [CHE 92, CHE 04].

If the diffractometer used is known, it is possible to generate the instrumental function by successive convolutions of the various elementary contributions. In that case, the parameters that can vary in the refinement are the device's physical parameters (divergence, transparency, widths of the slits, width of the source, etc.). An illustration of this kind of process is shown in Figure 3.12. The fitted pattern can be found in Figure 3.5. The fitting was obtained by setting the divergence of the beam, the transparency of the sample and the size of the source to their known values [MAS 01].

This process is particularly efficient when conducting microstructural studies by X-ray diffraction (see Part 2 of this book), but is particularly difficult to implement and it requires a very good knowledge of the equipment used. Since the end of the 1990s, some manufacturers have integrated it into their software.

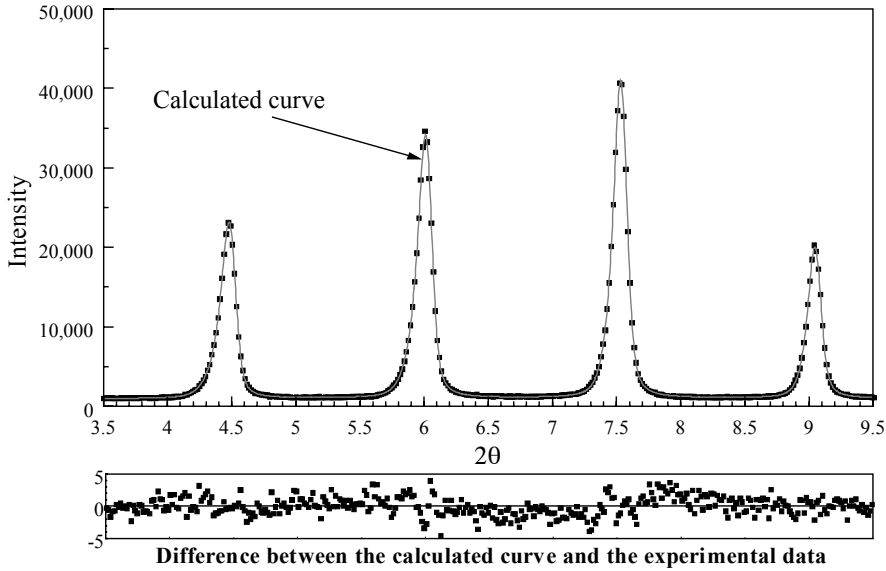

Figure 3.12. *Fitting of the pattern produced with the silver behenate by using functions generated from the diffractometer's physical parameters [MAS 01]*

3.3.2. *Quality standards*

Let us imagine that we have a diffraction diagram and that we have chosen the function that best describes the peak profiles. We still have to adjust the parameters that define this function in order to minimize the discrepancies between the measured peaks and the fitting functions. Generally speaking, this type of problem is most often solved by minimizing the sum of the square differences between the measured values and the calculated values, a process which is referred to as "least square refinement". Clearly, for a given peak or group of peaks, there can be several solutions that give minimum values of this sum of square differences. Therefore, this approach does not yield one solution but several, among which the user will have to choose the most reasonable one, from a physical point of view.

Refinements are performed by using successive calculations. It is important to be able to judge the quality of the refinement at every step of the process. There are various mathematical criteria which make it possible to evaluate this quality and its evolution. Two "reliability factors" can be used and they are expressed as follows:

$$R = \left[\frac{\sum \left(I_{2\theta_i}^{obs} - I_{2\theta_i}^{calc} \right)^2}{\sum \left(I_{2\theta_i}^{obs} \right)^2} \right]^{0.5} \qquad [3.15]$$

$$R_{wp} = \left[\frac{\sum \left[w_{2\theta} \left(I_{2\theta_i}^{obs} - I_{2\theta_i}^{calc} \right)^2 \right]}{\sum \left[w_{2\theta} \left(I_{2\theta_i}^{obs} \right)^2 \right]} \right]^{0.5} \qquad [3.16]$$

The use of factor R_{wp} (weighted residual error) makes it possible to associate each intensity in a point $2\theta_i$ with a weight that is inversely proportional to the number of counts measured at that point ($w_{2\theta i} = 1/I_{2\theta i}$). Therefore, this quality factor takes into account points that correspond to low intensity values as well as points that correspond to high values, which makes this parameter is a good indicator of the refinement quality for the peak tails.

Naturally, the values of these factors tend to zero when the calculated pattern fits the measurements accurately. However, in practice, this zero value is never achieved and, usually, a coefficient R_{wp} between 2 and 10% indicates a good result. Note that R and R_{wp} directly depend on the intensity measured, and hence on the exposure time chosen for the study.

Factor R_{exp} (expected error), which is based on counting statistics, is an estimate of the minimum possible value of R_{wp}.

$$R_{exp} = \left[\frac{N - P}{\sum \left[w_{2\theta} \left(I_{2\theta_i}^{obs} \right)^2 \right]} \right]^{0.5} \quad [3.17]$$

N being the number of observations and P the number of refined variables. The quality of the fitting can be estimated by comparing the values of factors R_{wp} and R_{exp}.

We can also use another factor which accounts for the number of variables used during the refinement process. This factor, called GofF (Goodness of Fit), is given by the relation written below and it makes it possible to assess the influence of adding new variables to the refinement process. A change in the peak profile or the introduction of an additional peak in the fitting zone leads to a modification of the number of refined parameters. Therefore, this factor shows whether introducing new variables can decrease the residual error.

$$GofF = R_{wp}/R_{exp} \quad [3.18]$$

3.3.3. *Peak by peak fitting*

In this type of study, the peaks are fitted independently from one another, either one by one or in groups when they partially overlap. This is referred to as peak by peak fitting. This method is the most commonly used, since it is very flexible and can be used to deal with a large number of situations.

The different steps of this process are illustrated in Figure 3.13. The preliminary step consists of defining, for each portion of the diagram, the number of diffraction peaks that it contains. Then, a fitting function is chosen, one that corresponds as best as possible to the shape of the peaks in question. A function is generated for each identified peak. The sum graph, which corresponds to all of the contributions from the peaks in the considered portion, is then calculated. It is the discrepancies between the points of this graph and the experimental points that are minimized by changing the values of the various parameters that define the graphs calculated for each peak. Once the fitting is over, the resulting calculated graph is extracted for each peak.

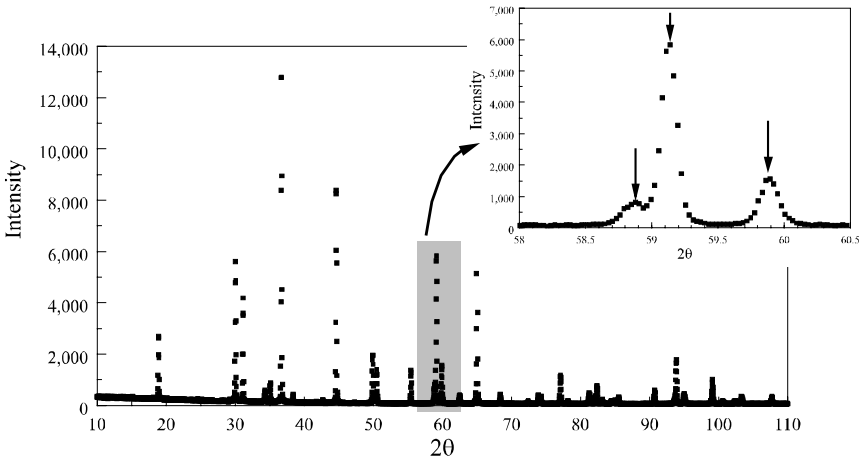

Figure 3.13a. *Unprocessed diagram*

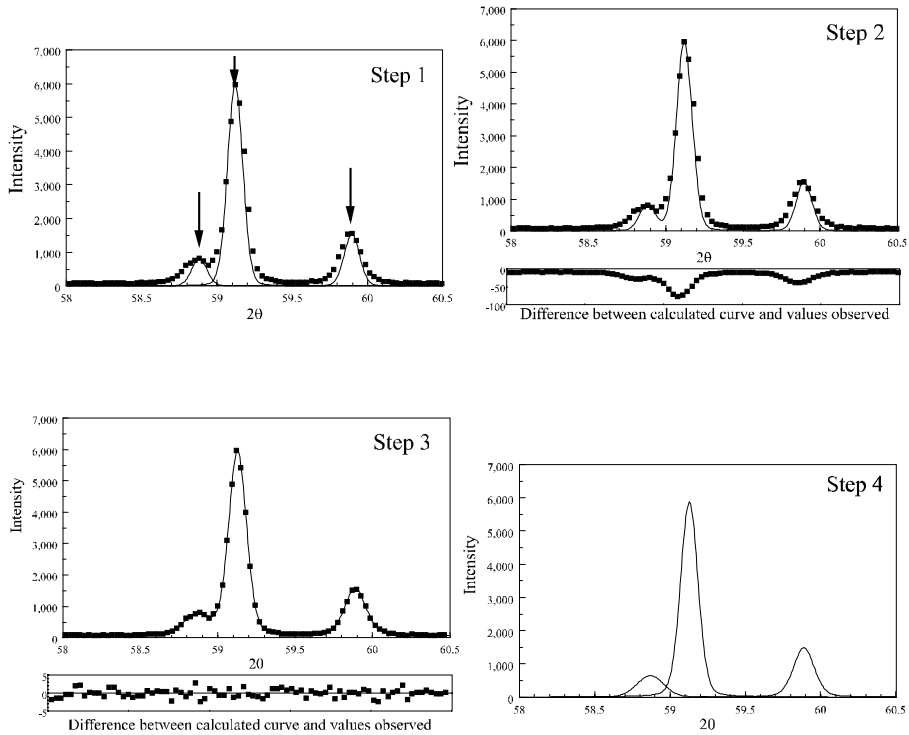

Figure 3.13b. *Methodology of peak by peak fitting*

Peak by peak analysis is widely used in X-ray diffraction and significant developments in digital calculations have made it possible to define very precisely the actual peak profiles. It sometimes happens, however, that the peaks overlap too much for it to be possible to separate their contributions. It then becomes necessary to provide additional information which makes it possible to correlate either the relative positions of the different peaks or their intensities. This is referred to as whole pattern fitting.

3.3.4. *Whole pattern fitting*

3.3.4.1. *Fitting with cell constraints*

This approach consists of correlating the position of the peaks with each other. In this method, we consider a Bravais lattice and set approximate values for the cell parameters. The changes in peak positions are made by modifying these cell parameters. It is easy to understand, in this case, that the position of each peak strongly depends on the positions of the other peaks.

The refinement method is the same as the one used in peak by peak fitting and the calculated profiles are chosen in the same way. Usually, the diagram is simultaneously refined over a large angular range, in order to significantly restrict variations in peak positions. Note that, with this approach, the values of the cell parameters can be directly determined.

3.3.4.2. *Structural simulation: the Rietveld method*

This comprehensive method to analyze the diffraction pattern consists of correlating the variations not only in peak positions, but also in their integrated intensities. We saw in Chapter 1 that the diffracted intensity is proportional to the square modulus of the structure factor. Therefore, this intensity is related to the positions and the nature of the atoms. We will describe this aspect in detail in Chapter 4, but we can already mention that if the chemical composition of the phase is known and if we wish to suggest a space group for this phase, it is possible to generate the value of the integrated intensity for each peak defined this way. Any variation in the position of an atom or a modification of the occupation rate of a site or of a thermal agitation coefficient causes variations in the integrated intensities of several peaks. In a Rietveld refinement, the integrated intensities of the diffraction peaks are refined by slightly varying the positions of the atoms, the occupation rates and the thermal agitation factors.

Unlike in the peak by peak method, each point is considered as a point. This method, named after its creator, was first suggested in 1967 [RIE 67, RIE 69]. It has attracted significant attention and its implementation in the determination of crystal

structures by X-ray diffraction on polycrystalline samples among other fields has been described in several books [YOU 93, DAV 02].

As we have already mentioned, each point of the diagram is considered and the refinement method consists of minimizing the following expression:

$$R = \sum w_i \left(y_i^{obs} - y_i^{calc} \right)^2 \qquad [3.19]$$

with:

– y_i^{obs} : intensity observed at point i;

– y_i^{calc} : intensity calculated at point i;

– w_i: coefficient that depends on the counting coefficient.

Each value of y_i can be caused by several Bragg peaks, so:

$$y_i^{calc} = \sum_{hkl} I_i(hkl) \qquad [3.20]$$

As we have already mentioned, experimental patterns include a continuous background resulting from the machine (electronic noise, scattering by the air, scattering by the slits, etc.) and the sample (incoherent scattering, fluorescence, amorphous phase, disorder, etc.). Therefore, the calculated intensity at point i of the pattern is described by the equation:

$$y_i^{calc} = y_i^b + \sum_{k=1}^{k=n} G_{ik} I_k \qquad [3.21]$$

with:

– y_i^b : intensity of the continuous background;

– G_{ik}: function that describes the peak profiles;

– $k_1, k_2, \ldots, k_n$: the reflections that contribute to the intensity in point i.

There are several ways of accounting for the background noise. It can be described by linear interpolation between selected points located between diffraction peaks, or by polynomial interpolation over the entire pattern. An accurate determination of the continuous background is relatively important since it affects the simulation of the tails of the diffraction peaks. Since the early 1990s, some

authors [RIE 95a, RIE 95b, RIE 98] have suggested simulating the continuous background by using functions that express the incoherent scattering, the coherent scattering by the amorphous part of the sample and the scattering by the air. This particularly efficient method is useful, for example, when the sample is a combination of an amorphous phase and crystals [RIE 98].

The choice of a function to describe the peak profiles is, of course, a fundamental element of fitting. The Rietveld method was initially designed for the fitting of neutron diffraction diagrams. As we have already mentioned, in this case, the peaks are accurately described by Gaussians, which is why the first computer programs used these functions. However, as we have seen, they are not well suited for expressing the shapes of X-ray diffraction peaks, hence the introduction of more complex profiles for structural refinements. In most cases, pseudo-Voigts or Pearson VIIs are used. Voigt functions are also quite suitable; however, they require a significant amount of calculation time, even more so than for peak by peak fitting, which is why the functions were only recently added to these programs [AHT 84, WU 98].

The shapes of the peaks change with the diffraction angle because, among other things, the deformation effects caused by the machine are functions of θ. Therefore, for this whole pattern refinement method it is necessary to use a peak profile describing function with a mathematical expression that varies with θ. This condition is met, for example, by the pseudo-Voigts if parameter η is a function of θ.

As we have already mentioned, one of the characteristic parameters of a peak's profile is its full width at half maximum. We saw that this width generally increases with the angle and that this evolution can, most of the time, be accurately described by a second degree polynomial in tangent θ (the Caglioti polynomial). In a Rietveld refinement, the parameters U, V and W are refinable. Their values express both the instrumental resolution function and the microstructural characteristics of the sample. We will discuss this point further in Part 2 of this book.

Implementation of a Rietveld refinement

The coincidence between the experimental and calculated patterns is obtained in the same manner as when fitting one or several peaks, as described above. The quality of the refinement is likewise estimated by using the reliability factors we defined.

The evolution of one or another of the parameters affects the entire calculated pattern. Therefore, the scope of variations in the values of the various refinement parameters is small and, most importantly, interdependent. The parameters are said to be constrained. During the refinement, the person conducting the experiment can include additional constraints, for example, imposing that the sum of two occupation

rates be equal to 1, etc. This situation, by greatly reducing the amplitude variations, is what makes it possible to determine a structure.

Although this method is efficient, it cannot directly tell us whether the result actually corresponds to the crystal structure that is being studied, since the number of mathematical solutions that minimize the gaps between the experimental pattern and the calculated one is very large. In order to properly deal with this problem, it is important to work according to a carefully planned refinement strategy.

These refinement strategies are the subject of wide debates [CUS 99], but some ideas should be kept in mind. During the first refinement cycle, only the scale factor and the continuous background are refined. The position of the peaks is then obtained by refining the cell parameters, since the atomic parameters are now set at constant values. The person conducting the experiment will then attempt to determine the right peak profile for describing the shapes of the experimental peaks, and determine one by one the parameters U, V and W that describe the behavior of the full width at half maximum according to the diffraction angle. Then, the actual structural refinement can finally begin. It consists of optimizing the position of each of the atoms, the occupation rates and the thermal agitation factors specific to each of the crystallographic sites.

At each step of the fitting the calculated and the experimental patterns as well as the difference between the two, can be visualized, which helps to avoid mistakes and particularly to find out if the refinement is straying toward an incoherent suggestion.

3.4. The resulting characteristic values

The processing of diffraction diagrams makes it possible to extract three essential values from each peak:

– the angular position;

– the integrated intensity;

– the intensity distribution.

Precisely determining one or another of these values requires taking precautions specific to the machine used. We will see in Chapter 4 that, depending on the information sought, one or several of these parameters have to be determined. The experimental conditions associated with the production of diffraction patterns are directly related to the information we wish to extract. In this section, we will give more details on the acquisition conditions and on the adequate processing methods for measuring each of these values.

3.4.1. *Position*

Peak positions, which correspond to the values of the diffraction angles, are the most commonly used information in the interpretation of diffraction patterns , since they make it possible to determine the material's specific interplanar distances with the use of Bragg's law ($n\lambda = 2d \sin\theta$).

Generally speaking, it can be shown that the accuracy of a diffractions peak's position increases with the diffraction angle. In fact, Bragg's law is written $n\lambda = 2d \sin\theta$ and therefore:

$$0 = 2 \sin\theta\, \delta d + 2d \cos\theta\, \delta\theta \Rightarrow \frac{\delta d}{d} = -\cot g\theta \delta\theta \qquad [3.22]$$

For a given non-zero $\delta\theta$, we have:

$$\frac{\delta d}{d} = 0 \Leftrightarrow \cot g\theta\, \delta\theta = 0 \Leftrightarrow \theta = 90 + k\pi \qquad [3.23]$$

This means that a given error in the measurement of θ will lead to an error on d that decreases when θ gets closer to 90°. Likewise, if we consider a set distance d, but a wavelength that can vary slightly, we get:

$$\lambda = 2d \sin\theta \Rightarrow 2d \cos\theta\, \delta\theta = \delta\lambda \qquad [3.24]$$

For a given non-zero $\delta\lambda$, $\delta\theta$ increases with $\frac{\delta\lambda}{2d\cos\theta}$.

$$\Rightarrow \cos\theta = 0 \Rightarrow \theta = 90 + k\pi \qquad [3.25]$$

Separating two peaks that correspond to the same family of planes but to different wavelengths will become easier as θ gets closer to 90° ($K_{\alpha 1}$-$K_{\alpha 2}$ separation).

Regardless of what type of device is used, when the desired accuracy for the interplanar distances is very high, a control sample with perfectly well known interplanar distances has to be incorporated into the sample studied. After taking note of this control sample's characteristic peaks, the user simply has to correct accordingly the peak positions of the sample being studied with respect to those of the control sample.

3.4.2. *Integrated intensity*

Quantitative energy measurements of the integrated intensities of the diffracted peaks rely essentially on the quality of the fitting. Particularly, the fitting function has to coincide as best as possible with the experimental profile. Figure 3.14 illustrates this issue. The same diffraction peak was fitted with a Gaussian, a Lorentzian and a Voigt function. The best agreement was obtained for the Voigt function. The Lorentzian function fitting leads to an error of over 5% for the value of the integrated intensity.

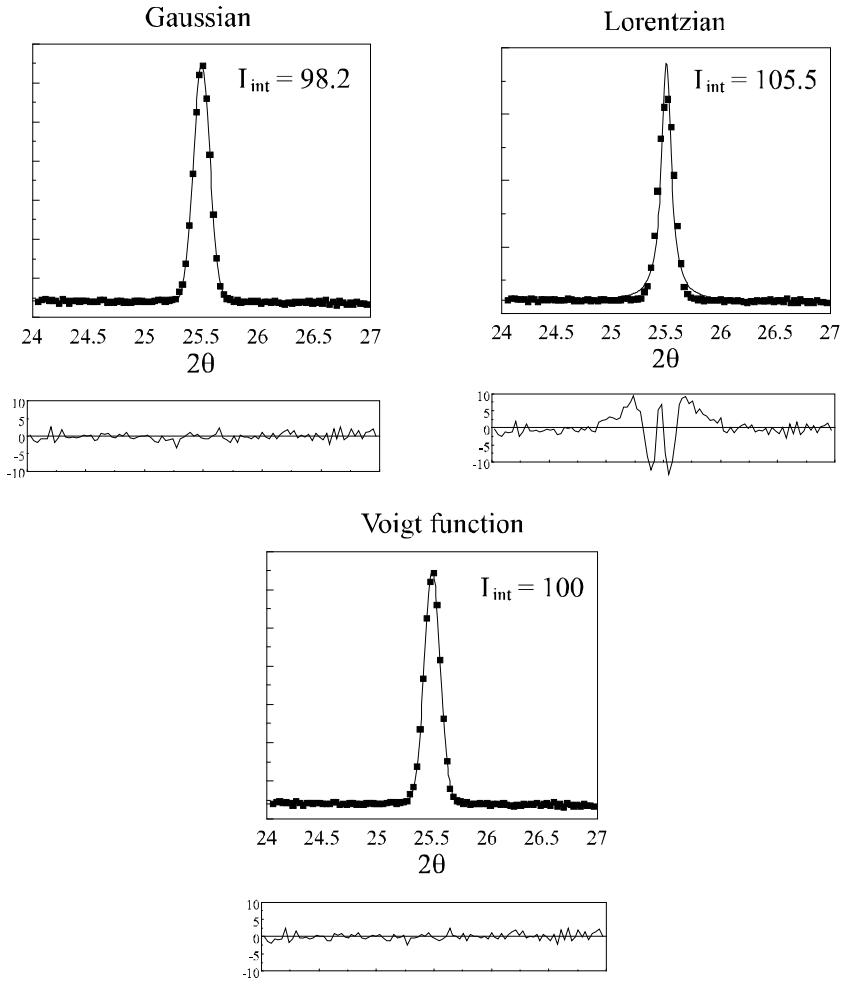

Figure 3.14. *Influence of the fitting function choice on the value of the integrated intensity*

Determining the integrated intensity becomes particularly difficult when the peaks partially overlap. A careful choice of fitting functions can somehow make it possible to properly deal with this issue and to separate the contributions of each peak. This is illustrated by Figure 3.15.

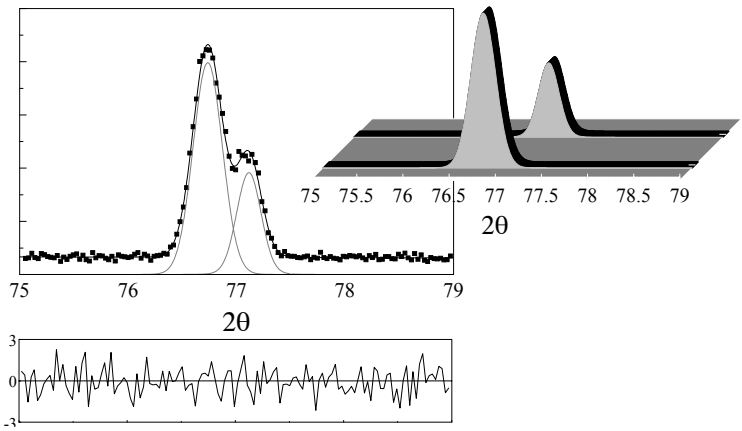

Figure 3.15. *Extraction of the integrated intensity for two partially overlapped peaks*

3.4.3. *Intensity distribution: peak profiles*

The study of the intensity distribution can be achieved by two methods: either by fitting this peak with a calculated function or by a direct analysis using the Fourier transform of that peak. The fitting requires prior knowledge of the profile, which, by definition, can never exactly correspond to the experimental profile, and the Fourier analysis can only be achieved if the peaks do not overlap. These aspects will be discussed further in Part 2 of this book, which deals with microstructural analysis.

The analysis of peak profiles generally requires a very high signal-to-noise ratio, hence long acquisition times for the diagrams. The number of measured counts is often in the range of hundreds of thousands for intense peaks and cannot be below tens of thousands for secondary peaks.

The essential application of peak profile analysis involves the microstructural studies of the samples, which means that the machine's contribution has to be as small as possible. Digital processing techniques make it possible to properly extract the pure profile, but the quality of the study is higher if the widening of the peaks is essentially due to the sample. In practice, for this type of study, high resolution diffractometers are chosen, since their instrumental function can be very accurately determined.

This page intentionally left blank

Chapter 4

Interpreting the Results

Along with optical and electron microscopy, X-ray diffraction is most certainly one of the most commonly used techniques for characterizing materials. So, clearly, the physical effect of diffraction can be put to use for many different types of studies, making it impossible to imagine a complete review of all the applications of X-ray diffraction or scattering. In this chapter, we will present the most common applications. We will start with methods for determining crystalline phases in an unknown sample, then we will discuss procedures for quantitative phase analysis. In a third part, we will deal with methods for identifying crystal systems and refining cell parameters. Finally, the fourth part deals with the basic elements of structural analysis. This final aspect has seen tremendous developments over the past 20 years. The goal here is only to describe the main ideas and to give references to readers who might want to look further into these questions. The quantitative microstructural study of imperfect materials constitutes a specific part of the X-ray diffraction applications. Understanding these methods requires a careful description of the diffraction signal. Microstructural analysis, in the same way as structural analysis, has become a technique of its own. The basics and the methods used for microstructural analysis through X-ray diffraction will be described in detail in Part 2 of this book.

4.1. Phase identification

We saw in Chapter 1 that the nature and the positions of the atoms have a direct effect on the intensity of the diffraction peaks. Likewise, the interplanar distances, and hence the positions of the diffraction peaks, are directly related to the values of the cell parameters. This shows that the list of relative intensities and interplanar

distances is a feature specific to each crystalline phase. The identification of the crystalline phase, or of the phases, present in the material is achieved by comparing the pairs (d_i,I_i), comprised of the interplanar distances and the relative intensities obtained for each peak from the experimental pattern with a file that contains this list for every phase that has been documented.

The first studies that involved this type of quantitative analysis were conducted by Hanawalt and his colleagues [HAN 36, HAN 38]. A first file, containing the interplanar distances and the relative intensities for every known phase, was compiled by the American Society for Testing Materials (ASTM) as early as 1942 and several modifications followed since. In 1969, the Joint Committee on Powder Diffraction Standards (JCPDS) was given the task of continuously updating this file. In 1977, this committee changed its name to the International Center for Diffraction Data (ICDD). This organization manages a file (the PDF, short for Powder Diffraction File) which currently contains over 70,000 entries.

For each known phase, an entry is added, that constitutes some kind of ID for that phase. Such an entry is shown in Table 4.1 and it includes, for each characteristic peak, the values of the interplanar distances, the integrated intensities and the Miller indices. Also, the crystal system, the cell parameters and the space group are mentioned. Generally, bibliographical information is included to specify the reference to the publication the entry was based on.

The comparison between the list of pairs (d_i, I_i) that were measured and the reference values is done with the help of adequate software. There are several methods[1], which often consist of considering the most intense peaks and searching for phases that present these peaks in the decreasing order of intensity obtained. Generally, the user knows something of the material's chemical nature, which makes it possible to restrict the scope of his investigation. The identification of the possible phases can be achieved from the three most intense peaks [HAN 38]. The list of peaks observed experimentally is then compared with the complete entries from the JCPDS. A definite conclusion can only be reached if all of the experimental peaks have been assigned and if the pattern produced contains every peak (except maybe for low intensity peaks) mentioned in the entries that correspond to the phases that were considered.

1 The methods used to compare experimental results and the characteristics of known crystal phases have been described in detail in other books. Readers who wish to study this aspect further can refer in particular to Jenkins and Snyder [JEN 96] or to the more recent book by Pecharsky and Zavalij [PEC 03].

27-997 JCPDS-ICDD Copyright 1988 Quality:	d (Å)	Int.	h k l
ZrO_2			
Zirconium oxide	2.93	100	1 1 1
	2.55	25	2 0 0
Rad: CuKα Lambda: 1.5418 Filter: Ni	1.801	50	2 2 0
Ref: Katz, *J.Am.Ceram.Soc*. 54, 531 (1971)	1.534	20	3 1 1
	1.471	5	2 2 2
	1.270	5	4 0 0
Sys: Cubic S.G.: Fm3m (225)	1.167	5	3 3 1
a:5.05 b: c:	1.135	5	4 2 0
α: β: γ: Z:4	1.038	1	4 2 2
	0.9796	1	5 1 1
	0.8999	1	4 4 0
Dx: 6.205	0.8604	1	5 3 1
Unit cell data: Cuver and Odell, *J.Am.Ceram.Soc*. 33, 274 (1950)	0.8048	1	6 2 0
Electron microscopy study of epitaxial grown thin film of ZrO2 (R.A. Ploc, *Proc. 7th Am. Meeting of Microscopy Soc. Canada* Vol. VII, 34 (1980) give a = 5.135(5) CaF2 PSC: cF12. To replace 14-534 and 7-337			
Strong lines: 2.93/x 1.80/5 1.53/2 1.47/1 1.27/1 1.17/1 1.14/1			

Table 4.1. *Example of a JCPDS entry*

In the past few years, a new method was developed [CAU 88]. It consists of directly modeling the pattern without determining beforehand the interplanar distances and the relative intensities. A calculated pattern is generated by gradually adding the contributions of the different possible phases. By adjusting the calculated pattern with the experimental data, the validity of the suggested phase combinations can be tested. This method seems to be particularly efficient.

There is an index published as a book every year which contains the list of all the substances, arranged with respect to their three most intense peaks and another list arranged in alphabetical order. This document can often be used to identify possible phases manually and it constitutes a good complement to computerized methods.

4.2. Quantitative phase analysis

When the nature of the material's crystalline phases is known, the volume of each of the phases present can be determined. We saw in Chapter 1 that the integrated intensity of each peak in a given phase is directly proportional to the volume of the phase. Therefore, quantitative phase analysis is performed from the very precise measurement of these integrated intensities. Quantitative phase analysis should not be confused, of course, with the quantitative chemical analysis which is used to determine the amount of each element present in a sample. The first quantitative phase analysis by X-ray diffraction was conducted in 1925 on a ceramic material, in order to determine the amount of mullite in burned clays [NAV 25]. Despite the fact that this type of quantitative measurement has existed for 80 years, these analyses remain very difficult to conduct [BIS 89, TOR 99a, TOR 99b] and require experimental precautions which we will now discuss. However, we should point out that X-ray diffraction is virtually the only method available for quantitative phase analysis[2].

4.2.1. *Experimental problems*

4.2.1.1. *Number of diffracting grains and preferential orientation*

As we have said, the diffracted integrated intensity is proportional to the quantity per volume of the phase. However, in a polycrystalline sample irradiated with a

2 This type of study can also be achieved with neutron diffraction. The method is the same as the one we will describe, but neutron diffraction studies are, of course, much more cumbersome to implement than those involving X-ray diffraction. Note that the volume studied in neutron diffraction is much larger than in X-ray diffraction, which is why it can be used to study the core of bulky samples.

monochromatic beam, only the crystals in the Bragg position diffract. We expressed the integrated intensity diffracted by a polycrystalline sample by considering that the tips of the normals to the families of diffracting planes form a spherical cap (see Chapter 1). This means we have to assume that, for every family of characteristic planes, a large number of grains diffract. It is therefore necessary that the sample is comprised of a very large number of crystals and, additionally, that these crystals have random orientations. This double condition is often difficult to meet and is the major source of errors in quantitative phase analyses [ELT 96].

This problem, which is common to all X-ray diffraction by polycrystalline samples, has been widely studied for over 50 years [ALE 48, WOL 59, ELT 96]. It can be illustrated in different ways. Figure 4.1 shows a study conducted on silicon powders that illustrates this problem [WOL 59, PAR 83]. Various samples of silicon powder, arranged in order of increasing crystal size, were produced. For each of the samples, the authors measured the integrated intensity of the (111) peak according to the sample's rotation around its normal axis (ϕ rotation).

When the size of the grains is smaller than 5 μm, the integrated intensity is constant over the course of the ϕ rotation. For crystals with diameters between 5 and 10 μm, the intensity fluctuations are smaller than 10%. They become larger when the crystals are greater than 10 μm in size. Since the irradiated volume is set, the number of crystals decreases as their size increases. Therefore, Figure 4.1 is a direct illustration of the influence of the number of grains on the measurement of the integrated intensity.

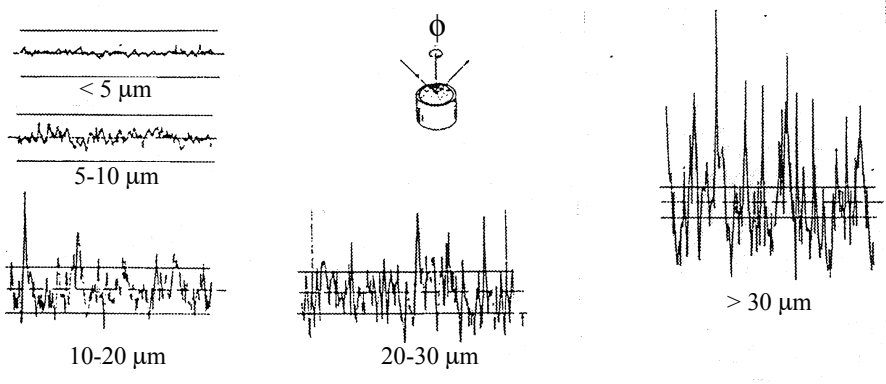

Figure 4.1. *Evolution, for different grain sizes, of the intensity diffracted by the family of planes (111) of a silicon powder sample over the course of its rotation around the axis normal to its surface [PAR 83]*

The irradiated volume is determined by the area of the beam's cross-section, the beam's incidence angle with the sample and the X-ray penetration depth in the sample. For most inorganic materials, this penetration depth is in the range of micrometers or tens of micrometers. The beam's cross-section and the incidence angle depend on the equipment used. Generally speaking, it is possible, however, to consider that for most diffractometers, the number of grains will be high enough if their size does not exceed 10 μm. The experiment described in Figure 4.1 shows the variations of the integrated intensity according to the ϕ rotation. A commonly used method for increasing the number of diffracting crystals is to rotate the sample around the normal to its surface during the acquisition of the pattern. Modern diffractometers are often equipped with this type of continuous rotation. An alternative is to make the sample oscillate around the axis ω, in other words to alternatively vary the incidence angle. The variations are usually in the range of a degree [BER 55]. This approach was very recently used again [SAR 05a] to compensate for the small size of the irradiated zone with a system equipped with a microsource (see Chapter 2).

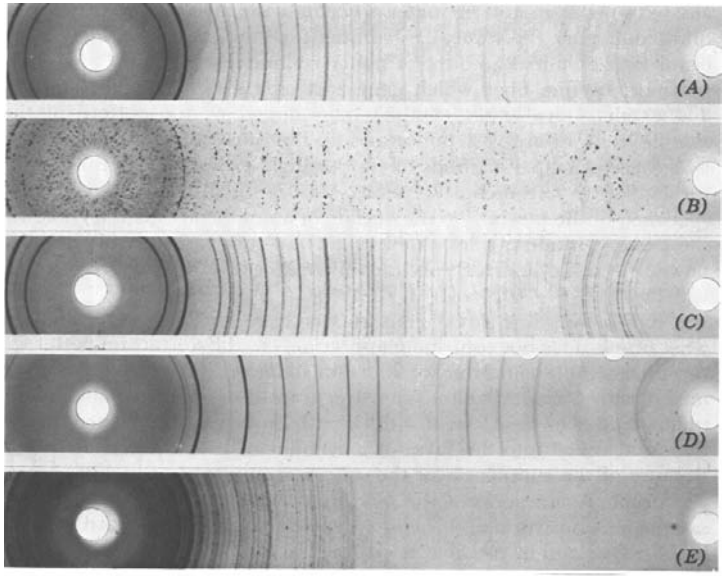

(A) Quartz powder < 5 μm, motionless sample; (B) quartz powder 15 μm-50 μm, motionless sample; (C) quartz powder 15 μm-50 μm, rotating sample; (D) NaCl powder (cubic) < 45 μm, rotating sample; (E) Feldspath powder (monoclinic) < 45 μm, rotating sample

Figure 4.2. *Observation of the influence of the number of grains on diffraction rings [KLU 74]*

Figure 4.2 shows another illustration of the problems related to the number of diffracting grains [KLU 74]. Different samples were studied using a diffractometer equipped with a photographic film detector. For each sample, a series of diffraction arcs is observed. Sample A is comprised of a fine grain quartz powder and its arcs are continuous and well defined. The quartz crystals in sample B are larger, which means that there are fewer of them in the irradiated volume. The diffraction arcs are no longer continuous and they form pointed lines. If the study of this sample is conducted while continuously rotating the sample holder around the axis ϕ, which we have already defined, we observe in case C that the diffraction arcs are continuous again. This result illustrates the fact that the rotation around ϕ increases each crystal's probability of being in the Bragg position and therefore increases the number of diffracting grains.

The last two films illustrate the influence of the multiplicity factor on the diffraction arcs. For a highly symmetrical crystal (which is the case for NaCl), the multiplicity factor of each peak is high, meaning that the number of families of planes that contribute to a given peak is larger than when symmetry is low (which is the case for Feldspath crystals).

In the previous sections, we discussed the influence of the number of crystals in the sample. The orientations of the crystals were assumed to be random, and obviously, this factor comes into play. Theoretically, quantitative analyses by X-ray diffraction are conducted on samples comprised of a very large number of micrometric crystals without any preferential orientation. This latter condition is sometimes difficult to meet, since it can be sometimes complicated to give the crystals in the sample a random orientation. This effect often occurs when crystals have an anisotropic shape. Clays are an extreme example of this behavior [BRI 80]. Their layered structure naturally causes a preferential orientation along the (00l) planes. Some authors [FLO 55, SMI 79, HIL 99] have used atomization methods to produce polycrystalline particles in which the clay crystals have a random orientation. Another approach consists of quantifying the preferential orientation and to take it into account when calculating the proportions of the phases in the sample. We will not be giving any details on this method, since it requires considerable skill in the production of pattern and data analysis. It is always better not to have a preferential orientation.

4.2.1.2. *Differential absorption*

The diffraction pattern of a phase which is obtained with a sample that contains several of them is not exactly what would be obtained if the sample contained only the phase in question. The intensity of the X-ray beam diffracted by the grains of the phase we are focusing on is modified by the absorption from the matrix surrounding these grains. Since the phases in the matrix have different absorption coefficients,

this effect disrupts the measurements. The farther apart the absorption properties of the different phases are, and hence their atomic number, the greater the magnitude of this effect. The influence of this absorption difference on the measurement of the diffracted intensity depends on the microstructure and, in particular, on the size of the crystals and their positions inside the sample [BRI 45].

The most common solution to this problem consists of introducing in the sample we wish to analyze a known amount of a crystal phase which is not found in the initial sample. The intensities are then measured for the various characteristic peaks of the phases we want to quantitatively analyze. The intensities of the control sample's diffraction peaks are affected by the absorption in the same way all the others are. The same study is then done on a control sample containing all of the crystalline phases found in the studied sample, but in known amounts and with the addition of the same amount of control powder. Let I_i be the intensity of a peak obtained in the unknown sample for a given phase i and $I_i(T)$ the one obtained in the test sample; then, for any phase i, we have:

$$\frac{I_i}{I_i(T)} = \alpha \frac{X_i}{X_i(T)} \qquad [4.1]$$

and in particular:

$$\frac{I_e}{I_e(T)} = \alpha \frac{X_e}{X_e(T)} \qquad [4.2]$$

where the index e indicates the control powder. Therefore we have:

$$\alpha = \frac{I_e X_e(T)}{I_e(T) X_e} \qquad [4.3]$$

We thus determine α and then all of the X_i values.

4.2.2. *Methods for extracting the integrated intensity*

4.2.2.1. *Measurements based on peak by peak fitting*

We saw in Chapter 3 that the integrated intensity can be determined with peak by peak fitting of the diffraction peaks. In the case of quantitative phase analysis,

the fitting has to be done carefully, as illustrated by Figure 3.14, hence the necessity of properly choosing the fitting function used.

The peak by peak fitting method is commonly used for this type of study because, since the fitting of each peak is completely independent and the calculated profiles can be adapted as best as possible, thus taking into account the possible differences in peak shapes between the various phases (microstructural effects).

4.2.2.2. *Measurements based on the whole fitting of the diagram*

When the pattern produced contains a large number of peaks, or when the peaks are wide, it becomes difficult to separate the contributions from each diffraction peak. Since the late 1980s, several authors have suggested using the Rietveld method to conduct quantitative phase analyses in these cases [BIS 88, BIS 93, HIL 87, TAY 91].

Since the various crystalline phases found in the sample are known, it is possible to generate for each one of them a calculated pattern. The experimental pattern corresponds, naturally, to the sum of all the patterns associated with each phase. Therefore, this sum pattern is calculated, and the refinement between the calculated points and the experimental points is achieved without modifying the structure parameters of each phase. Thus, we obtain the proportions of the different phases directly. When the agreement between the experimental values and the calculated values is almost complete, it is possible to refine the cell parameters and the atomic positions.

This method is particularly efficient [HIL 00] and has been widely implemented in the past few years. It is however necessary to have a good knowledge of the structures of the phases in the sample. Additionally, in this type of study, the number of refinement parameters can be very large, which means that the refinement strategy has to be carefully defined [CON 00].

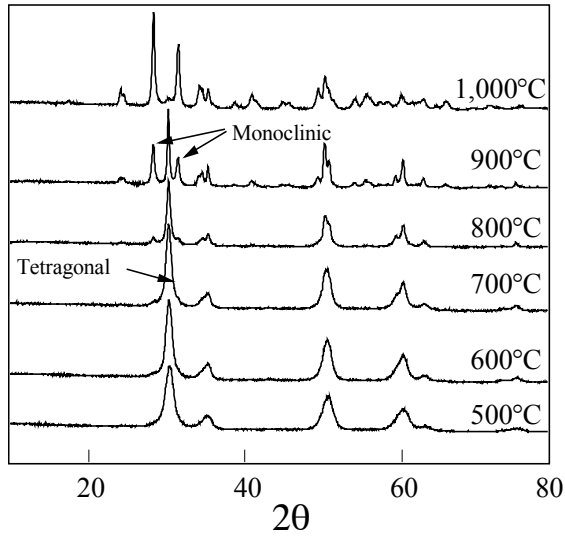

Figure 4.3a. *Evolution of the diffraction patterns of zirconia depending on the temperature of the thermal treatment*

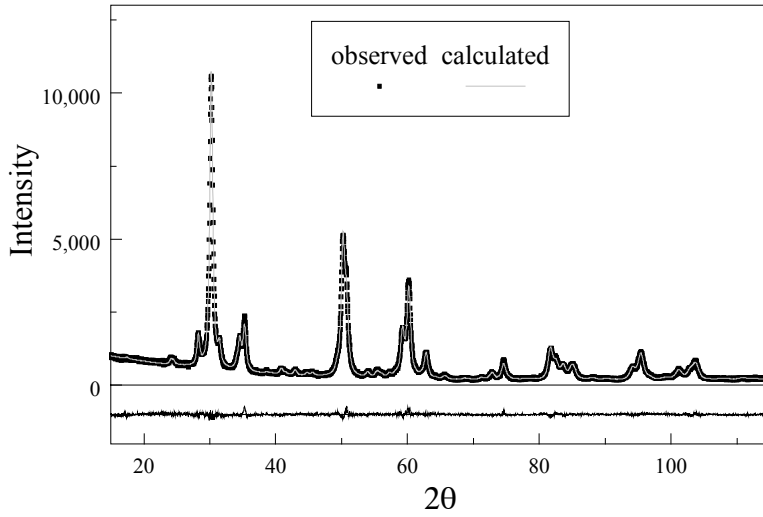

Figure 4.3b. *Fitting of the whole pattern obtained with a sample fired at 800°C*

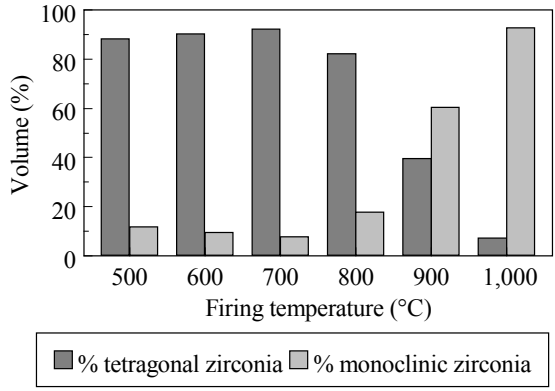

Figure 4.3c. *Relative amounts of tetragonal and monoclinic zirconium dioxide depending on the temperature of the thermal process*

A study of this type is shown in Figure 4.3a-c [GUI 96, SIL 96]. Zirconia samples were fired for an hour at different temperatures. The thermal treatment gradually transforms the zirconia from tetragonal to monoclinic (see Figure 4.3a). We studied this evolution according to the temperature of the process and all the patterns were fitted using the Rietveld method. Figure 4.3b shows the resulting pattern for the sample fired at 800°C. The evolution of the relative amounts of tetragonal and monoclinic zirconium dioxide is shown in Figure 4.3c. For this type of material, the second phase results from the transformation of the first phase, which means that the peaks of the two phases will be very close, making peak by peak fitting particularly difficult.

4.2.3. *Quantitative analysis procedures*

Independently of the method used for evaluating the integrated intensity, the quantitative phase analysis of a given sample can be achieved through several methods.

4.2.3.1. *The direct method*

The diffracted intensity of an arbitrary (hkl) peak with an arbitrary phase i is written (see Chapter 1):

$$I_{hkl} = I_0 r_e^2 \left(\frac{1+\cos^2 2\theta}{16\pi R \sin\theta \sin 2\theta} \right) \left(\frac{\lambda^3 n_{hkl} |F_{hkl}|^2}{V_c^2} \right) ADdV \qquad [4.4]$$

Knowing the crystalline structure of a phase makes it possible to calculate the structure factors and the cell volume of that phase. Based on this information, the phases we are trying to quantitatively analyze can be compared in pairs by calculating the ratios between the characteristic peak intensities of the various phases.

Thus, we obtain:

$$\frac{I^{i}_{hkl}}{I^{j}_{h'k'l'}} = \frac{K_i}{K_j}\frac{X_i}{X_j} \qquad [4.5]$$

The proportion of the different phases is given by the ratio:

$$\frac{X_i}{X_j} \qquad [4.6]$$

4.2.3.2. *External control samples*

This method consists of producing control samples that contain the same phases as the original sample, but in known amounts. An abacus is then drawn with the percentage of a phase as the x-coordinate and the intensity ratio of two peaks specific to each of the phases as the y-coordinate. In the same experimental conditions, the diffraction diagram of the sample we wish to study is then measured. The intensity ratio of the two peaks in question makes it possible to directly read, by using the abacus, the proportions of the different phases.

This method is efficient, and does not require an extensive knowledge of the crystal structures of the phases. It is, however, imperative for each of the phases to be pure. This is sometimes difficult to achieve, particularly if one of the phases is metastable. In that case, the first method is used.

4.2.3.3. *Internal control samples*

When the study requires a high accuracy, a variation of the second method can be used. In each of the control samples, a known percentage of an internal control sample with well-defined absorption characteristics is added. This time, the intensity measurements for the peaks of the analyzed phases are brought to scale with the intensity of a peak of the control sample.

As we saw above, this method makes it possible to take into account the absorption effects. Various samples are sold by the National Institute of Standard

and Technology (NIST) in the USA. The linear absorption coefficients of these samples range from a few hundred to a few thousand cm^{-1}. For each study, a control sample adequate to the phases we want to quantitatively analyze will be chosen. It is possible to simultaneously use several control samples.

Regardless of the calculation method the accuracy of quantitative phase analyses by X-ray diffraction strongly depends on the quality of the measurements. In particular, and as we have already seen, it is imperative to eliminate any preferential orientation effects. When the study is conducted under good conditions, the detection threshold is close to 1% and the accuracy of the analysis is in the range of a few percent.

4.3. Identification of the crystal system and refinement of the cell parameters

4.3.1. *Identification of the crystal system: indexing*

When studying an unknown phase, determining the crystal system is an unavoidable first step, since it is necessary to know the shape of the crystal cell and its dimensions before being able to determine the positions of the atoms inside this cell. The cell is a basis of the Euclidean space[3] in which the positions of the atoms are defined. We saw that we can associate this basis with a triplet of vectors $\left(\vec{a}^*, \vec{b}^*, \vec{c}^*\right)$ defined in the reciprocal lattice, where each family of direct lattice planes with Miller indices (hkl) is associated with a vector $\vec{r}^*$ that is normal to it, and has the triplet (hkl) as its coordinates in the reciprocal lattice. In the diffraction position, the point hkl is on the Ewald sphere and vector $\vec{r}^*$ is then equal to diffraction vector $\vec{s}$. For diffraction by polycrystalline samples, the measurement is equivalent to a projection of this three-dimensional lattice onto an arbitrary line that passes through the origin of the reciprocal lattice. We start with a three-dimensional object and end up with a one-dimensional information. This projection effect is shown in Figure 4.4. As you can see, the norm of vector $\vec{s}$ can be measured, but we have lost information regarding its direction. This well-known problem makes it much more difficult, of course, to determine a crystal's symmetry based on measurements made with polycrystalline samples than with studies conducted on single crystals.

3 The discovery of quasicrystals has led to the generalization of this crystallographic concept of space from a three-dimensional space to a six-dimensional space, in which the symmetry of the quasicrystals is described [JAN 98]. This generalization does not make the concepts described here any less valid.

Each point of the reciprocal lattice represents, as we have said, a family of crystal planes. The different families of planes define the crystal system, which is therefore determined by assigning a triplet of Miller indices to each diffraction spot or in diffraction on a polycrystalline sample, to each diffraction peak. This is referred to as the indexing of the diffraction peaks. The interplanar distance associated with a family of planes with indices (hkl) is a function of these Miller indices and of the cell parameters. We can write:

$$d_{(hkl)} = f(h, k, l, a, b, c, \alpha, \beta, \gamma) \quad [4.7]$$

As we have seen previously, the norm of the vector $\vec{r}^*$ with coordinates (hkl) in the reciprocal lattice is equal to 1/d. The term Q(hkl), referred to as the quadratic form, is given by:

$$Q_{(hkl)} = \left\| \vec{r}^*_{(hkl)} \right\|^2 = \frac{1}{d^2_{(hkl)}} \quad [4.8]$$

In the general case, it corresponds to a triclinic system and Q is expressed as follows:

$$Q_{(hkl)} = h^2a^{*2} + k^2b^{*2} + l^2c^{*2} + 2hka^*b^*\cos\gamma^* + 2hla^*c^*\cos\beta^* + 2klb^*c^*\cos\alpha^* \quad [4.9]$$

or also:

$$Q_{(hkl)} = h^2A + k^2B + l^2C + hkD + hlE + klF \quad [4.10]$$

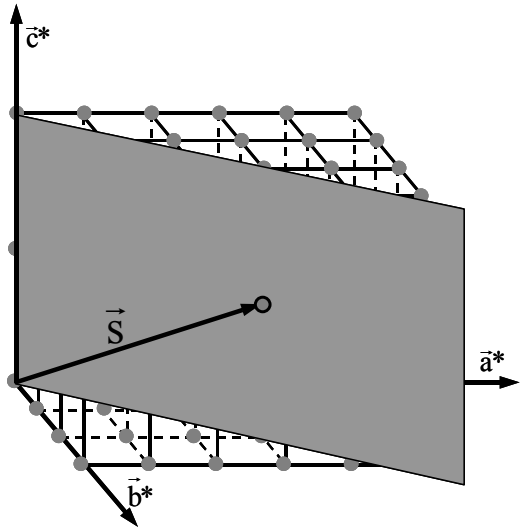

(a) Three-dimensional representation of the reciprocal lattice. If the family of planes (hkl) is in the Bragg position, then point hkl is located on the Ewald sphere and the vector connecting this point with the origin of the reciprocal lattice is diffraction vector $\vec{s}$

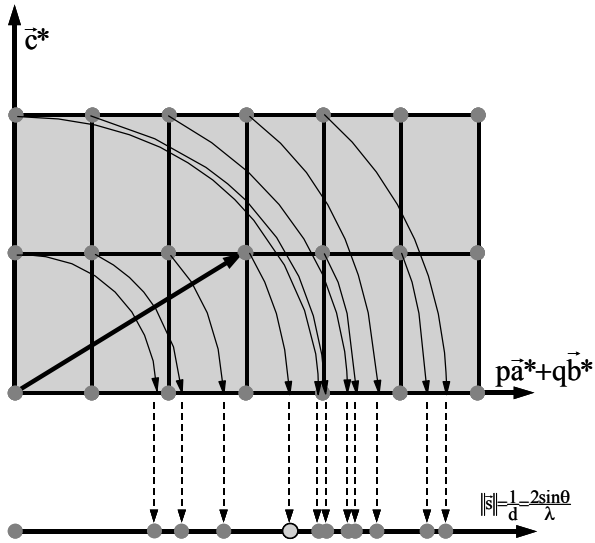

(b) Two-dimensional representation of the diffraction signal's projection onto an arbitrary line of the reciprocal space

Figure 4.4. *Representation of a reciprocal lattice line's projection when producing a diffraction pattern with a polycrystalline sample*

Determining the crystal lattice consists of finding the values of parameters A, B, C, D, E and F. We can see from Figure 4.4 that this is equivalent to finding the shape of a three-dimensional object based on its projection. Therefore, the problem we are trying to solve contains an indetermination and the methods used are based on a trial and error technique[4]. The crystal system is assumed to be cubic, for example, and if the series of peaks makes it possible, this crystal lattice is associated with the studied phase. The values of the quadratic forms are calculated from the interplanar distances. For the first values, we set possible values Miller indices, and a first estimate of the cell parameters is made. The quadratic forms for the other peaks are then calculated based on these cell parameters, in an attempt to find a calculated peak for each experimental peak. If the indexing fails, the hypothesis is changed by passing, for example to the next crystal system.

These methods cannot be used to determine a lattice with certainty and the quality of the indexing is characterized by various factors or figures of merit. The most commonly used figures of merit are the following.

The Wolff figure [WOL 68]:

$$M_n = \frac{Q_N}{2\langle \Delta Q \rangle N_{calc}} \qquad [4.11]$$

The Smith and Snyder figure [SMI 79]:

$$M_n = \frac{1}{\langle \Delta 2\theta \rangle} \frac{N}{N_{calc}} \qquad [4.12]$$

where Q_N is the value of Q for the N^{th} peak and N_{calc} the number of different values of Q calculated up to Q_N.

In the 1980s, many programs were developed to automatically perform this indexing process (for example [LOU 82, WER 85]). The calculations are usually quick, but leave the user "in the dark", since he takes no part in the process. The success in lattice identification is essentially determined by the quality of the measurements. Most of the time, a measurement error which is smaller than a hundredth of a degree is required. This a severe condition and it calls for strong precautions when making the measurements.

4 We will not give a comprehensive review of the calculations used. Readers who want to know more can refer to [DAV 02, PEC 03].

4.3.2. *Refinement of the cell parameters*

Once the crystal system of a given phase is known, each interplanar distance measured can be associated with a set of Miller indices. These indices express the relation between these distances and the cell parameters.

From an approximate value for the cell parameter, the interplanar distances are calculated and associated with the distances measured. The discrepancy between the experimental and the calculated distances is then minimized by slightly varying the values of the cell parameters [MAS 96b, PAW 81]. The system is comprised of six unknowns at the most (the six cell parameters) and of as many equations as there are diffraction peaks for the phase in question. Thus, the parameter values are obtained by gradual refinement, usually from least square calculations.

Once again, the essential point is the quality of the measurements. Additionally, the approximated values have to be as close as possible to the actual values. We saw in the previous chapter that, for a given error made on the measurement of the diffraction angle, the error made on the interplanar distance will decrease when the diffraction angle increases. Therefore, determining the cell parameters requires the peaks to be measured at high diffraction angles. However, the peaks located at low angles are those that correspond to the lowest Miller indices, which means that those are the peaks used to determine the crystal system. Furthermore, accurately determining the cell parameters clearly requires measuring the position of as many peaks as possible. Finally, this type of study imposes that the diffraction pattern should cover as wide an angular range as possible.

Measuring the positions of the peaks can be done with peak by peak fitting, but also by fitting the whole diffraction pattern [PAW 81, TOR 94]. The advantage of the latter method is significant, of course, when the phase's crystal symmetry is low, since the pattern will then be comprised of many partially overlapping peaks.

The accuracy obtained will depend on the extent of the measurement errors made on the peak positions and hence, naturally, on the system used. Generally speaking, parallel geometry systems can eliminate the error due to the position of the sample and therefore lead to very precise measurements of the cell parameters. However, a high angular resolution is needed in order to limit partial overlaps of the peaks, which can lead to mistakes when determining the crystal system. We saw in Chapter 2 that the resolution usually achieved with those laboratory equipments is average, poorer than the one obtained with focusing configurations. Aside from using configurations that associate a four-reflection monochromator with an analyzer crystal [FEW 95], the implementation of this type of system is difficult for this application if the crystal has a low symmetry.

Laboratory systems equipped with movements accurate to the ten-thousandth of a degree and that use parallel geometry can achieve an uncertainty in the range of 10 ppm. Very high resolution systems associated with synchrotron sources can achieve an uncertainty close to 1 ppm [HAR 90]. We have to point out, however, that the tests conducted on a same sample by several laboratories generally lead to much greater errors. The differences between the measured values are often in the range of 100 ppm [PAR 60, MAS 96b].

4.4. Introduction to structural analysis

We saw in the historical introduction that the study of crystal structure, that is the determination of the nature and the positions of the atoms inside the crystal cell, quickly became an essential application of X-ray diffraction. W.H. and W.L. Bragg, for example, were awarded the Nobel Prize for their works on the determination of the crystal structure of several simple phases. Throughout the 20^{th} century, the determination of crystal structure was one of the major driving forces in developing the study of condensed matter by X-ray diffraction with regard to both the improvements made to the instruments and the implementation of more efficient methods of data processing.

We saw in Chapter 1 that the nature and the positions of the atoms are variables involved in the value of the structure factors. This aspect will be discussed further in the following sections but, clearly, it is measuring the diffracted intensities, which makes it possible to characterize the crystal structure. In the previous section, which dealt with the determination methods of crystal systems and cell parameters, we illustrated the fact that diffraction patterns of polycrystalline samples are equivalent to one-dimensional projections of the diffraction signal's three-dimensional distribution. We are faced with the same problem here and the number of families of planes for which we will be able to estimate the diffracted integrated intensity is small compared to all of the measurements available with diffraction by single crystals. And yet, the structural analysis of polycrystalline samples began almost 60 years ago. We can mention, in particular, the works of Zachariasen, who determined, in 1948, the structure of various uranium based compounds by interpreting the diffraction measurements made on polycrystalline samples [ZAC 48a, ZAC 48b, ZAC 48c, ZAC48d, ZAC48e, ZAC48f]. We will see later on that whole pattern fitting methods for diffraction patterns, initiated by Rietveld in the late 1960s [RIE 67, RIE 69], led to a tremendous number of structures being solved by diffraction on polycrystalline samples. It remains very clear, however, that the determination of the crystal structure of a new compound will always be easier with a diffraction study on a single crystal. Structural analysis by diffraction on polycrystalline samples should only be implemented if no single crystal is available. This is why solid state chemists and experts in structural biology always make an

attempt at growing single crystals of new phases they have imagined and synthesized. It is very common in materials science, however, to be impossible to produce such single crystals, in which case the crystal structure of the compound in question has to be solved by a study on a polycrystalline sample.

The objective in the following sections is not to describe in detail the ideas and methods that govern the structural analysis of polycrystalline samples. Several books have been written about this particular field of X-ray diffraction. We will give here the basic elements and a few examples. In the past 30 years, structural analysis of polycrystalline samples has seen considerable developments. A recent book, published under the authority of the International Union of Crystallography, gives an overview of these aspects [DAV 02]. Also, you can find many examples in [PEC 03].

4.4.1. *General ideas and fundamental concepts*

4.4.1.1. *Relation between the integrated intensity and the electron density*

Generally, a crystal structure is defined as the three-dimensional, periodic repetition, parallel to the directions a, b and c of a pattern comprised of one or several atoms located in a position with coordinates (x,y,z). This structure can be represented by an electron density function, $\rho(x,y,z)$, a continuous function which is defined for any point (x,y,z) of the crystal and expressed in electrons per unit of volume. This function has maxima in the places where atoms are found. Determining a structure consists of finding, for every point (x,y,z) of the cell, the value of $\rho(x,y,z)$.

In any point (x,y,z) of the crystal, this triply periodic distribution can be written as a triple Fourier series of the general form:

$$\rho(x,y,z) = \sum_{h=-\infty}^{+\infty} \sum_{k=-\infty}^{+\infty} \sum_{l=-\infty}^{+\infty} A_{hkl} e^{-2\pi i(hx+ky+lz)} \qquad [4.13]$$

Note that, for each triplet (h,k,l), there is a Fourier plane wave, that is, a constant phase plane, which is defined by $hx + ky + lz = \text{constant}$ and parallel to the planes with indices (hkl) of the crystal lattice. Therefore, we can consider that, for each family of planes, there is a corresponding Fourier plane wave with its wavefront parallel to these planes and with its wavelength equal to the interplanar distance.

Fourier coefficients A_{hkl} can be evaluated from equation [4.13]. If we multiply each side of the equality by the term $e^{2\pi i(h'x + k'y + l'z)}$, then:

$$\rho(x,y,z)e^{2\pi i(h'x+k'y+l'z)} = \left(\sum_{h=-\infty}^{+\infty} \sum_{k=-\infty}^{+\infty} \sum_{l=-\infty}^{+\infty} A_{hkl} e^{-2\pi i(hx+ky+lz)} \right) e^{2\pi i(h'x+k'y+l'z)}$$

hence:

$$\int_0^a \int_0^b \int_0^c \rho(x,y,z)e^{2\pi i(h'x+k'y+l'z)}dxdydz = \sum_{h=-\infty}^{+\infty} \sum_{k=-\infty}^{+\infty} \sum_{l=-\infty}^{+\infty} A_{hkl} \int_0^a \int_0^b \int_0^c e^{2\pi i((h'-h)x+(k'-k)y+(l'-l)z)}dxdydz$$

if $h = h'$:

$$\int_0^a e^{2\pi i(h'-h)x}dx = \int_0^a dx = a \qquad [4.14]$$

if $h \neq h'$:

$$\Rightarrow \int_0^a e^{2\pi i(h'-h)x}dx = \int_0^a \cos 2\pi(h'-h)xdx + i\int_0^a \sin 2\pi(h'-h)xdx$$

$$\Rightarrow \int_0^a e^{2\pi i(h'-h)x}dx = \left[\frac{1}{2\pi(h'-h)} \sin 2\pi(h'-h)x \right]_0^a + i\left[-\frac{1}{2\pi(h'-h)} \cos 2\pi(h'-h)x \right]_0^a$$

$$\Rightarrow \int_0^a e^{2\pi i(h'-h)x}dx = \frac{1}{2\pi(h'-h)}\left[\left[\sin 2\pi(h'-h)a - \sin 0 \right] - i\left[\cos 2\pi(h'-h)a - \cos 0 \right] \right]$$

$h' - h$ is an integer, hence $\sin 2\pi (h' - h)\, a = 0$ and $\cos 2\pi (h' - h)\, a = 1$ and therefore, if $h \neq h'$:

$$\int_0^a e^{2\pi i(h'-h)x}dx = 0 \qquad [4.15]$$

Therefore, we can write:

$$\int_0^a \int_0^b \int_0^c \rho(x,y,z) e^{2\pi i(h'x+k'y+l'z)} dxdydz = abcA_{hkl} \quad [4.16]$$

Let us consider the elementary volume dV with sides dx, dy, dz. dV = Ndxdydz where N is a constant that depends on the angles between directions x, y and z. Likewise, the volume of the crystal cell is written V_c = Nabc. Therefore, we get:

$$\int \rho(x,y,z) e^{2\pi i(h'x+k'y+l'z)} dV = V_c A_{hkl} \quad [4.17]$$

The left side of this equation is the expression of the structure factor (see Chapter 1) and so, finally:

$$A_{hkl} = \frac{F_{hkl}}{V_c} \quad [4.18]$$

hence:

$$\rho(x,y,z) = \frac{1}{V_c} \sum_{h=-\infty}^{+\infty} \sum_{k=-\infty}^{+\infty} \sum_{l=-\infty}^{+\infty} F_{hkl} e^{-2\pi i(hx+ky+lz)} \quad [4.19]$$

4.4.1.2. *Structural analysis*

Relation [4.19] is one of the fundamental elements of structural analysis. This is because it shows that determining the various structure factors associated with each of the families of crystal planes makes it possible to calculate *a priori* the electron density distribution in each point of the crystal.

However, the problem remains complex. First, note that this expression indicates that properly determining ρ(x,y,z) requires knowing all of the crystal's structure factors. Experimentally, this condition will not be achieved. Instead, all we have is truncated Fourier series of various lengths.

The second restriction of this type of study is the determination of the structure factor. This is because this term is a complex number, whose phase has a random value in the general case. The determination of these structure factors is achieved based on the measurements of the intensities diffracted by each of the families of planes, but, as we showed in Chapter 1, the diffracted intensity is proportional to the square modulus of the structure factor. Therefore, the measurements do not make it

possible to know *a priori* the phases of these structure factors, which means that the overall problem of structural determination cannot be solved from a mathematical point of view. A given set of values of the intensity diffracted by a crystal corresponds to an infinite number of possible electron densities. However, most of these possibilities make no physical sense and, with the help of a few practical considerations, we will see that it is possible to identify the right solution and that, in a great number of cases, the measurement of the diffracted intensities can be used to determine the structure of the crystal in question.

As equation [4.19] shows, in general the electron density $\rho(x,y,z)$ is a complex number, meaning that the phase of the scattered wave is different from that of the incident wave. If we assume that the scattering does not cause any phase shift, then $\rho(x,y,z)$ becomes a real number in every point (x,y,z) of the crystal. Note that this implies that $F_{hkl} = F^{*}_{\overline{hkl}}$, meaning that the structure factor obtained on one side of the family of planes (hkl) is equal to the conjugate of the structure factor obtained on the other side of this family of planes.

Under these conditions, the series represented in equation [4.19] can be expressed as a sum of pairs:

$$F_{hkl}e^{-i\phi} + F_{\overline{hkl}}e^{i\phi} \qquad [4.20]$$

with $\phi = 2\pi(hx + ky + lz)$.

Let us recall that:

$$F_{hkl} = \left|F_{hkl}\right|e^{i\delta} \text{ and } F_{\overline{hkl}} = \left|F_{hkl}\right|e^{-i\delta} \qquad [4.21]$$

therefore:

$$F_{hkl}e^{-i\phi} + F_{\overline{hkl}}e^{i\phi} = 2\left|F_{hkl}\right|\cos(\phi - \delta) \qquad [4.22]$$

In the end:

$$\rho(x,y,z) = \frac{\left|F_{000}\right|}{V_c} + \frac{2}{V_c}\sum_{hkl}\left|F_{hkl}\right|\cos(\phi - \delta) \qquad [4.23]$$

The sum is made over all of Bragg reflections, by taking into account only one, however, of the two factors F_{hkl} or $F_{\overline{hkl}}$.

Particular case of centrosymmetric structures

When the structure includes a center of symmetry then, by definition, the electron density distribution is such that $\rho(x, y, z) = \rho(-x, -y, -z)$. If we expand the terms of the sum given in relation [4.22], we get:

$$|F_{hkl}|\cos(\phi - \delta) = |F_{hkl}|(\cos\phi\cos\delta + \sin\phi\sin\delta) \qquad [4.24]$$

The sign of $\cos\phi = \cos 2\pi (hx + ky + lz)$ does not change when x, y and z are replaced with –x, –y, and –z, whereas the sign of $\sin\phi$ does change. Therefore, we can only have $\rho(x,y,z) = \rho(-x, -y, -z)$ if $\sin\delta = 0$, hence $\delta = 0$ or π. Therefore, $\cos(\phi - \delta)$ is equal either to $\cos\phi$ or to $-\cos\phi$. Hence:

$$\rho(x,y,z) = \frac{|F_{000}|}{V_c} + \frac{2}{V_c}\sum_{hkl} \pm |F_{hkl}|\cos 2\pi(hx + ky + lz) \qquad [4.25]$$

This means that it is theoretically possible to determine, in every point (x,y,z) of any crystal with a centrosymmetric structure, the value of the electron density function based on the intensity measurements for all of the Bragg reflections predicted by the crystal's symmetry.

4.4.1.3. *The Patterson function*

As we saw earlier, the use of the electron density function in structural studies is not compatible with the fact that we are only measuring the square modulus of the structure factor, whereas it would actually be necessary to know the complex value of this factor. Patterson [PAT 34, PAT 35] thought of a method to obtain structural information based on the measured values of $|F_{hkl}|^2$. The coefficients of the Fourier series used are proportional to the square moduli of the structure factors.

Let us assume, as we did before, that the electron density in a point with coordinates (x,y,z) is denoted by $\rho(x,y,z)$ and given by relation [4.19]. The values of this function $\rho(x,y,z)$ are very small, except in certain points which correspond to the positions of the atoms. Now consider the function $\rho(x + u, y + v, z + w)$, where u, v and w are constant parameters for any values of x, y and z. The values of the product $\rho(x,y,z) \times \rho(x + u, y + v, z + w)$ are small, except when the triplet (u,v,w) is comprised of the components of a vector that connects the positions of two atoms in

the structure, or, in other words, when both electron density distributions are at a maximum.

The Patterson function is defined by the following relation:

$$P(u,v,w) = N\int_0^a \int_0^b \int_0^c \rho(x,y,z)\rho(x+u, y+v, z+w)dxdydz \qquad [4.26]$$

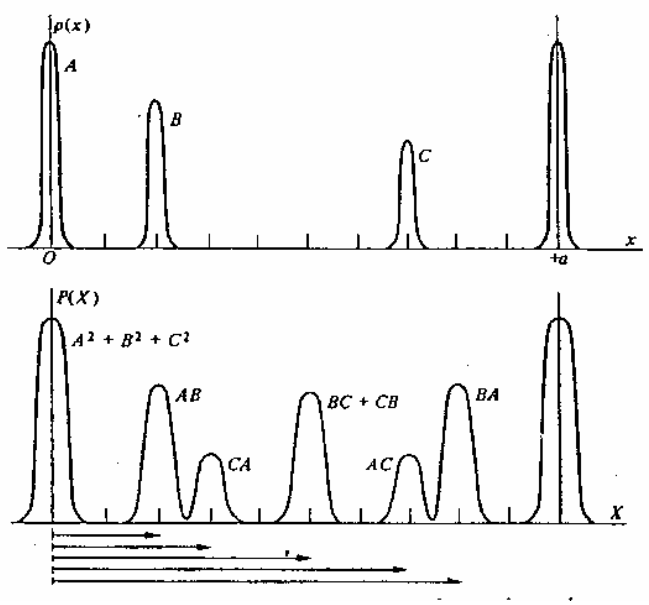

Figure 4.5. *Representation of a one-directional density function and of the associated Patterson function [JAM 67]*

This function is periodical with respect to the parameters a, b and c of the crystal cell and has maxima at the origin and at the points obtained from the translation of the basis vectors starting at the origin. Furthermore, this integral will reach its maximum values when the vector between the origin and the point with coordinates (u, v, w) is a vector connecting two atoms of the structure. Therefore, the Patterson function can be described as a correlation function that gives the position of each atom with respect to each of the other atoms in the structure (and not with respect to the origin of the lattice). The representation of a one-directional Patterson function is shown in Figure 4.5.

Let us now replace the two distributions with their expressions given in Relation 4.19:

$$P(u,v,w) = \frac{N}{V_c^2}\sum_{hkl}\sum_{h'k'l'}\int_0^a\int_0^b\int_0^c\left[F_{hkl}e^{-2\pi i(hx+ky+lz)}\right]\left[F_{h'k'l'}e^{-2\pi i[h'(x+u)+k'(y+v)+l'(z+w)]}\right]dx\,dy\,dz$$

These integrals are equal to zero, except if $h = -h'$, $k = -k'$ and $l = -l'$. In this case, $F_{hkl} = F^*_{hkl}$ and therefore:

$$P(u,v,w) = \frac{N}{V_c^2}\sum_{hkl} abc\left|F_{hkl}\right|^2 e^{-2\pi i(hu+kv+lw)} \qquad [4.27]$$

$$P(u,v,w) = \frac{1}{V_c}\sum_{h=-\infty}^{h=+\infty}\sum_{k=-\infty}^{k=+\infty}\sum_{l=-\infty}^{l=+\infty}\left|F_{hkl}\right|^2 e^{-2\pi i(hu+kv+lw)} \qquad [4.28]$$

If the structure is centrosymmetric:

$$P(u,v,w) = \frac{1}{V_c}\sum_{h=-\infty}^{h=+\infty}\sum_{k=-\infty}^{k=+\infty}\sum_{l=-\infty}^{l=+\infty}\left|F_{hkl}\right|^2 \cos 2\pi(hu+kv+lw) \qquad [4.29]$$

Generally, the projections of the Patterson function are used, rather than its three-dimensional representation.

If we denote by $\sigma(x,y)$ the projection onto the plane (x,y) of the electron density $\rho(x,y,z)$, the corresponding Patterson function will be written:

$$P(u,v) = \frac{A}{ab}\int_0^a\int_0^b \sigma(x,y)\sigma(x+u,y+v)dxdy \qquad [4.30]$$

and finally:

$$P(u,v) = \frac{1}{A}\sum_{h=-\infty}^{h=+\infty}\sum_{k=-\infty}^{k=+\infty}\left|F_{hkl}\right|^2 e^{2\pi i(hu+kv)} \qquad [4.31]$$

A function of this type, as well as the projection of the corresponding structure, are shown in Figure 4.6 which represents the cubic structure FeS_2 projected onto one of the cube's faces.

The advantage of these Patterson functions relies essentially on the fact that they only require values which can be measured and therefore can theoretically be completely determined by the diffracted intensity measurements. However, they are difficult to use and their interpretation is ambiguous. A detailed description of the use of these functions, based on data extracted from diffraction diagrams on polycrystalline samples, was recently suggested by Estermann and David [EST 02].

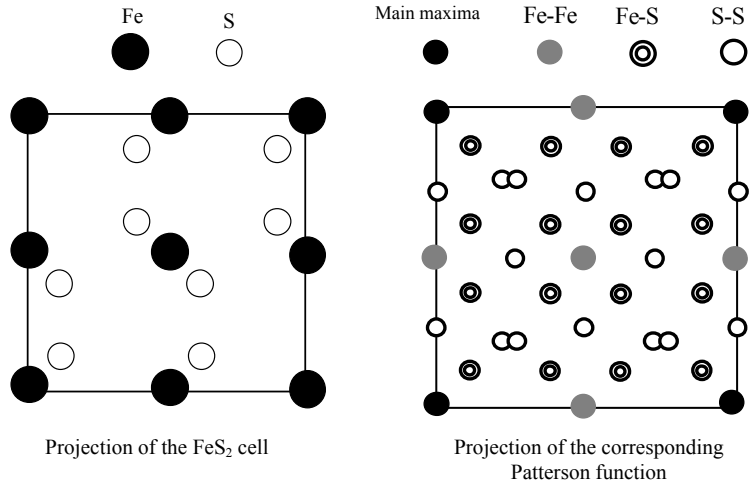

Figure 4.6. *Example of a Patterson projection and its associated structure [JAM 67]*

4.4.1.4. *Two-dimensional representations of the electron density distribution*

Generally, in order to apply the concepts we have just described, simplified representations are used for the triple Fourier series expressing the electron density at a given point of the crystal.

4.4.1.4.1. Fourier sections

Fourier sections are cross-sections of the distribution $\rho(x,y,z)$, at a given altitude z. They are expressed as follows:

$$\rho(x,y,z_1) = \frac{|F_{000}|}{V_c} + \frac{2}{V_c}\sum_{hkl}|F_{hkl}|\cos(2\pi(hx+ky+lz)-\delta) \qquad [4.32]$$

Although these Fourier maps are two-dimensional representations, calculating them requires for all of the structure factors to be known.

4.4.1.4.2. Fourier projections

Bragg [BRA 66] imagined a second two-dimensional representation of a crystal's structure. This time, it consists of a projection, parallel to the vector $\vec{c}$, onto the basis plane defined by the vectors $\vec{a}$ and $\vec{b}$, of the electron density in the cell defined by the triplet $(\vec{a},\vec{b},\vec{c})$.

Let $\sigma(x,y)$ be this projection; we then have:

$$\sigma(x,y)dA = \int_0^c \rho(x,y,z)dV \qquad [4.33]$$

If A is the area of side ab and, as we defined previously, if the cell's volume is $V_c = Nabc$, then:

$$dA = A\frac{dxdy}{ab} \quad \text{and} \quad dV = V_c\frac{dxdydz}{abc} \qquad [4.34]$$

therefore:

$$\sigma(x,y) = \frac{V_c}{Ac}\int_0^c \rho(x,y,z)dz \qquad [4.35]$$

If $\rho(x,y,z)$ is replaced with its expression given in [5.19], we get:

$$\sigma(x,y) = \frac{V_c}{Ac}\int_0^c \left[\frac{1}{V_c}\sum_{h=-\infty}^{h=+\infty}\sum_{k=-\infty}^{k=+\infty}\sum_{l=-\infty}^{l=+\infty} F_{hkl}e^{-2\pi i(hx+ky+lz)}\right]dz \qquad [4.36]$$

$$\Rightarrow \sigma(x,y) = \frac{1}{Ac}\left[\sum_{h=-\infty}^{h=+\infty}\sum_{k=-\infty}^{k=+\infty}\sum_{l=-\infty}^{l=+\infty} F_{hkl}e^{-2\pi i(hx+ky)}\left[\int_0^c e^{-2\pi ilz}dz\right]\right] \qquad [4.37]$$

As we have already shown, if $l = 0$, then:

$$\int_0^c e^{-2\pi ilz} dz = c$$

and if $l \neq 0$ then:

$$\int_0^c e^{2\pi ilz} dz = 0$$

so, in the end, all the terms are equal to zero, except those for which $l = 0$. Therefore:

$$\sigma(x, y) = \frac{1}{A} \sum_{h=-\infty}^{h=+\infty} \sum_{k=-\infty}^{k=+\infty} F_{hk0} e^{-2\pi i(hx+ky)} \qquad [4.38]$$

Let us note that, in order to achieve this projection onto the basis plane ab, only the structure factors of the type F(hk0) are necessary. Naturally, this concept of projection can be extended to any axis or plane of the crystal lattice. An example of this type of projection is shown in Figure 4.7.

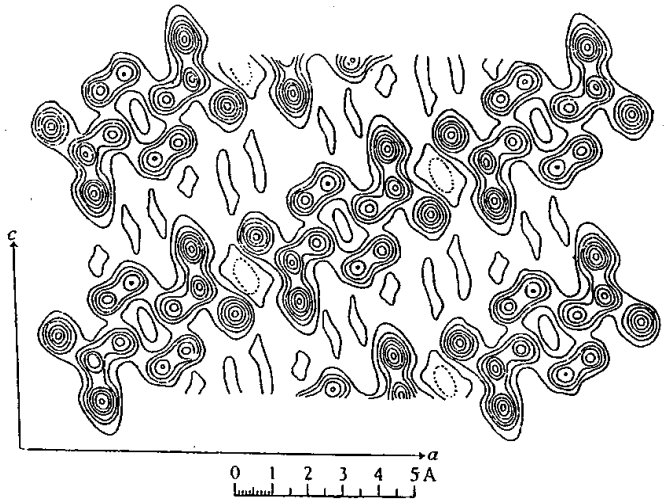

Figure 4.7. *Fourier projection of an electron density function [JAM 67]*

4.4.2. *Determining and refining structures based on diagrams produced with polycrystalline samples*

4.4.2.1. *Introduction*

We have just described in broad strokes how measuring all of the intensities diffracted by a given crystal makes it possible to tackle the structural analysis of that crystal. This measurement makes it possible to access the modulus values of the various structure factors specific to the sample studied and, although the resulting information is incomplete, it is possible to properly describe the nature and the position of each of the atoms that comprise the crystal cell. Up to now, we have considered the diffraction by a single crystal by placing it, for example, on a device which enables it to rotate around every axis of the direct space [ASL 98]. The integrated intensities are then measured for each Bragg position encountered during these rotations. This technique has seen significant developments over the past 20 years, particularly because new equipment has become available, which is practically automatic and controlled by a computer. It is common in this case for the acquisitions to be comprised of several thousand Bragg spots. The arrival on the market of two-dimensional detectors has made it possible to considerably reduce the duration of such measurements, which is now typically in the range of several hours to several days.

As we have already said, these very efficient methods still present an intrinsic disadvantage: they need to be capable of synthesizing a single crystal of the phase we wish to study. For a long time, researchers have therefore been trying to transpose this type of study onto diffraction patterns produced with polycrystalline samples. The structural analysis of polycrystalline samples remained, however, limited to very favorable examples until the early 1980s. The wider use of computers and the design of particularly efficient data processing methods have revived this type of study which is becoming more and more important.

Determining the structure of a phase from diffraction measurements on a polycrystalline sample can be divided into five steps:

(1) Measuring the positions of the peaks.

(2) Determining the crystal system and the cell parameters. Searching for systematic extinctions and determining the possible space groups.

(3) Measuring the integrated intensities.

(4) Suggesting a possible structure: creating a structural model with approximate values for the positions of the atoms.

(5) Refining the structure. This refinement is usually achieved using the Rietveld method.

The first two points of this list have already been discussed in other sections of this chapter. We will now describe how to deal with steps (3), (4) and (5).

4.4.2.2. *Measuring the integrated intensities and establishing a structural model*

4.4.2.2.1. Measuring the integrated intensities

Naturally, determining the integrated intensities is at the core of structural analysis. Clearly, the quality of the values obtained determines the rest of the study, especially since the number of reflections that are analyzed is necessarily much smaller than for the diffraction on single crystals. However, due to the problem caused by overlapping peaks (and also by possible preferential orientation effects), estimating these integrated intensities correctly is particularly difficult. There are essentially two different approaches, based on works published in the 1980s, referred to as the Pawley method [PAW 81] and the LeBail method [LEB 88]. In both case, the integrated intensities are extracted by using whole pattern fitting of the diffraction pattern, without introducing a structural model. The peak positions are refined from the values of the cell parameters. The difference between the two methods lies in how the contributions of overlapping peaks are separated and, particularly, in how they prevent fitting from leading to negative values. In the Pawley method, constraints imposed on the intensity variations of the different peaks located in a given area prevent these intensities from having negative values. In the LeBail method, the integrated intensities of the peaks in a given cluster of peaks are arbitrarily assumed to be equal initially and are then refined step by step. These two approaches are often used and their respective advantages and drawbacks have been discussed by many authors. We can mention several recent reviews on the subject. The Pawley method was discussed in detail by Toraya [TOR 93]. A comparison of the two approaches was given by Giacovazzo [GIA 96] and more recently by LeBail [LEB 05].

4.4.2.2.2. Establishing a structural model

Constructing a reasonable structural model is done differently depending on whether or not likely structures are known. It is common in diffraction by polycrystalline samples to suggest a structural model by analogy with known structures that serve as references. In this case, a new structure is conceived by changing the atoms, which modifies the values of their integrated intensities. The structural model is established by taking into account considerations involving the nature and the length of the interatomic bonds, ionic radii, etc. The structure is then refined by using methods which we will describe later on.

Another approach consists of starting directly with the results of the diffraction measurements and generating a structural model without any reference considerations; a method which is described as *ab initio* [GIA 96, PUT 99]. The

latter approach is similar to the one generally used for structural analysis whose measurements are made with single crystals. It requires a considerable amount of data, of course. The name of the method depends on how the structural model[5] is built: it is referred to as the direct method [PES 02] when the model is directly established after estimating, for each peak, the modulus of the corresponding structure factor, and as the Patterson method [EST 02] if representations of the associated Patterson function are used.

4.4.2.3. *Structure refinement: the Rietveld method*

Refinement methods, whether applied to structural determination or implemented in order to acquire other information, generally rely on the same idea: they consist of minimizing, with the help of an algorithm, the gap between a theoretical and an experimental graph. These aspects were discussed in Chapter 3. When the refinement is performed with the objective of determining the structure of the diffracting crystals, the parameters that can be refined are these structural parameters (nature and positions of the atoms, thermal agitation and occupation rates). At the end of the 1960s, Rietveld [RIE 67, RIE 69] suggested a general method for conducting the whole pattern fitting of diffraction patterns. In Chapter 3, we described the method from a formal standpoint. We will now explain how it can be applied to structural analysis.

The works of Rietveld led to significant progress in structural analysis from polycrystalline samples. A large number of inorganic materials [SMR 99] and, more recently organic materials [LOU 95], were thus solved. In 1993, a book edited by Young [YOU 93] was written entirely on the subject of this method. In the 1990s, the International Union of Crystallography Commission on Powder Diffraction organized two international tests on this method [HIL 92, HIL 94]. There are many programs available today designed for this type of study and even though this method is used by a growing number of researchers, it remains difficult to implement and requires a gradual approach toward the result. Before we go into the details of the issues that may arise, we will describe this method and illustrate it with a few actual examples[6].

4.4.2.3.1. Description of the method and illustration

Since the Rietveld method is a refinement method, it requires a structure suggestion in order to begin the fitting. Therefore, the person conducting the

---

5 Other, more recent approaches have been suggested, such as methods based on the entropy maximum [GIL 02]. These aspects will not be discussed here.

6 The Rietveld fittings described here are simple illustrations of the method. As we have already said, the objective in this chapter is to give a few elements on this refinement process which is described in much greater detail in other books. Readers interested in knowing more will find a complete presentation of Rietveld refinements, with every step described in detail, in [PEC 03].

experiment has to give, from the start, a crystal symmetry with the cell parameters, as well as a space group with the position and the nature of each of the atoms. As we have already said, this model was developed either by analogy with previously studied structures or directly from measurements of integrated intensities. All of this information is usually gathered into a control file where each parameter is assigned a code that defines its state. If a parameter is free, its value can change while the refinement is taking place; if it is set, it will remain constant during the refinement cycle in question. This goes for all of the refinement methods we described in Chapter 3, but in the case of the Rietveld refinement method there is a very large number of parameters, and choosing which of these parameters can vary often determines the success of the refinement process.

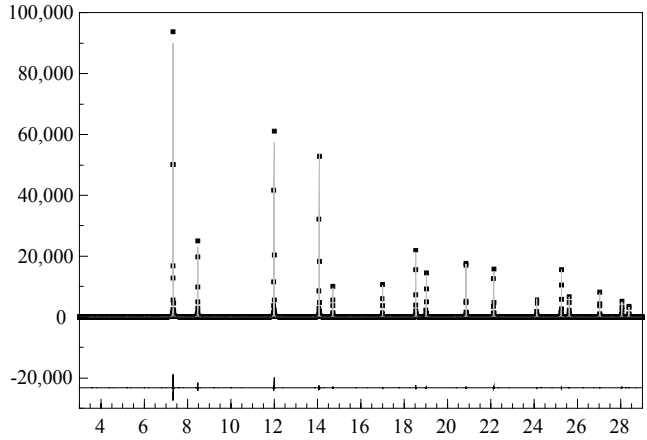

Figure 4.8. *Rietveld fitting of an X-ray diffraction pattern obtained with a sample of cerium oxide. This pattern was produced by using a high resolution system with a synchrotron radiation source at the ESRF, with a wavelength equal to 0.39982 Å [BAL 04]*

In order to describe this method, we will illustrate it with a first example chosen to be very simple on purpose. We decided to perform the Rietveld refinement of a diffraction patterns obtained with a sample of cerium oxide. This sample, mentioned earlier, was produced in Rennes, France, and was used in the context of an international test on a powder used for determining the instrumental functions of diffractometers [BAL 04]. Cerium oxide has a fluorine type structure and all of the atoms are in a set position. The patterns were obtained on the high resolution diffraction line with polycrystalline samples from the ESRF. The refinement was performed by the program FullProf[7], developed by Carvajal [ROD 92]. The experimental pattern and its fitting are shown in Figure 4.8.

7 A large number of programs can perform this type of refinement. Many are available at no cost on the international networks. You can find a selection of these programs on a website

Name of the diagram and comments		COMM CeO2 Size Strain Round Robin ESRF Data Files = > DAT-file: massonsh, PCR-file: CeO2
Parameters defining the conditions under which the diagram is produced and the profiles used for the peak fitting		Job Npr Nph Nba Nex Nsc Nor Dum Iwg Ilo Ias Res Ste Nre Cry Uni Cor 0 7 1 0 0 0 0 1 0 0 1 4 1 0 0 0 0 sharp.prn Ipr Ppl Ioc Mat Pcr Ls1 Ls2 Ls3 Syo Prf Ins Rpa Sym Hkl Fou Sho Ana 0 0 1 1 1 0 0 0 1 3 0 1 1 1 2 0 0 lambda1 Lambda2 Ratio Bkpos Wdt Cthm muR AsyLim Rpolarz 0.399820 0.399820 1.0000 50.0000 10.0000 0.0000 0.0000 29.00 0.0000 NCY Eps R_at R_an R_pr R_gl Thmin Step Thmax PSD Sent 0.5 0.50 0.50 0.50 0.50 0.50 3.0000 0.0004 29.0000 0.000 0.000
Number of refined parameters		8 Number of refined parameters
Coefficients of the polynomial fitting the continuous background	Values Codes	Background coefficients/codes 4.5655 0.75849 0.00000 0.00000 0.00000 0.00000 21.000 31.000 00.000 0.000 0.000 0.000
General data		Data for PHASE number: 1 CeO2 Nat Dis Mom Pr1 Pr2 Pr3 Jbt Irf Isy Str Furth ATZ Nvk Npr More 2 0 0 0.0 0.0 1.0 0 0 0 0 0 0.00 0 7 0 F M 3 M <--Space group symbol
Positions of the atoms	Values Codes Values Codes	Atom Typ X Y Z Biso Occ In Fin N_t /Codes CE CE + 4 0.00000 0.00000 0.00000 0.48555 0.50963 0 0 0 30.00 40.00 50.00 51.00 61.00 O O-2 0.25000 0.25000 0.25000 0.32603 1.06587 0 0 0 0.00 0.00 0.00 81.00 71.00
Scale factor and parameters defining a general model for microstructural effects	Name Values Codes	Scale Shape1 Bov Str1 Str2 Str3 Strain-Model 0.36564E-08 0.0000 0.0000 0.0000 0.0000 0.0000 0 11.00000 0.00 0.00 0.00 0.00 0.00
Parameters defining the evolution of the peak widths	Name Values Codes	U V W X Y GauSiz LorSiz Size-Model 0.00000 0.00000 0.00000 0.00010 0.00000 0.00000 0.00000 0 0.00 0.00 0.00 0.00 0.00 0.00 0.00
Cell parameters	Name Values Codes	a b c alpha beta gamma 5.410950 5.410950 5.410950 90.000000 90.000000 90.000000 41.00000 41.00000 41.00000 0.00000 0.00000 0.00000
Parameters defining the preferential orientation	Name Values Codes	Pref1 Pref2 Asy1 Asy2 Asy3 Asy4 0.00000 0.00000 0.00000 0.00000 0.00000 0.00000 0.00 0.00 0.00 0.00 0.00 0.00

Table 4.2. *Control file for the structural refinement of a pattern obtained with a sample of cerium oxide free of any structural defects*

The control file used for performing the refinement shown in Figure 4.8 is given in Table 4.2. The various parameters are written in the right column of this table. The first row contains a large number of parameters used, for a given refinement, to specify the conditions under which the pattern was produced. These programs are usually designed to be compatible with many measurement instruments corresponding to very different experimental conditions. Naturally, the pattern's characteristics directly depend on the measurement conditions.

In the second line, the number of refined parameters for a given cycle is specified and, regardless of the pattern's quality, it is always comprised of a continuous scattering background in addition to the diffraction peaks. There are

administered by the International Union of Crystallography at the following address: http://www.ccp14.ac.uk.

essentially two approaches to fit this continuous background. The first one consists of defining, point by point, an empirical curve that fits as best as possible. The other consists of describing this contribution with a previously defined curve, often a polynomial, which is adjusted by refinement. In the present case, the latter method was used and the polynomial's coefficients are shown in the third row. General characteristics defining the phase, or phases, present in the sample are given in the fourth row. The positions of the atoms, the thermal agitation factors and the occupation rates are all defined in the fifth row.

Naturally, the absolute intensity of the diffraction signal has no particular meaning. It depends on the acquisition conditions, the duration of the measurement, etc. Therefore, an additional parameter is introduced, referred to as the "scale factor". The calculated pattern is entirely adjusted with the observed pattern by multiplying it by this coefficient. This factor is given in the sixth row, where other parameters are mentioned, involving the microstructure refinement, and which will be discussed in Part 2 of this book. Parameters U, V and W given in the seventh row characterize the Caglioti polynomial (see Chapter 3), which defines the evolution of the width of the instrumental function according to the diffraction angle. The cell parameters are given in the eighth row, whereas the ninth row contains coefficients which make it possible to take into account a possible referential orientation.

This description clearly shows that structural refinement using the Rietveld method requires a specific refinement strategy. We have already discussed some of these aspects in Chapter 3 (see section 3.3.4). Obviously, when the objective, as in this case, is to accurately determine the structural parameters, this refinement process must be conducted with the utmost care.

This first example enabled us to illustrate the use of a control file, but the structure we described is very simple, since all of the atoms are in a set position and since there are only two types of atoms in this structure. We will continue with a new example based on a phase with a more complex structure, which was solved by diffraction on a polycrystalline sample [CHA 95]. The chemical formula of the compound in question is $NaBi_2Sb_3O_{11}$ and its crystal structure was solved based on the pattern shown in Figure 4.9a. This pattern was produced by using a Bragg-Brentano system equipped with a back monochromator made of graphite. Therefore, the incident beam is comprised of the two radiations $K_{\alpha 1}$ and $K_{\alpha 2}$ (see insert). Furthermore, the pattern was produced without Soller slits, which is why the beam's divergence caused a certain peak dissymmetry at low angles. When the structure was refined, peaks at angles below 20° in 2θ were voluntarily omitted.

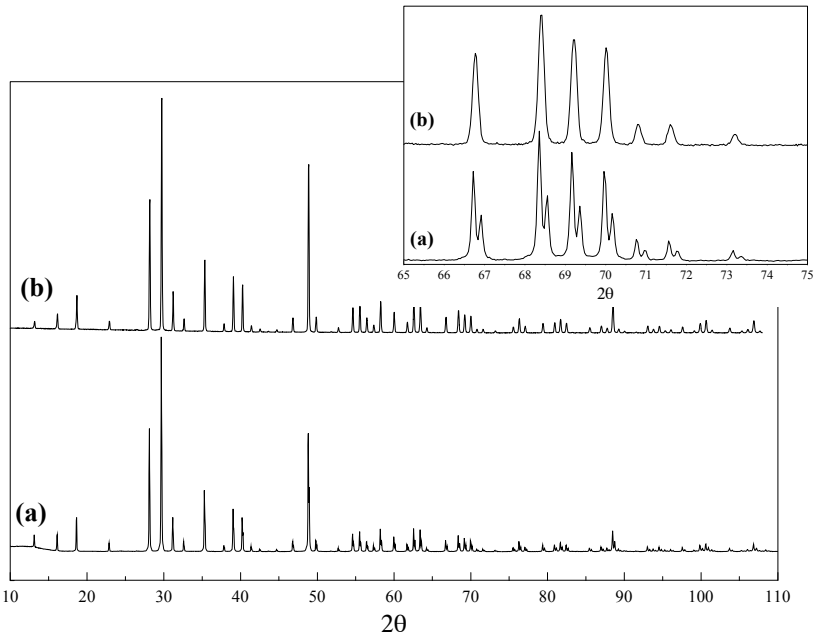

Figure 4.9. *Diffraction patterns of the compound $NaBi_2Sb_3O_{11}$. The pattern shown in (a) was produced by using a Bragg-Brentano diffractometer equipped with graphite back monochromator. The pattern shown in (b) was produced with a Debye-Scherrer-Hull system equipped with a quartz front monochromator*

We then produced another diffraction pattern for the same sample with a system equipped with a front monochromator and a curved position sensitive detector [MAS 96a]. The pattern, produced in reflection on a flat plate sample (see Chapter 3) is shown in Figure 4.9b. This time, the peaks are unique and the use of a position sensitive detector has made it possible to significantly reduce the acquisition time of the pattern. We note that the peak widths measured in this case are higher than those obtained with the Bragg-Brentano system. As we showed in Chapter 3, this effect is caused by the fact that the diffracted beams are not focused in Debye-Scherrer systems. Finally, this study enables us to compare the influence on the structural refinement under two different acquisition conditions [MAS 96a]:

– focusing system: peaks split in two because of the presence of the $K_{\alpha 2}$ radiation and dissymmetry caused by the divergence;

– average resolution system: strictly monochromatic radiation, symmetrical peaks and significantly reduced acquisition time.

The fittings performed on these two diagrams are shown in Figure 4.10.

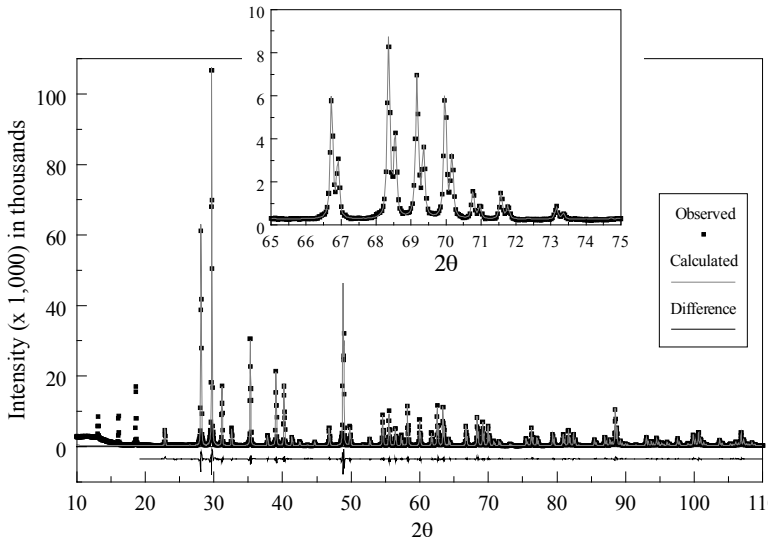

(a) Rietveld fitting of the pattern produced by using a Bragg-Brentano system

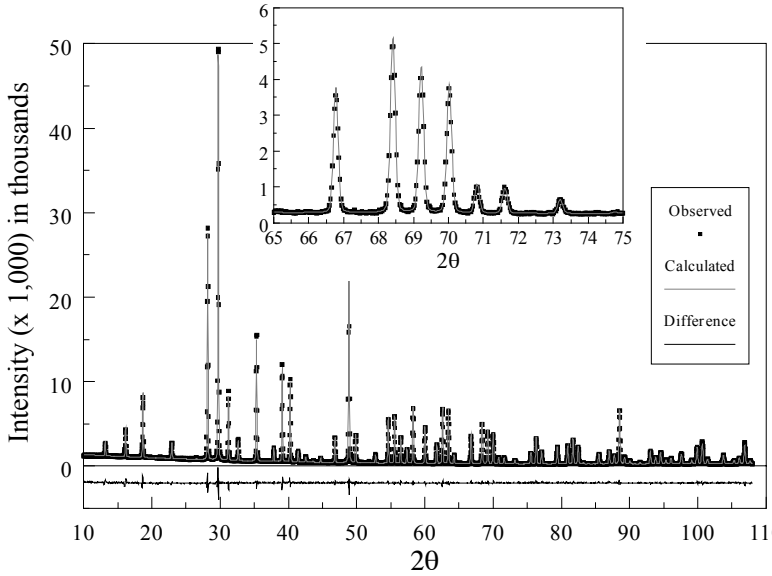

(b) Rietveld fitting of the pattern produced in asymmetrical diffraction with a front monochromator and a curved position sensitive detector

Figure 4.10. *Rietveld refinements of diffraction patterns obtained with a powder of* $NaBi_2Sb_3O_{11}$

The refinement results are shown in Table 4.3.

Atoms	**Na**	**Bi**	**Sb**	**O_1**	**O_2**	**O_3**
Site	4(b)	8(e)	12(g)	24(h)	12(f)	8(e)
X_{DS}	0	0.37666 (5)	0.5885 (1)	0.5395 (10)	0.6140 (9)	0.1451 (7)
X_{BB}	0	0.37648 (6)	0.5430 (1)	0.5430 (11)	0.6104 (10)	0.1444 (9)
Y_{DS}	0	X	0.75	0.2495 (6)	0.25	X
Y_{BB}	0	X	0.75	0.2537 (8)	0.25	X
Z_{DS}	0	X	0.25	0.5910 (7)	0.25	X
Z_{BB}	0	X	0.25	0.5881 (9)	0.25	X
B_{DS} ($Å^2$)	0.11 (15)	0.84 (17)	0.42 (20)	1.16 (20)	1.04 (20)	2.06 (30)
B_{BB} ($Å^2$)	0.21 (18)	0.59 (2)	0.23 (2)	0.81 (23)	0.78 (29)	1.44 (34)

Table 4.3a. *Comparison of the positions and thermal agitation factors of the atoms obtained from the refinements of the patterns produced with a Debye-Scherrer system (DS) and with a Bragg-Brentano (BB) diffractometer*

	R_p (%)	**R_{wp} (%)**	**R_{exp} (%)**	**R_{Bragg} (%)**	**Goodness of fit**
DS	7.88	8.4	4.73	2.14	1.8
BB	6.88	9	2.71	2.49	3.32

Table 4.3b. *Comparison of the reliability factors for the refinements of the two patterns*

The structural characteristics and the quality of the fittings are very close. The phase we studied has a cubic symmetry and therefore has a small number of peaks, which decreases the influence of the diffraction signal distortion caused by the $K_{\alpha 2}$ radiation. This experimental study shows that solving the structures of relatively simple crystal phases does not require very high resolution diffractometers. Also, this comparison illustrates the fact that in this type of analysis peak shapes play a small role. This is why, even though the Bragg-Brentano system used is not optimized, which causes a number of significant aberrations in the shapes of the measured peaks, we were able to fit these peaks and the determination of the integrated intensities is relatively correct. Of course, the situation is different when studying a phase with a lower crystal symmetry, in which case it would be highly recommended to use a system with a monochromatic beam [CUS 99, HIL 87]. This aspect is even more important when the sample presents a certain density of structural defects that would modify the shape of the peaks. We will see in Part 2 of this book that whole pattern fitting can be used to quantify these defects. It is then necessary to define the instrumental function as best as possible.

Beyond this illustration with examples, we will define different parameters that affect the quality of the structural determination when using the Rietveld method.

4.4.2.3.2. Influence of the measurement increment and of the counting duration

Hill and Madsen [HIL 84, HIL 86] have focused on defining the influence of the measurement increment and of the acquisition time per point on the resolution of the structure. Naturally, the number of points has to be high and the exposure time long enough. However, it is useless to greatly reduce the measurement increment, since the value has to be chosen with respect to the full width at half maximum of the measured peaks. A decrease in the increment for a constant full width at half maximum simply leads to an increase in the number of points defining each peak. The authors have shown that the optimal increment is between a fifth and a half of the full width at half maximum.

Increasing the measurement duration per point improves the quality of the diagrams and in particular the definition of the peak profiles. Generally speaking, we can assume that the exposure time is long enough if the maximum intensity of the peaks reaches a few thousands for the average intensity peaks. Naturally, the peaks at high angles are less intense than those located at the beginning of the diagram, making it a good idea to divide the diagram into several sections, and to increase the acquisition time for the peaks located at high angles [CUS 99].

Note finally that the range of the study has to be as wide as possible. In particular, taking into account peaks diffracted at high angles improves the refinement of the cell parameters and of the thermal agitation factors.

4.4.2.3.3. Preferential orientation

Likewise, for quantitative phase analyses, the quality of the structure determination is related to limits set on the modifications of the diffracted intensity, caused by preferential orientation effects. This problem which is specific to diffraction on polycrystalline samples generally constitutes one of the limitations of the studies on these types of samples and deserves attention particularly in the case of structural studies.

The number of crystals comprising the sample has to be very large and their orientation has to be random (see section 4.2). It sometimes happens, however, that this condition is impossible to fulfill, resulting in discrepancies between the integrated intensities of the peaks in the pattern and the values strictly related to structural parameters. When the nature of this preferential orientation is known, it is possible to take it into account in the refinement. This led several authors [ALT 96, PES 95] to incorporate, into their Rietveld refinement programs, preferential orientation parameters based on the use of the March function which was first introduced by Dollase [DOL 86]. Nonetheless, it is still better to avoid any texture effects.

This page intentionally left blank

PART 2

Microstructural Analysis

In real crystals, the triply periodic and infinite arrangement of crystal cells that describes ideal crystals is distorted by a large number of defects. The real structure of crystals includes punctual defects (vacancies, interstitial atoms), linear defects (dislocations), plane defects (stacking faults) and volume defects (finite sizes of the crystals, microstrains, composition fluctuations). The presence of these crystal imperfections modifies the distribution of the diffracted intensity. If the defects are localized and if their positions are not correlated, the intensity is distributed over the whole pattern, something which is referred to as Laue scattering or diffuse scattering. When the defects extend over large areas, the intensity distribution around the Bragg peaks widens[1] and is distorted either symmetrically or dissymmetrically.

Some of these effects were observed shortly after the discovery of X-ray diffraction [SCH 18]. However, the precise description of their influence on the diffraction signal required considerable work, and the quantitative analysis of these defects by X-ray diffraction only became widespread a few decades ago. Improvements in the instrumentation and the calculation capabilities now make this type of analysis possible with measurements conducted on traditional diffractometers. This led to the creation of a new field for X-ray diffraction, referred to as microstructural analysis by X-ray diffraction [SYN 99]. In Chapters 6 and 7, we will describe the main methods used for the quantitative study of these various

1 Therefore, these defects lead to an increase in peak width. We can also consider that the peaks obtained correspond to the overlapping of the diffraction signal related to the perfect crystals to which is added another signal caused by the defects. This signal, located mostly around the Bragg peaks, is also called diffuse scattering [WEL 04].

defects, both in randomly oriented polycrystalline materials (Chapter 6) and in epitaxial films (Chapter 7). Chapter 5 describes the influence of defects on the intensity distribution. This approach will be explained in the context of the kinematic theory of X-ray diffraction.

Chapter 5

Scattering and Diffraction by Imperfect Crystals

5.1. Punctual defects

The amplitude diffracted by a crystal cell free of any defects is given by:

$$F(\vec{S}) = \sum_i f_i e^{2\pi i \vec{s}.\vec{r}_i} \qquad [5.1]$$

If we consider all of the crystal cells, the diffracted intensity is obtained by adding for every cell the products J = FF*, which leads to:

$$I(\vec{S}) = \sum_{crystal} J(\vec{S}) \qquad [5.2]$$

with:

$$J(\vec{S}) = \sum_i \sum_j f_i f_j^* e^{2\pi i \vec{s}.(\vec{r}_i - \vec{r}_j)} \qquad [5.3]$$

5.1.1. *Case of a crystal containing randomly placed vacancies causing no relaxation*

In order to make matters simpler, we will assume that the crystal is only comprised of one kind of atom. It contains N atomic sites, but n sites are vacant. The double sum defining the expression of the factor J can be divided into two parts:

– for i = j, there are (N – n) vectors $\vec{r}_i$ for which the scattering factor is equal to $f = f_i = f_j$ and n vectors for which the associated value of the scattering factor is zero. Therefore, this contribution is equal to $(N - n)f^2$;

– for all the other vectors $\vec{r}_i$, the probability of having an atom in the position defined by r_i is equal to (N – n)/N. This probability is the same for any i (since the positions of the vacancies are random). Therefore, the contribution of this part is:

$$\left(\frac{N-n}{N}\right)^2 f^2 e^{2\pi i \vec{s}.(\vec{r}_i - \vec{r}_j)} \qquad [5.4]$$

We obtain:

$$J(\vec{S}) = (N-n)f^2 + \left(\frac{N-n}{N}\right)^2 f^2 \sum\sum_{i \neq j} e^{2\pi i \vec{s}.(\vec{r}_i - \vec{r}_j)} \qquad [5.5]$$

This double sum can be extended to all values of i and j by adding and subtracting a term equal to zero:

$$J(\vec{S}) = (N-n)f^2 + \left[\left(\frac{N-n}{N}\right)^2 f^2 \sum_i \sum_j e^{2\pi i \vec{s}.(\vec{r}_i - \vec{r}_j)}\right] - \frac{(N-n)^2}{N} f^2 \qquad [5.6]$$

which leads to:

$$J(\vec{S}) = \left[\left(\frac{N-n}{N}\right)^2 f^2 \sum_i \sum_j e^{2\pi i \vec{s}.(\vec{r}_i - \vec{r}_j)}\right] + f^2 \left[(N-n) - \frac{(N-n)^2}{N}\right] \qquad [5.7]$$

hence:

$$J(\vec{S}) = \left[\left(\frac{N-n}{N} \right)^2 f^2 \sum_i \sum_j e^{2\pi i \vec{s}.(\vec{r}_i - \vec{r}_j)} \right] + f^2 \left[\frac{n(N-n)}{N} \right] \qquad [5.8]$$

The first term of this expression corresponds to the diffraction by a crystal free of any defects, but comprised of atoms with an average scattering factor equal to (1 – n/N)f. The second term leads to a continuous distribution of the scattered intensity. This intensity decreases as the square of the diffusion factor; its value is proportional to the number of vacancies and equal to the scattering by n independent atoms.

We illustrated this effect in Figure 5.1 by considering an imaginary crystal with a cubic symmetry, a cell parameter of 5 Å and comprised of lithium atoms located on all of the cube's vertices[1]. Lithium has three electrons, and if we assume that the two atomic orbitals K and L can be approximated by spheres with diameters $a_K = 0.2$ Å and $a_L = 1.6$ Å, respectively, then the scattering factor f of each electron is given by the equation:

$$f_e = \int_0^\infty 4\pi r^2 \frac{e^{-(2r/a)}}{\pi a^3} \frac{\sin kr}{kr} dr = \frac{1}{\left[1 + (2\pi a \sin\theta/\lambda)^2\right]^2} \qquad [5.9]$$

Therefore, the scattering factor of lithium is given by:

$$f_{Li} = \frac{2}{\left[1 + (2\pi a_K \sin\theta/\lambda)^2\right]^2} + \frac{1}{\left[1 + (2\pi a_L \sin\theta/\lambda)^2\right]^2} \qquad [5.10]$$

1 This imaginary crystal was chosen out of a concern for simplicity and is only presented to illustrate, in a simple case, how to formalize the influence of the presence of vacancies on the diffraction signal.

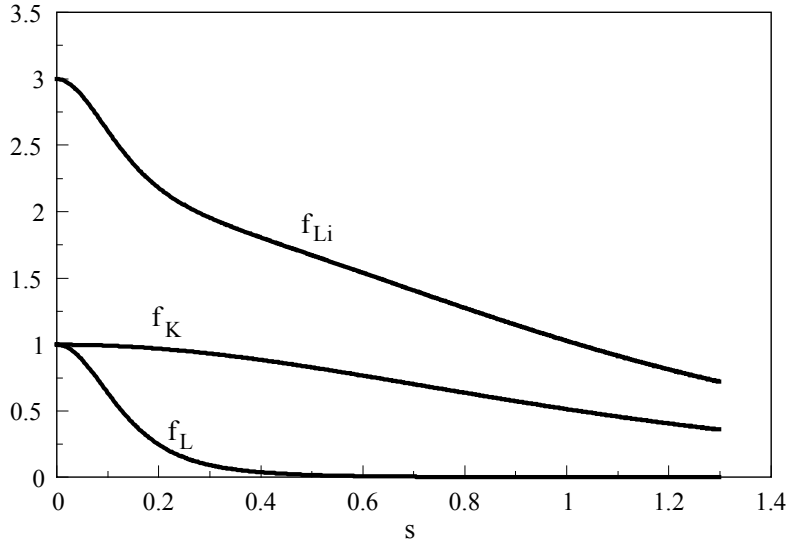

(a) Evolution of the scattering factor of a lithium atom according to the scattering vector

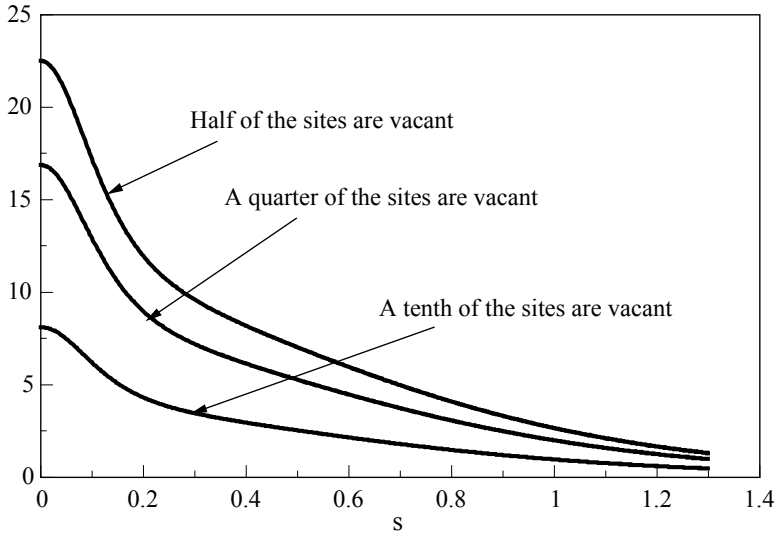

(b) Diffuse scattering associated with the presence of vacancies randomly distributed over the sites

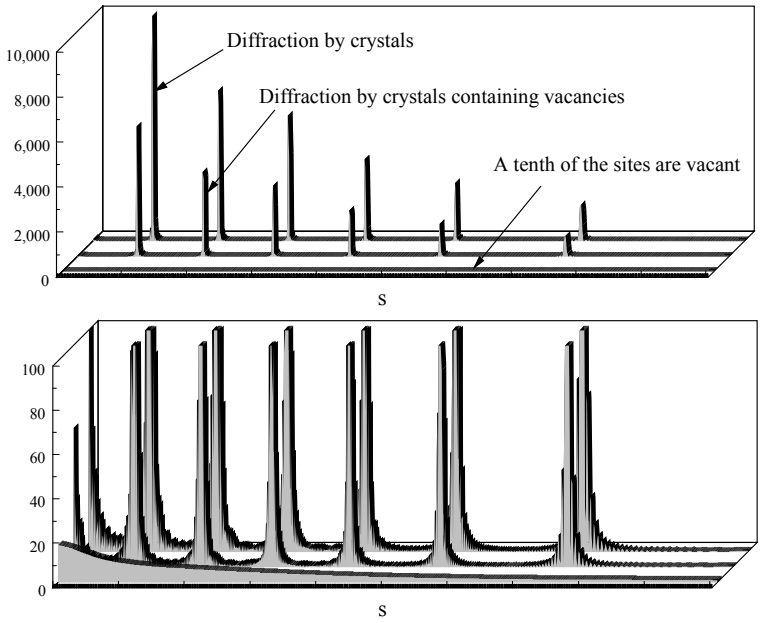

(c) Combination of the diffraction signal and of the diffuse scattering signal

Figure 5.1. *Observation of diffuse scattering associated with the presence of randomly distributed vacancies*

The intensity of the diffuse scattering is obtained by multiplying the square of this diffusion factor with the term $n(N - n)/N$. Figure 5.1b shows several examples for different numbers of vacancies n.

These first results call for a few general and simple comments. First of all, as you can see, the diffuse scattering signal is much flatter than the diffraction signal. Its maximum intensity is roughly 30 times smaller than the maximum diffracted intensity. The diffuse scattering, spread out as it is in this case over the entire reciprocal space, is difficult to measure and requires adequate equipment. Note that, on the other hand, the decrease in the diffracted intensity maxima is quite visible.

5.1.2. *Case of a crystal containing associated vacancies*

Vacancies in a crystal can be associated together and form clusters. Let us consider a crystal containing, as before, n vacancies which are, this time, associated in pairs. The probability of finding a vacancy is no longer uniform over the entire crystal. In fact, the probability of finding a vacancy at any distance from another

vacancy is equal to half the probability of finding that vacancy at a distance equal to zero.

The number of vacancies is identical as that in the previous case, so the diffracted intensity is the same but, this time, the diffuse scattering is modulated with maxima located in the positions of the Bragg peaks. The intensity distribution associated with that scattering is expressed as:

$$f^2\left[\frac{n(N-n)}{N}\right]\left(1+\cos\left(2\pi\vec{a}.\vec{s}\right)\right) \qquad [5.11]$$

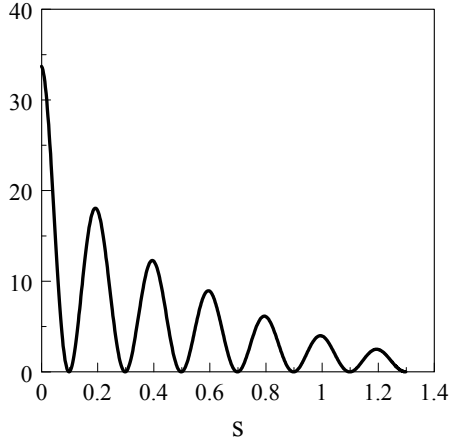

(a) Diffuse scattering due to the presence of vacancy clusters

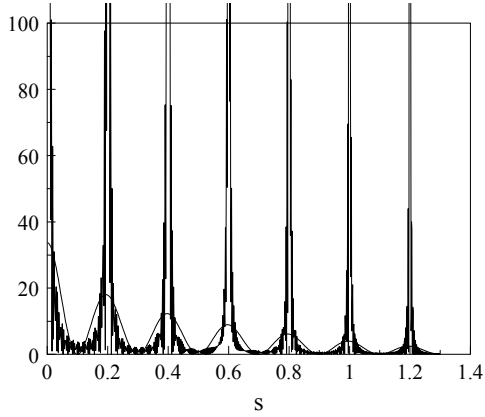

(b) Combination of the diffraction pattern and the diffuse scattering

Figure 5.2. *Modulation of the diffuse scattering associated with the presence of vacancy clusters*

If the number of vacancies contained in each cluster increases, then the contribution from diffuse scattering becomes more and more localized on the Bragg peaks and the associated distribution becomes more refined.

This description presented in the case of presence of vacancies can be made in a similar way when the crystal contains atoms in interstitial positions.

5.1.3. *Effects of atom position relaxations*

We first showed the influence of vacancies or interstitial atoms on the diffracted and scattered signals by overlooking the effects of local cell deformations associated with the presence of these defects.

When the crystal cell contains vacancies or atoms in interstitial positions, the positions of the neighboring atoms of this localized defect are affected and these atoms are no longer exactly in their reference position. This is called position relaxation. The farther away atoms are from the defect, the smaller the variations of their positions. Usually, only the first and second neighbors are assumed to be affected.

In order to illustrate the influence of this effect on the diffracted intensity and on the diffuse scattering signal, we will consider the simple case where only the first two neighbors surrounding the interstitial atom are affected and we will assume that the atoms are moved by a distance of a/4.

If we assume as we did before that the cell contains n vacancies, the probability of an atom's presence on a site is $(N - n)/N$ and the diffracted intensity of each peak will be decreased by a factor corresponding to this term. Furthermore, secondary peaks associated with the atomic displacements appear. The structure factor and hence the diffracted intensity are modulated (see Figure 5.3a).

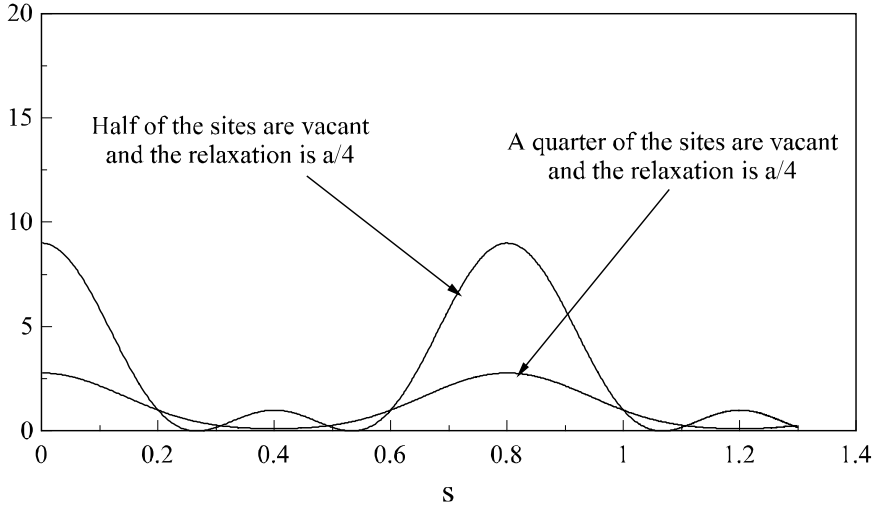

(a) Modulation function of the diffracted intensity

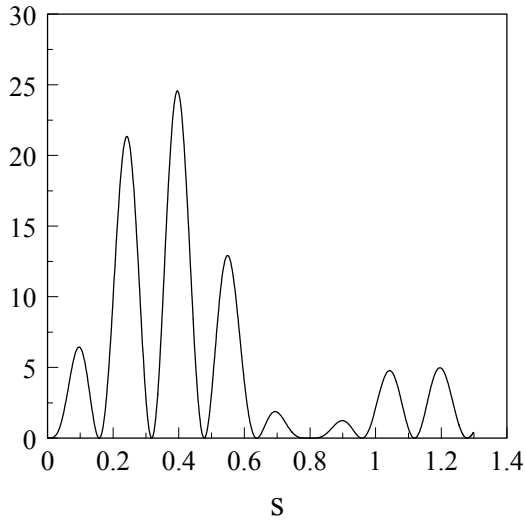

(b) Associated diffuse scattering

Figure 5.3. *Effects of the atom position relaxation caused by the presence of vacancies or interstitial atoms*

The structure factor is modulated by the term:

$$\frac{(N-n)}{N}+2\frac{n}{N}\cos\left(2\pi\frac{\vec{a}.\vec{s}}{4}\right) \qquad [5.12]$$

The diffracted intensity is then multiplied by the square of this expression, or:

$$\left(\frac{(N-n)}{N}\right)^2\left(1+2\frac{n}{N-n}\cos\left(2\pi\frac{\vec{a}.\vec{s}}{4}\right)\right)^2 \qquad [5.13]$$

Therefore, the diffraction peaks that correspond to the product of the Laue function and of a function of the same form as the one shown in Figure 5.3a have secondary maxima, also called satellite peaks.

The diffuse scattering distribution is expressed according to the equation:

$$f^2\left[\frac{n(N-n)}{N}\right]\left(1-\cos\left(2\pi\frac{\vec{a}.\vec{s}}{4}\right)\right)\left(1-\cos\left(2\pi\frac{5\vec{a}.\vec{s}}{4}\right)\right) \qquad [5.14]$$

This function is equal to zero when s = 0, then increases as we get farther away from the origin of the reciprocal lattice. The positions of the maxima are related to the displacements with respect to the reference positions of the atomic sites.

5.2. Linear defects, dislocations

Figure 5.4a shows a representation of an edge dislocation. This type of defect is very common, particularly in metals, and corresponds to major local deformations of the atomic arrangement. The diffracted amplitude is affected by the displacements of the atoms with respect to their reference positions in the same crystal without defects.

Let us consider a crystal containing a certain number of dislocations. In the vicinity of one of these dislocations, a given crystal cell undergoes a displacement $\vec{\delta}$ with respect to its reference position defined by the vector $\vec{R}$ in the crystal without defects. The amplitude diffracted by a displaced cell n is expressed as:

$$A_n = F_n e^{2\pi i\vec{s}.(\vec{R}_n+\vec{\delta}_n)} \qquad [5.15]$$

Let $J_{n,m} = A_n.A_m^*$. Note that the total intensity diffracted by the crystal is given by:

$$I=\sum_{n,m} J_{n,m}$$

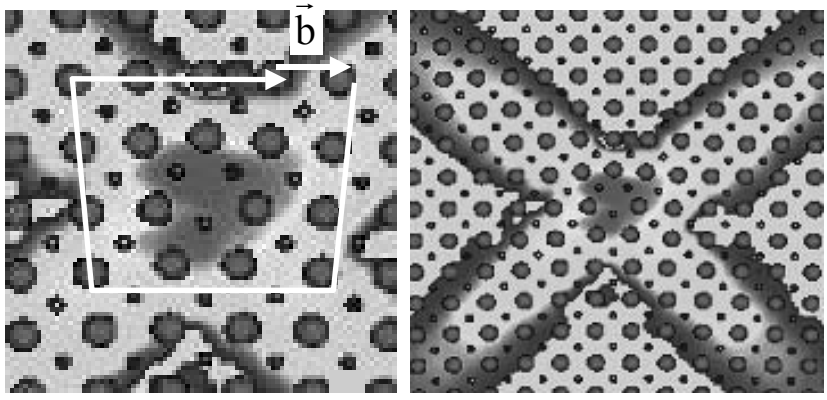

(a) (b)

Figure 5.4. *Simplified representation of an edge dislocation. (a) Drawing a path around the core of the dislocation helps visualize the Burger vector of that dislocation. (b) Representation of the displacement field of the atoms surrounding the dislocation*

The product $J_{n,m}$ is written:

$$J_{n,m}=\left[F_n e^{2\pi i\vec{s}.(\vec{R}_n+\vec{\delta}_n)}\right]\left[F_m^* e^{-2\pi i\vec{s}.(\vec{R}_m+\vec{\delta}_m)}\right] \quad [5.16]$$

hence:

$$J_{n,m}=F_n F_m^* e^{2\pi i\vec{s}.(\vec{R}_n-\vec{R}_m)} e^{2\pi i\vec{s}.(\vec{\delta}_n-\vec{\delta}_m)} \quad [5.17]$$

and by noting that $F_n = F_m = F$, since all the cells are identical[2], we get:

$$I=|F|^2 \sum_{n,m} e^{2\pi i \vec{s}.(\vec{R}_n-\vec{R}_m)} e^{2\pi i \vec{s}.(\vec{\delta}_n-\vec{\delta}_m)} \quad [5.18]$$

5.2.1. *Comments on the displacement term*

Figure 5.4b shows the displacement field associated with the dislocation described in Figure 5.4a. The presence of a dislocation causes atomic displacements which are too significant to be overlooked, even for atoms located relatively far away. Thus, in a crystal containing a certain dislocation density, the positions of the atoms are altered by displacements $\vec{\delta}$ that correspond to the sum of elementary displacements $\vec{u}$ associated with each of the dislocation.

We have:

$$\vec{\delta}_n=\sum_t c_t \vec{u}_{t,n} \quad [5.19]$$

where $\vec{u}_{t,n}$ is the displacement caused by the dislocation found in $\vec{R}_t$ for the atom found in $\vec{R}_n$ and:

$$\begin{cases} c_t = 1 \text{ if there is a defect in t} \\ c_t = 0 \text{ if there is no defect in t} \end{cases}$$

We obtain:

$$I=|F|^2 \sum_{n,m} e^{2\pi i \vec{s}.(\vec{R}_n-\vec{R}_m)} e^{2\pi i \vec{s}.\left(\sum_t c_t \vec{u}_{t,n}-\sum_t c_t \vec{u}_{t,m}\right)} \quad [5.20]$$

hence

$$I=|F|^2 \sum_{n,m} e^{2\pi i \vec{s}.(\vec{R}_n-\vec{R}_m)} e^{2\pi i \vec{s}.\sum_t c_t\left(\vec{u}_{t,n}-\vec{u}_{t,m}\right)} \quad [5.21]$$

2 We assume here that there are no variations in the chemical composition.

and

$$I=\left|F\right|^2\sum_{n,m}e^{2\pi i\vec{s}.(\vec{R}_n-\vec{R}_m)}\prod_t e^{2\pi i\vec{s}.\left(\vec{u}_{t,n}-\vec{u}_{t,m}\right)c_t} \qquad [5.22]$$

If we consider that the positions of the dislocations are random, the term in the product can be expressed by its mean value according to c_t. We then assume that these variables are not correlated, in other words, that each dislocation is independent of the others. Let us assume that $c_t = 1$ with a probability c which corresponds to the concentration of defects and a probability $1 - c$ to have $c_t = 0$ with a probability $1 - c$. This leads to:

$$\left\langle e^{2\pi i\vec{s}.(\vec{u}_{t,n}-\vec{u}_{t,m})c_t}\right\rangle = c\left(e^{2\pi i\vec{s}.(\vec{u}_{t,n}-\vec{u}_{t,m})}\right)+(1-c)e^{2\pi i\vec{s}.(\vec{u}_{t,n}-\vec{u}_{t,m})0} \qquad [5.23]$$

$$=1+c\left(e^{2\pi i\vec{s}.(\vec{u}_{t,n}-\vec{u}_{t,m})}-1\right)$$

Let $U_t = c\left(e^{2\pi i\vec{s}.(\vec{u}_{t,n}-\vec{u}_{t,m})}-1\right)$. We then have:

$$\prod_t\left\langle e^{2\pi i\vec{s}.(\vec{u}_{t,n}-\vec{u}_{t,m})c_t}\right\rangle=\prod_t\left(1+U_t\right) \qquad [5.24]$$

By noting that $a^x = e^{xlna}$, we get:

$$\prod_t\left\langle e^{2\pi i\vec{s}.(\vec{u}_{t,n}-\vec{u}_{t,m})c_t}\right\rangle=e^{\sum_t\ln\left(1+U_t\right)} \qquad [5.25]$$

If we write the logarithm's first order Taylor expansion about 0, we get:

$$\prod_t\left\langle e^{2\pi i\vec{s}.(\vec{u}_{t,n}-\vec{u}_{t,m})c_t}\right\rangle=e^{\sum_t U_t} \qquad [5.26]$$

$$\Rightarrow\prod_t\left\langle e^{2\pi i\vec{s}.(\vec{u}_{t,n}-\vec{u}_{t,m})c_t}\right\rangle=e^{-c\sum_t\left(1-e^{2\pi i\vec{s}.(\vec{u}_{t,n}-\vec{u}_{t,m})}\right)} \qquad [5.27]$$

$$\Rightarrow \prod_t \left\langle e^{2\pi i \vec{s}.(\vec{u}_{t,n}-\vec{u}_{t,m})c_t} \right\rangle = e^{-T} \qquad [5.28]$$

with

$$T = c\sum_t \left(1 - e^{2\pi i \vec{s}.(\vec{u}_{t,n}-\vec{u}_{t,m})}\right) \qquad [5.29]$$

Finally:

$$I = |F|^2 \sum_{n,m} e^{2\pi i \vec{s}.(\vec{R}_n - \vec{R}_m)} e^{-T} \qquad [5.30]$$

This relation, established in 1963 by Krivoglaz [KRI 63, KRI 69], is the fundamental equation for describing the expression of the total intensity diffracted by a crystal containing a concentration c of dislocations. As you can see, this intensity corresponds to the one diffracted by a crystal free of any dislocations multiplied by a factor (e^{-T}) smaller than 1 and that decreases when T increases, and hence when the dislocation density increases (see equation [5.29]). This generic form of the effect of dislocations on the diffracted intensity is similar to the one describing the effect of temperature, which actually corresponds to variations in atomic mobility and therefore to a certain form of atom displacements with respect to their reference position.

Likewise, note that the intensity distribution's form is related to the term T and therefore will depend on the displacement field $\vec{u}$ surrounding each dislocation, which means that, in the end, it has to be studied separately for every type of dislocation. Krivoglaz began by analyzing the case of a cylindrical crystal containing screw dislocations with Burger vectors parallel to the cylinder's axis. In this case, he showed that the intensity distribution is a Gaussian function. These studies were pursued and generalized and finally, we can consider to a first approximation[3] that the intensity distribution is a Voigt function [LEV 97], the width of which is written:

$$\beta = \sqrt{\rho\chi} f(M) \tan\theta \qquad [5.31]$$

3 Other authors [MUG 86, GRO 88] have shown that the shape of the intensity distribution associated with the presence of dislocations is asymmetric.

where ρ is the dislocation density, χ is the contrast factor that depends on the dot product $\vec{s}.\vec{b}$, M is a dimensionless factor given by the relation $M = r_c\sqrt{\rho}$ and r_c is the cut-off radius beyond which the dislocation is no longer noticeable.

Many studies have focused on accurately determining term χ as well as function f(M).

5.2.2. *Comments on the contrast factor*

Before we give the expressions of the contrast factor and of its different components, we have to specify the relative orientations of the various vectors involved. These orientations are defined in Figure 5.5. Generally speaking, vector $\vec{l}$ which is parallel to the dislocation line and Burger vector $\vec{b}$ define the glide plane. The right-handed coordinate system (Ox,Oy,Oz) is defined so that the axes Oy and Oz are in the glide plane and, by convention, the Oz axis is parallel to $\vec{l}$. The position of the diffraction vector $\vec{s}$ with respect to the glide plane is arbitrary. The vectors $\vec{l}$ and $\vec{s}$ define a second plane. We will specify the direction of the diffraction vector with respect to the glide plane by using three angles. The angle between $\vec{s}$ and $\vec{l}$ is denoted by ψ_3. The angle ψ_1 is the angle between the projection of $\vec{b}$ onto the Oy axis and $\vec{s}$. Finally, ψ_2 denotes the angle between the cross product $\vec{l} \wedge \vec{b}$ and $\vec{s}$.

Wilkens [WIL 70] followed by Klimanek and Kuzel [KLI 88] established the expression of the contrast factor based on diagrams similar to the one found in Figure 5.5. Generally, this factor χ is expressed as follows:

$$\chi = \chi_v \cos^2\gamma + \chi_c \sin^2\gamma + \chi_i \sin\gamma\cos\gamma \qquad [5.32]$$

with:

χ_v: contrast factor for screw dislocations;

χ_c: contrast factor for edge dislocations;

x– χ_i: contrast factor resulting from the interactions between the different kinds of dislocations.

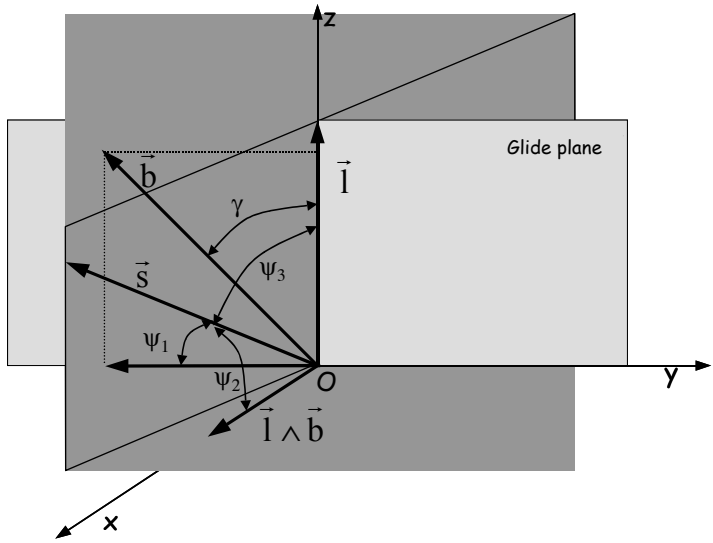

Figure 5.5. *Representation of the angles between the different vectors that characterize a dislocation*

As Figure 5.5 shows, γ is the angle between the dislocation line and the Burger vector. Note that $\gamma = 0$ or π for a screw dislocation and $\gamma = \pm\pi/2$ for an edge dislocation.

χ_v, χ_c and χ_i are given, respectively, by the following expressions [WIL 70, KLI 88]:

$$\chi_v = \cos^2\psi_3 \sin^2\psi_3 \qquad [5.33]$$

$$\chi_c = \frac{1}{4(1-\nu^2)}\left[(5/2-6\nu+4\nu^2)\cos^4\psi_1 + (1/2-2\nu+4\nu^2)\cos^4\psi_2 + (3-8\nu+8\nu^2)\cos^2\psi_1\cos^2\psi_2\right] \qquad [5.34]$$

and

$$\chi_i = \cos\psi_1 \cos\psi_3 \sin^2\psi_3 \left(\frac{6-14\nu+8\nu^2}{4(1-\nu)^2}\right) \qquad [5.35]$$

where ν is the Poisson coefficient.

5.2.3. Comments on the factor f(M)

We saw that $M = r_c\sqrt{\rho}$, which means that when the dislocations are associated with long range deformation fields, M is much greater than 1. If the dislocations are evenly and almost regularly distributed, M is close to 1. Finally, if the dislocations cause short range deformations, M is much smaller than 1.

Wilkens [WIL 76] showed that the influence of this parameter M was noticeable essentially in the shape of the intensity distribution. When M is much smaller than 1, the profile is Lorentzian, whereas it is Gaussian when M is much greater than 1. Experimentally, this term M typically varies between 0.1 and 10.

Based on these considerations, some authors [WU 98] have suggested more recently to digitally express an approximation of the function f(M). They laid out the following relation:

$$f(M) = a \ln(M + 1) + b \ln^2(M + 1) + c \ln^3(M + 1) + d \ln^4(M + 1) \qquad [5.36]$$

with: a = –0.173; b = 7.797; c = –4.818 and d = 0.911.

5.3. Planar defects

Ideal crystals can be defined as a series of evenly stacked atomic planes. Breaks in this stacking caused by the presence of two-dimensional defects modify the diffraction signal. Only the crystal cells located between two planar defects scatter in phase. From this perspective, the effect of planar defects is similar to the size effect, which is described later on. In other words, the number of crystal cells that lead to coherent scattering is limited, resulting in an increase in diffraction peak widths, as shown in Figure 1.10. However, in the case of planar defects, this effect is limited to the direction normal to these defects and therefore only certain peaks will be affected. Thus, in the diffractogram obtained with a polycrystalline sample, the increase in width of the peaks will strongly depend on the Miller indices. This dependence is related to the symmetry of the crystals in question [SYN 99]. We will only describe the general effect without describing the various cases in detail.

Let us consider a crystal comprised of an arbitrary number of different layers. The electron density of the i^{th} layer is $\rho_i(\vec{r})$ and these layers are evenly stacked along the direction of the translation vector $\vec{R}_i$. The presence of a stacking fault in the series of layers is equivalent to replacing a layer with electron density $\rho_i(\vec{r})$ with a layer with density $\rho_j(\vec{r})$ associated with a translation vector $\vec{R}_j$. Locally,

this means an additional electron density $\Delta_{ij}(\vec{r})$ and the replacement of the vector $\vec{R}_i$ with $\vec{R}_i + \vec{\delta}_{ij}$. The probability of such a fault is denoted by α_{ij}.

The diffracted amplitude associated with a layer i with electron density $\rho_i(\vec{r})$ is equal to:

$$F_i\left(\vec{S}\right) = \int \rho_i(\vec{r}) e^{2\pi i \vec{s}.\vec{r}} d\vec{r} \qquad [5.37]$$

and the diffracted amplitude associated with the stacking fault is denoted by G_{ij}, hence:

$$G_{ij}\left(\vec{S}\right) = \int \Delta_{ij}(\vec{r}) e^{2\pi i \vec{s}.\vec{r}} d\vec{r} \qquad [5.38]$$

The total diffracted intensity can be expressed as a sum of terms I_n, each one associated with an inter-layer vector $\vec{R}_n$. For the vector with modulus equal to 0, the intensity is expressed:

$$I_0\left(\vec{S}\right) = N\sum_i g_i\left(1 - A_i\right)\left|F_i\left(\vec{S}\right)\right|^2 + \sum_j \alpha_{ij}\left|F_i\left(\vec{S}\right) + G_{ij}\left(\vec{S}\right)\right|^2 \qquad [5.39]$$

N is the number of cells and the term A_{ij} is defined by:

$$A_{ij} = \sum_j \alpha_{ij} \qquad [5.40]$$

where $(1 - A_{ij})$ is the probability that i is not disturbed by the fault. Also, g_i is the probability for a type i layer to be present in a given position in the stacking.

Likewise, the term I_1 is written:

$$I_1\left(\vec{S}\right) = N\left[\sum_i g_i\left[\left(1 - A_i\right)F^*_i\left(\vec{S}\right)\left(F_i\left(\vec{S}\right) + \sum_j \alpha_{ij} G_{ij}\left(\vec{S}\right)\right)\right] e^{2\pi i \vec{s}.\vec{R}_i}\right] + \left[\sum_i g_i \sum_j \alpha_{ij}\left[\left(F^*_i\left(\vec{S}\right) + G^*_{ij}\left(\vec{S}\right)\right).\left(F_j\left(\vec{S}\right) + \sum_k \alpha_{jk} G_{ij}\left(\vec{S}\right)\right)\right] e^{2\pi i \vec{s}.\left(\vec{R}_i + \vec{\delta}_{ij}\right)}\right] \qquad [5.41]$$

The first term corresponds to the contribution from the part free of any faults, and the second term is the diffraction associated with the presence of a fault between two neighboring layers.

The term $F'_i\left(\vec{S}\right)$ can be defined as the mean amplitude diffracted by a layer that is modified or not by the fault. This amplitude is written:

$$F'_i\left(\vec{S}\right) = F_i\left(\vec{S}\right) + \sum_j \alpha_{ij} G_{ij}\left(\vec{S}\right) \qquad [5.42]$$

Additionally, we define:

$$B_i\left(\vec{S}\right) = \left(1 - A_i\right) F'_i\left(\vec{S}\right) + \sum_j \alpha_{ij} F'_i\left(\vec{S}\right) e^{2\pi i \vec{s}.\vec{\delta}_{ij}} \qquad [5.43]$$

The diffracted intensity associating layers with their second neighbors is written as follows:

$$I_2\left(\vec{S}\right) = N\left[\sum_i g_i F^*_i\left(\vec{S}\right) B_i\left(\vec{S}\right) e^{2\pi i \vec{s}.2\vec{R}_i}\right] + \left[\sum_i g_i \sum_j \alpha_{ij}\left(F^*_i\left(\vec{S}\right) + G^*_{ij}\left(\vec{S}\right)\right).B_i\left(\vec{S}\right) e^{2\pi i \vec{s}.\left(\vec{R}_i + \vec{R}_j + \vec{\delta}_{ij}\right)}\right] \qquad [5.44]$$

The contribution to the total diffracted intensity from the unaffected part is written:

$$1 + \left(1 - A_i\right) e^{2\pi i \vec{s}.\vec{R}_i} + \left(1 - A_i\right)^2 e^{2\pi i \vec{s}.2\vec{R}_i} + \ldots \qquad [5.45]$$

The sum of this series is equal to:

$$X_i = \frac{1}{1 - \left(1 - A_i\right) e^{2\pi i \vec{s}.\vec{R}_i}} \qquad [5.46]$$

By noticing that $I_{-n} = I^*_n$ we can give the complete expression of the distributed intensity:

$$I(\vec{S}) = N\left[\sum_i g_i(1-A_i)\left|F_i(\vec{S})\right|^2 + \sum_i g_i \sum_j \alpha_{ij}\left|F_i(\vec{S}) + G_{ij}(\vec{S})\right|^2\right] +$$
$$\left[\sum_i\left[g_i(1-A_i)F^*_i(\vec{S})e^{2\pi i\vec{s}.\vec{R}_i}\right]\left[F'_i(\vec{S}) + X_i e^{2\pi i\vec{s}.\vec{R}_i}\left[B_i + \sum_j \alpha_{ij}X_j e^{2\pi i\vec{s}.(\vec{R}_j+\vec{\delta}_{ij})}\left[B_j + \sum_k \alpha_{jk}X_k e^{2\pi i\vec{s}.(\vec{R}_k+\vec{\delta}_{kj})}[B_k + ...]\right]\right]\right]\right] +$$
$$\sum_i g_i \sum_j \alpha_{ij}\left(F^*_i(\vec{S}) + G^*_{ij}(\vec{S})\right)e^{2\pi i\vec{s}.(\vec{R}_i+\vec{\delta}_{ij})}\left[F'_j(\vec{S}) + X_i e^{2\pi i\vec{s}.\vec{R}_j}[B_j + ...]\right] + \text{etc...}$$

[5.47]

The terms contained in the first bracket correspond to the internal contribution from the layers. The next terms are associated with the presence of faults. When the probability of having faults is low, only a few terms have to be taken into consideration.

This general expression of the distribution of the intensity diffracted by a crystal that contains stacking faults can be directly used to model the measured diffraction peaks [TRE 91]. This method was implemented, for example, for the study of graphite [TRE 91] and also for fitting the intensities diffracted by phyllosilicates [PLA 75, PLA 76].

However, when the crystals that are studied contain few faults, simplified expressions can be found. For example, when crystals contain only one type of layer and if the presence of faults does not modify the structure of these layers, the intensity distribution is written:

$$I(\vec{S}) = N\frac{F^*(\vec{S})}{1-(1-\alpha)e^{2\pi i\vec{s}.\vec{R}}}\left[F(\vec{S}) + \frac{\alpha e^{2\pi i\vec{s}.(\vec{R}+\vec{\delta})}}{1-(1-\alpha)e^{2\pi i\vec{s}.\vec{R}}}\left[F(\vec{S}) + \frac{\alpha e^{2\pi i\vec{s}.(\vec{R}+\vec{\delta})}}{1-(1-\alpha)e^{2\pi i\vec{s}.\vec{R}}}\left[F(\vec{S}) + ...\right]\right]\right]$$
$$+ \ ... \ - \left|F(\vec{S})\right|^2$$

[5.48]

The expression between brackets is a sum of geometric sequences and therefore we get:

$$I\left(\vec{S}\right) = \frac{N\left|F\left(\vec{S}\right)\right|^2 \alpha(1-\alpha)\left(1-\cos 2\pi\vec{s}.\vec{\delta}\right)}{1-\alpha+\alpha^2-(1-\alpha)\cos 2\pi\vec{s}.\vec{R}-\alpha\cos 2\pi\vec{s}.\left(\vec{R}+\vec{\delta}\right)+\alpha(1-\alpha)\cos 2\pi\vec{s}.\vec{\delta}} \quad [5.49]$$

The presence of stacking faults modifies the shape of the diffraction peaks and, furthermore, changes the positions of the maxima in this distribution. From the expression above, we can show that the maximum is displaced by a value ε given by the expression:

$$\varepsilon = \frac{\alpha \sin 2\pi\vec{s}.\vec{\delta}}{1-\alpha\left(1-\cos 2\pi\vec{s}.\vec{\delta}\right)} \quad [5.50]$$

Figure 5.6 illustrates this peak distortion effect with a simple example. The displacement vector $\vec{\delta}$, associated with the presence of faults, was chosen parallel to the scattering vector $\vec{s}$. This simply means that we are considering the peaks of a given family of planes (hkl), characterized by an interplanar distance d given by the norm of the vector $\vec{R}$ and that, sometimes, certain planes of this family are displaced by a value equal to the norm of $\vec{\delta}$ in the direction normal to these planes (see Figure 5.6a).

When the stacking fault rate varies from 5 to 20%, a very clear shift is observed for the maximum of each peak, as well as an increase in width (see Figure 5.6b). The graphs shown in that figure were obtained directly from equation [5.47] by considering that the displacement associated with the stacking fault was equal to a tenth of the interplanar distance.

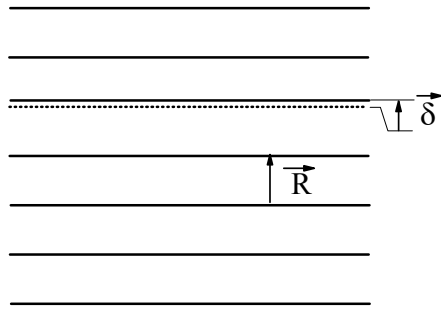

(a) Stacking fault

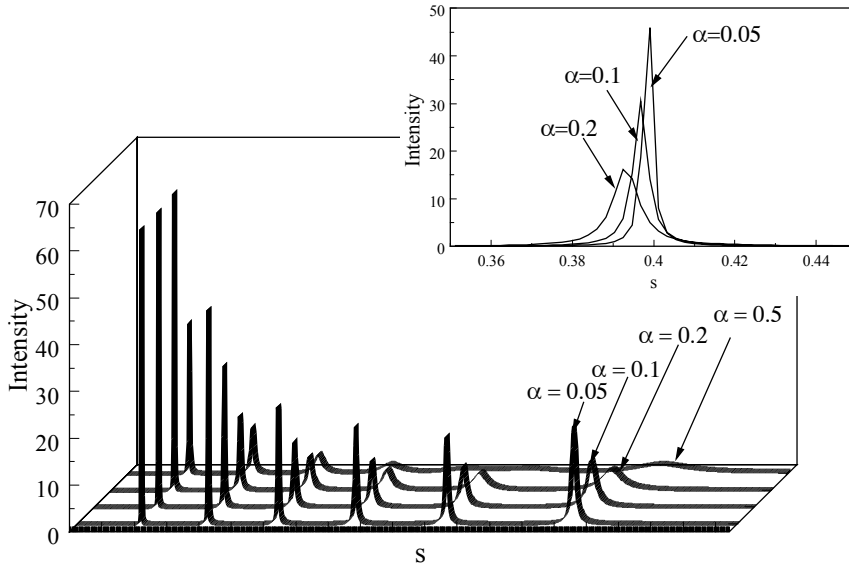

(b) Effect on the diffraction peaks

Figure 5.6. *Deformation of the peaks caused by stacking faults. The displacement associated with the faults was chosen according to the normal to the diffracting planes*

The patterns shown in Figure 5.6 correspond to the distribution of the intensity diffracted by a single crystal. The generalization of this effect to polycrystalline samples was developed by Warren [WAR 69], among others, and more recently by Ustinov [UST 99, UST 04]. In a simplified approach, Wilson [WIL 62a] showed that, when the number of faults is not too high, the intensity distribution can be described by a Lorentzian function. However, as we have already mentioned, the

actual shapes of the peaks depend on the symmetry of the crystal in question. We will not describe here the various cases, which would require tedious mathematical developments. Readers who wish to know more can refer to the works cited above.

5.4. Volume defects

5.4.1. *Size of the crystals*

The simplest three-dimensional effect imaginable is the one corresponding to the fact that crystals are never infinite, something referred to as the size effect. In the case of nanometric characteristic sizes[4], the size and shape of the diffracting crystals can be determined. In a crystal free of any other defects, the position of each cell is described by the vector $\vec{R} = u\vec{a} + v\vec{b} + w\vec{c}$ and the number of cells in each direction is limited. This situation is illustrated by Figure 5.7.

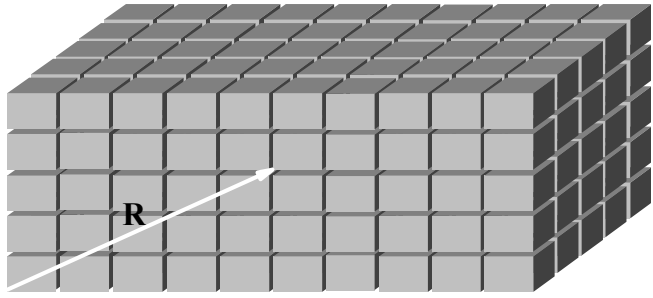

Figure 5.7. *Three-dimensional representation of a finite crystal*

In order to describe the influence of this defect on the diffraction signal, we will determine how size modifies the width of the intensity distribution. This method, which will also be applied to the description of the effects of microstrains, was developed by Stokes and Wilson [STO 42, STO 44] and reviewed by Warren [WAR 69].

4 In practice, the greater the size, the smaller the effect on the intensity distribution. So, clearly, the limit to what size can be measured depends on the instrument's angular resolution. With traditional laboratory diffractometers, the limit size is commonly considered to be in the range of 100 nm. The most recent instruments developed for synchrotron radiation source achieve angular resolutions of up to a few thousandths of a degree [MAS 03], in which case the limit size that can be measured is in the range of a few micrometers.

The width of a diffraction peak can be defined as the ratio between the integral of the peak and its maximum value, something called the integral breadth [LAU 26].

Hence:

$$\beta = \frac{\int I(2\theta)d\theta}{I_m(2\theta)} \qquad [5.51]$$

We will determine the maximum value of the intensity distribution and, therefore, lay out first the relation that gives the expression of this intensity distribution. We showed in Chapter 1 that the integrated intensity of a diffraction peak for a polycrystalline sample, when taking into account all of the diffracting grains, is expressed as:

$$I = \left(\frac{Mn}{2}\cos\theta\right)\left(\frac{1}{2\pi R \sin 2\theta}\right)\frac{1}{\sin 2\theta}\frac{\lambda^3}{V_c}\iiint i_{hkl}\,dhdkdl \qquad [5.52]$$

or also:

$$I = \int I(2\theta)d(2\theta) = \left(\frac{Mn}{8\pi R \sin\theta}\right)\frac{1}{\sin 2\theta}\frac{\lambda^3}{V_c}\iiint i_{hkl}\,dhdkdl \qquad [5.53]$$

$I(2\theta)$ being the distribution of the intensity diffracted about the Bragg position.

From this relation, we will calculate the expression of this distribution. In order to simplify the calculations, we will consider a peak of the form (001). The tip of the scattering vector, in this case, describes a reciprocal lattice point with coordinates (h,k,l), the extent of which increases when the mean crystal size decreases. The diffracted intensity is different from zero only when the values of h and k are very small (see Figure 5.8) and the norm of the scattering vector can be expressed by the relation:

$$\left\|\vec{s}\right\| = \left\|h\vec{a}^* + k\vec{b}^* + l\vec{c}^*\right\| \approx l\left\|\vec{c}^*\right\| \qquad [5.54]$$

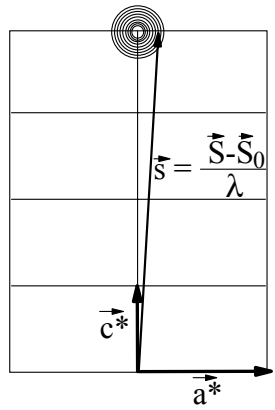

Figure 5.8. *Reciprocal lattice point associated with the diffraction by (001) planes of nanometric crystals*

However:

$$\left\|\vec{s}\right\| = \frac{2\sin\theta}{\lambda} \qquad [5.55]$$

therefore, we can write:

$$\frac{2\cos\theta d\theta}{\lambda} = \left\|\vec{c}^*\right\| dl \qquad [5.56]$$

which means that:

$$d(2\theta) = \left(\frac{\lambda\left\|\vec{c}^*\right\|}{\cos\theta}\right) dl \qquad [5.57]$$

By using this expression in the equation that gives us the intensity, we get:

$$\left(\frac{\lambda\left\|\vec{c}^*\right\|}{\cos\theta}\right)\int I(2\theta)dl = \left(\frac{Mn}{8\pi R\sin\theta}\right)\frac{1}{\sin 2\theta}\frac{\lambda^3}{V_c}\iiint i_{hkl}\,dh\,dk\,dl \qquad [5.58]$$

If we integrate with respect to l, we get:

$$I(2\theta) = \left(\frac{\cos\theta}{\lambda\left\|\vec{c}^*\right\|}\right)\left(\frac{Mn}{8\pi R\sin\theta}\right)\frac{1}{\sin 2\theta}\frac{\lambda^3}{V_c}\iiint i_{hkl}\,dhdk \qquad [5.59]$$

Finally, the intensity distribution is written:

$$I(2\theta) = \frac{Mn}{16\pi R\sin^2\theta}\frac{\lambda^2}{\left\|\vec{c}^*\right\|V_c}\iiint i_{hkl}\,dhdk \qquad [5.60]$$

Let us assume that:

$$K = \frac{Mn}{16\pi R}\frac{\lambda^2}{\left\|\vec{c}^*\right\|V_c} \qquad [5.61]$$

we obtain

$$I(2\theta) = K\frac{1}{\sin^2\theta}\iiint i_{hkl}\,dhdk \qquad [5.62]$$

As presented in Part 1 of this book, the expression of i_{hkl} can be calculated by considering the crystal as a series of crystal cells, forming columns along each direction of the direct lattice (see Figure 5.7). Inside a column, the cells are arranged in pairs which are characterized by a distance between two cells equal to $n\left\|\vec{t}\right\|$ (see Figure 5.9). Each of these cells diffracts the same amplitude[5] given by:

$$F_{hkl} = \sum f_i e^{2\pi i(hu+kv+lw)} \text{ or } F_{hkl} = \sum f_i e^{2\pi i(hu'+kv'+lw')} \qquad [5.63]$$

5 We are assuming here that the only defect found in the diffracting crystals is their limited size.

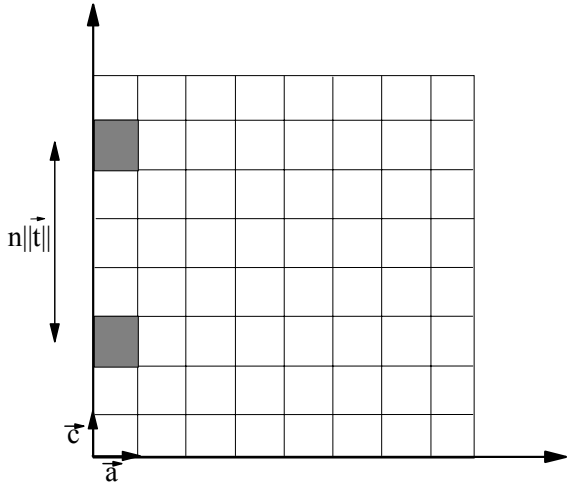

Figure 5.9. *Representation of the crystal as a series of columns of cells arranged in pairs*

i_{hkl} is obtained by adding products $J_n = FF^*$ over the entire column and over all of the crystal's columns; therefore:

$$i_{hkl} = I_e \left|F_{hkl}\right|^2 \sum_{uvw} \sum_{u'v'w'} e^{2\pi i\left[h(u'-u)+k(v'-v)+l(w'-w)\right]} \qquad [5.64]$$

By using this equation in the expression of the intensity distribution, we get:

$$I(2\theta) = I_e \left|F_{hkl}\right|^2 K \frac{1}{\sin^2\theta} \iint \left[\sum_{uvw} \sum_{u'v'w'} e^{2\pi i\left[h(u'-u)+k(v'-v)+l(w'-w)\right]}\right] dhdk \qquad [5.65]$$

We can consider that the variation range of h and k is completely described if these terms vary between + 1/2 and – 1/2. However:

$$\int_{-\frac{1}{2}}^{\frac{1}{2}} e^{2\pi i\left[h(u'-u)\right]} dh = \int_{-\frac{1}{2}}^{\frac{1}{2}} \cos 2\pi\left(u'-u\right) hdh + i\int_{-\frac{1}{2}}^{\frac{1}{2}} \sin 2\pi\left(u'-u\right) hdh$$

$$\Rightarrow \int_{-\frac{1}{2}}^{\frac{1}{2}} e^{2\pi i\left[h(u'-u)\right]} dh = \frac{1}{2\pi\left(u'-u\right)}\left[\left[\sin 2\pi\left(u'-u\right)\right]_{-\frac{1}{2}}^{\frac{1}{2}} - i\left[\cos 2\pi\left(u'-u\right)\right]_{-\frac{1}{2}}^{\frac{1}{2}}\right]$$

$$\Rightarrow \int_{-\frac{1}{2}}^{\frac{1}{2}} e^{2\pi i\left[h(u'-u)\right]} dh = \frac{\sin\pi(u'-u)}{\pi(u'-u)}$$

The terms $\frac{\sin\pi(u'-u)}{\pi(u'-u)}$ are equal to zero except if u' = u, in which case they are equal to 1; therefore, the intensity distribution is written:

$$I(2\theta) = I_e\left|F_{hkl}\right|^2 K \frac{1}{\sin^2\theta} \sum_u \sum_v \sum_w \sum_{w'} e^{2\pi i(w'-w)l} \qquad [5.66]$$

If $N_3(uv)$ is the number of cells along the direction given by $\vec{c}$ in the (uv) column, then the sum with respect to w and w' can be expressed as:

$$\sum_0^{N_3-1} e^{2\pi i w'l} \sum_0^{N_3-1} e^{-2\pi i w l} \qquad [5.67]$$

As we have show previously, this product is equal to:

$$\sum_0^{N_3-1} e^{2\pi i w'l} \sum_0^{N_3-1} e^{-2\pi i w l} = \frac{\sin^2\pi N_3 l}{\sin^2\pi l} \qquad [5.68]$$

and therefore:

$$I(2\theta) = I_e\left|F_{hkl}\right|^2 K \frac{1}{\sin^2\theta} \sum_u \sum_v \frac{\sin^2\pi N_3 l}{\sin^2\pi l} \qquad [5.69]$$

The maximum value of the ratio of sines is equal to $N_3(u,v)$, therefore the maximum of the diffraction peak is given by:

$$I_m(2\theta) = I_e\left|F_{hkl}\right|^2 K \frac{1}{\sin^2\theta} \sum_u \sum_v N_3^2(u,v) \qquad [5.70]$$

The integrated intensity is given by the relation (see equation [1.57]):

$$I_{hkl} = I_0 r_e^2 \left(\frac{1+\cos^2 2\theta}{16\pi R \sin\theta \sin 2\theta} \right) \left(\frac{\lambda^3 n_{hkl} |F_{hkl}|^2}{V_c^2} \right) dV \qquad [5.71]$$

or also:

$$I_{hkl} = I_e \left(\frac{1}{8\pi R \sin\theta \sin 2\theta} \right) \left(\frac{\lambda^3 n_{hkl} |F_{hkl}|^2}{V_c^2} \right) dV \qquad [5.72]$$

with $dV = M\delta V$ and therefore:

$$\beta = \frac{\int I(2\theta) d\theta}{I_m(2\theta)} = \frac{I_e \left(\frac{1}{8\pi R \sin\theta \sin 2\theta} \right) \left(\frac{\lambda^3 n_{hkl} |F_{hkl}|^2}{V_c^2} \right) M\delta V}{I_e |F_{hkl}|^2 \frac{M n_{hkl}}{16\pi R \sin^2\theta} \frac{\lambda^2}{\|\vec{c}^*\| V_c} \sum_u \sum_v N_3^2(u,v)} \qquad [5.73]$$

or also:

$$\beta = \frac{\|\vec{c}^*\| \lambda \left(\frac{1}{V_c} \right) \delta V}{\cos\theta \sum_u \sum_v N_3^2(u,v)} \qquad [5.74]$$

By noting that for an orthorhombic lattice we have $\|\vec{c}^*\| = \frac{1}{\|\vec{c}\|}$, the integral breadth can be written:

$$\beta = \frac{\lambda \delta V}{V_c \|\vec{c}\| \cos\theta \sum_u \sum_v N_3^2(u,v)} \qquad [5.75]$$

Let T(uv) be the size in the direction defined by $\vec{c}$ of the (uv) cell column. The double sum can then be replaced with an integral over the axes x and y of the direct space. We can write:

$$\sum_u \sum_v N_3^2(u,v) = \iint \frac{T^2(x,y)}{\|\vec{c}\|^2} \frac{dxdy}{\|\vec{a}\|\|\vec{b}\|} \quad [5.76]$$

Since the crystals have an orthorhombic symmetry, the volume V_c of the crystal cells is equal to:

$$V_c = \|\vec{a}\| \ \|\vec{b}\| \ \|\vec{c}\| \quad [5.77]$$

The expression of the integral breadth becomes:

$$\beta = \frac{\lambda \delta V}{\cos\theta \iint T^2(x,y)dxdy} \quad [5.78]$$

Note that $T = \int dz$, since T is the size of the crystal along the direction defined by $\vec{c}$. Therefore:

$$\beta = \frac{\lambda \delta V}{\cos\theta \int T dV} \quad [5.79]$$

or:

$$\beta = \frac{\lambda}{L\cos\theta} \quad [5.80]$$

with:

$$L = \frac{1}{\delta V} \int T dV \quad [5.81]$$

L is the mean size of the crystals in the direction defined by the normal to the diffracting planes, with respect to the volume of these crystals.

Equation [5.80], which directly relates the average size of the diffracting crystals to the integral breadth of the peaks, is similar to the one that was established in 1918 by Scherrer [SCH 18]. Note that the mean size measured here is a dimension in a given crystallographic direction, which means that measuring the width of several peaks will make it possible to determine the shapes of the crystals. We will see an illustration of this type of study in the next chapter.

5.4.2. *Microstrains*

Generally speaking, microstrains[6] correspond to atom displacements with respect to their position in crystals which are free of any defects. The presence of dislocations causes this type of displacement, but in this specific case, which we detailed previously, atomic displacements are local, and related to the presence of a linear defect. We will now discuss the general case of displacements that are completely independent of one another.

In order to express the effect of this type of defect on the width of the peaks, we will assume that each crystal is an imperfect crystal lattice, which can be described as a three-dimensional repetition of identical cells that have undergone displacements with respect to their original position (see Figure 5.10). These cell displacements are one way of representing the atomic displacements occurring in the crystals in question. These local strains (microstrains) can be significant, even though the mean values of the cell parameters remain the same as those in crystals free of any defects. The typical example of this situation is provided by cold worked metal crystals, but it is also observed in other situations, often in nanocrystals for example, where it corresponds in particular to the fact that the interplanar distances vary between the core and the surface of these crystals.

6 These are sometimes improperly referred to as microstresses. Clearly, the diffraction signal can only be sensitive to displacements. The transposition from the determination of a displacement field to the evaluation of a state of stress requires information on the elastic and plastic characteristics of the materials in question. This goes, of course, beyond the scope of this book.

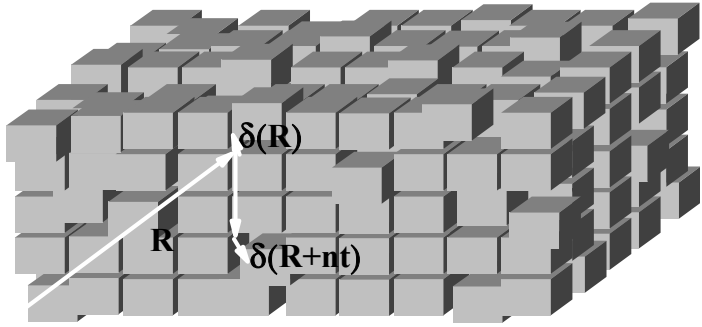

Figure 5.10. *Simplified representation of a crystal containing microstrains*

We will calculate the effect of these distortions on the width of the diffracted intensity distribution. The diffracted intensity is expressed as before (see equation [5.62]), but the expression of i_{hkl} is different since the atomic displacement vectors have to be taken into account.

Let us consider a cell with its initial position with respect to the origin of the lattice specified by the vector $\vec{R}$, which has undergone a displacement characterized by the vector $\vec{\delta}$. Such a displacement is usually the result of a translation and a rotation. If we consider that the rotation is significant enough, then its effect on the scattered radiation's phase is negligible and will not be taken into account when we calculate the diffracted amplitude. If we denote by A_p the amplitude diffracted by the displaced cell p, we can write:

$$A_p = F_{hkl} e^{2\pi i \vec{s}.\left(\vec{R}_p + \delta(\vec{R}_p)\right)} = F_{hkl} e^{2\pi i \vec{s}.\vec{R}_p} e^{2\pi i \vec{s}.\delta(\vec{R}_p)} \qquad [5.82]$$

If we consider a second cell q located at a distance n from the first one in the direction defined by the unit vector $\vec{t}$, the amplitude diffracted by this cell is written:

$$A_q = F_{hkl} e^{2\pi i \vec{s}.\left(\vec{R}_q + \delta(\vec{R}_q)\right)} = F_{hkl} e^{2\pi i \vec{s}.\vec{R}_q} e^{2\pi i \vec{s}.\delta(\vec{R}_q)} \qquad [5.83]$$

In this part, we will only focus on the effect of the microstrains. The terms in $e^{2\pi i \vec{s}.\vec{R}_p}$ correspond to the contribution from the size effect, which has been already expressed. In order to make matters simpler, we will only keep the terms involving displacements.

If we consider that the displacements are non-periodical, then the products $A_pA_q^*$ are equal to zero for high values of n. For small values of n we can expand the expression of the displacement vector. By noting that $\vec{R}_q = \vec{R}_p + n\vec{t}$, we obtain:

$$\delta(\vec{R}_q) = \delta(\vec{R}_p + n\vec{t}) = \delta(\vec{R}_p) + n\vec{t}.\nabla\delta \qquad [5.84]$$

Let J_n be the mean value of the products of the form $A_pA_q^*$, then we can write:

$$J_n = \left\langle A_p A_q^* \right\rangle = \left|F_{hkl}\right|^2 \left\langle e^{2\pi i\vec{s}.\left(\delta(\vec{R})-\delta(\vec{R})-n\vec{t}\nabla\delta\right)} \right\rangle \qquad [5.85]$$

which leads to:

$$J_n = \left|F_{hkl}\right|^2 \left\langle e^{-2\pi i\vec{s}.n\vec{t}\nabla\delta} \right\rangle \qquad [5.86]$$

If we assume that the vector $\vec{t}$ is perpendicular to the diffracting family of planes (hkl), then the scattering vector $\vec{s}$ is written $\vec{s} = \|\vec{s}\|\vec{t}$. Also, we know that $\|\vec{s}\| = \frac{2\sin\theta}{\lambda}$, hence:

$$J_n = \left|F_{hkl}\right|^2 \left\langle e^{-\frac{4\pi\sin\theta}{\lambda}i\vec{t}.n\vec{t}\nabla\delta} \right\rangle \qquad [5.87]$$

The product $\vec{t}.\vec{t}\nabla\delta$, or also $\|t\|^2\nabla\delta$, corresponds to the strain in the direction perpendicular to the family of planes (hkl); let ε_{xy} be this strain, which is a component of the strain tensor and let $\vec{q} = 2\pi\vec{s}$, or $\|\vec{q}\| = \frac{4\pi\sin\theta}{\lambda}$. Out of concern for simplicity, we will write "q" instead of $\|\vec{q}\|$. We obtain:

$$J_n = \left|F_{hkl}\right|^2 \left\langle e^{-iqn\varepsilon_{xy}} \right\rangle \qquad [5.88]$$

Just like before, the diffracted intensity is obtained by summing all of the products J_n. It can be shown [JAM 67] in the same way that, for the size effect, the integral breadth of the peak is written:

$$\beta(2\theta) = \frac{\lambda \left|F_{hkl}\right|^2}{\cos\theta \int J_n dn} \qquad [5.89]$$

In order to calculate this integral, Stokes and Wilson [STO 42, STO 44] suggested assuming a Gaussian function as the strain distribution.

Since we know that the distribution is Gaussian, we can write $\left\langle e^{ix} \right\rangle \approx e^{-\frac{\left\langle x^2 \right\rangle}{2}}$ and therefore, $J_n = \left|F_{hkl}\right|^2 \left\langle e^{-iqn\varepsilon_{xy}} \right\rangle$ can be written:

$$J_n = \left|F_{hkl}\right|^2 e^{-\frac{1}{2}q^2 \left\langle \varepsilon_{xy}^2 \right\rangle n^2} \qquad [5.90]$$

hence:

$$\int_{-\infty}^{+\infty} J_n dn = \left|F_{hkl}\right|^2 \int_{-\infty}^{+\infty} e^{-\frac{1}{2}q^2 \left\langle \varepsilon_{xy}^2 \right\rangle n^2} dn \qquad [5.91]$$

$$\Rightarrow \int_{-\infty}^{+\infty} J_n dn = \left|F_{hkl}\right|^2 \frac{\lambda}{2\sin\theta} \left(2\pi \left\langle \varepsilon_{xy}^2 \right\rangle\right)^{-\frac{1}{2}} \qquad [5.92]$$

We then obtain:

$$\beta(2\theta) = 2\left(2\pi \left\langle \varepsilon_{xy}^2 \right\rangle\right)^{+\frac{1}{2}} \tan\theta \qquad [5.93]$$

By defining:

$$\eta = 2\left(2\pi\left\langle \varepsilon_{xy}^2 \right\rangle\right)^{+\frac{1}{2}} \approx 5\left\langle \varepsilon_{xy}^2 \right\rangle^{+\frac{1}{2}} \quad [5.94]$$

we obtain:

$$\beta = \eta \tan\theta \quad [5.95]$$

This result was achieved by assuming a Gaussian strain distribution. When this condition is not fulfilled, a similar expression can nonetheless be obtained, simply with a change in the meaning of η. For example, Stokes and Wilson [STO 42, STO 44] suggested assuming that all the values of $\left|\varepsilon_{xy}\right|$ had equal probabilities. We then get $\beta = \eta \tan\theta$ with

$$\eta = 4\varepsilon_{xy}^{max} \quad [5.96]$$

We saw that the link between this microstrain amount η and the microstrains ε depends on the hypotheses involving the strain distribution. Furthermore, the physical meaning of η depends on what causes these microstrains to appear and, most of the time, their link with the actual atomic displacements requires the elaboration of a relevant microstructural model. However, the determination of this microstrain amount is often realized, particularly for characterizing powders and bulky samples. By comparing relations [5.80] and [5.95], we notice that the width has a dependence on size, on the one hand, and on the microstrains, on the other hand, in $1/\cos\theta$ and $\tan\theta$, respectively. We will see later on that this difference in behavior serves as the basis for methods designed to separate the size effect from effects due to microstrains in nanocrystals.

Determining the mean size of the crystals and the microstrain amount, as we have just described it, relies on measurements of the integral breadths of the peaks. This type of analysis is used to obtain the mean values that characterize defects. We will see in Chapter 6 that the Fourier series analysis of the peak profiles makes it possible to access the distributions that characterize these defects. In the following section, we will give details on how to express the peak profile as a Fourier series with terms related to the size of the microstrains.

5.4.3. *Effects of the grain size and of the microstrains on the peak profiles: Fourier analysis of the diffracted intensity distribution*

We have just seen how measuring these breadths enables us to quantify the defects. This analysis method implies the fitting of the peaks and therefore requires us to define *a priori* the shape of the diffraction peaks. Bertaut [BER 49] followed by Warren and Averbach [WAR 50, WAR 55, WAR 69] showed that with the help of a Fourier series decomposition of the peak profiles, any material with volume structural defects can be analyzed without having to make hypotheses on the shape of the peaks. This analysis, which we will now describe, when it can be implemented, remains even today one of the most extensive ways to study microstructural effects based on the profiles of the diffraction peaks.

We will use the same notations as in the last two sections and assume that the vector $\vec{\delta}$ which characterizes the displacement of any cell located in a position defined by the vector $\vec{R}$ can be expressed as a linear combination of the cell's basic vectors. We have $\vec{\delta}(R) = X\vec{a} + Y\vec{b} + Z\vec{c}$. By using relation [5.65], we obtain:

$$I(2\theta) = \frac{Ki_e |F_{hkl}|^2}{\sin^2\theta} \sum_u \sum_v \sum_w \sum_{w'} e^{2\pi i[(w'-w)l+(Z'-Z)l]_{uv}} \qquad [5.97]$$

For the set values of u and v, the sums with respect to w and w' correspond to the contributions from all of the cell pairs contained in the (uv) column. As for the sums with respect to u and v, they represent the contributions from all of the columns.

Let us assume that $n = w' - w$ and $Z_n = Z' - Z$ and, for a set value of n, let N_n^e be the total number of cells with an n^{th} neighbor in the same column. Let $\left\langle e^{2\pi i l Z_n} \right\rangle$ be the mean value over all of these pairs of n^{th} neighbors in the same column of the strain for the whole sample. The expression above can then be written in the form of a single sum with respect to n:

$$I(2\theta) = \frac{Ki_e |F_{hkl}|^2}{\sin^2\theta} \sum_{n=-\infty}^{n=+\infty} N_n^e \left\langle e^{2\pi i l Z_n} \right\rangle e^{2\pi i n l} \qquad [5.98]$$

We now define:

– N: number of cells in the entire sample;

– N_{col}: number of columns in the sample;

– $N_3 = N/N_{col}$: mean number of cells per column along the direction defined by $\vec{c}$;

– $N_n = N_n^e / N_{col}$: mean number of pairs per column.

We can then write:

$$I(2\theta) = \frac{Ki_e |F_{hkl}|^2 N}{\sin^2 \theta} \sum_{n=-\infty}^{n=+\infty} \frac{N_n}{N_3} \left\langle e^{2\pi i l Z_n} \right\rangle e^{2\pi i n l} \qquad [5.99]$$

By expanding this sum, we get:

$$\sum_{n=-\infty}^{n=+\infty} \frac{N_n}{N_3} \left[\left\langle \cos 2\pi l Z_n \right\rangle \cos 2\pi n l - \left\langle \sin 2\pi l Z_n \right\rangle \sin 2\pi n l + i \left[\left\langle \cos 2\pi l Z_n \right\rangle \sin 2\pi n l + \left\langle \sin 2\pi l Z_n \right\rangle \cos 2\pi n l \right] \right]$$

Note that $Z_{-n} = -Z_n$. If we separate the sum in two parts with respect to n = 0, we obtain, for the imaginary part, terms of the form:

$$P_1 = \left[\left\langle \cos 2\pi l Z_n \right\rangle \sin 2\pi n l + \left\langle \cos 2\pi l (-Z_n) \right\rangle \sin 2\pi (-n) l \right] \qquad [5.100]$$

$$\Rightarrow P_1 = \left[\left\langle \cos 2\pi l Z_n \right\rangle \sin 2\pi n l - \left\langle \cos 2\pi l Z_n \right\rangle \sin 2\pi n l \right] \qquad [5.101]$$

$$\Rightarrow P_1 = 0 \qquad [5.102]$$

and likewise, we get the terms:

$$P_2 = \left[\left\langle \sin 2\pi l Z_n \right\rangle \cos 2\pi n l + \left\langle \sin 2\pi l (-Z_n) \right\rangle \cos 2\pi (-n) l \right] \qquad [5.103]$$

$$\Rightarrow P_2 = \left[\left\langle \sin 2\pi l Z_n \right\rangle \cos 2\pi n l - \left\langle \sin 2\pi l Z_n \right\rangle \cos 2\pi n l \right] \qquad [5.104]$$

$$\Rightarrow P_2 = 0 \qquad [5.105]$$

Finally, we notice that the entire imaginary part of the sum is equal to zero. Hence, if we define:

$$A_n = \frac{N_n}{N_3} \left\langle \cos 2\pi l Z_n \right\rangle \text{ and } B_n = -\frac{N_n}{N_3} \left\langle \sin 2\pi l Z_n \right\rangle \qquad [5.106]$$

we can express the intensity distribution as a Fourier series:

$$I(2\theta) = \frac{Ki_e N|F_{hkl}|^2}{\sin^2\theta} \sum_{n=-\infty}^{n=+\infty} A_n \cos 2\pi nl + B_n \sin 2\pi nl \qquad [5.107]$$

The variable in this series is the term l which is a function of the cell parameter in the crystallographic direction we are considering:

$$l = \frac{2\sin\theta}{\lambda\|\vec{c}^*\|} = \frac{2\|\vec{c}\|\sin\theta}{\lambda} \qquad [5.108]$$

The harmonic of this series is given by the term n which is related to the distance $L = n\|\vec{t}\|$ between the two cells in a pair in the column perpendicular to the (00l) planes.

The cosine coefficient of this series, A_n, is a product of the two quantities N_n/N_3 and $\langle \cos 2\pi l Z_n \rangle$. N_n/N_3 only depends on the length of the columns and therefore corresponds to a size. The other term depends on Z_n, which means that it is related to the distortions of the lattice. It represents the contributions from the microstrains. This means that the cosine term is the product of the size and distortion coefficients. If we denote these two terms by A_n^T and A_n^D, respectively, we get:

$$A_n = A_n^T A_n^D \qquad [5.109]$$

This relation and equation [5.107] serve as the basis for the use of Fourier series analysis of diffraction peak profiles to quantitatively characterize structural defects found in crystals. We will see in the following chapter how this result can help us determine, in particular, the size and microstrain distribution functions.

This page intentionally left blank

Chapter 6

Microstructural Study of Randomly Oriented Polycrystalline Samples

In Chapter 5, we described in detail the effect on the diffracted intensity's distribution of the discrepancies between a crystal's mean structure and its actual structure. The quantitative study of these effects makes it possible to accurately determine the density of punctual defects, of dislocations or of stacking faults, the size of the grains, as well as the microstrain rate, etc. This type of analysis was developed in the second half of the 20th century and, due to the tremendous progress made by computers, became widespread in the late 1980s. In 1999, the International Union of Crystallography published a book describing most of the aspects of microstructural analysis by X-ray diffraction on polycrystalline samples [SYN 99].

In addition to the necessary mathematical details, in this chapter we will give actual experimental examples of the approaches used. From the very start, it is impossible to be comprehensive, which is why this chapter is limited to the study of volume defects and, more precisely, to estimating the sizes and shapes of nanocrystals as well as determining microstrain amount. Also, we will give an illustration of how the density of stacking faults is studied. Readers who want to know more will find, in particular, in [UNG 99] an in-depth presentation of the analysis of the influence of the dislocations on the peak profile. In Chapter 5, we described the influence of the presence of vacancies on the scattered and diffracted signal. The experimental explanation for this type of approach essentially involves the study of single crystals and remains a field for specialists. We will not give any examples of these works.

Three different methods have been designed to quantitatively study structural volume defects. The integral breadth method, based on the theoretical considerations we discussed in Chapter 5, was introduced in 1918 by Scherrer [SCH 18] and generalized by Stokes and Wilson [STO 42], among others. Later on, Tournarie [TOU 56a, TOU 56b] followed by Wilson [WIL 62b, WIL 63] suggested a different analysis based on the variance of the intensity distribution. We described how Bertaut [BER 49] showed in 1949 that the Fourier series decomposition of the peak profile makes it possible to obtain the mean value and the distribution of the different effects that cause the increase in peak width. This method was further elaborated by Warren and Averbach [WAR 50, WAR 55, WAR 69].

Aside from a few authors [BER 93, GRO 98b, SAN 97] who still implement it, the variance method is hardly used anymore. This chapter will deal with the integral breadth method and the Fourier analysis.

Regardless of which of the two methods is used, it is important to separate the microstructural effects from the instrumental contribution in the peak profiles. We saw, in the first part of this book, how the different elements that comprise the instrument can modify the shape of the diffraction peaks. Obviously, microstructural analysis is easier when the instrument's contribution is small. However, this contribution has to be taken into account in order to extract the experimental profile, i.e. the "pure profile" which is induced by the microstructural defects.

6.1. Extracting the pure profile

In Chapter 3, we saw that the distribution of the measured intensity h(x) can be expressed as the convolution product of the pure profile f(x) and the instrumental function g(x). We can write:

$$h(x) = \int_{-\infty}^{+\infty} f(y)g(x-y)dy \qquad [6.1]$$

This relation was first suggested[1] by Jones in 1938 [JON 38]. We have already noted, however, that this expression neglects not only the measurement noise, denoted by ε(x), but also the contribution from the continuous background, denoted by b(x). In fact, the profile of a diffraction peak looks more like:

1 This relation and the next one have already been explained in Chapter 3 in references [3.1] and [3.2], respectively. They are shown here only to simplify the reading.

$$h(x) = \left(\int_{-\infty}^{+\infty} f(y)g(x-y)dy \right) + \varepsilon(x) + b(x) \qquad [6.2]$$

The problem is therefore to determine the nature and the density of the structural defects from the measurement of the experimental profile h(x) which contains the contribution from the instrument. There are two ways to go about solving this problem. The first method consists of deconvoluting this equation by using, in particular, the properties of Fourier transforms and extracting the pure profile which induced only by the defects. The second approach is described as "convolutive". This time, the structural defects are described without extracting the pure profile, but instead by taking into account the instrument's contribution, which is assumed to be an analytical function, either known or directly calculated from the characteristics of the diffractometer. This instrumental function is then convoluted with the functions expressing the contributions from the various microstructural effects that are assumed to be present.

Regardless of which approach is used, it is necessary, of course, to know the instrumental function. As we have previously recalled, one of the methods for determining the contribution from the instrument is to calculate it from the diffractometer's physical characteristics [CHE 04]. This aspect has been the subject of research for about 20 years and was described in Chapter 3. However, the most commonly used method consists of producing a diffraction pattern with a sample assumed to be comprised of perfect crystals. In practice, several materials are used. Only one of them, lanthanum hexaboride which is sold by the NIST [NIST] is a standard acknowledged by the international community.

If, one way or another, the instrument function is known, it is then possible to analyze the profile of the diffraction peaks for the sample that contains defects. The first methods that were suggested relied on solving equations [6.1] and [6.2] by deconvolution.

6.1.1. *Methods based on deconvolution*

The different approaches used to extract the pure profile by deconvolution were described and compared in particular by Louer and Weigel [LOU 69b], and more recently by Armstrong and Kalceft [ARM 99]. Cernansky [CER 99] gave a detailed description of the inherent mathematical aspects of this deconvolution process. Aside from Stokes' historical method [STO 48], the various approaches will not be explained here, only the basic ideas will.

6.1.1.1. *Constraint free deconvolution method: Stokes' method*

The oldest method used to extract the pure profile was suggested in 1948 by Stokes [STO 48]. It consists of neglecting the experimental noise and the contribution from the continuous background, and inverting the convolution product by a Fourier analysis of the peak profile.

The different functions f, g and h can be written as Fourier series, with x varying in an interval – a/2, + a/2 outside which the intensity is considered to be zero. Thus, we get:

$$f(y)=\sum_{-\infty}^{+\infty}F(t)e^{-2\pi iy\frac{t}{a}}\quad g(z)=\sum_{-\infty}^{+\infty}G(t')e^{-2\pi iz\frac{t'}{a}}\quad h(x)=\sum_{-\infty}^{+\infty}H(t'')e^{-2\pi ix\frac{t''}{a}}$$

with, for example:

$$F(t)=\frac{1}{a}\int_{-\frac{a}{2}}^{+\frac{a}{2}}f(y)e^{2\pi iy\frac{t}{a}}dy \qquad [6.3]$$

hence:

$$h(x)=\sum_{t}\sum_{t'}F(t)G(t')\int_{-\frac{a}{2}}^{+\frac{a}{2}}e^{-2\pi iy\frac{t}{a}}e^{-2\pi i(x-y)\frac{t'}{a}}dy \qquad [6.4]$$

$$\Rightarrow h(x)=\sum_{t}\sum_{t'}F(t)G(t')e^{-2\pi ix\frac{t'}{a}}\int_{-\frac{a}{2}}^{+\frac{a}{2}}e^{-2\pi iy\frac{(t'-t)}{a}}dy \qquad [6.5]$$

but if t = t', we have:

$$\int_{-\frac{a}{2}}^{+\frac{a}{2}}e^{-2\pi iy\frac{(t'-t)}{a}}dy=a$$

and if $t \neq t'$, we have, on the other hand:

$$\int_{-\frac{a}{2}}^{+\frac{a}{2}} e^{-2\pi i y \frac{(t'-t)}{a}} dy = 0$$

Therefore, the double sum is reduced to only the terms such that $t = t'$; hence:

$$h(x) = a \sum_{t} F(t) G(t) e^{-2\pi i x \frac{t}{a}} \qquad [6.6]$$

Note that $H(t) = a\, F(t)\, G(t)$. This classic result is equivalent to saying that if h is the convolution product of f and g, then the Fourier transform of h is equal to the product of the Fourier transforms of f and g.

Therefore, we can write:

$$F(t) = \frac{H(t)}{aG(t)}$$

hence:

$$f(y) = a \sum_{t} \frac{H(t)}{G(t)} e^{-2\pi i y \frac{t}{a}}$$

The Fourier coefficients are complex numbers that can be written:

$$F(t) = F_r(t) + iF_i(t) = \frac{H_r(t) + iH_i(t)}{G_r(t) + iG_i(t)} \qquad [6.7]$$

By multiplying the numerator and the denominator by G*(t), and by making the real and imaginary parts equal, we obtain:

$$F_r(t) = \frac{H_r(t)G_r(t) + H_i(t)G_i(t)}{G_r^2(t) + G_i^2(t)} \text{ and } F_i(t) = \frac{H_i(t)G_r(t) - H_r(t)G_i(t)}{G_r^2(t) + G_i^2(t)} \qquad [6.8]$$

In the end, we have the following equation:

$$f(y) = \sum_t F_r(t)\cos 2\pi y\frac{t}{a} + F_i(t)\sin 2\pi y\frac{t}{a} \qquad [6.9]$$

In order to illustrate this approach, we will use patterns produced as part of the international test organized by Balzar under the authority of the International Union of Crystallography, aimed at studying nanocrystal powders free of any microstrains [BAL 04]. Two diffraction patterns of cerium oxide were produced by Masson, by using the same diffractometer from beamline BM16[2] at the ESRF. One was obtained with a powder comprised of nanometric grains and the other with a sample free of any structural defects. A qualitative comparison of the two patterns is given in Figure 6.1. A diffraction peak from each of the patterns is shown in Figure 6.2a. The associated Fourier coefficients are given in Figure 6.2b. From these values, it is possible to determine the Fourier coefficients of the pure profile, and finally the pure profile itself (see Figure 6.2c).

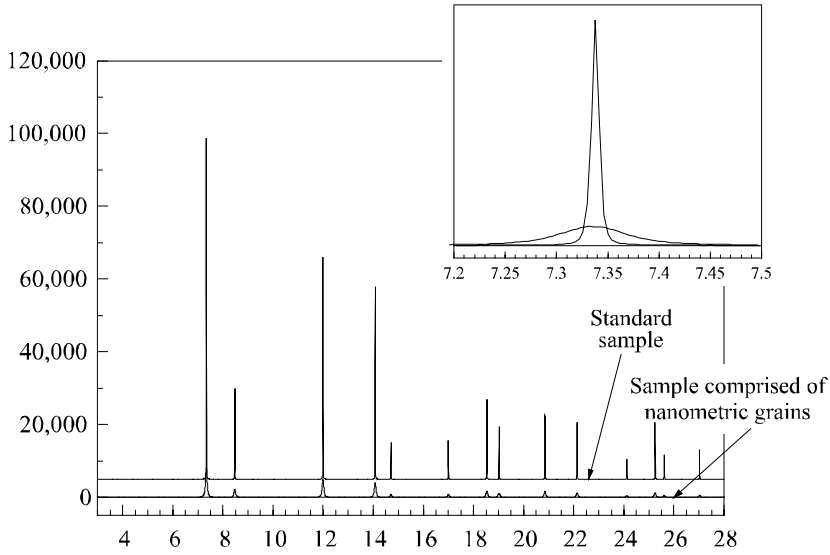

Figure 6.1. *Diffraction patterns recorded with samples of cerium oxide at the ESRF*

2 This line is the high resolution station for diffraction by polycrystalline samples at the ESRF. In the time since this experiment was conducted, the diffractometer in question was transferred to an X-ray beamline with an even stronger intensity originating from an insertion device. This system is now on beamline ID31 of the ESRF.

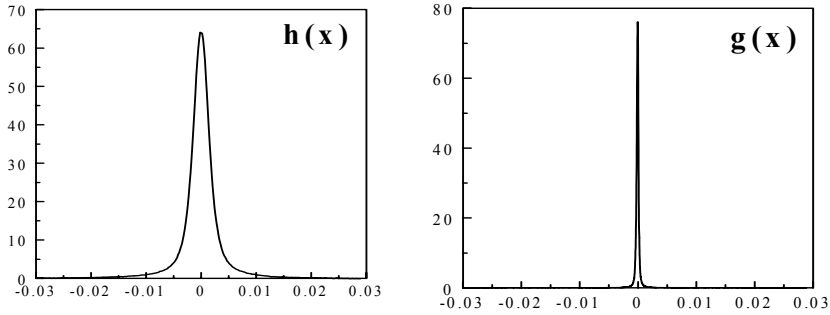

Figure 6.2a. *Initial patterns*

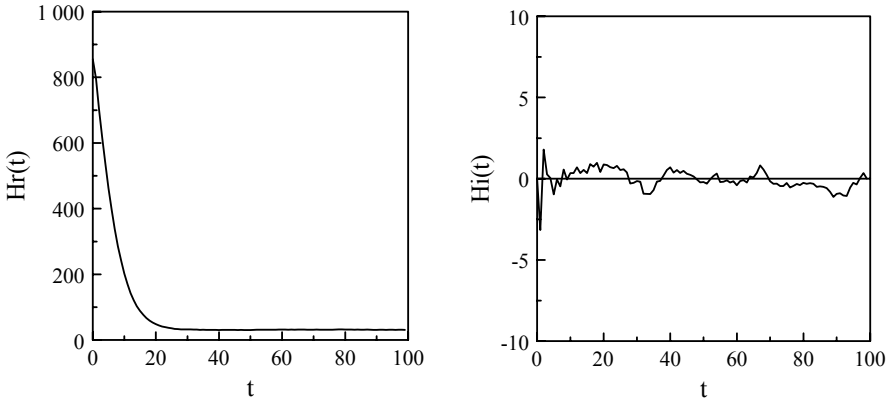

(i) Fourier coefficients of the widened peak

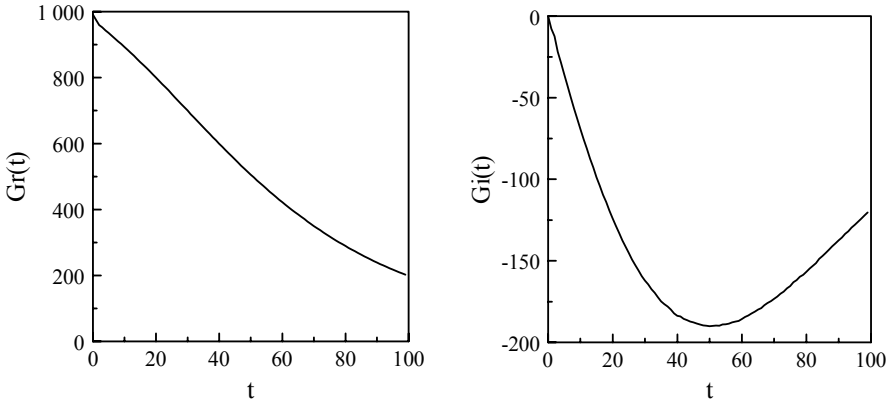

(ii) Fourier coefficients of the instrumental function

Figure 6.2b. *Fourier analysis*

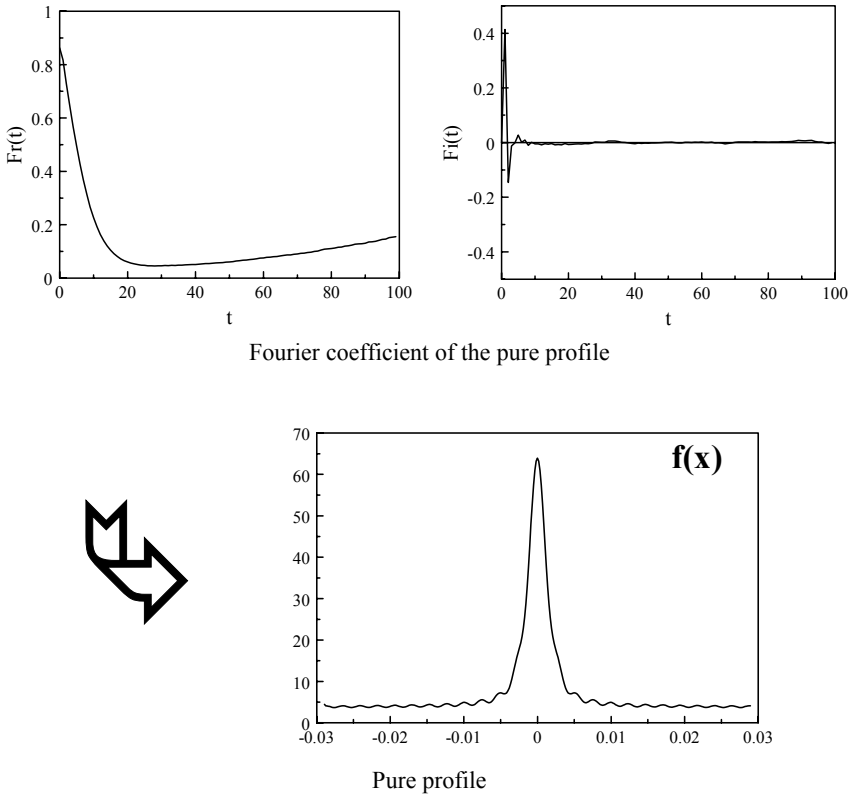

Figure 6.2c. *Determining the pure profile*

This method of extracting the pure profile by Fourier analysis has seen major developments and modern computational capabilities have made it rather easy to implement. However, the calculation of the Fourier coefficients imposes that there must be no peak overlaps. This condition considerably limits the application field of this method. Additionally, as we have already mentioned, the experimental noise is assumed to be zero. The presence of a non-zero noise causes oscillations in the resulting signal after deconvolution. This problem can be solved by using the methods described below.

6.1.1.2. *Deconvolution by iteration*

In 1968, Ergun [ERG 68] suggested extracting the pure profile of X-ray diffraction peaks by using an iterative method initially described by van Citter and

Burger [CIT 31, BUR 32]. In order to keep the notations simple, we will replace the expression of equation [6.2] with:

$$h = f*g + \varepsilon + b \qquad [6.10]$$

where the * symbol indicates a convolution product.

We obtain:

$$h - f*g = U \qquad [6.11]$$

where U corresponds to the contribution from the experimental noise and the continuous background. Let f_n be the function such that:

$$f_{n+1} = f_n + U_n \qquad [6.12]$$

with:

$$h - f_n*g = U_n. \qquad [6.13]$$

The initial function f_1 is chosen equal to h. The functions f_n are successive approximations of the function f we are looking for. Therefore, this method consists of iteratively calculating these functions f_n. Based on the relations we have just given, we have:

$$\begin{cases} f_1(x) = h(x) \\ f_2(x) = 2h(x) - h_1(x) \text{ with } h_1(x) = \int_{-\infty}^{+\infty} h(y)g(x-y)dy \\ f_3(x) = 3h(x) - 3h_1(x) + h_2(x) \text{ with } h_2(x) = \int_{-\infty}^{+\infty} h_1(y)g(x-y)dy \\ f_n(x) = nh(x) - \dfrac{n(n-1)}{2!}h_1(x) + \dfrac{n(n-1)(n-2)}{3!}h_2(x) \ldots \pm h_{n-1}(x) \text{ with } h_i(x) = \int_{-\infty}^{+\infty} h_{i-1}(y)g(x-y)dy \end{cases} \qquad [6.14]$$

This process consists of obtaining the pure profile f, towards which tend the functions f_n when n increases, by convoluting the measured function h with the instrumental function. One of the difficult aspects of this type of method is achieving the convergence of the iterative process toward the solution. This problem was studied by Ruland [RUL 71], who defined an efficient convergence criterion.

6.1.1.3. *Stabilization methods*

This stabilization approach was introduced by Phillips [PHI 62] and Tikhonov [TIK 63, TIK 77], and is often referred to as the "Tikhonov stabilization". It consists of a general approach to "ill-posed" problems, when the signal resulting from a convolution is used to try to determine the pure profile. The main idea is to limit the number of solutions to equation [6.2] by including additional information. This information, suggested by Tikhonov, is that the function is smooth or, in other words, that its second derivative is as close as possible to zero.

Equation [6.2] is written again as follows:

$$h = Af + \varepsilon \qquad [6.15]$$

where A is a linear operator that depends on g.

The objective is then to find f such that $\|h - Af\|$ is as small as possible. However, Tikhonov had the idea instead of minimizing the parameters:

$$\|Af - h\|^2 + \alpha\|f\|^2 \qquad [6.16]$$

The parameter α is a positive number called the regularization parameter, which controls the smoothness of the solution. Minimizing this parameter is a stable and converging problem.

This approach was first applied to the study of X-ray diffraction peaks by Louer and his collaborators [LOU 69a, LOU 69b, LOU 72]. These authors showed that this method can prevent the oscillations observed after the Stokes deconvolution.

6.1.1.4. *The maximum entropy or likelihood method, and the Bayesian method*

Other approaches, based on the probability analysis of the profile of the diffraction peaks, were developed over the past decade. Three methods should be mentioned: the maximum entropy method, the maximum likelihood method and the Bayesian techniques, based on Bayes' theorem.

We will not be discussing recent methods here. Readers interested in knowing more can refer to [CER 99] and [REE 99] for an overview of the mathematical considerations involved, and [KAL 95, GIL 96, ARM 98, ARM 04] for a detailed description, illustrated with examples, of the maximum entropy method.

6.1.1.5. *Methods based on a priori assumptions on the profile*

In all the methods we have just described, no assumption is made beforehand on the shape of the peak profiles. Simple conditions are laid out, such as the fact that the second derivative has to be as small as possible (stabilization method).

Naturally, it is also possible to set more stringent conditions. One common method consists of making an assumption *a priori* on the shape of the functions describing the contributions from the device and from structural defects. These functions can be defined either analytically or numerically. Usually, the relation between the measured profile h(x) and the pure profile is expressed as a simple relation involving the integral breadths or the full widths at half maximum.

Thus, if we assume, for example, that the contributions from the device and from the sample are both described by Gaussian functions, then the measured profile h(x) is also a Gaussian function and:

$$\beta_h^2 = \beta_f^2 + \beta_g^2 \qquad [6.17]$$

Likewise, if we assume that f and g are Lorentzian functions, then:

$$\beta_h = \beta_f + \beta_g \qquad [6.18]$$

As we have already mentioned in Part 1 of this book, one of the most often used functions for simulating diffraction peaks is the Voigt function [VOI 12]. In this case, the pure integral breadth is obtained by decomposing the breadths of the different contributions depending on their Gaussian and a Lorentzian part. The total pure breadth is obtained from the following relation:

$$\beta_f = \beta_{fG} \frac{e^{-k^2}}{1 - \mathrm{erf}(k)} \qquad [6.19]$$

with

$$k = \frac{\beta_{fL}}{\sqrt{\pi}\beta_{fG}} \qquad [6.20]$$

The pure Gaussian and Lorentzian breadths, respectively β_{fG} and β_{fL}, are obtained from relations [6.17] and [6.18]. Halder and Wagner [HAL 66] gave a simplified expression of relation [6.19]:

$$\beta_f^2 = \beta_{fL}\beta_f + \beta_{fG}^2 \qquad [6.21]$$

Of course, this method is easier to implement than those we mentioned previously. Its main limitation, however, is that the shape of the experimental profiles is not quite the same as the one that was assumed *a priori*. This major approximation can be a problem, depending on the cases.

6.1.2. *Convolutive methods*

The purpose of the process we explained in the previous sections is to extract from the experimental profile, h(x), the pure profile, f(x), which will then be used to determine the microstructural characteristics of the sample.

An alternative approach consists of working directly with the measured profile h(x), by expressing it as a Fourier series that includes the various components associated with each of the effects that modify the experimental profile [SCA 02] (instrumental function, size effect, microstrains, etc.). The intensity distribution h(x) or I(2θ) is then expressed from equation [5.98] which was obtained in Chapter 5 by including in this equation the Fourier transform G(x) of the instrumental function, and finally:

$$I(2\theta) = \frac{Ki_e |F_{hkl}|^2 N}{\sin^2\theta} \sum_{n=-\infty}^{n=+\infty} G(n) \frac{N_n}{N_3} \left\langle e^{2\pi i l Z_n} \right\rangle e^{2\pi i n l} \qquad [6.22]$$

We are considering here a sample comprised of nanocrystals with microstrains. When other microstructural effects are involved, we simply have to include the associated Fourier transforms in expression [6.22].

The experimental profile is directly modeled[3] from this expression. Determining the instrumental function's Fourier transform requires knowing that function, of course. As we have already mentioned, two methods are used. The first method consists of estimating the instrumental function based on a diffraction diagram produced with a reference sample and fitted, for example, with Voigt functions. Then, the Fourier coefficients of this Voigt function are introduced in equation [6.22]. In the second method, the instrumental function is calculated by taking into account all the contributions [CHE 04]. In this case, the Fourier coefficients of each of the contributions are substituted into equation [6.22].

The use of this convolutive approach has grown in the past few years. Note that, in this case, each of the effects that modify the peak profile is dealt with the same way, whether it is an intrinsic microstructural feature of the sample or a contribution from the device. The effects are not separated *a priori* before the actual microstructural analysis. We will come back to this point at the end of this chapter.

6.2. Microstructural study using the integral breadth method

In Chapter 5, we showed that the integral breadth of the diffraction peaks can be linked to the apparent size of the crystals and to their microstrains. Likewise, we have seen that, when the crystals contain stacking faults, the modification of the diffraction peak profiles associated with the family of planes that contain these faults is similar to that caused by a size effect.

In this section, we will deal with the separation of these different contributions based on the measurement of the integral breadths and the equations we have laid out. Throughout this section, we will assume that the experimental profiles have been corrected and that the suggested methods are applied to the pure profiles.

Therefore, the integral breadth of the peaks diffracted by crystals with volume defects is written:

$$\beta = \frac{\lambda}{L\cos\theta} \text{ and } \beta = \eta \tan\theta$$

3 The word "modeling" is used in this context as opposed to the word "fitting". Generally speaking, modeling indicates that the calculated function that is adjusted with the experimental signal is expressed based on the physical phenomena that lead to the observed intensity distribution. The word fitting is used when the measured signal is described by a function chosen without any particular physical considerations.

with regard to the effect due to the size (or due to stacking faults) and the widening induced by microstrains, respectively.

When only one of these two effects occurs, plotting the integral breadth according to the diffraction angle has to make it possible to determine the cause of the increase in width. In most cases the two effects occur simultaneously, meaning that hypotheses have to be made on the peak profile in order to separate them.

6.2.1. *The Williamson-Hall method*

In 1953, Williamson and Hall [WIL 53] suggested a simple method for solving this problem. It works by considering that both the limited size of the crystals and the presence of crystallographic distortions lead to Lorentzian intensity distributions.

This is a very simplistic assumption, of course, but it provides a simple way of dealing with the problem. As we have already said, the convolution product of two Lorentzian functions is a Lorentzian function and, additionally, the residual breadth is the sum of the elementary breadths caused by each of these effects. If we denote by β_p the pure breadth and by β^T and β^D the breadths related to size and microstrains, respectively, then we obtain:

$$\beta_p = \beta^T + \beta^D \qquad [6.23]$$

and therefore:

$$\beta = \frac{\lambda}{L\cos\theta} + \eta\tan\theta \qquad [6.24]$$

or:

$$\frac{\beta\cos\theta}{\lambda} = \frac{1}{L} + \eta\frac{\sin\theta}{\lambda} \qquad [6.25]$$

If we plot $(\beta \cos \theta)/\lambda$ according to $(\sin \theta)/\lambda$, we get a straight line with a y-intercept equal to the inverse of the size and a slope equal to the value of the microstrains. This plot is known as the Williamson-Hall plot.

We notice that:

$$\frac{\sin\theta}{\lambda} = \frac{\|\vec{s}\|}{2} = \frac{1}{2d} = \frac{d^*}{2} \qquad [6.26]$$

if we define $\beta^* = (\beta\cos\theta)/\lambda$, equation [6.24] becomes:

$$\beta^* = \frac{1}{L} + \frac{\eta}{2} d^* \qquad [6.27]$$

A plot of this kind is shown in Figure 6.3. It was obtained from the diffraction pattern of a cerium oxide sample comprised of nanometric grains and used for the international test organized by Balzar [BAL 04]. This pattern is shown in Figure 6.1.

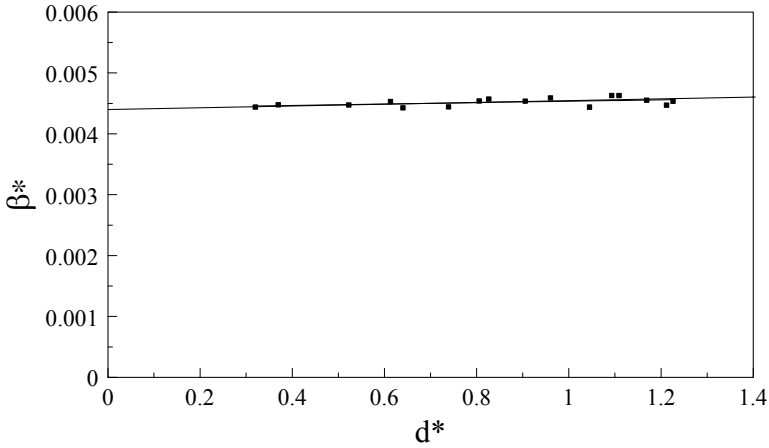

Figure 6.3. *Williamson-Hall plot obtained by using peak by peak fitting of the diffraction pattern produced by the ESRF with nanocrystallized cerium oxide*

The y-intercept enables us to determine a mean value of the size, which is in this case about 22 nm. The slope of this line is small, which shows that the sample contains a small amount of microstrains. The measured value is 0.13%.

This approximated method makes it possible to obtain a qualitative mean value characterizing each of the effects that cause the increase in peak width. In particular, if the slope of the line is almost horizontal, it means that the crystals in question

contain a small amount of microstrains. Likewise, if the line passes through the origin, then the crystals are large enough not to increase the peak width.

6.2.2. *The modified Williamson-Hall method and Voigt function fitting*

Generally speaking, volume structural defects widen the peaks without leading to Lorentzian distributions. However, it is generally assumed that the peak profiles associated with these defects evolve between a Gaussian and a Lorentzian distribution, and therefore can be described by Voigt functions. Based on this hypothesis, Langford [LAN 78, LAN 92] suggested a method for separating the size contribution, which does not depend on the diffraction order of the microstrain contribution, which does. Each peak is fitted with a Voigt function and the Gaussian and Lorentzian parts of the intensity distribution's width are determined for each of the peaks.

When different types of defects modify the shape of the peaks and if it is assumed that each of these defects leads to a Voigtian intensity distribution, then the profile observed for each peak is a Voigt function obtained from the convolution of each of the elementary Voigt functions. We have seen that the width of the distribution corresponding to the convolution product of several Lorentzian functions is obtained by adding the widths of the elementary functions. As for Gaussian functions, we have to add the squared widths. Therefore, we can say that the resulting Gaussian and Lorentzian parts are written:

$$\begin{cases} \beta_G^2 = \left(\beta_G^T\right)^2 + \left(\beta_G^D\right)^2 + \left(\beta_G^F\right)^2 + \ldots \\ \beta_{L=}\beta_L^T + \beta_L^D + \beta_L^F + \ldots \end{cases} \qquad [6.28]$$

with:

– $\beta_G{}^T$: Gaussian contribution from size;

– $\beta_G{}^D$: Gaussian contribution from lattice distortions;

– $\beta_G{}^F$: Gaussian contribution from stacking faults;

– $\beta_L{}^T$: Lorentzian contribution from size;

– $\beta_L{}^D$: Lorentzian contribution from lattice distortions;

– $\beta_L{}^F$: Lorentzian contribution from stacking faults.

By analogy with the works of Williamson and Hall, Langord suggested plotting the evolution of the Lorentzian part of the breadth according to the sine of the

diffraction angle, while plotting the evolution of the square of the Gaussian part of the breadth according to the square of this sine. Determining the y-intercept and the slope of the resulting lines leads, respectively, to the Gaussian and Lorentzian contributions from size and microstrains. The breadths of the Voigt functions associated, on the one hand, with size and with microstrains, on the other hand, are obtained by recombination, using relations [6.19] and [6.20], which give the link between the breadth of a Voigt function and its different components.

An example of this method is shown in Figure 6.4. The sample is still the cerium oxide used for the international test [BAL 04]. This time, the diffraction peaks were fitted with Voigt functions. The result confirms that the increase in peak width for this sample is essentially due to the size effect.

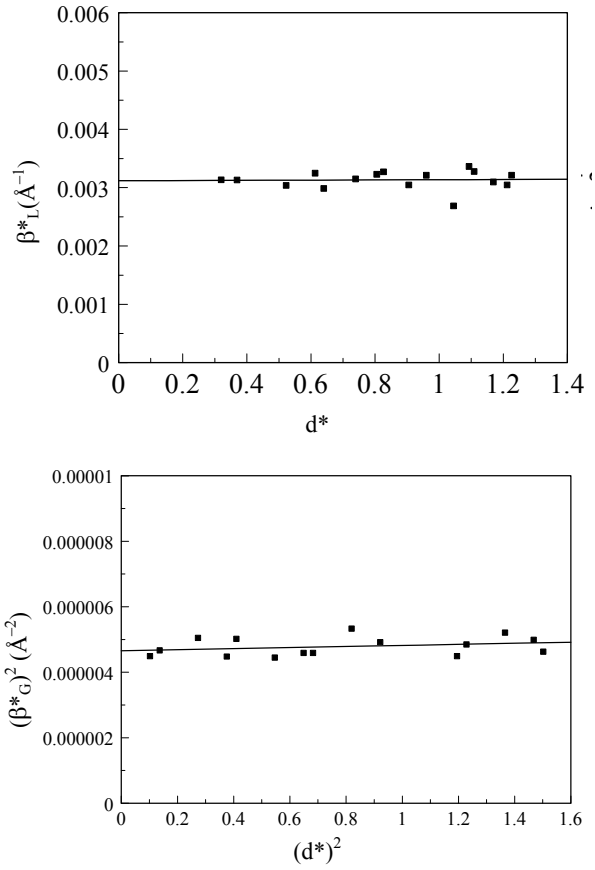

Figure 6.4. *Williamson-Hall plots obtained by using the Langford method based on diffraction peak fitting of cerium oxide*

Determining the mean crystal size and the microstrain rate from these Williamson-Hall plots (whether modified or not) of course requires to be able to measure several diffraction peaks and, in particular, several orders of the same reflections. It is sometimes difficult to measures several peaks with a high enough quality, especially without too much overlap. Therefore, an alternative method consists of trying to quantify the microstructural effects based on the measurement and the fitting of only one peak. This method which is often based on the use of the Voigt function is knowing as the "single line method". It was described, in particular, by Delhez and his colleagues [DEL 82] [KEI 82]. It requires additional hypotheses. Generally speaking, it is necessary to associate each of the Gaussian and Lorentzian component of the peak profile, which is assumed to be Voigtian, with a specific microstructural contribution. Most of the time people using this method are considering that the Lorentzian component of the profile is due to size, whereas the Gaussian component is due to microstrains. This assumption relies mostly on considerations made by Schoening [SCH 65]. Other authors [NAN 78, HAL 66] have shown experimentally that this approach makes it possible to fit the measured peak properly. The actual shape of the profiles caused by the size of the crystals and their microstrains is, obviously, more complex and strongly depends on the shape of the distributions associated with each of these microstructural effects. This is why this simplified approach to the study of the microstructure, based on the measurement and the analysis of a single peak, remains a highly qualitative method.

6.2.3. *Study of size anisotropy*

The width of the cerium oxide diffraction peaks, studied in the previous sections, has values that vary regularly with the diffraction angle. Thus, for the graphs shown in Figures 6.3 and 6.4, all of the points are lined up on the regression line. This result means that the effects that cause the peaks to widen are isotropic. It is possible to imagine a situation where the increase in peak width would strongly depend on the Miller indices of the peaks. This situation can correspond to the fact that diffracting nanocrystals are non-spherical or that the microstrain tensor is anisotropic or that the crystals contain stacking faults[4], an effect, which, by nature, is anisotropic.

Louer and Langford [LAN 86, LAN 93, LAN 96] in particular studied this situation. These authors showed that it is possible, through a careful study of how the peak widths behave with respect to the Miller indices, to accurately determine the average shape of nanocrystals. This method can be illustrated by a study we

4 This list is not comprehensive and other type of defects can lead to an anisotropic widening of the diffraction peaks.

conducted on anatase nanocrystals produced by a sol-gel method [MAS 96c, MAS 98a, MAS 98b].

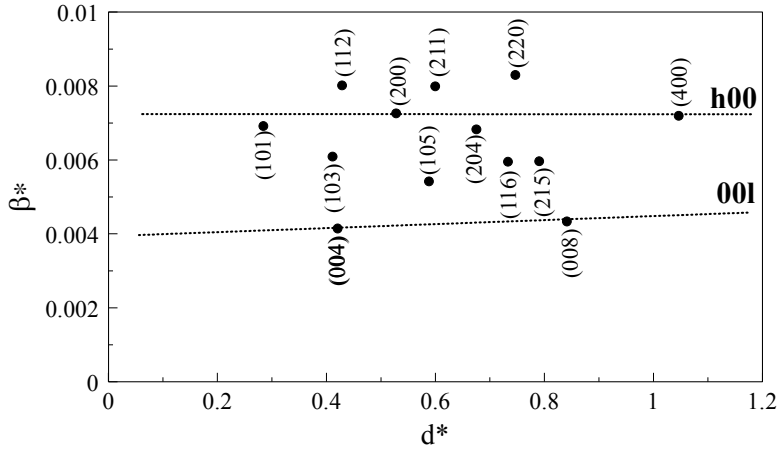

Figure 6.5. *Williamson-Hall plot obtained from the diffraction pattern of a non-annealed titanium oxide aerogel*

Figure 6.5 shows a Williamson-Hall plot obtained by fitting a diffraction pattern produced for a titanium oxide aerogel with Voigt functions. The widths, expressed in the reciprocal lattice, are very different, depending on whether we are focusing on the families of planes (h00) or (00l). The y-intercept of the line obtained for the (00l) planes is higher than for the (h00) planes. Furthermore, these lines are almost horizontal, thus indicating the absence of microstrains. These two results enable us to show that the crystals are significantly extended along the $\vec{c}$ axis of the anatase crystal cell.

Figure 6.6 shows the inverse value of the width, drawn in a polar set of coordinates. α is the angle between the considered direction and the [001] direction. All of the measured values fit lines that were plotted by assuming that the crystals had a prismatic shape with a square base. Finally, this study shows that the nanocrystals we are studying are prisms with a height of roughly 25 nm long and parallel to $\vec{c}$, whereas the sides of the square base are about 15 nm long.

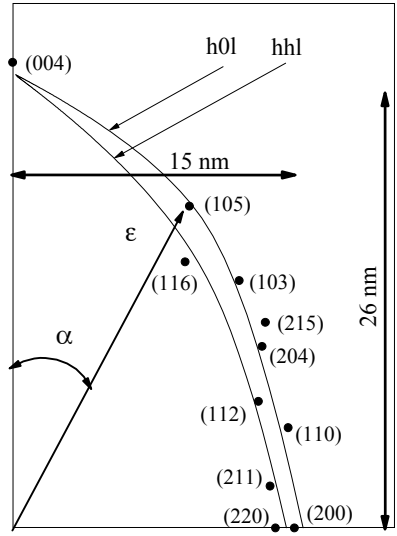

Figure 6.6. *Polar plot illustrating the anisotropic shape of anatase crystals*

Figure 6.7 shows an image, obtained using a transmission electron microscope, of one aerogel anatase crystal. The extended shape along the $\vec{c}$ axis is clearly visible.

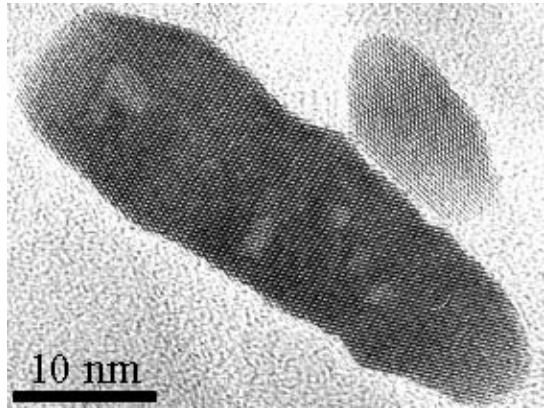

Figure 6.7. *High resolution observation of an anatase crystal by using transmission electron microscopy*

6.2.4. *Measurement of stacking faults*

In Chapter 5, we described in detail the effects of stacking faults on the diffracted intensity. Stacking faults can significantly alter the peak profiles and modify the positions of the peaks (see Figure 5.6). However, when the mean fault density is not too high, it is possible to assume that the position change is small and that the distortion of the intensity distribution consists merely of an increase in peak width. In this section, we will make this restrictive assumption.

We noted earlier that if the regular stacking of index planes (hkl) is interrupted by the presence of a fault, this break is similar to that caused by a size effect and, in both cases, the increase in width is independent of the reflection order. The main difference with the size effect is that the presence of stacking faults causes a strongly anisotropic effect. This is because, if the scattering vector $\vec{s}$ associated with a given family of planes (hkl) is normal to the displacement vector $\vec{\delta}$, which corresponds to the fault, then the width of the peak with indices (hkl) will remain the same (see Chapter 5). It would appear from this observation that size effects can be distinguished from stacking faults. However, these studies are difficult and have only been conducted since the early 1990s [LAN 93].

We will illustrate this method for measuring the stacking fault density with the example of a study [BOU 01b, BOU 01c, BOU 02b] we recently conducted on a ferroelectric material with the chemical formula $SbBi_2Nb_2O_9$. This compound crystallizes in the form of an Aurivillius phase that can be described as a stack of perovskite blocks with the composition $[A_{(m-1)}B_mO_{(3m+1)}]^{2-}$, separated by sheets of $[Bi_2O_2]^{2+}$. The stacking of perovskite blocks often shows stacking faults [BOU 01c, CHO 01, DIN 02], corresponding to local variations in the number of perovskite blocks that cause a displacement along the $\vec{c}$ axis and a local modification in the electron density. Figure 6.8 shows a diffraction pattern obtained with a powdery sample of a material synthesized by using a sol-gel method. The widths of the diffraction peaks increases but, as the insert in Figure 6.8 shows, this increase varies significantly from one peak to the next.

We fitted each peak in this pattern with a Voigt function and drew a Williamson-Hall plot based on the recombined breadths using the method described above. Figure 6.8b clearly shows that the increase in width is strongly anisotropic. The straight line that passes through the points corresponding to the (200) and (400) peaks also passes through the origin, which shows that the size of the crystal along that direction is large and does not increase the width of the peak. Many peaks with indices (001) are visible and the straight line that passes through these points has a non-zero y-intersept. The value obtained corresponds to the mean distance between two faults along the (001) plane stacking direction [BOU 01b, BOU 02b].

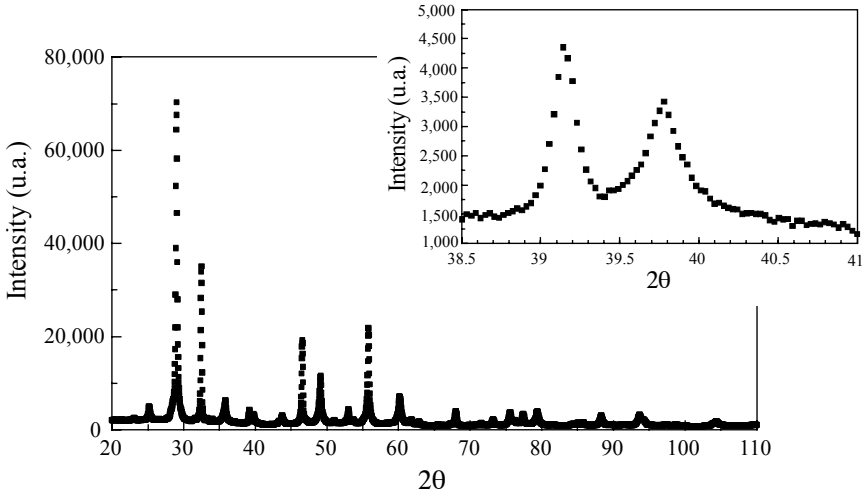

(a) Diffraction pattern of a powder of $SbBi_2Nb_2O_9$ fired for 10 hours at 700°C

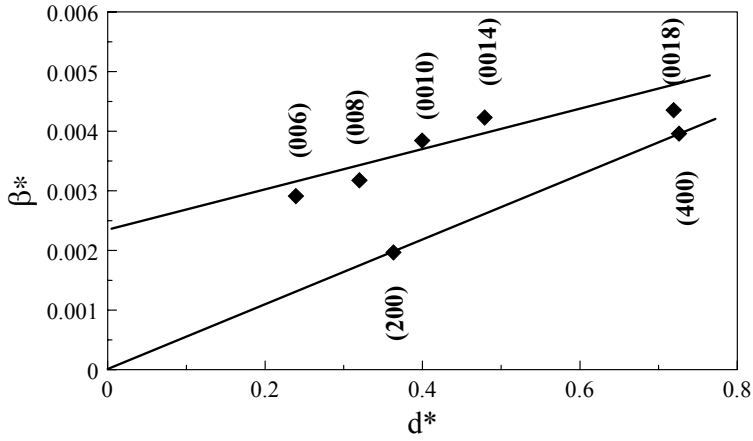

(b) Williamson-Hall plot obtained by fitting the pattern shown in Figure 6.8a with Voigt functions

Figure 6.8. *Study of the fault stacking density in a ferroelectric compound*

Regardless of why the integral breadth of the peaks is estimated, the peak fitting has to be done carefully in order to obtain truly significant widths, particularly when it comes to the peak tails. Generally speaking, microstructural studies require very

high quality patterns. However, this method shows an intrinsic difficulty: the increase in peak width causes them to overlap and it sometimes becomes difficult to distinguish each peak's contribution inside a cluster. Whole pattern fitting of the diffraction patterns makes it possible to limit the effect of this intrinsic flaw.

6.2.5. *Measurements of integral breadths by whole pattern fitting*

Since the early 1980s, a new way of quantifying structural defects has appeared. It consists of applying the developments implemented in structural analysis to the increase in peak width [KEI 83, LUT 90, THO 87b, LEB 92, LEB 99]. This method, which relies on Rietveld's structural analysis method, consists of a whole pattern fitting of the diffraction pattern.

In Chapter 3, we saw that the evolution of the peaks widths according to the diffraction angle can be represented by a function known as the Caglioti polynomial [CAG 58]:

$$H^2 = U \tan^2 \theta + V \tan \theta + W \qquad [6.29]$$

We showed that the grain size depends on the inverse of the cosine of the Bragg angle, whereas the microstrains are a function of the tangent of that angle. The method that was suggested consists of including, in the expression of the Caglioti polynomial, terms that can be refined and that depend either on $\tan \theta$ or on $1/\cos\theta$.

Naturally, the effects of size and microstrains are expressed as convolution products of the pure profile and the profiles resulting from each of these effects. Therefore, the modified expression of the Caglioti polynomial will depend on the hypotheses made on the shape of the profiles of each of the contributions. If we assume that the size effect leads to a Lorentzian profile, and microstrains to a Gaussian profile, we can write the following expressions:

$$H^2_G = (U_0 + D^2) \tan^2 \theta + V \tan \theta + W \text{ and } H_L = X \tan \theta + T/\cos \theta \qquad [6.30]$$

where H_G and H_L are the Gaussian and Lorentzian components of the full width at half maximum, respectively. The parameter D can then be used to obtain a value of the microstrains, whereas the size of the grains can be estimated from the value of T.

From a more general point of view, we can assume that each of the effects related to the grain size or to microstrains leads to Gaussian and Lorentzian contributions to the peak profile [THO 87b]. Furthermore, we can consider the possibility that the shape of the grains and the microstrain tensor are anisotropic

[GRE 85, LEB 92, LEB 97, NUT 99]. This type of refinement is available in recent software. We then get the following relations:

$$H_G^2 = (U + D_G^2)\tan^2\theta + V\tan\theta + W + \frac{T_G^I}{\cos^2\theta} \quad [6.31]$$

$$H_L = (X + D_L^I)\tan\theta + Y + \frac{T_L}{\cos\theta} \quad [6.32]$$

with:

– D_G: anisotropic Gaussian contribution from lattice distortions;

– D_L^I : isotropic Lorentzian contribution from lattice distortions;

– T_G^I : isotropic Gaussian contribution from grain size;

– T_L: anisotropic Lorentzian contribution from grain size;

– Y: isotropic Lorentzian contribution from grain size.

When using anisotropy parameters, it is common to suggest a model for the shape of the grains. Possible shapes include needles (infinite along one direction), plates (infinite in two directions) or ellipsoids. These models make it possible to bind together the values of the size or microstrain parameters along each crystallographic direction. These "constraints" limit the relative variation range of these parameters and therefore restrict the refinement.

Regardless of whether this general description or the one described earlier is used, the study of size and microstrains will always require determining the instrument's own contribution. As we showed in the equations above, this contribution is expressed through the values of the parameters U, V, W and X. Therefore, in this case, the instrumental function will be determined by refining these parameters based on a pattern obtained with a standard sample that does not cause any increase in peak width.

In any case, this type of approach is difficult, particularly because of the high number of parameters that can be refined, for which the approximate values of the structural parameters are needed beforehand. Most of the time, it is necessary to refine a sample that contains the same phases as in the one being studied, but with little or no microstructural effects. The parameters that define the structure are set and the effect of the microstructural defects will be included by assuming, in a first step, that this effect is isotropic.

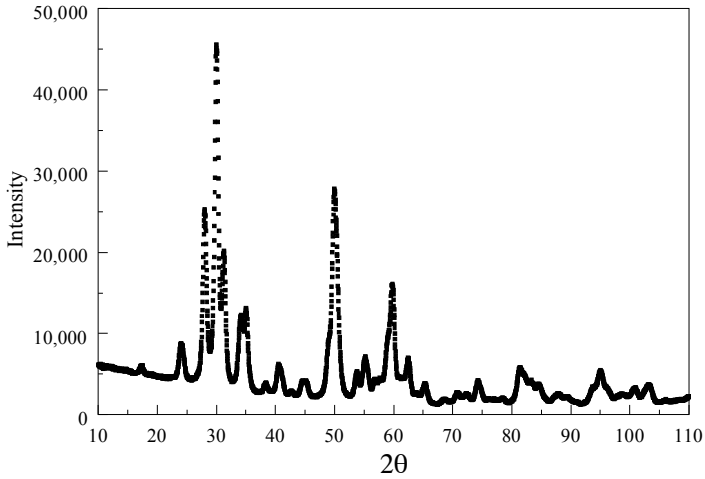

Figure 6.9. *X-ray diffraction pattern of a zirconia aerogel fired for 1 hour at 350°C*

We will illustrate this method by studies led on powders of zirconia nanocrystals. The diffraction pattern shown in Figure 6.9 was obtained with a zirconia aerogel as the sample, produced by drying a precursor gel of zirconia in supercritical conditions [SIL 96, SIL 97, LEC 98]. A qualitative illustration of this material's microstructure, obtained by transmission electron microscopy, is shown in Figure 6.10.

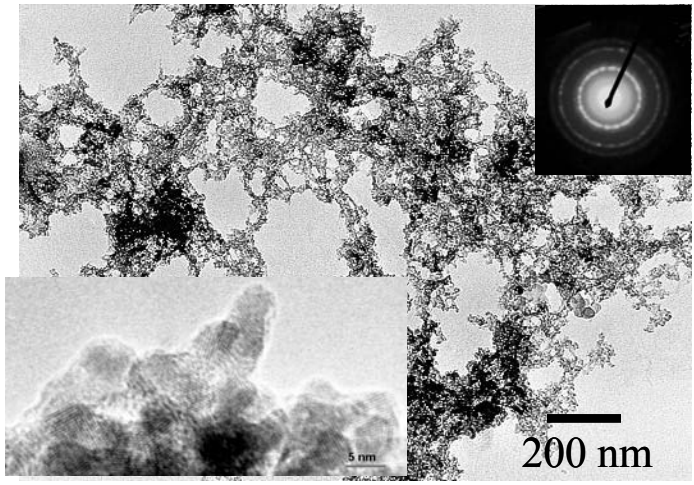

Figure 6.10. *Micrographs of a zirconium dioxide aerogel burned for 1 hour at 350°C, obtained by using transmission electron microscopy*

The analysis of the diffraction pattern in Figure 6.9 shows us that the sample is comprised of two phases, a combination of tetragonal and monoclinic zirconia. The peaks are very wide and overlap a great deal, which is why we conducted a whole pattern fitting by using the Fullprof software [ROD 92]. The resulting fit is shown in Figure 6.11. When the thermal treatment temperature increases, the crystals become larger and therefore the sample contains more and more monoclinic zirconia. Keeping track of this transformation is a complex task, since amounts of each phase varies simultaneously with the microstructural parameters. We managed, however, by whole pattern fitting, to determine, from the measurements of the peak widths, the evolution of the mean size of the crystals according to the thermal processing temperature. The sizes obtained for the tetragonal crystals of zirconia are shown in Table 6.1. Note that, for small thermal treatment temperatures, the sizes measured are extremely small (roughly 2 nm).

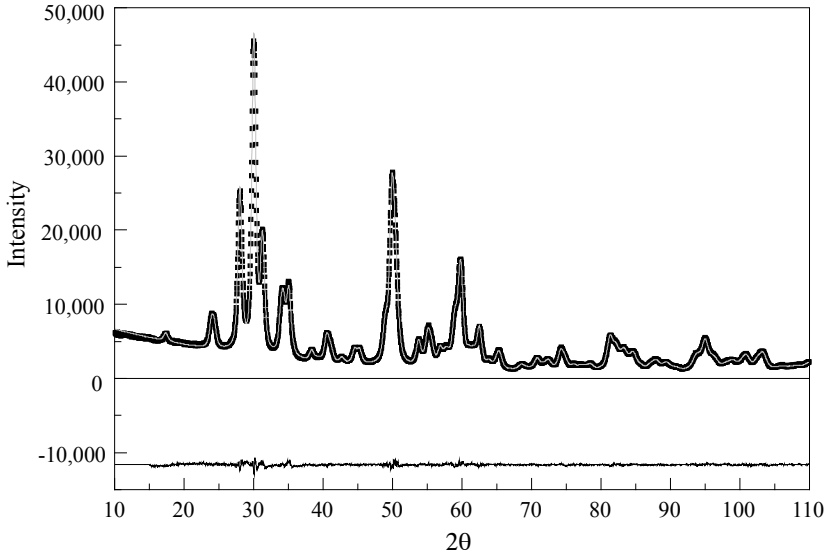

Figure 6.11. *Whole pattern fitting of the diffraction pattern reported in Figure 6.9. The calculated curve is shown in grey*

Thermal treatment temperature	350°C	450°C	600°C	700°C	900°C	1,000°C
Mean size (nm)	1.9	3.5	4.5	5.1	10.8	21.1

Table 6.1. *Mean size of the crystals in a zirconia aerogel depending on the thermal treatment temperature*

The next experimental illustration involves a zirconia xerogel. The samples and diffraction patterns used in this study have already been described in Part 1 of this book, when we discussed the quantitative phase analysis by whole pattern fitting of diffraction patterns (see section 4.2.2.2). In order to make the reading easier, we will show again the evolution of the diffraction patterns according to the temperature, as well as an example of whole pattern fitting. These two graphs correspond to Figures 4.3a and 4.3b from Chapter 4.

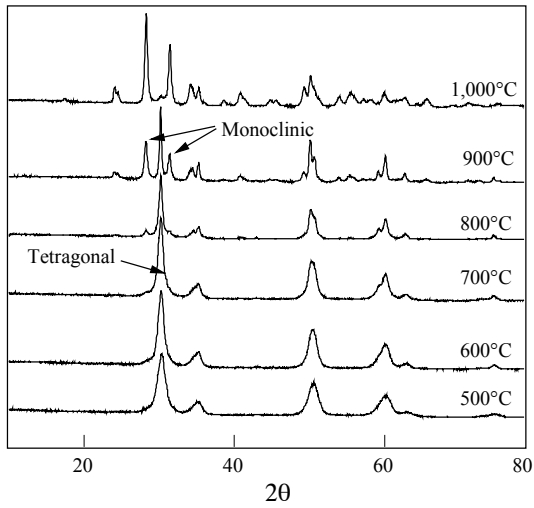

(a) Evolution of the X-ray diffraction patterns of zirconia xerogels fired for 1 hour at different temperatures

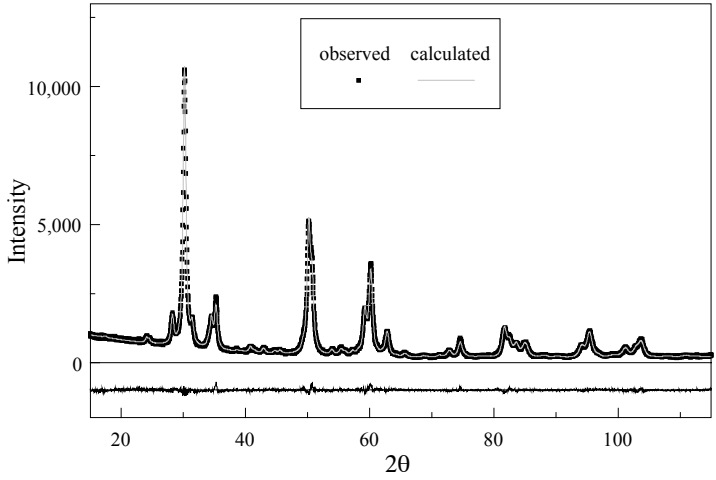

(b) Whole pattern fitting of the diffraction pattern obtained with a sample fired at 800°C

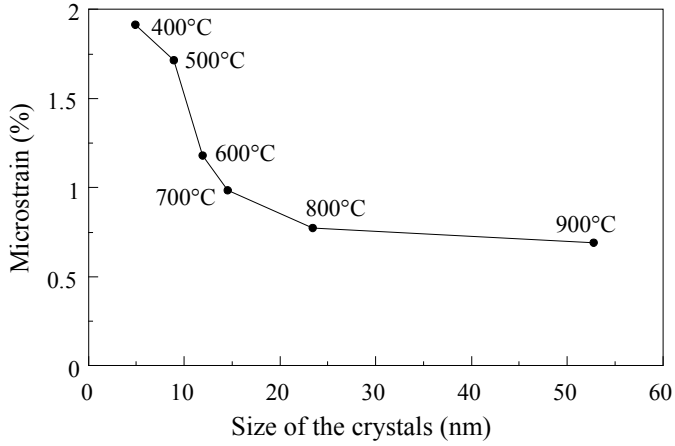

(c) Evolution of the microstrains according to the size of the crystals in a zirconia xerogel fired for 1 hour at different temperatures

Figure 6.12. *Combined study of the evolution of the mean grain size and of the amount of microstrain rate, according to the temperature of the thermal treatment, in zirconia xerogels*

The experimental and fitted diffraction patterns obtained for the xerogel fired for one hour at 800°C are shown in Figure 6.12b. As we showed in Part 1 of this book, the increase of the thermal treatment temperature causes the transformation from tetragonal to monoclinic zirconia. This process is related to how the crystals grow. We tracked this phenomenon by studying the evolution of the mean crystal size and of the microstrain amount inside the crystals according to the temperature. The result is shown, for tetragonal zirconia crystals, in Figure 6.12c. As you can see, the increase in mean size occurs alongside a significant decrease in the microstrain amount [SIL 96, GUI 96].

In the two examples we have just described, the diffraction peaks associated with the different phases of zirconia show a significant overlap. Only whole pattern fitting can lead to reliable results.

6.3. Microstructural study by Fourier series analysis of the peak profiles

6.3.1. *Direct analysis: the Bertaut-Warren-Averbach method*

In Chapter 5, we showed that the diffracted intensity distribution can be written as a Fourier series with coefficients which are directly related to the microstrain amount. Thus, the peak profile is expressed as:

$$I(2\theta) = \frac{Ki_e N |F_{hkl}|^2}{\sin^2 \theta} \sum_{n=-\infty}^{n=+\infty} A_n \cos 2\pi nl + B_n \sin 2\pi nl \qquad [6.33]$$

with:

$$A_n = \frac{N_n}{N_3} \langle \cos 2\pi l Z_n \rangle \text{ and } B_n = -\frac{N_n}{N_3} \langle \sin 2\pi l Z_n \rangle \qquad [6.34]$$

and we can write that the cosine term is the product of the coefficients related to the size by the coefficients related to the microstrains. Thus:

$$A_n = A_n^T A_n^D \qquad [6.35]$$

From these relations, Warren and Averbach suggested, in the 1950s, a method to separate the effects of size from the effects of microstrains. They observed that the size term which is written in the form $A_n^T = N_n/N_3$ does not depend on the diffraction order l, whereas this order plays a role in the expression of the term related to the microstrains.

The microstrains found inside the crystals correspond to small amplitudes displacements, which means that the value of Z_n must be small. The cosine can thus be expanded closer to zero. We obtain:

$$\langle \cos 2\pi l Z_n \rangle \to 1 - 2\pi^2 l^2 \langle Z_n^2 \rangle \qquad [6.36]$$

and therefore:

$$A_n = A_n^T - A_n^T \left(2\pi^2 l^2 \langle Z_n^2 \rangle \right) \qquad [6.37]$$

Warren and Averbach suggested switching to the logarithm of this expression, leading to:

$$\ln \langle \cos 2\pi l Z_n \rangle = \ln \left(1 - 2\pi^2 l^2 \langle Z_n^2 \rangle \right) \qquad [6.38]$$

For small values of l, we can expand the logarithm and write:

$$\ln \langle \cos 2\pi l Z_n \rangle = -2\pi^2 l^2 \langle Z_n^2 \rangle \qquad [6.39]$$

and finally:

$$\ln A_n = \ln A_n^T - 2\pi^2 l^2 \left\langle Z_n^2 \right\rangle \qquad [6.40]$$

If, for a given sample, we measured several reflection orders (001), (002), (003) etc., and if we extracted the cos A_n coefficients, we could plot the evolution of $\ln A_n$ according to l^2 for a set value of n. The y-intercepts give us the size coefficients A_n^T, whereas the coefficients related to the distortions are obtained from the slopes of these lines.

The distance $L = n\|\vec{c}\|$ represents the distance between the two cells before the distortion. The lattice deformation causes a variation $\Delta L = \|\vec{c}\| Z_n$. The ratio $\Delta L/L$ corresponds to the deformation along the direction defined by $\vec{c}$. Let ε_L be this ratio. Note that $\varepsilon_L = Z_n/n$ and that the slopes of the lines shown in Figure 6.13 is written $-2\pi^2 l^2 \left\langle Z_n^2 \right\rangle$. Therefore, the slopes of these lines lead us to a mean value of the square of the deformation along the direction in question.

The graph shown in Figure 6.13 assumes that l is small. Note that if several reflection orders are taken into account, this is no longer true. We only get straight lines when l is small, but that it is precisely the situation in which the lines are extrapolated in order to find the values at points l = 0.

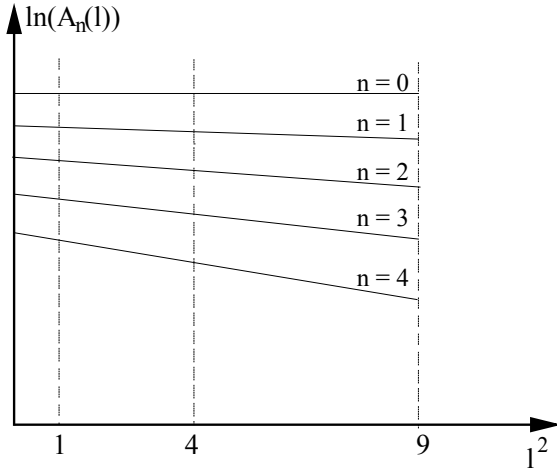

Figure 6.13. *Evolution of the logarithm of the Fourier series cosine coefficient according to the square of the Miller index l*

However, an additional hypothesis makes it possible to solve this problem. If we assume that the deformation distribution is a Gaussian function, we can write:

$$p(Z_n) = \frac{k}{\sqrt{\pi}} e^{-k^2 Z_n^2} \quad [6.41]$$

$$\Rightarrow \left\langle Z_n^2 \right\rangle = \frac{k}{\sqrt{\pi}} \int_{-\infty}^{+\infty} Z_n^2 e^{-k^2 Z_n^2} dZ_n = \frac{1}{2k^2} \quad [6.42]$$

Additionally:

$$\left\langle \cos 2\pi l Z_n \right\rangle = \frac{k}{\sqrt{\pi}} \int_{-\infty}^{+\infty} (\cos 2\pi l Z_n) e^{-k^2 Z_n^2} dZ_n \quad [6.43]$$

$$\Rightarrow \left\langle \cos 2\pi l Z_n \right\rangle = e^{-\pi^2 \frac{l^2}{k^2}} \quad [6.44]$$

$$\Rightarrow \left\langle \cos 2\pi l Z_n \right\rangle = e^{-2\pi^2 l^2 \left\langle Z_n^2 \right\rangle} \quad [6.45]$$

Therefore, we get:

$$A_n^D = e^{-2\pi^2 l^2 \left\langle Z_n^2 \right\rangle} \quad [6.46]$$

Thus, with a Gaussian deformation distribution, relation [6.40] is valid for any l and therefore the lines in Figure 6.13 are straight. This condition on the shape of the microstrain distribution is known as the Warren and Averbach hypothesis.

Nevertheless, there is no reason to assume *a priori* that the microstrain distribution is in fact Gaussian. Delhez and his colleagues [DEL 76, DEL 80] suggested an alternative to the Warren and Averbach hypothesis. Based on equation [6.37], obtained after expanding the cosine, if we plot the evolution of A_n according to l^2, the resulting line makes it possible to determine directly the size and the microstrain rate.

In order to interpret the values of the terms A_n^T related to the size of the crystal, and obtained from the graph in Figure 6.13, we will consider a new variable, denoted by p(i), which is the fraction of columns (with respect to all of the cell columns), that contains i cells. The values of the term N_n are written:

$$N_0 = \sum_{i=0}^{\infty} ip(i) = N_3 \qquad [6.47]$$

$$N_1 = \sum_{i=1}^{\infty} (i-1)p(i) \qquad [6.48]$$

$$N_2 = \sum_{i=2}^{\infty} (i-2)p(i) \qquad [6.49]$$

$$N_n = \sum_{i=|n|}^{\infty} (i-|n|)p(i) \qquad [6.50]$$

If we consider a continuous function p(i), the size term has the following expression:

$$A_n^T = \frac{1}{N_3}\int_{i=|n|}^{\infty} (i-|n|)p(i)di \qquad [6.51]$$

In order to determine the mean length of a column, which is given by $N_3\|\vec{c}\|$, we will assume that A_n^T continuously varies according to n and calculate the derivative of this function with respect to n. We get:

$$\frac{dA_n^T}{dn} = -\frac{1}{N_3}\int_{i=|n|}^{\infty} p(i)di \qquad [6.52]$$

The limit of this derivative when n tends to 0 is written:

$$\lim_{n\to 0}\left(\frac{dA_n^T}{dn}\right) = -\frac{1}{N_3}\int_{i=|0|}^{\infty} p(i)di = \frac{1}{N_3} \qquad [6.53]$$

This result shows that the intersection of the tangent to the line $A_n^T = f(n)$ at point n = 0 with the x-axis is equal to N_3. Therefore, the graph of $A_n^T = f(n)$ can be used to determine the value of $N_3\|\vec{c}\|$, which is the mean crystal dimension in the direction perpendicular to the (001) planes. This result is illustrated qualitatively in Figure 6.14.

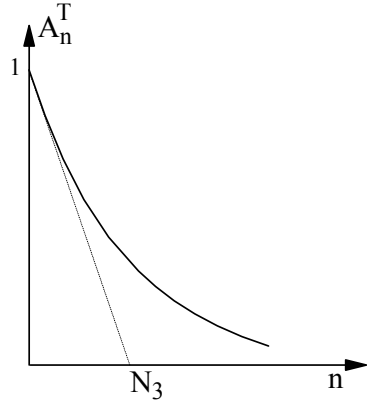

Figure 6.14. *Measurement of the mean crystal size in the direction perpendicular to the (001) planes based on the Fourier analysis*

If we go back to equation [6.52], we can calculate the second derivative with respect to n of the coefficients A_n^T. This derivative is written:

$$\frac{d^2 A_n^T}{dn^2} = \frac{p(|n|)}{N_3} \qquad [6.54]$$

This relation, first laid out by Bertaut [BER 49], shows that the Fourier analysis of the peak profiles makes it possible to obtain the size distribution. Later on, we will give an experimental illustration of this method, which constitutes one of the main purposes of Fourier analysis.

Methods based on the Fourier analysis of the peak profiles have an intrinsic flaw, since it is necessary for each studied peak to be clearly isolated. If several peaks partially overlap, the resulting experimental signal corresponds to the sum of the elementary contributions, in which case it is impossible to extract the Fourier coefficients of each peak. This is why, in practice, the method suggested by Bertaut, and then by Warren and Averbach was essentially applied to crystals with a cubic

symmetry. In the early 1990s, an indirect Fourier analysis method was suggested [BAL 93, BAL 99].

6.3.2. *Indirect Fourier analysis*

Balzar suggested combining the fitting of functions that had been chosen *a priori* with Fourier analysis. This process applies both to peak by peak and whole pattern fitting. It consists of fitting the experimental peaks mostly with Voigt functions and calculating the Fourier coefficients of the obtained functions.

Kielkopf [KIE 73] showed that the Fourier coefficients of a Voigt function are written as follows:

$$A_n(l) = e^{-\left(2l\beta_L + \pi l^2 \beta_G^2\right)} \qquad [6.55]$$

where β_L and β_G are the breadths of the Lorentzian and Gaussian components of the Voigt functions.

On the other hand, we will assume that the effects of both size and lattice distortions are described by a Voigt function, meaning that the resulting function will also be a Voigt function. We can then write:

$$\beta_L = \beta_L{}^T + \beta_L{}^T \text{ and } \beta_G{}^2 = (\beta_G{}^T)^2 + (\beta_G{}^T)^2 \qquad [6.56]$$

hence:

$$A_n^T(l) = e^{-\left(2l\beta_L^T + \pi l^2 (\beta_G^T)^2\right)} \text{ and } A_n^D(l) = e^{-\left(2l\beta_L^D + \pi l^2 (\beta_G^D)^2\right)} \qquad [6.57]$$

From these relations and by applying equation [6.53], we get the mean crystal size:

$$\langle D \rangle = \frac{1}{\lim_{l \to 0}\left[-\left(2\beta_L^T + 2\pi l (\beta_G^T)^2\right) e^{-\left(2l\beta_L^T + \pi l^2 (\beta_G^T)^2\right)}\right]} \qquad [6.58]$$

hence:

$$\langle D \rangle = \frac{1}{2\beta_L^T} \qquad [6.59]$$

We showed that, if we assumed a Gaussian microstrain distribution, then the Fourier coefficients related to these microstrains can be written:

$$A_n^D(l) = e^{-2\pi^2 l^2 \langle Z_n^2 \rangle} \qquad [6.60]$$

Let us recall that $L = n\|\vec{c}\|$, $\varepsilon = Z_n / n$ and $l = \|\vec{c}\| / d$. From this, we infer that the relation above can be written as:

$$A_n^D(l) = e^{-2\pi^2 l^2 \frac{1}{d^2} \langle \varepsilon_l^2 \rangle} \qquad [6.61]$$

Therefore,

$$A_n^D(L) = e^{-\left(2L\beta_L^D + \pi L^2 (\beta_G^D)^2\right)} = e^{-2\pi^2 L^2 \frac{1}{d^2} \langle \varepsilon_l^2 \rangle} \qquad [6.62]$$

and finally:

$$\langle \varepsilon_l^2 \rangle = d^2 \left(\frac{\beta_G^D)^2}{2\pi} + \frac{1}{L} \frac{\beta_L^D}{\pi^2} \right) \qquad [6.63]$$

This means that Voigt function fitting makes it possible to determine the size and the microstrain rate of each family of planes, along the direction perpendicular to this family of planes.

We will illustrate this process by considering again the study of the sample, comprised of oxide cerium nanocrystals, that was used in the international test led by Balzar [BAL 04]. Each of the peaks was fitted with a Voigt function and the Fourier coefficients of these fitting functions were then determined. The size measurement is shown in Figure 6.15.

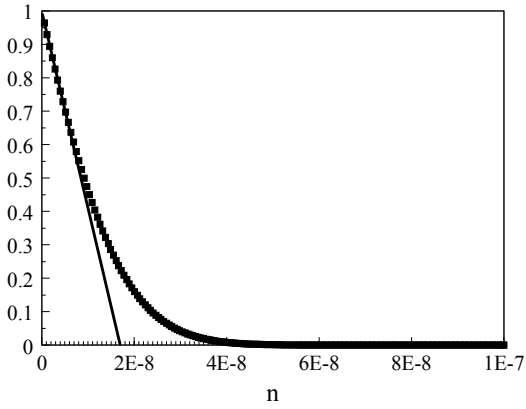

Figure 6.15. *Mean size of oxide cerium crystals measured by Fourier analysis of the peaks fitted with Voigt functions*

Likewise, from this Fourier analysis, we determined the size distribution of these crystals as well as the microstrain distribution. The results are shown in Figure 6.16.

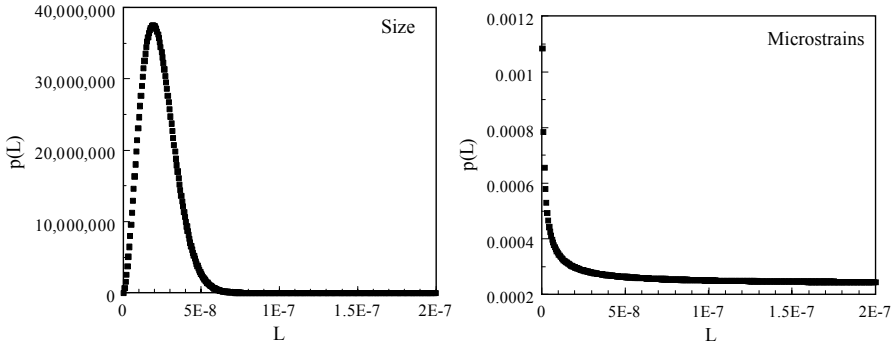

Figure 6.16. *Size and microstrain distributions measured by Fourier analysis of peaks fitted with Voigt functions*

6.4. Microstructural study based on the modeling of the diffraction peak profiles

The intensity distribution, as we have explained several times in this chapter, is the result of the convolution of a set of functions expressing, on the one hand, the contribution from the instruments and, on the other hand, various contributions

associated with each of the microstructural features specific to the sample. So far, the methods we have described for studying microstructures have consisted of a deconvolution, either directly by using the approach designed by Bertaut, Warren and Averbach or by reducing the profile problem to an integral breadth problem. In any case, the goal is always to extract microstructural parameters by decomposing the profile into different contributions.

Over the past few years, an alternative method has appeared. This time, it consists of directly comparing the measured signal with the one that was calculated by the successive convolutions of functions expressing the different effects of the instrument and the microstructure. We already mentioned this "modeling approach" in the first part of this chapter. We will now explain how it is implemented in order to determine the size and the microstrains.

Current developments of this approach often lead to modeling the entire diagram at the same time, with the benefit of better dealing with peaks that overlap. Naturally, the modeling can also be performed peak by peak.

The general idea consists of expressing each microstructural effect by way of the Fourier coefficients associated with the intensity distribution it generates. As we have already said in section 6.1.2, the integrated intensity is then written according to the following equation:

$$I(2\theta) = K \sum_{n=-\infty}^{n=+\infty} G(n) A_n^T A_n^D \ldots e^{2\pi i n l} \qquad [6.64]$$

where G(n) corresponds to the instrumental function's Fourier coefficients, A_n^T to the size effect's Fourier coefficients, A_n^D to those related to the microstrains, etc. As you can see, it is possible to generate a profile model that accounts for all of the sample's microstructural characteristics.

Several authors, and in particular the group led by Scardi [SCA 99, SCA 02, SCA 04a, LEO 04, SCA 06], applied this method to the combined study of grain size and microstrains, and even of stacking faults [SCA 99]. The same method is used to estimate the dislocation density [UNG 99a].

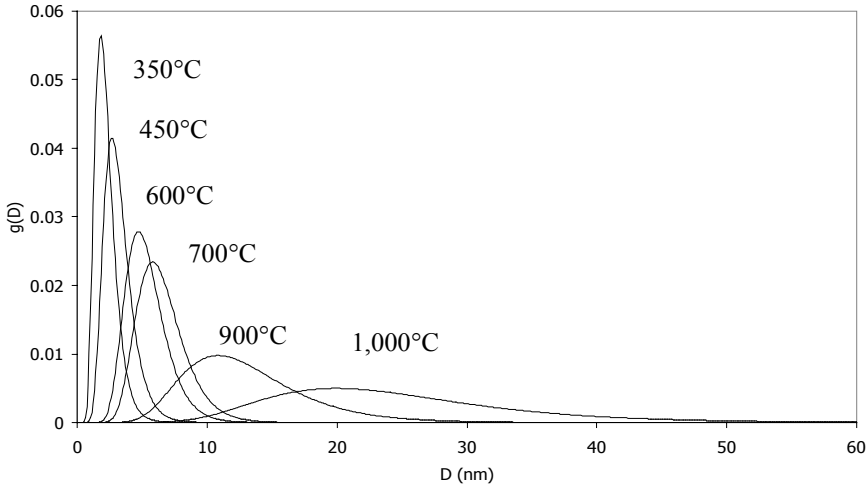

Figure 6.17. *Evolution of the size distribution in zirconia aerogels according to the thermal treatment temperature*

We will illustrate this method by going back to the study of zirconia aerogels that was presented in section 6.2.5. This study was led by Conchon as part of his final project as a student engineer [CON 04].

Several patterns, similar to that shown in Figure 6.9, were produced for different thermal treatment temperatures. These patterns were modeled according to the method we have just described, and we extracted, in particular, the size distribution functions of the tetragonal zirconia crystals. The resulting curves are shown in Figure 6.17. Clearly, increasing the thermal treatment temperature significantly widens the crystal size distribution.

The mean sizes and standard deviations characterizing the distributions shown in Figure 6.17 are listed in Table 6.2. These values are compared with those given before in Table 6.1, which were obtained by using the integral breadth method.

Thermal processing temperature	350°C	450°C	600°C	700°C	900°C	1,000°C
Mean sizes obtained by modeling (nm)	2.2	3.2	5.3	6.5	13	24.6
Standard deviations obtained by modeling	0.8	1.1	1.5	1.8	4.7	9.5
Mean sizes obtained by using the integral breadth method (nm)	1.9	3.5	4.5	5.1	10.8	21.1

Table 6.2. *Mean values and standard deviations of crystal size in the zirconia aerogels according to the thermal annealing temperature*

As you can see, the mean sizes obtained by modeling are slightly greater than those found from the integral breadth method. Naturally, the main advantage of the modeling method is that the distribution functions of the microstructural characteristics are known.

This page intentionally left blank

Chapter 7

Microstructural Study of Thin Films

Over the past 20 years, there have been many developments in the field of thin film analysis by X-ray diffraction, leading to the possibility, with the adequate equipment as we saw in Part 1, of studying films tens of nanometers or even a few nanometers in thickness [ACK 94].

There are two different ways to conduct this type of study. Many consist simply of optimizing the measurement conditions (incidence angle, etc.) and producing diffraction pattern diagrams of polycrystalline films, whether textured or not. The information is then interpreted as if the patterns had been produced with bulky samples. The study of epitaxial films constitutes another aspect of thin film diffraction. This time, the measurements are made in very specific conditions with the adequate equipment, which was described in Part 1 of this book. The information gathered this way, as well as how it is interpreted, is specific to this field of X-ray diffraction. In this regard, the study of epitaxial thin films deserves a chapter of its own in the field of X-ray diffraction [DUN 97, HOL 99, PIE 04]. The methods used often borrow from concepts developed in the context of single crystal studies and the instruments used are described as high resolution systems. When the crystals inside epitaxial films show a very small disorientation, typically smaller than a tenth of a degree, it is often necessary to rely on the dynamic theory of diffraction to process the data. We will not be dealing with this particular area, that is, all of the experimental illustrations described here will be explained in the context of the kinematic theory of diffraction. In this chapter, we will first present the study of polycrystalline films with or without texturation and in the second part, we will discuss the study of epitaxial films.

Regardless of what type of film is studied, the sample has to be positioned with great accuracy. In particular, it has to be possible, most of the time, to precisely define the X-ray beam's incidence angle on the film. We will start this chapter by presenting a methodology for positioning the sample inside the diffractometer in the optimal way. In practice, when conducting actual measurements, the sample is not always positioned as accurately as in what we will describe, but this constitutes *a priori* a limitation for the study. In Part 1 of the book, we described sample holders that were adequate for studying films. As we have already mentioned, these sample holders were often designed based on equipment developed for studying single crystals. In the following section, we will present a typical sample holder and describe how it is adjusted. Actual sample holders are more or less close to this equipment, but the adjustments described have to be performed.

7.1. Positioning and orienting the sample

The sample has to be placed on a sample holder that enables the user to orient it so as to have the normal to its surface parallel to the rotation axis ϕ. That way, during the acquisition of the diagram, the sample can be rotated around ϕ without modifying the incidence angle. When the film is deposited on a single crystal substrate, the adjustments consist of using the crystallographic axes of this single crystal as the frame of reference. If the substrate is polycrystalline or amorphous, the sample's frame of reference is then the surface of the substrate or of the film[1].

We will first describe how to orient the sample when the substrate is a single crystal, in which case this single crystal has to be in a fixed frame of reference attached to the diffractometer. The diagram of a complete sample holder that can be used to obtain a suitable orientation was shown in Figure 2.68 (Chapter 2) but is also shown in Figure 7.1, out of convenience for the reader.

1 Usually, in this case, only two reference directions are available, which are those that define the surface, whereas, of course, if the substrate is a single crystal, the frame of reference is comprised of three directions. Note, however, that if the substrate is amorphous or polycrystalline, the film is rarely epitaxial and therefore knowing the orientation with respect to two directions is usually enough.

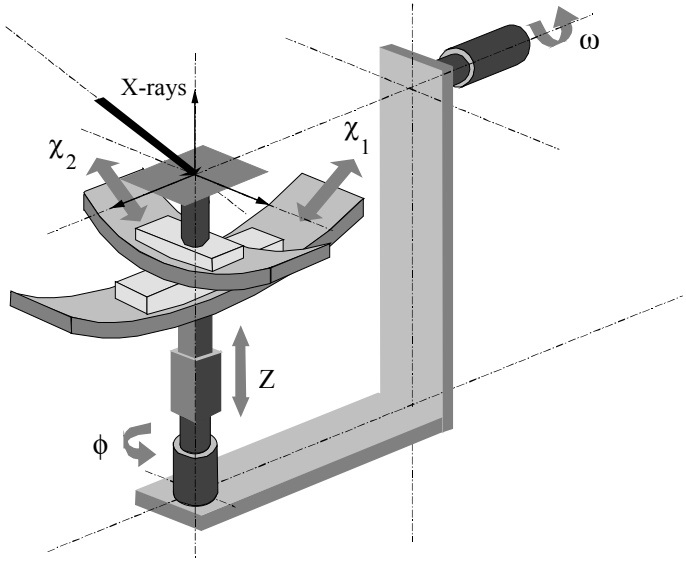

Figure 7.1. *Kinematic diagram of a five-axis sample holder*

We will consider five different orthonormal sets of coordinates:

$$R_1 = \begin{cases} \text{X-ray beam} \\ \text{Rotation axis } \omega \\ \text{translation axis of the entire sample holder} \end{cases}$$

$$R_2 = \begin{cases} \text{Rotation axis } \omega \\ \text{Rotation axis } \phi \\ \text{normal to the axis } \phi \end{cases} \qquad R_3 = \begin{cases} \text{Rotation axis } \phi \\ \text{Rotation axis } \chi_1 \\ \text{normal to the axis } \chi_1 \end{cases}$$

$$R_4 = \begin{cases} \text{Rotation axis } \chi_1 \\ \text{Rotation axis } \chi_2 \\ \text{normal to the axis } \chi_2 \end{cases} \qquad R_5 = \begin{cases} \text{Rotation axis } \chi_2 \\ \text{Diffracting plane} \end{cases}$$

The basic transformation matrices between these different sets of coordinates are written:

$$M_{1\to 2} = \begin{bmatrix} \cos\omega & 0 & \sin\omega \\ 0 & 1 & 0 \\ -\sin\omega & 0 & \cos\omega \end{bmatrix} \qquad M_{2\to 3} = \begin{bmatrix} \cos\phi & -\sin\phi & 0 \\ \sin\phi & \cos\phi & 0 \\ 0 & 0 & 1 \end{bmatrix}$$

$$M_{3\to 4} = \begin{bmatrix} 1 & 0 & 0 \\ 0 & \cos\chi_1 & -\sin\chi_1 \\ 0 & -\sin\chi_1 & \cos\chi_1 \end{bmatrix} \qquad M_{4\to 5} = \begin{bmatrix} \cos\chi_2 & 0 & \sin\chi_2 \\ 0 & 1 & 0 \\ -\sin\chi_2 & 0 & \cos\chi_2 \end{bmatrix}$$

Based on these matrices, we can lay out a simple relation between the Bragg angle of a given family of planes and the angles ω, ϕ, χ_1 and χ_2:

$$\sin\theta = \cos\omega\,(\cos\phi\sin\chi_2 + \sin\phi\sin\chi_1\cos\chi_2) + \sin\omega\cos\chi_1\cos\chi_2 \qquad [7.1]$$

The solution to this equation is:

$$\omega = \arcsin\left(\frac{BC - A\sqrt{A^2+B^2+C^2}}{A^2+B^2}\right) \qquad [7.2]$$

with:

$$\begin{aligned} A &= \cos\phi\sin\chi_2 + \sin\phi\sin\chi_1\cos\chi_2 \\ B &= \cos\chi_1\cos\chi_2 \\ C &= \sin\theta \end{aligned} \qquad [7.3]$$

Based on this relation, the positioning method goes as follows: the sample is placed on the sample holder with arbitrary values given to χ_1 and χ_2. For several values of ϕ along a semi-circle, the angle ω is adjusted so as to have the chosen family of planes diffract at a maximum intensity. From the pair (ϕ, ω), we can easily obtain the values of χ_1^0 and χ_2^0 by using least squares refinement. An example of such a refinement is shown in Figure 7.2.

This method requires the film to be produced on a single crystal substrate. This is the best situation, since the X-ray diffraction selectivity on the single crystal makes it possible to orient the sample with an accuracy in the range of a thousandth of a degree [BOU 01a]. When the film is deposited on a polycrystalline or amorphous substrate, others methods exist, derived from the one we have just described.

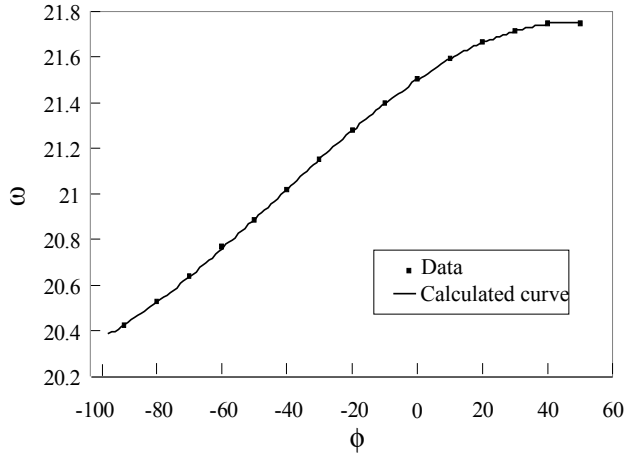

Figure 7.2. *Determining the values of χ_1^0 χ_2^0 and ω^0 by refining the evolution of ω according to ϕ*

The sample is placed the same way as before on the sample holder. For a given value of ϕ, the angle ω is changed by observing the evolution of the intensity of the direct beam. When ω increases, this intensity increases and then decreases beyond a certain value. When the value of the intensity is at its maximum, the surface of the sample is parallel to the direction of the incident beam and therefore the incidence angle is zero. As before, this measurement is made for several values of ϕ by taking note each time of the value obtained for ω. The pairs (ϕ, ω) are plotted in a refinement procedure, such as the one shown in Figure 7.2, and we thus infer the adjustment values for the cradles, as well as the value of ω, such that the incidence angle is zero for any ϕ.

The same method can be chosen by using the X-ray beams reflected on the surface of the film. This method is more difficult to implement than the previous one, since it requires separating the contributions from the reflected beam and those from the direct beam. However, if the quality of the incident beam (parallelism and monochromaticity) is high enough to enable this separation, then the adjustment will be accurate.

7.2. Study of disoriented or textured polycrystalline films

7.2.1. *Films comprised of randomly oriented crystals*

As we showed in Chapter 1, when a bulky sample, comprised of an infinite number of grains with perfectly random orientations, is irradiated with a

monochromatic X-ray beam, the locus of the beams diffracted by all of the crystals is a series of cones with half opening angles 2θ, where θ is the Bragg angle. When the polycrystalline sample is a thin film in which the crystals always have a random orientation, the phenomenon described above is still true. The problem is essentially experimental, but it is a difficult one. First, the X-ray beam has to hit enough matter to obtain a significant signal. Furthermore, even if the irradiated volume is sufficient, the number of grains must be very high, which means that the size of the grains must be much smaller than the thickness of the film. When this latter condition is not met, the orientation can no longer be described as random, which is a case we will discuss later on. We saw in Chapter 2 how the sample has to be irradiated at a low incidence angle, in the range of a fraction of a degree. The corresponding configuration is shown in Figure 7.3.

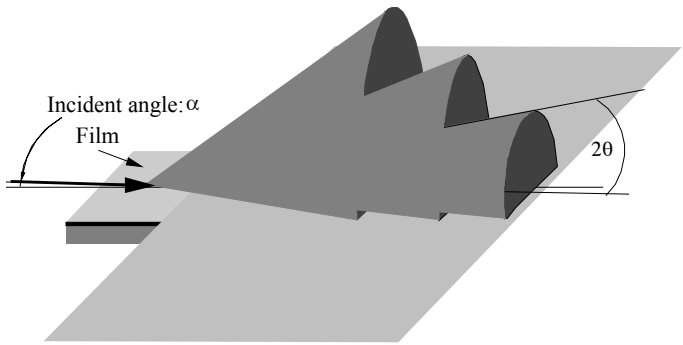

Figure 7.3. *Observation at a low incidence angle of a polycrystalline thin film in which the crystals are randomly oriented*

Once an estimate of the film thickness width is known, it is possible to choose the incidence angle that will lead to the highest possible irradiated volume. This angle is determined from the mass absorption coefficient and the density. We have seen in Chapter 2 that the adequate incidence angles for films which are a few tens of nanometers thick are in the range of a few tenths of a degree.

However, we have to point out three limitations to this approach. First of all, it is easy to determine the absolute density of the material in question if the film's chemical nature is known but, most of the time, the films produced have a significant residual porosity and, there is a chance that the path of the X-ray beams inside the material will be longer than estimated. Additionally, when a sample is irradiated at a very low angle, the beam is completely reflected and do not penetrates the film at all. Therefore, we have to work beyond the critical angle characteristic of this effect. The value of this angle, which depends on the density of the phase, is usually between 0.2 and 0.5°. Finally, it is important to choose an

incidence angle such that the irradiated surface is no larger than the sample's actual surface.

We will illustrate these considerations with the example of a study of a thin film of zirconia deposited on a single crystal of magnesia. The sample was produced by dipping the substrate in a precursor solution of zirconia. After the drying, a first thermal processing for one hour at 600°C led to the crystallization of the zirconia [GUI 98, GUI 99]. A qualitative observation was made by electron microscopy on a cross-section of the sample. A characteristic micrography is shown in Figure 7.4a. The thickness of the zirconia film is about 50 nm. This is very small for a randomly oriented polycrystalline film and obtaining a useable signal is the main problem. Very often, the only solution is to use a diffractometer with a synchrotron radiation source. We conducted this study in a laboratory by using the diffractometer shown in Figure 2.36. The pattern, produced in these conditions with an incidence angle equal to 0.35° and an acquisition time of 12 hours, is shown in Figure 7.4b [GUI 98, GUI 99]. The diffraction peaks characteristic of tetragonal zirconia are clearly visible and the measured intensities are consistent with the JCPDS entry for that phase.

(a) Transmission electron microscopy observation of a section of the sample

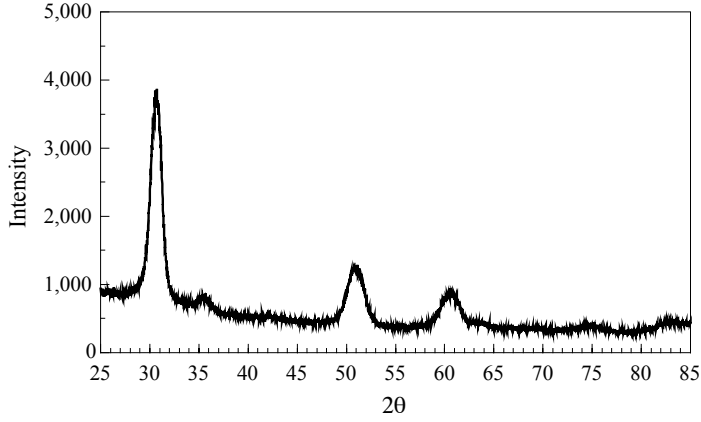

(b) X-ray diffraction pattern obtained at an incidence of 0.35°

Figure 7.4. *Study of a 50 nm thick, randomly oriented, polycrystalline film of zirconia*

Figure 7.5 shows a series of patterns obtained for identical samples annealed at different temperatures. The increase in the processing temperature causes a clearly visible decrease in peak width. The complete process will not be explained here, but this phenomenon corresponds to the growth of zirconia grains, similar to what we described in Chapter 6 with the study of the microstructure of aerogels and xerogels. This result indicates that the study, beyond simply determining which phases are present, also makes it possible to track, at least qualitatively, the microstructural evolution of the film in question. Some authors have thus implemented methods which are specific to the microstructural analysis on patterns obtained with polycrystalline films [BIM 83, SCA 97, SUT 95]. This type of study is particularly difficult since, generally speaking, the beam's incidence angle with the sample is small and the contribution from the instrument to the widths of the peak is significant. We note, however, that this effect will be limited if the diffractometer is equipped with long back analyzer slits, or if a synchrotron source is used.

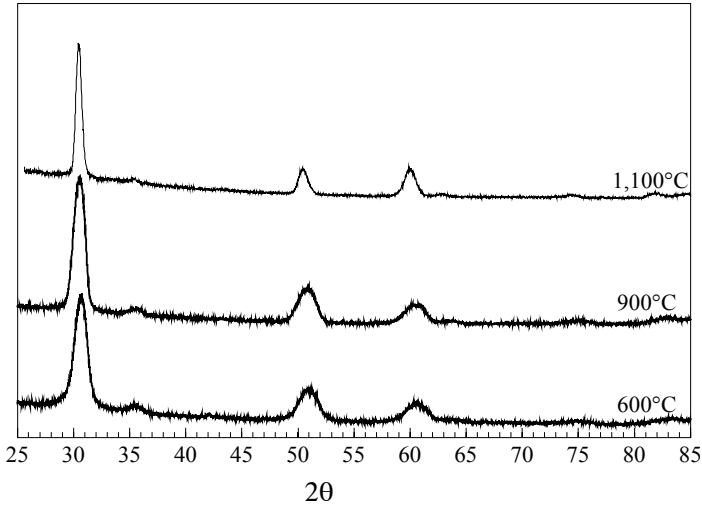

Figure 7.5. *Evolution of the diffraction pattern according to the sample annealing temperature*

The choice of the experimental illustration shown in Figures 7.4 and 7.5 was deliberate, based on the fact that a thickness of a few tens of nanometers for the film makes the measurement difficult. Note that when the thickness reaches a few hundred nanometers, the measurement quickly becomes much easier and the problem is close to the general case of studying randomly oriented polycrystalline samples. When the film is very thin, as it is here, one of the necessary conditions is to have a perfectly plane substrate.

The design of functional systems often leads to the production of multi-layered objects in which each layer has a specific function which is different from the function of the layer that supports it. It is common to come across samples comprised of three or four different layers[2]. These systems are sometimes the result of superficial changes in the substrate (an oxidation, for example) or they are produced by creating consecutive deposits. In both cases, the nature and the relative rate of each phase is a key question. X-ray diffraction is one of the only non-destructive techniques that can be used to determine these parameters.

Consider a sample comprised of *n* films with given nanometric thicknesses *e*. If we irradiate this sample at a high incidence angle, the resulting pattern will contain the characteristic peaks of all the phases contained in each film. By decreasing the incidence angle, the outer films will be favored and for a low incidence angle, which can easily be determined if the thicknesses of the films are known, only the characteristic peaks of the phases contained in the last film of the sample will be visible (see Figure 7.6).

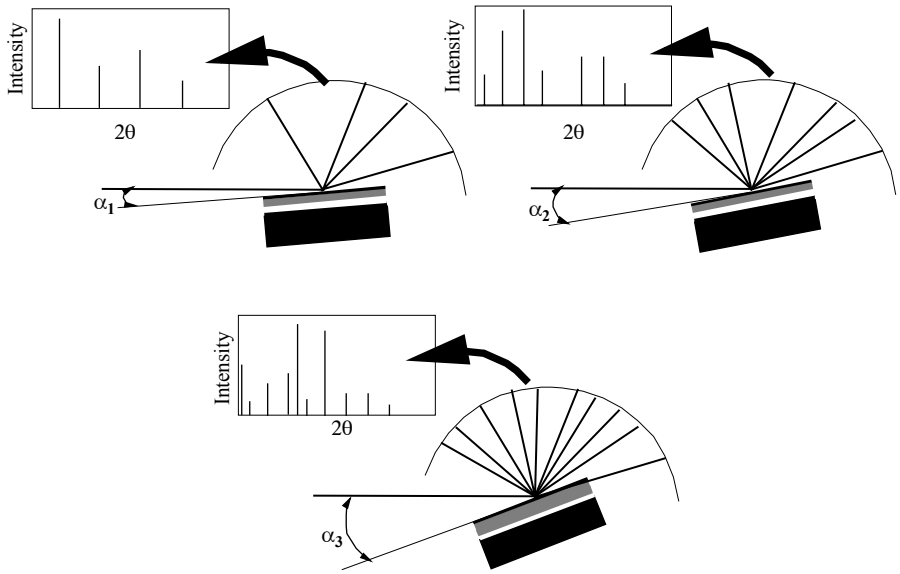

Figure 7.6. *Study of a multi-layered sample comprised of randomly oriented crystals*

2 We are dealing here with polycrystalline layers comprised of randomly oriented crystals. Multi-layered objects comprised of epitaxial films often include dozens of layers (see, for example, [KID 03]) but this is beyond the scope of this section.

From a more general standpoint, if we consider a polyphase sample with a concentration gradient that extends over a depth of a few tens of micrometers, then X-ray diffraction at a fixed incidence can be used for producing concentration profiles based on measurements of diffracted intensities. Quantitatively determining concentrations requires accurately taking into account the irradiated volumes. Relations inferred from the equations given in section 2.3.1.2 have been laid out and are nowadays relatively often used [SCA 93].

An experimental illustration of the study of such objects, made of several polycrystalline films, is shown in Figure 7.7. We realized a sample comprised of a titanium oxide film placed on top of a zirconia film, all of this deposited on a sapphire substrate. The titanium oxide film is roughly 20 nm wide and the zirconia film about 50 nm wide. Two diffraction patterns obtained with the incidence angles 0.25 and 0.5°, respectively, are shown in Figure 7.7. Each pattern contains, in the zone we are focusing on, the main peak for the anatase and that for the tetragonal zirconium dioxide. As you can see, however, the incidence angle significantly modifies the intensity ratio of these two peaks. When the incidence angle decreases, the diffraction signal corresponding to the titanium oxide increases.

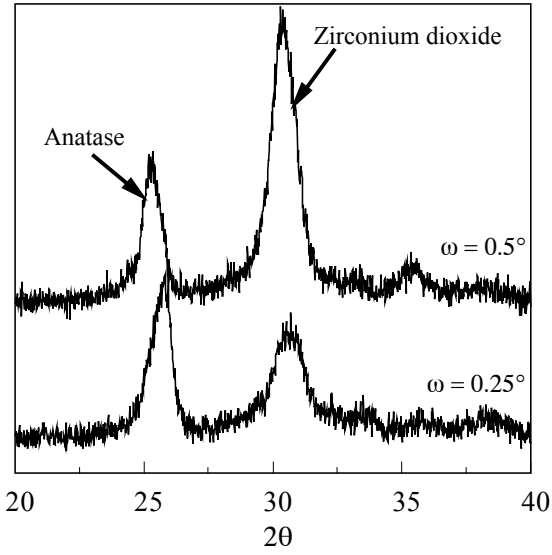

Figure 7.7. *Influence of the incident X-ray beam's incidence angle on the diffraction pattern of a sample comprised of a titanium oxide film and a zirconia film, deposited on a sapphire substrate*

7.2.2. *Studying textured films*

A layer, by definition, is two-dimensional. This macroscopic situation often leads to a non-random orientation of the crystals that comprise the deposit. It is understandable that, inside a polycrystalline film growing on an oriented single crystal, the crystals tend to grow in non-random crystallographic directions. This is why the idea of studying the structure is often associated with the study of crystal orientation. In the previous section, we saw how to characterize randomly oriented polycrystalline films. In this section, we will describe the methods that make it possible to determine and study crystallographic orientations inside textured thin films. Generally speaking, the word texture is used when the crystals inside the sample have non-random orientations. The situation where all the crystals have the same orientation in the three directions of space is called epitaxy and it will be discussed later on.

7.2.2.1. *Determining the texture*

Let us go back to Figure 7.3 and imagine that the crystals inside the film no longer have random orientations. This situation can be described by Figure 7.8a. The diffraction cones are no longer continuous. For a given angle 2θ, some directions characterized by a given angle ϕ are favored. It is also possible to observe the absence of certain diffraction cones corresponding to families of planes specific to the phases in the film.

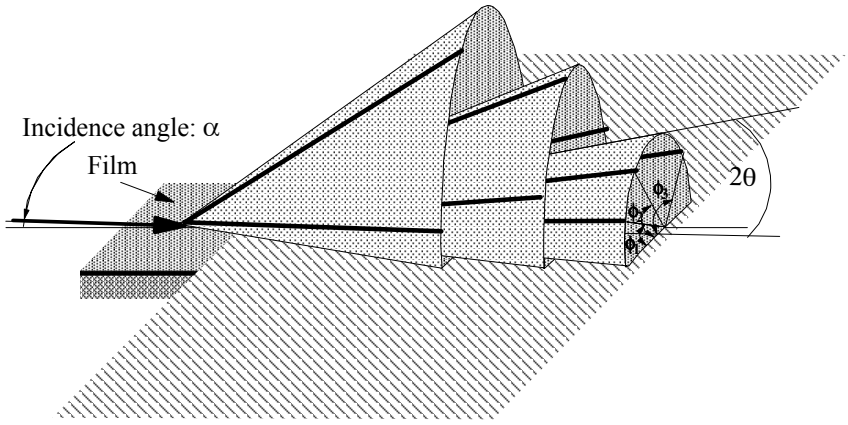

(a) Diagram of the diffraction signal's spatial distribution obtained with a textured film

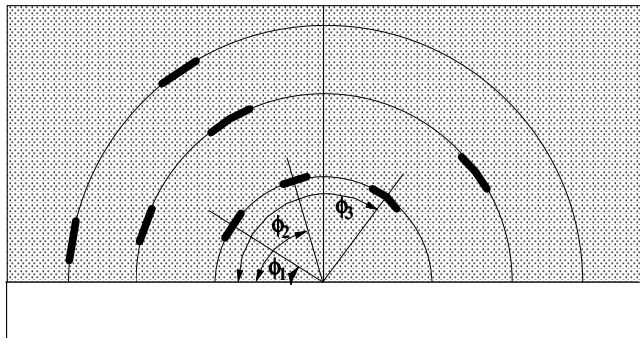

(b) Demonstrating a texture by using a diffractometer equipped with a plane detector

Figure 7.8. *Observing a textured film*

Experimentally, the effect of texture on the resulting signal depends on the device used. If a large plane film is placed perpendicularly to the axis of the incident beam shown in Figure 7.8a, the resulting figure will correspond to the intersection of the diffraction cones with that plane. If the film is textured, the diffraction figure will be similar to the one shown in Figure 7.8b.

We saw that studying thin films makes it necessary for the diffraction patterns to be produced at a fixed and controlled incidence. We will assume that we are conducting an experiment with this type of equipment and that we want to find out whether the film is textured or not.

The first way of showing a texture effect directly corresponds to the diagram shown in Figure 7.8. If a plane detector is placed as shown in this figure, the texture effect is directly visible. The simplest plane detector is a photographic film, but texture systems based on plane photographic films hardly exist anymore. Lately, however, this geometry has sparked some interest since large plane solid detectors have become available (see Chapter 2). The use of these detectors, whether gas or solid, is constantly growing and they are beginning to be built on laboratory devices [HE 02, DIC 02], whereas only a few years ago, they were only used with synchrotron radiation.

When producing a diffraction pattern in asymmetrical geometry with a punctual detector, the presence of a preferential orientation of the crystals comprising the film should, for a given phase, lead to discrepancies between the measured intensities and those found in the JCPDS entry for that phase. When the film is irradiated at a low angle, the value of this angle should have no particular relation with the angular positions of the diffracting planes. As a result, all we observe are intensity gaps

which would be unwise to interpret directly. Note, additionally, that even if no variation with respect to the JCPDS entry is observed, the film can still be partly oriented. For example, if the film contains a certain amount of grains for which the (hkl) planes are parallel to the substrate's surface, they will not diffract when this film is irradiated at a low incidence angle and therefore will not affect the intensity measurements. However, by varying the incidence angle slightly at random, a textured film will show non-random intensity variations.

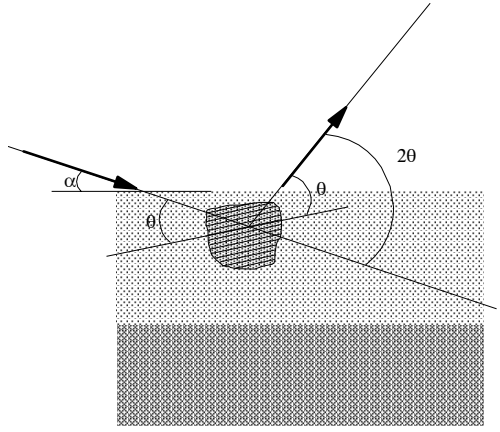

(a) Measurement configuration

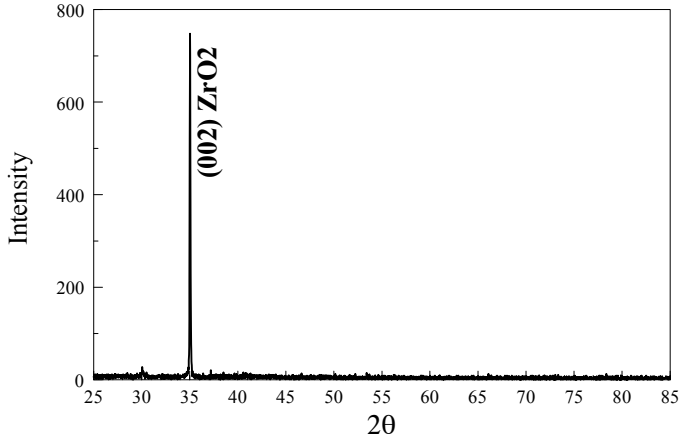

(b) Observation of a zirconia film in which the grains are oriented so as to have the (002) planes parallel to the surface of the sample. The incidence angle ω is equal to the Bragg angle $\theta_{(002)}$

Figure 7.9. *Illustration of a preferential orientation*

When the film is suspected of being textured either from intuition or from preliminary observations similar to what was described above, finding evidence of these preferential orientations has to be done according to a rigorous method. By using an asymmetrical diffraction configuration, the sample is irradiated at an incidence angle α, such that the angle between certain planes of the oriented grains and the beam is equal to the Bragg angle θ_i of this family of planes (see Figure 7.9a). In this situation, a high intensity should be observed, with only one peak[3] in the pattern, the position of which should be equal to $2\theta_i$. This configuration is illustrated experimentally in Figure 7.9b [MAR 98].

If, for a given family of planes (hkl), the situation described above occurs, then knowing the angle between this family of planes and another with Miller indices (h'k'l'), we can determine the angle at which the sample should be irradiated in order for this family of planes (h'k'l') to be in the Bragg position. This will enable us to confirm that the sample is, in fact, textured. From this standpoint, it is simple and better to irradiate the sample at an angle such that the family of planes (2h2k2l) is in the Bragg position. Note that this process implies irradiating the sample at angles that are not necessarily small. The volume and hence the number of diffracting grains are usually small. However, most of the time, the observed signal is significant because there is a large number of crystals precisely oriented in the position in question, which diffract a considerable intensity.

Other methods for finding evidence of preferential orientations, slightly different from the one described above, are sometimes found in other works. The sample is studied by symmetrical diffraction (Bragg-Brentano system). In the case of textured films, the resulting pattern is very peculiar and it is important not to misinterpret it. Thus, for a diffraction pattern produced with this type of system, the angle between the sample and the X-ray beam varied continuously while the measurement was taking place (see Chapter 2). If the film contains grains in which a family of planes is parallel to the surface of the substrate, when the beam's incidence angle with the sample reaches the value of the Bragg angle for that family, a high intensity will be measured. We could then conclude to the existence of a preferential orientation but we would still have to characterize it. On the other hand, if no abnormally high intensity is measured when the incidence angle varies, there is no reason to conclude that there is no preferential orientation inside the film, since it is quite possible that the grains have a non-random orientation but they are not parallel to the surface of the substrate[4]. A Bragg-Brentano system, in some specific cases, makes it possible

3 Other peaks can appear if the incidence angle is such that other planes are approximately in the Bragg position, or if part of a film is comprised of randomly oriented grains.

4 Aside from this intrinsic aspect of the sample, Bragg-Brentano systems usually are not equipped with a support that makes it possible to orient the sample accurately with respect to the diffractometer's frame of reference. Thus, an angular error in the positioning of the

to find evidence of preferential orientation rather quickly. However the interpretation of the observed signal is difficult [TIZ 96]. The concept of an orientation factor, which is sometimes found in other works and mentioned from patterns realized in these conditions, has no physical meaning.

We described in detail the method for illustrating a non-random orientation of grains in a film. We are now going to continue by describing the methods for quantifying this orientation.

7.2.2.2. *Quantification of the crystallographic orientation: studying texture*

Quantitative texture studies are conducted with the specific instruments we described in Part 1. Chapter 4 dealt with the traditional applications of diffraction on polycrystalline samples and not with quantitative texture study. It is clear, however, that this kind of measurement, which involves polycrystalline materials in general, whether in the form of films or not, is an important and very old application [KNI 13] of X-ray diffraction. We have decided, however, not to deal with this particular field, since other books are available that discuss it in detail [BUN 82, BUN 99].

Regardless of what type of sample or instrument is used, the results of the measurements are usually given in the form of pole figures. Without going into detail, we will describe these figures and explain how they can be drawn.

The concept of pole figures

The pole of a crystal plane with indices (hkl) is the intersection of the normal with that plane that passes through the point C and a sphere, centered in C, and with an arbitrary diameter.

Consider a polycrystalline sample placed at a point O. A crystal within this sample diffracts for a family of planes (hkl) if and only if the reciprocal lattice point associated with this family is on the Ewald sphere with radius $1/\lambda$. By definition, the tip of the vector $\vec{k}_0 = (1/\lambda)\vec{S}_0$ is the origin of the reciprocal lattice and the scattering vector $\vec{S}$, which links point C with lattice point hkl*, has a norm equal to $1/d_{hkl}$. For all the crystals contained in the sample which diffract for a given family of planes (hkl), we observe a set of lattice points hkl* located on a sphere with radius $1/d_{hkl}$, which is centered in C. By definition, the directions [hkl]* are normal to the (hkl) planes and therefore the distribution map of the hkl* lattice points on the surface of this sphere is the hkl pole figure. This configuration is shown in Figure 7.10.

sample can significantly modify the intensity diffracted by one peak or another, making the measurement highly qualitative.

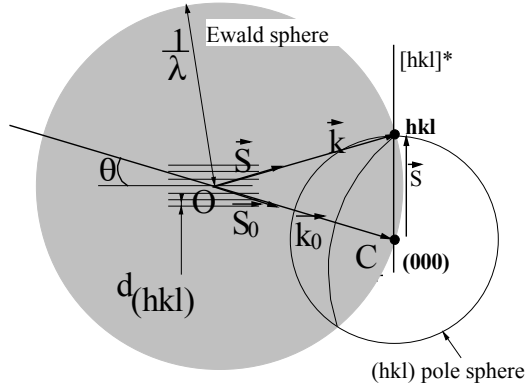

Figure 7.10. *Representation of the pole sphere*

The traditional representation of a pole figure is its stereographic projection, which associates each point on the surface of the sphere with a point located in that sphere's equatorial plane. This projection is obtained as shown in Figure 7.11. For an arbitrary point P located on the northern hemisphere[5], the line segment PS is drawn, linking that point with the sphere's south pole. The intersection of this line with the equatorial plane is a point p, defined as the stereographic projection of P. We will not go into details about this projection, but we should point, however, that it leaves angles unchanged, which means that a stereographic projection can be used to measure the angles between different directions and, hence, between families of planes.

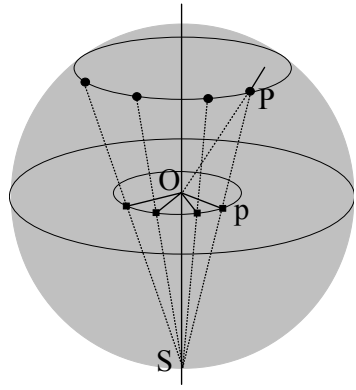

Figure 7.11. *Stereographic projection*

5 Of course, the reverse situation is true for a point located on the southern hemisphere.

Therefore, an (hkl) pole figure is a disc on which are drawn the projections of the contour lines of the diffracted intensity measured on the pole sphere, each line corresponding to a given intensity value. An example of such a map is shown in Figure 7.12. Modern texture measuring systems are combined with software that can directly draw these figures based on the intensity measurements.

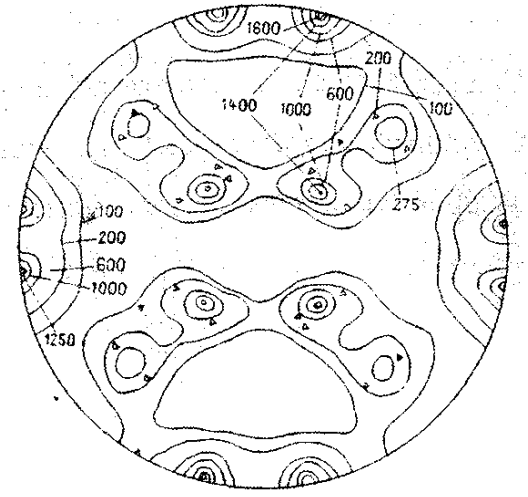

Figure 7.12. *Example of a pole figure*

Based on the experimental result, determining preferential crystallographic orientations observed for a pole figure is done by comparing this figure with the corresponding, theoretical stereographic projection for the phase in question. Complete texture studies can help determine the orientation density function, which is equal, for a given orientation, to the volume fraction of the sample with that orientation. General methods have been designed to directly draw such density functions based on the intensity measurements.

As we have already mentioned, this description of quantitative texture measurements based on pole figures involves both bulky samples and thin films. The experimental conditions may differ in order to optimize the diffracting volumes, but this has already been discussed in Part 1 of this book. We will not go into any further detail on the study of textured films since, most of the time, it can all be reduced to the general case of quantitative texture analysis.

7.3. Studying epitaxial films

When the crystals that comprise the films are all oriented the same way, the first study that should be conducted is, naturally, to determine this common orientation. The evaluation of the disorientation with respect to the normal to the film-substrate interface is performed with the use of rocking curves, whereas the orientation within the plane is determined by ϕ-scans, which consist of measuring the evolution of the intensity diffracted by planes that are not parallel to the interface, while the sample is rotating around the normal to this interface. These techniques have become common and most manufacturers sell diffractometers adapted to this kind of study.

More recently, measurements have been developed based on the complete evaluation of the intensity distribution over the entire diffraction spot. This "reciprocal space mapping" [FEW 97] can be used to give an account of all the microstructural effects that have an influence on the diffraction signal. Thus, it is possible to obtain the distribution functions of orientation, size, morphology and the size distribution of the diffracting domains, as well as the microstrains.

We will first describe the methods for accurately determining the orientation of the crystals and then, in a second step, we will explain in detail how reciprocal space mapping can be used to quantitatively analyze the microstructure of epitaxial films.

7.3.1. *Studying the crystallographic orientation and determining epitaxy relations*

If two crystals are placed side by side, it is possible to define vector relations that express the characteristic crystallographic directions of one of the crystals in a set of coordinates defined by the cell of the other crystal. These are referred to as epitaxy relations. By extrapolation, when the grains that comprise a polycrystalline film all have virtually the same orientation, it is possible to define crystallographic axes specific to this orientation and to find the relation between these axes and those, for example, of the single crystal on which the film is deposited. If the film and the substrate share the same crystal nature, we are dealing with homoepitaxy, otherwise, it is referred to as heteroepitaxy. Epitaxy relations are three-dimensional and therefore they are usually written as follows:

$$\begin{cases} (hkl)_{substrate} // (h'k'l')_{film} \\ [uvw]_{substrate} // [u'v'w']_{film} \end{cases} \qquad [7.4]$$

In the following sections, we will show how we can find these relations from X-ray diffraction measurements. As we have just explained, in order for relations of this type to make sense, the crystals in the film must all be oriented the same way, which means that the film is a quasi-single crystal[6]. As a result, the relevant techniques and vocabulary are often taken from single crystal diffraction.

7.3.1.1. *Measuring the normal orientation: rocking curves*

Consider a heteroepitaxial film on a single crystal substrate. For a given family of planes (hkl), specific to the crystal phase that comprises the film, when the sample is irradiated at an incidence angle enabling these (hkl) planes to diffract, each crystal within the film diffracts and contributes to the intensity of a peak located at the angle 2θ given by the Bragg relation.

However, the angular selectivity of this diffraction effect is very high. If we assume that the beam irradiating the crystal is strictly parallel and strictly monochromatic, then only the grains that are strictly in the Bragg position will diffract for a given value of the incidence angle. When this incidence angle is modified, over a certain angular range, other crystals, slightly disoriented compared to the previous ones, diffract. The width of this angular range for which a diffracted intensity is observed at the angle 2θ is a direct expression of the disorientation of the crystals that comprise the film. This process is similar to the one used for estimating the mosaicity of single crystals and makes it possible to determine the relative disorientation of the grains comprising an epitaxial film.

An experimental illustration of this kind of measurement is shown in Figure 7.13 [MAR 00]. The film in the example is comprised of zirconia crystals and has been deposited on a sapphire substrate cut parallel to the $(11\bar{2}0)$ planes.

The diffraction pattern shown in Figure 7.13a is similar to the one shown in Figure 7.9b. It shows that the zirconia crystals are oriented so as to have their family of planes (111) parallel to the substrate's family of planes $(11\bar{2}0)$. A set of diffraction patterns similar to this one was produced by modifying the incidence angle inside an angular range of about a degree. As you can see in Figure 7.13b, the intensity of the (111) peak diffracted by the zirconia crystals increases and then decreases. The resulting rocking curve, obtained by digitally integrating each of the patterns, is shown in Figure 7.13c. If we consider that the film is comprised of crystals free of any defects, and with a mean size such that there is no widening of the diffraction signal, then each diffracting crystal can be associated with a

6 We will see later on that we can determine the relative disorientation of the crystals in these films. It is often greater, by about a few tenths of a degree, than disorientations between the domains of a single crystal. Therefore, the phrase quasi-single crystal should be used with care.

reciprocal lattice point that is infinitely punctual. The signal spreading out can only be caused by the fact that the crystals are slightly disoriented with respect to one another[7]. Therefore, the rocking curve's width gives a direct evaluation of the relative disorientation of the crystals around the normal defining the mean orientation. In the case of the illustration shown in Figure 7.13, the relative disorientation of the crystals is 0.2°.

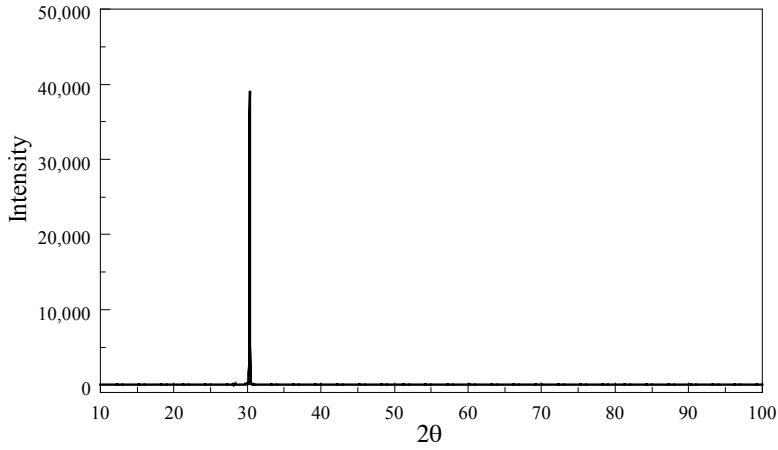

(a) Diffraction pattern obtained at an incidence angle equal to the Bragg angle $\theta_{(111)}$

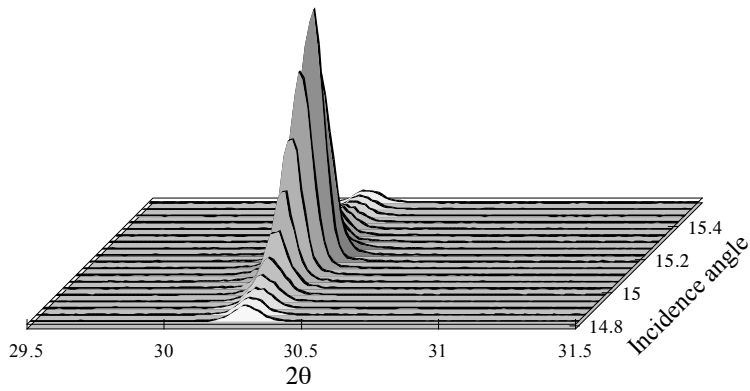

(b) Evolution of the diffracted intensity plotted according to the incidence angle

7 The contribution from the instrument is neglected here.

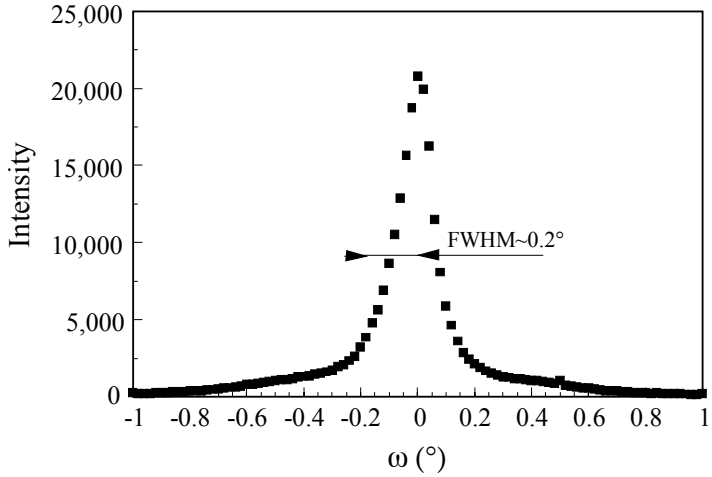

(c) Evaluation of the relative disorientation of the zirconia crystals by measuring the width of the rocking curve

Figure 7.13. *Illustration of the normal orientation and evaluation of the relative disorientation of the zirconia crystals deposited on a sapphire substrate [MAR 00]*

7.3.1.2. *Measuring the in-plane orientation: ϕ-scan*

Consider a film with a known normal orientation such that a given family of planes (hkl) is parallel to a family of planes in the single crystal substrate. There are two possibilities: either the crystallographic directions, in the (hkl) plane, of the crystals comprising the film have random orientations, or these directions are oriented the same way for all the crystals. We will study the latter case.

If we wish to know the orientation of this (hkl) planes by X-ray diffraction, it is necessary, by definition, to conduct a complementary study by making another family of planes (h'k'l') diffract; a family such that its intersection with the (hkl) planes is a characteristic crystallographic direction. By choosing as a reference the angular position of these (hkl) planes, and by knowing the angle between any (h'k'l') angle of the phase in question and these (hkl) planes, it is possible to determine the incidence angle at which the film should be irradiated in order for the (h'k'l') family to be in the Bragg position. Only the families of planes for which this incidence angle is positive can be characterized.

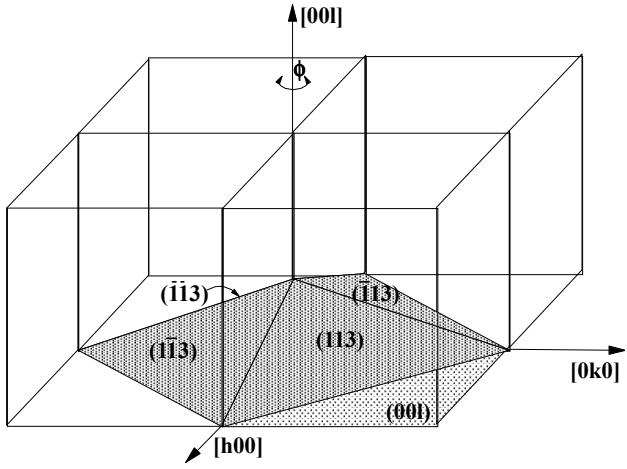

Figure 7.14. *Relative positions of the (113) planes in a film comprised of cubic crystals*

Even if a film is irradiated at the adequate incidence angle, a diffraction signal will only be observed if the corresponding planes are in the Bragg position. If the in-plane orientation is random, diffraction will occur whatever the value of ϕ. On the contrary, if this orientation is precisely defined, then no signal is obtained, except for certain values of ϕ. The angular gaps between these values only depend on the crystal symmetry of the phase in question. Figure 7.14 shows that, when studying a film comprised of crystals with a cubic symmetry and a normal orientation such that the (h00) planes are parallel to the surface of the substrate, then for four different angles ϕ which are 90° apart, diffraction by the (113) planes should be observed. Therefore, evidence of an in-plane orientation can be found by conducting measurements incrementally, by varying the angle ϕ while maintaining the incidence angle at a value such that the family of planes that was chosen is always irradiated at its Bragg angle. This is called a ϕ-scan. There are various experimental methods for producing this kind of diagram. Most of the time, the sample is placed on a sample holder like the one shown in Figure 7.1 and irradiated with a parallel beam. A widely open punctual detector is then placed at the angle 2θ that was chosen. For each value of ϕ, the integrated intensity diffracted in the vicinity of the angle 2θ is measured. The evolution of this intensity is then plotted according to ϕ. Figure 7.15 shows such a diagram, in which you can see the four peaks located at 90° from each other. A diagram like this shows that the film is completely oriented in the plane. The four peaks then correspond to the four families of planes (113) for which the diffraction is observed. Naturally, the widths of the peaks measured during a ϕ-scan are not equal to zero. These widths are related in particular to the relative disorientation according to ϕ of the different

crystals that comprise the film, but also to the axial divergence of the incident and diffracted beams. Generally speaking, as we have seen in Chapter 2, these axial divergences are in the range of one degree for most systems, even those in high resolution configurations. This is why it is important to take this effect into account when estimating the in-plane disorientation.

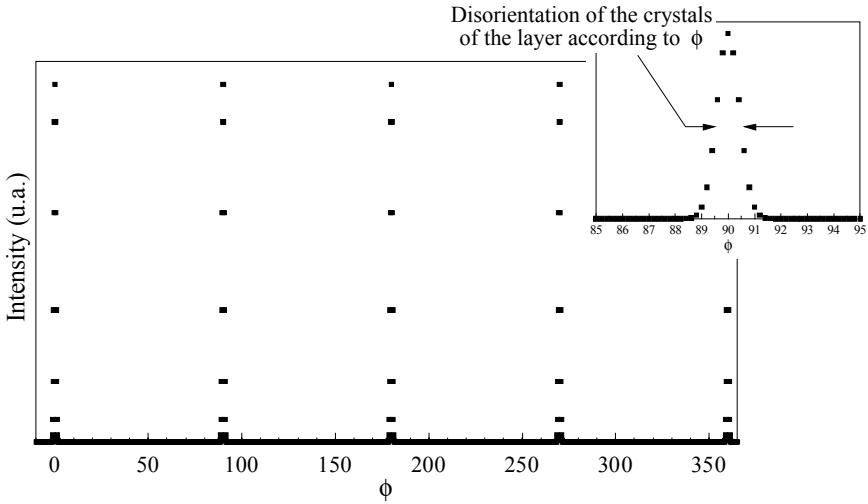

Figure 7.15. *Diagram of a ϕ-scan*

In order to experimentally illustrate this kind of measurement, we will describe a study conducted, once again, on zirconia films, deposited this time on a single crystal magnesia substrate which is cut parallel to its (001) planes. As we have described in section 7.2, these films are synthesized by dipping the substrate in a solution containing a zirconia precursor. A first thermal treatment leads to the formation of a randomly oriented polycrystalline film (see Figure 7.4 and the relevant comments). A second thermal treatment, conducted at a high temperature, causes the formation of small epitaxial islands of zirconia on the magnesia substrate [GUI 98, GUI 99]. A qualitative illustration of the microstructure of these films is shown in Figure 7.16a. This micrographic obtained by plane-view transmission electron microscopy clearly shows that the zirconia islands are a fraction of a micrometer wide. A preliminary study showed that the zirconia's (001) planes are parallel to the magnesia's (001) planes. Therefore, we measured the in-plane orientation of these crystals by using a ϕ-scan performed on the zirconia's (113) planes. The resulting graph is shown in Figure 7.16b. The angle $\phi = 0$ corresponds to the angle for which the magnesia's (113) planes diffract. This measurement clearly shows that the zirconia's islands are oriented in the interface plane and, by

taking into account the normal orientations determined earlier, the epitaxy relations can be written:

$$\begin{cases} (00l)_{ZrO2} // (00l)_{MgO} \\ [100]_{ZrO2} // [100]_{MgO} \end{cases}$$

This situation is often described as “cube-on-cube epitaxy”.

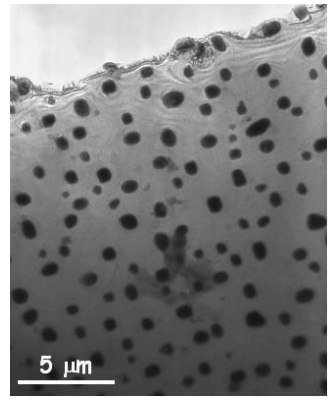

(a) Transmission electron microscopy observation

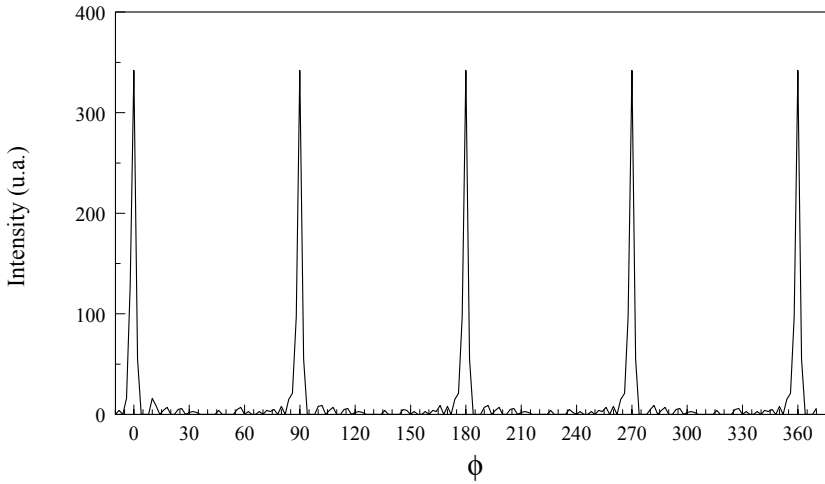

(b) Determining the in-plane orientation of the zirconia crystals. Creation of a ϕ-scan on the zirconia (113) planes

Figure 7.16. *Study of an epitaxial zirconia film on a single crystal magnesia substrate [GUI 98, GUI 99]*

This first case is relatively simple, since it consists of cube-on-cube epitaxy. Another, more complex, experimental study is shown in Figure 7.17 [LEG 99]. This time, the film is comprised of crystals of $SrBi_2Nb_2O_9$ deposited on a single crystal substrate of $SrTiO_3$ which is cut parallel to its (001) planes. We have already described a study of this compound, which crystallizes in an Aurivillius phase, in section 6.2.4. In this example, the family of planes (00l) of the $SrBi_2Nb_2O_9$ phase are parallel to the (001) planes of $SrTiO_3$. A ϕ-scan of the film was conducted by measuring the intensity diffracted by the (1115) family of planes in the crystals of the film. Knowing that the (00l) planes of these crystals are parallel to the surface of the substrate, the sample has to be irradiated at an angle equal to $\omega = 6.935°$ in order for the (1115) planes of the film's crystals to diffract. The values of the angle ϕ were referenced with the use of a ϕ-scan of the single crystal conducted on the (113) planes of $SrTiO_3$. Therefore, the angle $\phi = 0$ corresponds to the [110] direction in the plane of the substrate-film interface. The graphs shown in Figure 7.17 clearly show that the crystals have a strong orientation in the plane, and the epitaxy relations are written:

$$(00l)_{SrBi2Nb2O9} \,//\, (00l)_{SrTiO3} \text{ and } [110]_{SrBi2Nb2O9} \,//\, [100]_{SrTiO3}$$

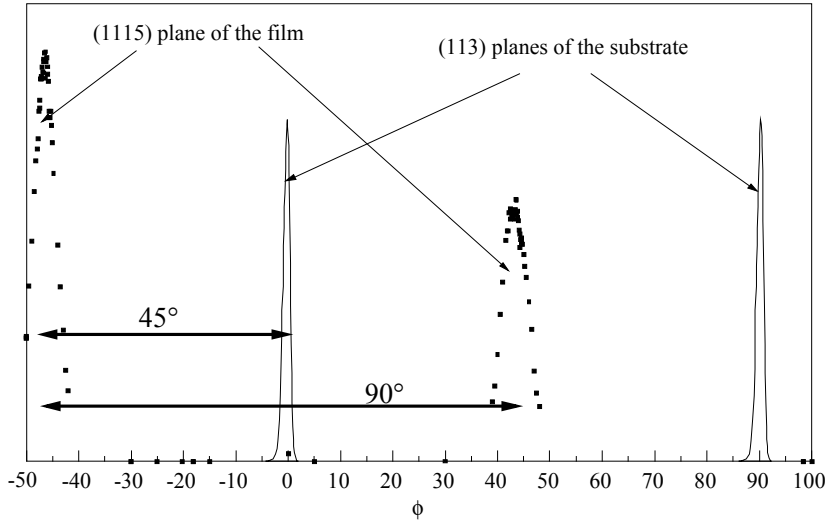

Figure 7.17. *Determining the in-plane orientation of a film of $SrBi_2Nb_2O_9$ deposited on a single crystal of $SrTiO_3$*

Determining, on the one hand, whether a family of planes of the film is parallel to a family of planes of the single crystal substrate[8], associated with the rocking curve of these planes on the film, and on the other hand, the orientation in the plane that was studied with the ϕ-scan, makes it possible to completely define the epitaxy relations between a film and its substrate. These relations are sometimes complex, but most of the time, they are laid out between dense planes (low Miller indices) of the phases in question. It also happens that the film contains several grain families, with some crystals having a given orientation and others being eptiaxial according to different crystallographic relations.

7.3.2. *Microstructural studies of epitaxial films*

Films, by definition, have a finite extension along the normal to the interface. We assumed at the beginning of this chapter that the word film referred to any object through which an X-ray beam could pass. This means that the usual thicknesses are generally smaller than a micrometer. Therefore, the sizes along this direction of the coherent diffracting domains will be finite. This results, as we have seen in Chapter 5, in an extension of the reciprocal lattice point associated with the direction perpendicular to the film-substrate interface. The analysis of this intensity distribution should make it possible, in a similar way to what we showed with powdery or bulky samples, to determine the size along this direction of the coherent domains. If the quality of the film is good enough, that is, if it has few structural defects (stacking faults, dislocation pile-ups, grain boundaries, etc.), then the size that was measured from this width increase will be equal to the thickness of the film. Likewise, the presence of microstrains will lead to a wider intensity distribution. Therefore, it will be possible, by measuring the intensity distribution corresponding to different orders of the same family of planes (hkl, 2h2k2l, 3h3k3l, etc.) to estimate the microstrain amount and its evolution inside the film.

Unlike what we described in Chapter 2, the sample, in this case, is comprised of crystals that practically all have the same orientation. Figure 7.18 shows the effect of the different microstructural characteristics on the diffracted intensity distribution with diagrams drawn in the reciprocal lattice. The diffraction vector $\vec{q}$ is represented by its components $\vec{q}_x$, $\vec{q}_y$ and $\vec{q}_z$. By convention, $\vec{q}_z$ is chosen as

8 Specific synthesis conditions lead to films in which all of the crystals have the same orientation, even though these deposits are made on amorphous substrates. In this case, it is possible to study the disorientation between the crystals of the film. The methods used are similar to those described above, even though in this instance the substrate can no longer serve as a reference.

being normal to the film-substrate interface. Vector $\vec{q}_x$ is the incident X-ray beam's projection onto the film's plane, and vector $\vec{q}_y$ is orthogonal to the previous two.

If we assume, first of all, that the film is a perfect crystal, then we can associate each family of planes with a reciprocal lattice node which is a point (see Figure 7.18a). As we have already mentioned, the film's thickness is finite, thus causing the intensity to spread out along $\vec{q}_z$, which corresponds, for every lattice point, to a Laue function (see Figure 7.18b). Note, however, that all the crystals do not have exactly the same size. Therefore, the intensity distribution is the sum of a set of Laue functions with maximum positions that can vary a little, and the interference patterns are somewhat damped (Figure 7.18c). These crystals may contain a certain amount of microstrains in the direction perpendicular to the interface. This results in additional length for the reciprocal lattice points, a length that increases proportionally to the Miller indices of the lattice point in question (Figure 7.18d).

We have just described the effect of the intensity distribution on the structural defects in the direction perpendicular to the interface. Naturally, the size of the crystals can also have a finite dimension in the interface plane. This leads to wider lattice points in the direction defined by $\vec{q}_x$ (Figure 7.18e). Likewise, the microstrains in the interface plane may lead to an increased width along $\vec{q}_x$.

The crystals do not all have exactly the same orientation, which is why the measured signal is the sum of vertices that are slightly disoriented with respect to one another (Figure 7.18f). Note also that interfacial strains can lead to global variations of the cell parameters. This leads to displacements of the vertices with respect to their reference positions.

This shows that decomposition of the diffracted intensity's two-dimensional distribution[9] should enable us to determine the microstructural characteristics of the film. It is initially necessary to measure these intensity distributions, which is something referred to as reciprocal space mapping.

9 Obviously, the diffracted intensity is three-dimensional. We have neglected the spreading-out along $\vec{q}_y$. Three-dimensional mapping would seem possible, but it has been tried only recently [GOL 04], particularly because of experimental problems, since the axial divergence of the X-ray beam is usually much larger than the equatorial divergence, which is why the instrumental contribution along $\vec{q}_y$ is often the most significant.

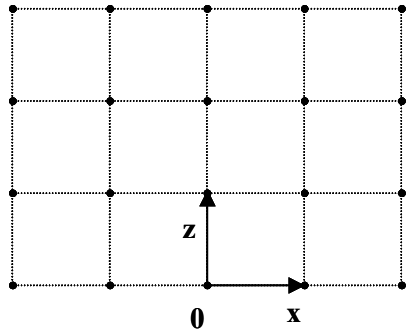

(a) Diffraction by a perfect crystal

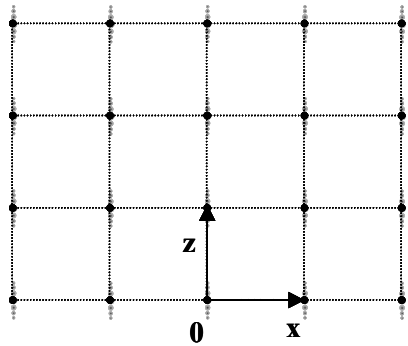

(b) Influence of the crystal size in the direction normal to the interface

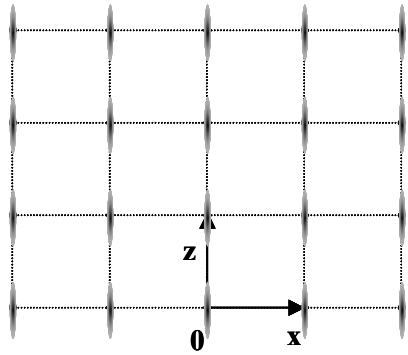

(c) Influence of the crystal size distribution

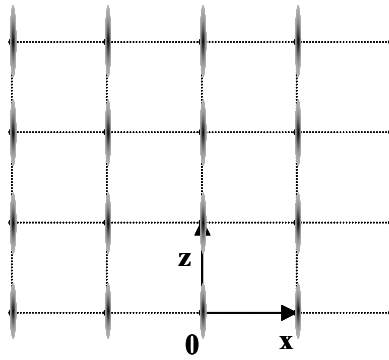

(d) Influence of microstrains

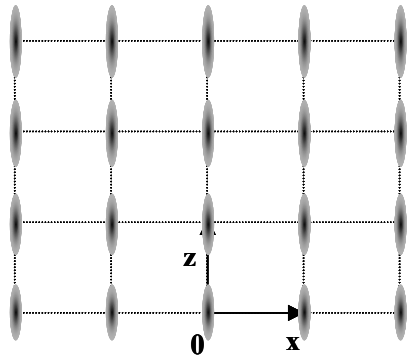

(e) Influence of the crystal size in the interface plane

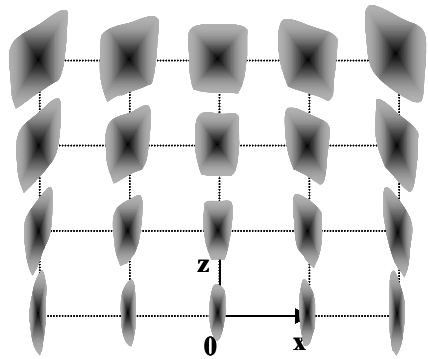

(f) Influence of the relative disorientation of the crystals

Figure 7.18. *Diagrams, drawn in the reciprocal lattice, showing the influence of the microstructural characteristics on the two-dimensional intensity distribution*

7.3.2.1. *Reciprocal space mapping and methodology*

As we have mentioned already, reciprocal space mapping for a given family of planes consists of measuring the entire intensity distribution inside the reciprocal lattice node associated with this family of planes. However, these measurements are only relevant if the intensity is relatively focused, that is, if the lattice node being explored is not too spread out. Generally speaking, this approach was initially implemented for the study of single crystals [NES 00], and later to characterize very high quality films. Most of the studies involve characterizing semiconductor materials [FEW 93a, FEW 93b, FEW 97, HOL 95, HOL 97, HOL 99]. These past few years, we have implemented this method for the characterization of oxide films. The examples given in these last sections are taken from studies of oxide films.

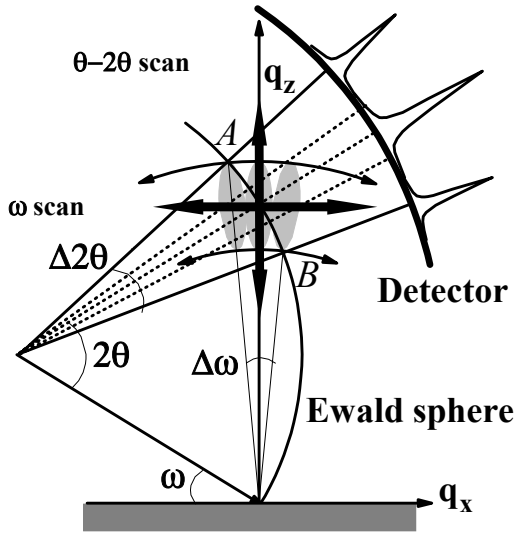

Figure 7.19. *Reciprocal lattice mapping. The intensity distribution is measured when the reciprocal lattice node associated with the family of diffracting planes passes through the Ewald sphere*

The method used for measuring these maps for a given lattice point is shown in Figure 7.19. The incident beam irradiates a given family of planes at an angle ω which is close to the Bragg angle associated with this family of planes. When angle ω varies, the vertex of the reciprocal lattice associated with this family of planes passes through the Ewald sphere. For each angle ω, the intensity distribution measured around diffraction angle 2θ is noted. This distribution is represented on a map $I = f(\omega, 2\theta)$, which is then converted into units of the reciprocal lattice by drawing the intensity distributions along axes q_z and q_x.

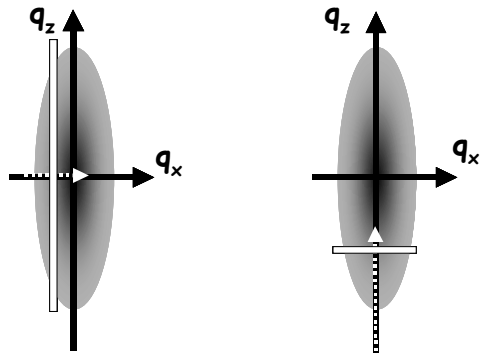

Figure 7.20. *Diagram of the different possible measurement modes on a system equipped with a punctual detector*

If the system is equipped with a punctual detector, it is necessary at each incidence angle to move the detector over a certain amplitude in 2θ. This gives rise to two different measurement modes. In the first case, the value of the incidence angle and that of the measurement angle vary simultaneously so as to ensure that the measurement angle is always equal to twice the incidence angle; this is referred to as θ – 2θ scan. This measurement consists of creating, along q_Z, a set of sections of the reciprocal lattice node (see Figure 7.20a). In the second case, a measurement according to 2θ is made for each value of the incidence angle ω and the mapping is comprised of a set of measurements for different values of ω. This is called ω scan. This time, the sections are drawn along q_X (see Figure 7.20b).

Whichever of these two modes is chosen, this type of incremental measurement necessarily implies long measurement times. An alternative to these methods consists of using a curved position sensitive detector. For each value of the incidence angle ω, a direct measurement of the intensity distribution according to 2θ is made [BOU 02a, BOU 02c, BOU 04]. This makes the mapping much quicker, between 10 and 100 times shorter more than with a punctual detector. We should point out, however, that this method prohibits the use of analyzer crystals.

Figure 7.21 shows a mapping of the (111) lattice point in a silicon single crystal cut parallel to this family of planes. The evolution of the diffracted intensity according to the incidence angle of the X-ray beam on the crystal is shown in Figure 7.21a. This evolution can also be drawn in two dimensions by using iso-intensity lines (see Figure 7.21b). The conversion of this diagram into units of the reciprocal lattice is shown in Figure 7.21c.

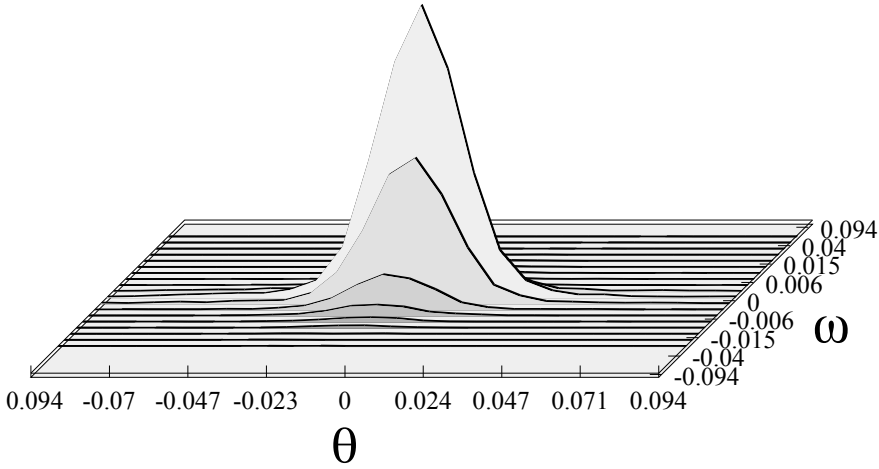

(a) Evolution of the diffracted intensity according to the incidence angle

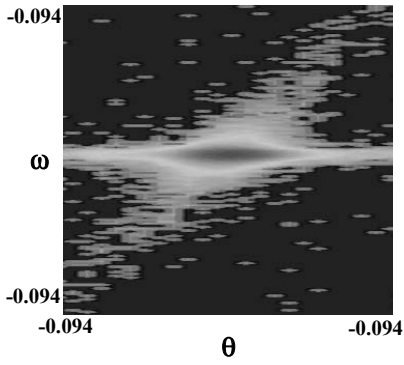

(b) Contour line representation

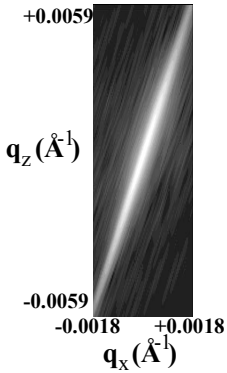

(c) Mapping in the reciprocal space

Figure 7.21. *(a) Mapping of the (111) node of a silicon single crystal. The intensity is shown in a logarithmic scale in (b) and (c)*

From such a mapping, it is possible to extract the different kinds of one-dimensional distributions of the diffracted intensity. Thus, the rocking curves are obtained by adding all of the intensity along the line AB for each ω (see Figure 7.19). By measuring the diffracted intensity in 2θ, for each angle $\omega = \theta$, we get a $\theta - 2\theta$ scan. This plot is equivalent to a section parallel to the q_Z axis. Sections along the q_X axis are obtained by measuring the evolution of the diffracted intensity, for a set value of 2θ when the incidence angle ω varies. Finally, if for each angle 2θ, we add all of the intensity diffracted for each ω, we get a $\omega - 2\theta$ scan, which is

equivalent to a projection of all the diffracted intensity onto q_Z, along a direction parallel to q_X. The latter type of graph is sometimes called a "powder profile", since it integrates the intensity diffracted while the crystal or the film is rotating in the vicinity of the Bragg angle. The various sections and projections obtained from the mapping of the silicon single crystal's (111) node are shown in Figure 7.22.

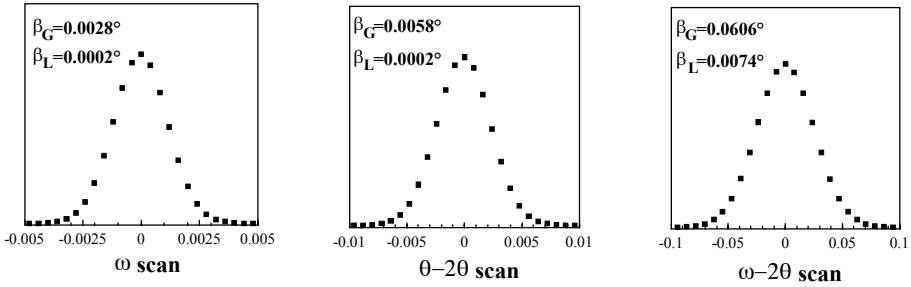

Figure 7.22. *Shapes and widths of the different one-dimensional intensity distributions, obtained from the mapping shown in Figure 7.21. The resulting plots were fitted with Voigt functions, with the Gaussian and Lorentzian widths of these Voigt functions denoted by β_G and β_L, respectively*

7.3.2.2. *Quantitative microstructural study by fitting the intensity distributions with Voigt functions*

We will illustrate this quantitative characterization method of the microstructure with a study [BOU 03] conducted on a sample comprised of a lithium niobate film which is which is about 500 nm thick, deposited on a sapphire substrate cut parallel to the (0006) planes. This film was produced by laser ablation and is epitaxial so as to have the (0006) planes of $LiNbO_3$ parallel to the interface and the in-plane orientation is characterized by two variables. The epitaxy relations can be written:

$$\begin{cases} (0006)_{LiNbO3} // (0006)_{Sapphire} \\ [100]_{LiNbO3} // [100]_{Sapphire} \text{ or } [100]_{LiNbO3} // [110]_{Sapphire} \end{cases}$$

Two maps obtained in the vicinity of the lithium niobate's reciprocal lattice nodes (0006) and (00012) are shown in Figure 7.23. A qualitative observation of these maps shows that the intensity distributions are rather spread out. We first studied the microstructure of this film along the direction normal to the interface. The section along q_z, obtained at $q_x = 0$ in the (0006) map, is shown in Figure 7.24. The observed profile is typical of an imperfect film: the intensity distribution is rather wide and the measured profile does not show interference fringes. The absence of fringe is due to the existence of a certain distribution in vertical crystals

size. We analyzed this profile by using methods initially designed for diffraction on randomly oriented polycrystalline samples (see Chapter 6). Thus, the q_z sections obtained for the two (0006) and (00012) maps were fitted with Voigt functions.

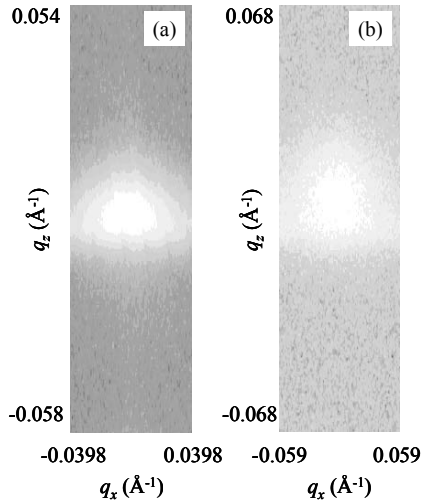

Figure 7.23. *Reciprocal lattice maps in the vicinity, respectively, of the lithium niobate's lattice nodes (0006), (a) map, and (00012), (b) map*

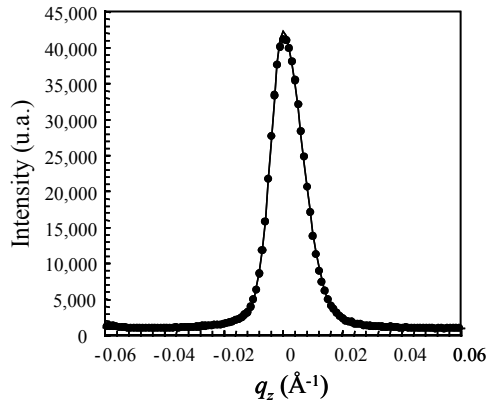

Figure 7.24. *Section along q_z, at q_x=0, of the (a) map. The experimental data were fitted with a Voigt function*

We then analyzed the widths we had obtained by using Williamson-Hall plots. These are shown in Figure 7.25. They clearly show the presence of a relatively high rate of microstrains, causing a purely Gaussian effect. The effect of size results in an essentially Lorentzian increase in width. The microstrain amount and the mean crystal size along the normal to the interface are given in Table 7.1. The mean size we obtained is 163 nm. Therefore, the crystals comprising the film have a vertical size equal to about a third of the film's thickness.

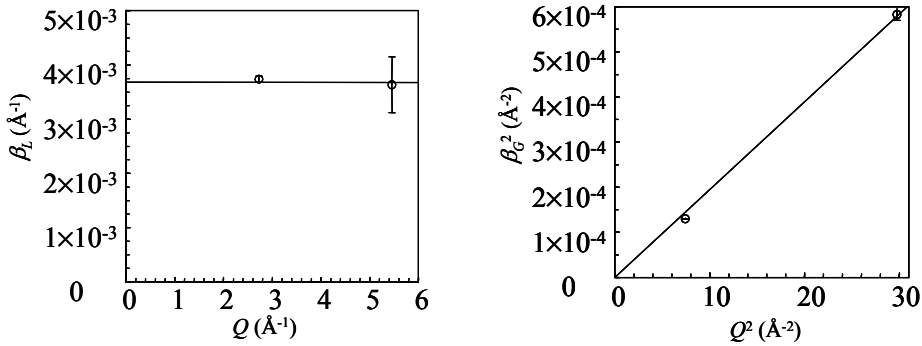

Figure 7.25. *Williamson-Hall plots produced for the q_z cross-sections of the (0006) and (00012) maps*

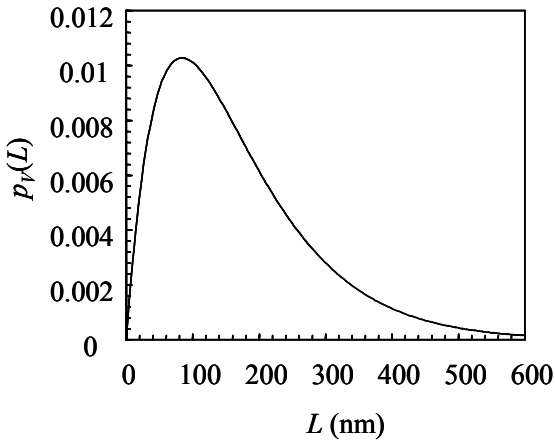

Figure 7.26. *Vertical size distribution of the crystals comprising the film*

Likewise, from the fitting achieved with the Voigt functions and by using the approach developed by Balzar (see Chapter 6), we were able to extract the size

distribution along the normal to the interface. This distribution is shown in Figure 7.26. Note that the distribution tends to zero near 500 nm, which corresponds to the film's thickness. Furthermore, note that the size distribution is rather wide. This confirms the interpretation of the absence of fringes.

The microstructural characteristics in the interface plane were determined based on sections, along q_x, of the maps shown in Figure 7.23. The two main contributions are the lateral crystal size and the relative disorientations of the crystals [MIC 95]. The q_x section, obtained at $q_z = 0$, of the (0006) map is shown in Figure 7.27. Again, we fitted these q_x sections with Voigt functions. The respective contributions from size and disorientation were separated, the same way as before, based on Williamson-Hall plots. These are shown in Figure 7.28. The resulting numerical values are listed in Table 7.1. The crystal disorientation is equal to 1.2°, whereas their mean size in the interface plane is equal to 25 nm.

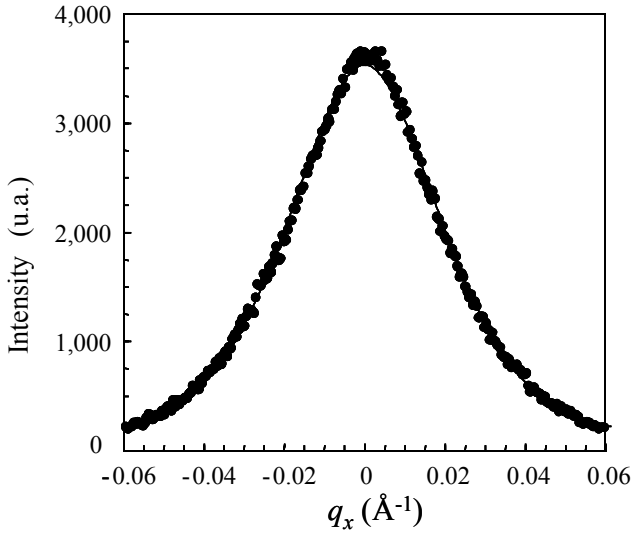

Figure 7.27. *q_x section, at qz = 0, of the lithium niobate's (0006) reciprocal lattice node*

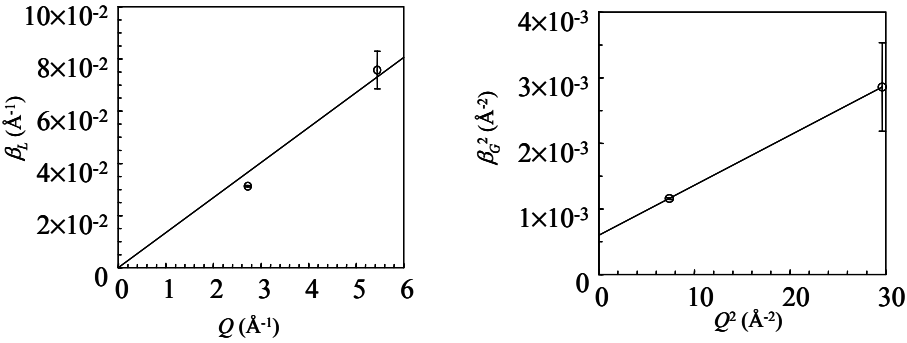

Figure 7.28. *Williamson-Hall plots produced from q_x sections of the (0006) and (00012) maps*

The results listed in Table 7.1 can be summed up as follows: The film is comprised of columns with a mean radius of 25 nm and a mean height of 500 nm, and each column is made up of about 3 crystals. Overall, these crystals are disoriented by about 1.2° with respect to one another.

Film width	500 nm
Mean size of the crystals along the normal to the surface	163 nm
Microstrain rate along the normal to the surface	0.17%
Mean crystal size in the interface plane	25 nm
Relative disorientation of the crystals, mosaicity	1.2°

Table 7.1. *Quantitative microstructural characteristics of the niobate lithium film*

This first experimental illustration shows how an analysis, based on methods developed for the study of randomly oriented crystals, can be transposed to epitaxial thin films. The use of this methodology is particularly relevant, since the film we are studying is imperfect (wide size distribution, rather high relative disorientation of the crystals, etc.). The assumptions made on the shape of the intensity profiles, however, are restrictive. In the following examples, we will see how more sophisticated models can lead to more accurate analyses, when the quality of the film is high enough. However, we should point out that the process suggested here

is particularly effective and rather simple to implement for the study of imperfect films.

7.3.2.3. *Quantitative microstructural study by modeling of one-dimensional intensity distributions*

In the example we have just described, the size of the crystals shows a rather wide distribution, which is why the diffraction profiles measured in the direction perpendicular to the interface or in the interface plane are bell curves, similar to those obtained for diffraction peaks measured with samples comprised of randomly oriented crystals. We will move on to a different case, in which virtually all of the crystals, or diffracting domains, are similar in size.

The samples studied in this section are zirconia films deposited on sapphire substrates. These films are produced by using a sol-gel method based on a dipping process which we have already described. After drying the sample and firing it at a low-temperature, we get a polycrystalline film comprised of randomly oriented nanocrystals (see section 7.2.1). A high temperature process, in this case, lasting one hour at 1,500°C, would yield a set of epitaxial islands of zirconia (see sections 7.3.1.1 and 7.3.1.2). In our example, and under certain conditions, the zirconia crystals grow in directions parallel to the interface [MAR 98]. This leads to somewhat interconnected islands with lateral dimensions of about one fraction of a micrometer and which are particularly flat. An example of such a microstructure is shown in Figure 7.29. These islands are oriented so as to have their (200) planes parallel to the film-substrate interface.

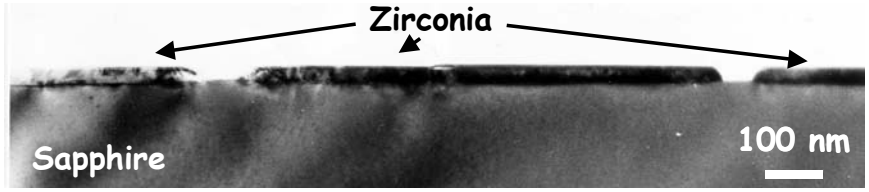

Figure 7.29. *Cross-sectional observation, by transmission electron microscopy, of flat islands of epitaxial zirconia on a sapphire substrate [MAR 98]*

Figure 7.30a shows reciprocal space maps obtained for the zirconia (200) and (400) lattice nodes. The sections along q_z of these mappings clearly show the presence of fringes directly related to the finite dimension of the thicknesses of the islands. The section along q_z of the (200) lattice node is shown in Figure 7.31a. Intensity modulations are clearly visible in this logarithmic plot. These variations are corresponding to equal thickness fringes. The resulting curve is similar to a Laue function (see Chapter 1). The width of this curve as well as the distance between

rings are proportional to the inverse of the size of the diffracting domains (in this case, the thickness of the film) [FEW 93a, HOL 99]. The presence of these fringes is evidence of a relatively low defect amount in the zirconia crystals and also of the film's planar form, or rather of the fact that all the islands have almost the same thickness. A variation in this thickness, as we explained above, would result in a smoother curve and eliminate these fluctuations.

The intensity distribution obtained can be fitted based on the film's microstructural characteristics. The fitting shown in Figure 7.31b was obtained by generating a curve calculated by successive convolutions and taking into account the mean thickness of the film, the thickness distribution, the strains and the variations of these strains along the thickness of the film. The instrumental contribution was included from the evaluation described above. This modeling made it possible to show that the film in question has a mean thickness of 62 nm, with a standard deviation equal to 6 nm, and mean strains inside the film of 0.2% [BOU 02d].

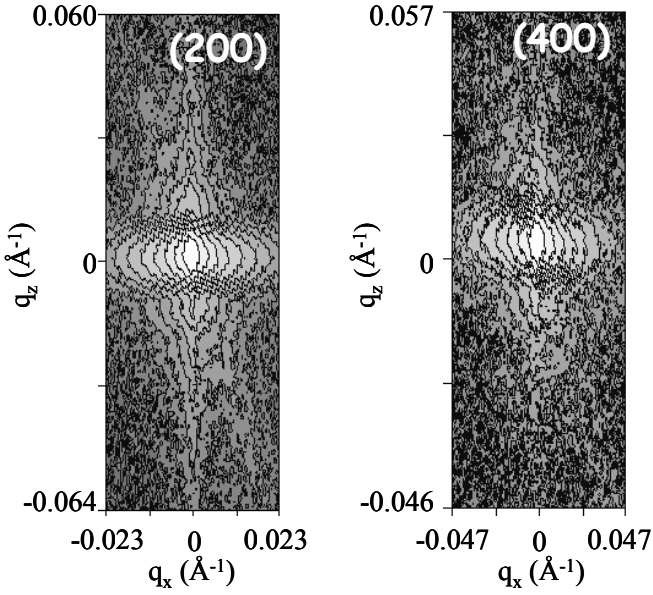

Figure 7.30. *Reciprocal lattice maps of the zirconia film's (200) and (400) reciprocal lattice nodes*

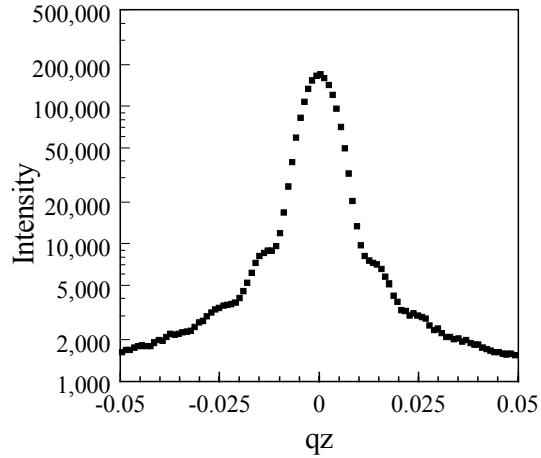

(a) Section along the q_Z axis of the (200) map shown in Figure 7.30

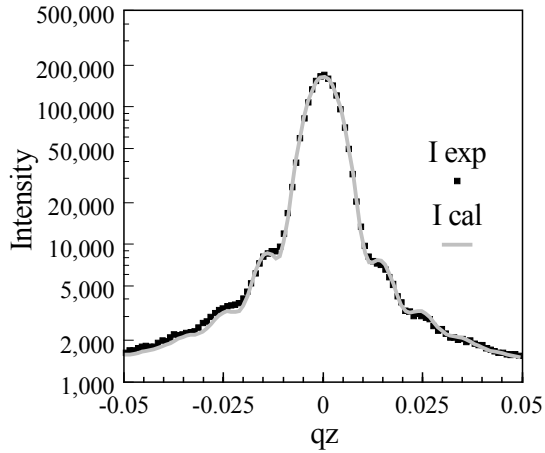

(b) Fitting the q_z section shown in (a)

Figure 7.31. *Evaluation of the microstructural characteristics along the normal to the interface by fitting the q_z sections of the diffracted intensity*

The ω scan of the (200) lattice node, obtained for the section along the q_x axis at $q_z = 0$, is shown in Figure 7.32. As we illustrated in the previous example dealing with the study of lithium niobate, the increase in peak width is a result, in particular, of the relative disorientations of the crystals. Therefore, the width of this distribution yields an estimate of this mosaicity. For this film, we obtained a relative disorientation of 0.2°.

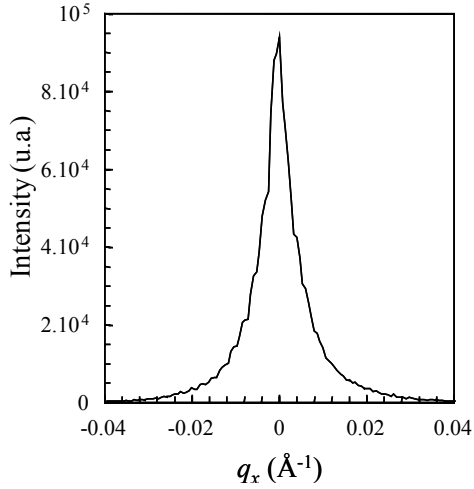

Figure 7.32. *Section parallel to the q_x axis at $q_z = 0$ of the (200) map*

However, an additional phenomenon is observed in the profile shown in Figure 7.32, with the appearance of fringes with a small period. We produced another q_x section, but this time, one that does not pass through the center of this reciprocal lattice node. This cross-section, obtained at $q_z = -5.10^{-3}$ Å^{-1}, is shown in Figure 7.33. This time, the fringes are clearly visible.

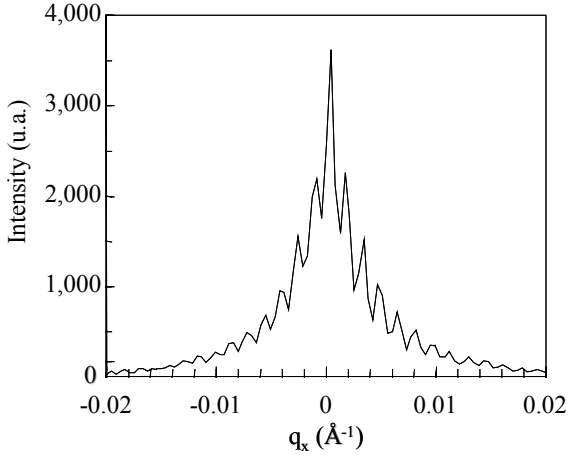

Figure 7.33. *Section of the (200) map, parallel to the q_x axis, at $q_z = -5.10^{-3}$ Å^{-1}*

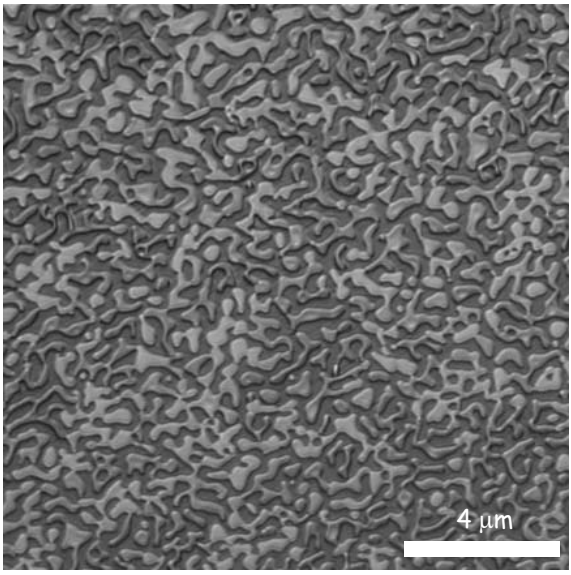

Figure 7.34. *Observation by in plane-view optical microscopy of the zirconia film*

An observation by in plane-view optical microscopy is shown in Figure 7.34. The dark areas correspond to the substrate and the lighter ones to the islands. At this scale, the film shows a very peculiar microstructure that indicates a non-random distribution of matter. In other words, the relative distances between the islands are not random, something which is described as an organized microstructure in the interface plane. The fringes shown by X-ray diffraction, in the profile from Figure 7.33, have a period that is directly related to the correlation length that characterizes the distribution of matter observed by optical microscopy. We took this correlation length into account when we modeled [BOU 04] the experimental profile. The process we used is similar to the one implemented for fitting the q_z section but, in this case, we included a parameter expressing the periodicity of the distribution of matter. The experimental and calculated profiles are shown in Figure 7.35. We obtained a correlation length of 410 nm.

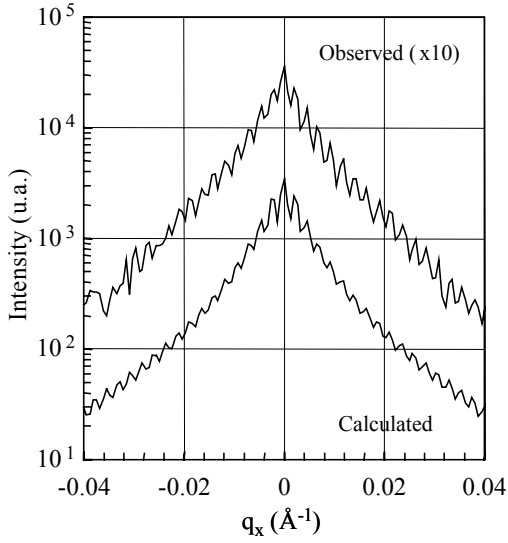

Figure 7.35. *Modeling the intensity profile from Figure 7.33. The fringes are the result of the correlation length between the diffracting domains*

This second part of the study shows that, beyond simply measuring the lateral size of the crystals, the profiles can be used to obtain dimensions that characterize the inter-particle arrangement [PIE 04]. In this regard, X-ray diffraction is an excellent way of characterizing organized structures, the use of which is growing, for example, in systems with applications in photonics.

The intensity distribution along q_x, in the case of this sample, is the result of two effects: first, the disorientations of the crystals, corresponding to a relatively wide signal, which could be described as diffuse scattering, and second, a very structured signal, with rings associated to the periodicity of the distribution of matter. The total intensity distribution corresponds to the sum of these two contributions. Depending on the altitude at which the sections are realized, one of the two effects dominates the measured signal.

Generally speaking, the profiles often correspond to the combination of a rather wide, diffuse scattering signal, related to the disorder (relative disorientation of the crystals, deformation field, etc.), and a sharp signal corresponding to the diffraction by the coherent domains, the width of which essentially expresses the size of these domains. The most recent methods for processing these two-component profiles consist of modeling the experimental profile with a curve calculated from these two contributions [BOU 05a, BOU 05b].

In everything we have just said, the determination of the film's microstructural characteristics was achieved through the analysis of specific one-dimensional sections of the diffracted intensity's two-dimensional distribution. An alternative approach would consist, of course, of directly modeling these two-dimensional distributions. This method has seen some developments in recent years [PIE 04, BOU 06] and is effective but it requires information beforehand on the nature of the defects responsible for the resulting intensity distribution, which is why this approach applies mainly to very high quality films with few defects.

Bibliography

[ACK 94] VAN ACKER K., DE BUYSER L., CELIS J.P., VAN HOUTTE P., "Characterization of thin nickel electrocoatings by the low incident beam angle diffraction method", *J. Appl. Cryst.*, vol. 27, p. 56-66, 1994.

[AHT 84] AHTEE M., UNONIUS L., NURMELA M., SUORTTI P., "A Voigtian as profile shape function in Rietveld refinement", *J. Appl. Cryst.*, vol. 17, p. 352-357, 1984.

[ALE 48] ALEXANDER L., KLUG H.P., KUMMER E., "Statistical factors affecting the Intensity of x-rays diffracted by crystalline powders", *J. Appl. Phys.*, vol. 19, p. 742-753, 1948.

[ALE 80] ALEKSEEV G.D., KALININA N.A., KARPUKHIN V.V., KHAZINS D.M., KRUGLOV V.V., "Investigation of self-quenching streamer discharge in a wire chamber", *Nucl. Instum. Meth.*, vol. 177, p. 385-397, 1980.

[ALT 96] ALTOMARE A., BURLA M.C., CASCARANO G., GIACOVAZZO C., GUAGLIARDI A., MOLITERNI A.G.G., POLIDORI G., "Early finding of preferred orientation: applications to direct methods", *J. Appl. Cryst.*, vol. 29, p. 341-345, 1996.

[ARM 98] ARMSTRONG N., KALCEFF W., "Eigensystem analysis of x-ray diffraction profile deconvolution methods explains ill conditioning" , *J. Appl. Cryst.*, vol. 31, p. 453-460, 1998.

[ARM 04] ARMSTRONG N., KALCEFF W., CLINE J.P., BONEVICH J., "A Bayesian/maximum entropy method for the certification of a nanocrystallite size NIST standard reference material", in MITTEMEIJER E.J., SCARDI P. (eds.), *Diffraction analysis of the microstructure of materials*, Springer Series in Materials Science, vol. 68, p 187-227, 2004.

[ARN 66] ARNDT U.W., WILLIS B.T.M., *Single crystal diffractometry*, Cambridge University Press, 1966.

[ARN 90] ARNDT U.W., "Focusing optics for laboratory sources in X-ray crystallography", *J. Appl. Cryst*., vol. 23, p. 161-168, 1990.

[ARN 98] ARNDT U.W., DUNCUMB P., LONG J.V.P., PINA L., INNEMAN A., "Focusing mirrors for use with microfocus x-ray tubes", *J. Appl. Cryst.*, vol. 31, p. 733-741, 1998.

[ARN 98] ARNDT U.W., LONG J.V.P., DUNCUMB P., "A microfocus x-ray tube used with focusing collimators", *J. Appl. Cryst.*, vol. 31, p. 936-944, 1998.

[ASL 98] ASLANOV L.A., FETISOV G.V., HOWARD J.A.K., *Crystallographic instrumentation*, IUCr Monograph on crystallography, no. 7, Oxford University Press, 1998.

[ATA 82] ATAC M., TOLLESTRUP A.V., POTTER D., "Self-quenching streamers", *Nucl. Instum. Meth.*, vol. 200, p. 345-354, 1982.

[AUF 90] AUFFRÉDIC J.P., PLÉVERT J., LOUËR D., "Temperature-resolved X-ray powder diffractometry of a new cadmium hydroxide nitrate", *J. Solid State Chem.*, vol. 84, p. 58-70, 1990.

[AUT 05] AUTHIER A., "Dynamical theory of x-ray diffraction" IUCr Monograph on crystallography, no. 11, Oxford University Press, 2005.

[BAL 83] BALLON J., COMPARAT V., POUXE J., "The blade chamber: a solution for curved gaseous detectors", *Nucl. Instrum. Meth.*, vol. 217, p. 213-216, 1983.

[BAL 93] BALZAR D., LEDBETTER H., "Voigt function modeling in Fourier analysis of size and strain broadened x-ray diffraction peaks", *J. Appl. Cryst.*, vol. 26, p. 97-103, 1993.

[BAL 99] BALZAR D., "Voigt function modeling diffraction broadening analysis", in R.L. SNYDER, J. FIALA, H.J. BUNGE (eds.), *Defect and microstructure analysis by diffraction*, IUCr Monographs on crystallography, no. 10, Oxford University Press, 1999.

[BAL 04] BALZAR D., AUDEBRAND N., DAYMOND M.R., FITCH A., HEWAT A., LANGFORD I.J., LEBAIL A., LOUËR D., MASSON O., MCCOWAN C.N., POPA N.C., STEPHENS P.W., TOBY B.H., "Size-strain line-broadening analysis of the ceria round-robin sample", *J. Appl. Cryst*., vol. 37, p. 911-924, 2004.

[BAR 92] BARNEA Z., CREAGH D.C., DAVIS T.J., GARRETT R.F., JANKY S., STEVENSON A.W., WILKINS S.W., "The Australian diffractometer at the photon factory", *Rev. Sci. Instrum.*, vol. 63, p. 1069-1072, 1992.

[BAR 05] BARKLA C.G., "Polarized Röntgen radiation", *Phil. Trans. A.*, vol. 204, p. 467-479, 1905.

[BAR 06a] BARKLA C.G., "Polarisation in secondary Röntgen radiation", *Proc. Roy. Soc. Lond.*, vol. 77, p. 247-255, 1906.

[BAR 06b] BARKLA C.G., "Secondary Röntgen radiation", *Phil. Mag.*, vol. 11, p. 812-828, 1906.

[BAR 08a] BARKLA C.G., "Note on x-rays and scattered x-rays", *Phil. Mag.*, p. 288-296, 1908.

[BAR 08b] BARKLA C.G., "Phenomena of x-ray transmission", *Proc. Camb. Phil. Soc.*, vol. 15, p. 257-268, 1909.

[BAR 08b] BARKLA C.G., SADLER C.A., "Homogeneous secondary Röntgen radiations", *Phil. Mag.*, p. 550-584, 1908.

[BAR 11] BARKLA C.G., AYRES T., "The distribution of secondary x-ray and the electromagnetic pulse theory", *Phil. Mag.*, vol. 21, 270-278, 1911.

[BAR 13] BARKLA C.G., MARTYN G.H., "An x-ray fringe system", *Nature*, vol. 90, no. 2259, p. 647, 1913.

[BAR 14] BARLOW W., "On the interpretation of the indications of atomic structure present crystals when interposed in the path of x-rays", *Proc. Roy. Soc. Lond.*, vol. 91, p. 1-16, 1914.

[BAR 78] BARTELS W.L., NIJMAN W., "X-ray double crystal diffractometry of $Ga_{1-x}Al_xAs$ epitaxials layers", *J. Cryst. Growth*, vol. 44, p. 518-525, 1978.

[BAR 83] BARTELS W.J., "Characterization of thin layers on perfect crystals with a multipurpose high resolution x-ray diffractometer", *J. Vac. Sci. Tech. B*, vol. 1, no. 2, p. 338-345, 1983.

[BAR 97] BARLOW W., "A mechanical cause of homogeneity of structure and symmetry", *Proc. Roy. Soc. Dublin*, 1897.

[BAT 96] BATTELLI A., GARBASSO A., "Sur quelques faits se rapportant aux rayons de Röntgen", *Comptes Rendus Acad. Sci.*, p. 603, 1896.

[BEN 93] BÉNARD P., AUFFRÉDIC J.P., LOUËR D., "High-temperature x-ray powder diffractometry of the decomposition of zirconium hydroxide nitrates", *Powder Diffr.*, vol. 8, p. 39-46, 1993.

[BEN 96] BÉNARD P., AUFFRÉDIC J.P., LOUER D., "Dynamic studies from laboratory x-rays", *Mater. Sci. Forum*, Trans Tech. Pub., Switzerland, vol. 228-231, p. 325-334, 1996.

[BER 49] BERTAUT F., "Etude aux rayons X de la répartition des dimensions des cristallites dans une poudre cristalline", *Comptes Rendus Acad. Sci.*, vol. 228, p. 492-494, 1949.

[BER 55] BERTHOD R., "Neue Hilfsmittel der Röntgen Interferensmessung mit Zählrohr Goniometer", *Z. Angew. Phys.*, vol. 7, p. 433-446, 1955.

[BER 93] BERTI G., "Variance and centroid optimization in x-ray powder diffraction analysis", *Powder Diffraction*, vol. 8, no. 2, p. 89-97, 1993.

[BIM 95] BIMBAULT L., BADAWI K.F., GOUDEAU P., BRANGER V., DURAND N., "Profile analysis of thin film X-ray diffraction peaks", *Thin Sol. Films*, vol. 275, p. 40-43, 1995.

[BIS 88] BISH D.L., HOWARD S.A., "Quantitative phase analysis using the Rietveld method", *J. Appl. Cryst.*, vol. 21, p. 86-91, 1988.

[BIS 89] BISH D.L., POST J.E., "Modern powder diffraction", *Review in mineralogy*, vol. 20, Mineralogy Society of America, 1989.

[BIS 93] BISH D.L., POST J.E., "Quantitative mineralogical analysis using the Rietveld full pattern fitting method", *Am. Miner.*, vol. 78, p. 932-940, 1993.

[BOH 20] BOHLIN H., "Eine neue Anordnung für röntgenkristallographische Untersuchungen von Kristallpulver", *Annalen der Physik*, vol. 61, p. 421-439, 1920.

[BOU 01a] BOULLE A., MASSON O., GUINEBRETIÈRE R., DAUGER A., "Miscut angles measurement and precise sample positioning with a 5-axis diffractometer", *Appl. Surf. Sci.*, vol. 180, p. 322-327, 2001.

[BOU 01b] BOULLE A., LEGRAND C., GUINEBRETIÈRE R., MERCURIO J.P., DAUGER A., "Application of X-ray diffraction line profile analysis to the study of planar faults in layered Bi – containing perovskites", *J. Appl. Cryst.*, vol. 34, p. 699-703, 2001.

[BOU 01c] BOULLE A., LEGRAND C., GUINEBRETIÈRE R., MERCURIO J.P., DAUGER A., "X-ray diffraction line broadening by stacking faults in $SrBi_2Nb_2O_9/SrTiO_3$ epitaxial thin films", *Thin Sol. Film,* vol. 391, p. 42-46, 2001.

[BOU 02a] BOULLE A., MASSON O., GUINEBRETIÈRE R., LECOMTE A., DAUGER A., "A high resolution x-ray diffractometer for the study of imperfect materials", *J. Appl. Cryst.*, vol. 35, p. 606-614, 2002.

[BOU 02b] BOULLE A., LEGRAND C., GUINEBRETIÈRE R., MERCURIO J.P., DAUGER A., "Planar defects in Aurivillius compounds: An X-ray diffraction study", *Phil. Mag. A.*, vol. 82, no. 3, p. 615-631, 2002.

[BOU 02c] BOULLE A., "Diffraction des rayons X sur couches d'oxydes épitaxiés. Elaboration et analyse microstructurale", PhD Thesis, University of Limoges, 2002.

[BOU 02d] BOULLE A., PRADIER L., MASSON O., GUINEBRETIÈRE R., DAUGER A., "Microstructural analysis in oxide epitaxial layers", *Appl. Surf. Sci.*, vol. 188, p. 80-84, 2002.

[BOU 03] BOULLE A., CANALE L., GUINEBRETIÈRE R., GIRAULT-DIBIN C., DAUGER A., "Defect structure of pulsed laser deposited $LiNbO_3/Al_2O_3$ layers determined by XRD reciprocal space mapping" *Thin Sol. Films*, vol. 429, p. 55-62, 2003.

[BOU 04] BOULLE A., MASSON O., GUINEBRETIÈRE R., DAUGER A., "Two dimensional XRD profile modelling in imperfect epitaxial layers", in MITTEMEIJER E.J., Scardi P., *Diffraction analysis of the microstructure of materials*, Springer Series in Materials Science, vol. 68, p 505-526, 2004.

[BOU 05a] BOULLE A., GUINEBRETIÈRE R., DAUGER A., "Highly localized strain fields due to planar defects in epitaxial $SrBi_2Nb_2O_9$ thin films", *J. Appl. Phys.*, vol. 97, p. 073503-1-073503-7, 2005.

[BOU 05b] BOULLE A., GUINEBRETIÈRE R., DAUGER A., "Phenomenological analysis of heterogeneous strain fields in epitaxial thin films using X-ray scattering", *J. Phys. D: Appl. Phys*, vol. 38, p. 3907-3920, 2005.

[BOU 06] BOULLE A., CONCHON F., GUINEBRETIÈRE R., "Reciprocal space mapping of epitaxic thin films with crystallite size and shape polydispersity", *Acta. Cryst. A.*, vol. 62, p. 11-20, 2006.

[BOW 98] BOWEN D.K., TANNER B.K., *High resolution x-ray diffractometry and topography*, Taylor & Francis, 1998.

[BRA 07] BRAGG W.H., "On the properties and natures of various electric radiations", *Phil. Mag.*, vol. 14, p. 429-449, 1907.

[BRA 09] BRAGG W.H., GLASSON J.L., "On a want of symmetry shown by secondary x-ray", *Phil. Mag.*, vol. 17, p. 855-864, 1909.

[BRA 11] BRAGG W.H., "Energy transformation of x-rays", *Proc. Roy. Soc. Lond.*, vol. 85, p. 349-365, 1911.

[BRA 12a] BRAGG W.H., "X-ray and crystals", *Nature*, vol. 90, no. 2243, p. 219, 1912.

[BRA 12b] BRAGG W.H., "X-ray and crystals", *Nature*, vol. 90, no. 2248, p. 360-361, 1912.

[BRA 12c] BRAGG W.L., "The diffraction of short electromagnetic waves by a crystal", *Proc. Camb. Phil. Soc.*, vol. 17, p. 43-57, 1912.

[BRA 12d] BRAGG W.L., "The specular reflection of x-rays", *Nature*, vol. 90, no. 2250, p. 410, 1912.

[BRA 13a] BRAGG W.H., "X-ray and crystals", *Nature*, vol. 90, no. 2256, p. 572, 1913.

[BRA 13b] BRAGG W.H., BRAGG W.L., "The reflection of x-rays by crystals", *Proc. Roy. Soc. Lond. A*, vol. 88, p. 428-438, 1913.

[BRA 13c] BRAGG W.H., BRAGG W.L., "The reflection of x-rays by crystals. II", *Proc. Roy. Soc. Lond. A*, vol. 89, p. 246-248, 1913.

[BRA 13d] BRAGG W.L., "The structure of some crystals indicate their diffraction of x-rays", *Proc. Roy. Soc. Lond. A*, vol. 89, p. 248-277, 1913.

[BRA 13e] BRAGG W.H., BRAGG W.L., "The structure of the diamond", *Proc. Roy. Soc. Lond. A*, vol. 89, p. 277-291, 1913.

[BRA 14a] BRAGG W.H., "Crystalline structures as reveal x-rays", *Nature*, vol. 93, no. 2318, p. 124-126, 1914.

[BRA 14b] BRAGG W.H., "X-rays and crystalline structure", *Nature*, vol. 93, no. 2332, p. 494-498, 1914.

[BRA 15] BRAGG W.H., "Bakerian lecture – x-rays and crystal structure", *Phil. Trans. Roy. Soc.*, vol. 215, p. 253-274, 1915.

[BRA 21] BRAGG W.H., "Application of the ionisation spectrometer to the determination of the structure of minute crystals", *Proc. Phys. Soc. Lond.*, vol. 33, p. 222-224, 1921.

[BRA 66] BRAGG W.L., "The crystalline state. I General survey", G. Bell & sons, London, 1966.

[BRE 17a] BRENTANO J.C.M., "Monochromateur pour rayons Röntgen", *Arch. Sci. Phys. Nat.*, vol. 44, p. 66-68, 1917.

[BRE 17b] BRENTANO J.C.M., "Sur un dispositif pour l'analyse spectrographique de la structure des substances à l'état de particules desordonnées par les rayons Röntgen", *Arch. Sci. Phys. Nat.*, vol. 1, p. 550-552, 1917.

[BRE 46] BRENTANO J.C.M., "Parafocusing properties of microcrystalline powder layers in x-ray diffraction applied to the design of X-ray goniometers", *J. Appl. Phys.*, vol. 17, p. 420-434, 1946.

[BRI 45] BRINDLEY G.W., "The effect of grain or particle size on x-ray reflections from mixed powders and alloys, considered in relation to a quantitative determination of crystalline substances by x-ray methods", *Phil. Mag.*, vol. 36, p. 347-369, 1945.

[BRI 80] BRINDLEY G.W., "Quantitative x-ray mineral analysis of clay" in *Crystal structure of clay minerals and their x-ray identification*, Mineralogical Society, London, p 438-441, 1980.

[BRO 13] DE BROGLIE M., "Reflection of x-rays and x-ray fringes", *Nature*, vol. 91, no. 2268, p. 161-162, 1913.

[BUN 82] BUNGE H.J., "Texture and structure of polycrystals ", in SNYDER R.L., FIALA J., BUNGE H.J., *Defect and microstructure analysis by diffraction*, IUCr Monographs on crystallography, no. 10, Oxford University Press, p. 264-317, 1999.

[BUN 82] BUNGE H.J., *Texture analysis in materials science*, Butterworths, London, 1982.

[BUR 32] BURGER H.C., VAN CITTER P.H., "Wahre und scheinbare Intensitätsverteilung in Spektrallinien", *Z. Phys.*, vol. 79, p. 722-730, 1932.

[CAG 58] CAGLIOTI G., PAOLETTI A., RICCI F.P., "Choice of collimators for a crystal spectrometer for neutron diffraction", *Nucl. Instr.*, vol. 3, p. 223-228, 1958.

[CAU 88] CAUSSIN P., NUSICOVICI J., BERARD D., "Using digitized x-ray powder diffraction scans as an input for a new PC-AT sarh/match program", *Adv. X-ray Anal.*, vol. 31, p. 423-430, 1988.

[CER 99] CERNANSKY M., "Restoration and preprocessing of physical profiles from measured data", in SNYDER R.L., FIALA J., BUNGE H.J., *Defect and microstructure analysis by diffraction*, IUCr Monographs on crystallography, no. 10, Oxford University Press, p. 264-317, 1999.

[CHA 11] CHAPMAN J.C., "The intensity of secondary homogeneous Röntgen radiation from compounds", *Proc. Camb. Phil. Soc.*, vol. 16, p. 136-141, 1911.

[CHA 70] CHARPAK G., RAHN D., STEINER H., "Some developments in the operation of multiwire proportional chambers", *Nucl. Instrum. Meth.*, vol. 80, p. 13-34, 1970.

[CHA 95] CHAMPARNAUD-MESJARD J.C., FRIT B., AFTATI A., EL FARISSI M., "$NaBi_2Sb_3O_{11}$: an ordered structure related to the cubic $KSbO_3$ type", *Eur. J. Sol. Stat. Inorg. Chem.*, vol. 32, p. 493-504, 1995.

[CHE 00] CHEARY R.W., DOORYHEE E., LYNCH P., ARMSTRONG N., DLIGATCH S., "X-ray diffraction line broadening from thermally deposited gold films", *J. Appl. Cryst.*, vol. 33, p. 1271-1283, 2000.

[CHE 92] CHEARY R.W., COELHO A., "A fundamental parameters approach to x-ray line profile fitting", *J. Appl. Cryst.*, vol. 25, p. 109-121, 1992.

[CHE 98] CHEARY R.W., COELHO A., "Axial divergence in a conventional x-ray powder diffractometer. I. Theoretical foundations", *J. Appl. Cryst.*, vol. 31, p. 851-861, 1998.

[CHE 04] CHEARY R.W., COELHO A.A., CLINE J.P., "Fundamental parameters line profile fitting in laboratory diffractometers", *J. Res. Nat. Inst. Stand. Technol.*, vol. 109, p. 1-25, 2004.

[CIT 31] van CITTER P.H., "Zum Einfluss der Spaltbreite auf die Intensitätsverteilung in Spektrallinien. II", *Z. Phys.*, vol. 69, p. 298-308, 1931.

[COM 23] COMPTON A.H., "A quantum theory of the scattering of x-rays by light elements", *Phys. Rev.*, vol. 21, p. 483-502, 1923.

[COM 35] COMPTON A.H., ALLISON S.K., *X-rays in theory and experiment*, 2nd edition, New York, 1935.

[CON 00] O'CONNOR B., "Influence of refinement strategy on Rietveld phase composition determinations", *Adv. X-ray Anal.*, vol. 42, p. 204-211, 2000.

[CON 04] CONCHON F., "Elaboration et étude structurale et microstructurale d'un aérogel de zircone dopée à l'oxyde d'yttrium", Project, University of Limoges, 2004.

[COO 13] COOLIDGE W.D., "A powerful Röntgen ray tube with pure electron discharge", *Phys. Rev.*, vol. 2, p. 409-430, 1913.

[COS 53] COSSLETT V.E., NIXON W.C., "The x-ray shadow microscope", *J. Appl. Phys.*, vol. 24, p. 616-623, 1953.

[COU 88] COURBION C., FEREY G., "$Na_2Ca_3Al_2F_{14}$: A new example of a structure with independent F. A new method of comparison between fluorides and oxides of different formula", *J. Sol. Stat. Chem.*, vol. 76, p. 426-431, 1988.

[COW 95] COWLEY J.M., *Diffraction physics*, Elsevier, Amsterdam, 3rd edition, 1995.

[CRO 10] CROWTHER J.A., "On the distribution of the secondary Röntgen radiations round the radiator", *Proc. Camb. Phil. Soc.*, vol. 16, p. 112-120, 1910.

[CRO 11a] CROWTHER J.A., FELLOW M.A., "On the energy and distribution of scattered Röntgen radiation", *Proc. Roy. Soc. Lond.*, vol. 85, p. 29-32, 1911.

[CRO 11b] CROWTHER J.A., "On a attempt to detect diffusion in a pencil of Röntgen rays", *Proc. Camb. Phil. Soc.*, vol. 16, p. 177-187, 1911.

[CRO 12a] CROWTHER J.A., "On a theory of the dissymmetrically distributed secondary Röntgen radiation", *Proc. Camb. Phil. Soc.*, vol. 16, p. 534-539, 1912.

[CRO 12b] CROWTHER J.A., FELLOW M.A., "On the distribution of the scattered Röntgen radiation", *Proc. Roy. Soc. Lond.*, vol. 86, p. 478-494, 1912.

[CUS 99] McCUSKER L.B., VON DREELE R.B., COX D.E., LOUËR D., SCARDI P., "Rietveld refinement guidelines", *J. Appl. Cryst.*, vol. 32, p. 36-50, 1999.

[DAR 14a] DARWIN C.G., "The theory of x-ray reflexion", *Phil. Mag.*, vol. 27, p. 315-333, 1914.

[DAR 14b] DARWIN C.G., "The theory of x-ray reflexion. Part II", *Phil. Mag.*, vol. 27, p. 675-690, 1914.

[DAV 02] DAVID W.I.F., SHANKLAND K., MAC CUSKER L.B., BAERLOCHER C., *Structure determination from powder diffraction data*, Oxford University Press, 2002.

[DEB 16] DEBYE P., SCHERRER P., "Interferenzen an regellos orientierten Teilchen im Röntgenlicht", *Physik Zeitschrift*, vol. 17, p. 277-282, 1916.

[DEL 76] DELHEZ R., MITTEMEIJER E.J., "The elimination of an approximation in the Warren Averbach analysis", *J. Appl. Cryst.*, vol. 9, p. 233-234, 1976.

[DEL 80] DELHEZ R., MITTEMEIJER E.J., "Accuracy of crystallite size and strain values from X ray diffraction line profiles using Fourier series", *Proc. accuracy in powder diffraction*, S. BLOCK, C.R. HUBBARD (eds.), NBS Spec. Pub., no. 567, p. 213-253, 1980.

[DEL 82] DELHEZ R., DE KEIJSER T.H., MITTEMEIJER E.J., "Determination of crystallite size and lattice distorsions through x-ray diffraction line profile analysis", *Fresenius Z. Anal. Chem.*, vol. 312, p. 1-16, 1982.

[DEN 93] DENIARD P., EVAIN M., BARBET J.M., BREC R., "The Inel x-ray position sensitive detector: a study of d-spacing accuracy and exposure time", *Mater. Sci. Forum*, Trans. Tech. Publications, Switzerland, vol. 79-82, p. 363-370, 1993.

[DEN 95] DENT A.J., OVERSLUIZEN M., GREAVES G.N., ROBERT M.A., SANKAR G., CATLOW C.R.A., THOMAS M.J., "A furnace design for use in combined X-ray absorption and diffraction up to a temperature of 1200°C: Study of cordierite ceramic formation using fluorescence QEXAFS/XRD", *Physica B*, vol. 208-209, p. 253-255, 1995.

[DEU 95] DEUTSCH M., HÖLZER G., HÄRTWIG J., WOLF J., FRITSCH M., FÖRSTER E. "K *alpha* and K *beta* x-ray emission spectra of copper", *Phys. Rev. A*, vol. 51, p. 283-296, 1995.

[DEU 96] DEUTSCH M., GANG O., HÄMÄLÄINEN K., KAO C.C., "Onset and near threshold evolution of the Cu K alpha x-ray satellites", *Phys. Rev. Lett*., vol. 76, p. 2424-2427, 1996.

[DIA 00] DIAMANT R., HUOTARI S., HÄMÄLÄINEN K., KAO C.C., DEUTSCH M., "Evolution from threshold of a hollow atom's x-ray emission spectrum: the Cu K^h $alpha_{1,2}$ hypersatellites", *Phys. Rev. Lett.*, vol. 84, p. 3278-3281, 2000.

[DIC 02] DICKERSON M.B., PATHAK K., SANDHAGE K.H., SNYDER R.L., BALACHANDRAN U., MA B., BLAUGHER R.D., BHATTACHARYA R.N., "Applications of 2D detectors in x-ray analysis", *Adv. X-ray Anal.*, vol. 45, p. 338-344, 2002.

[DOL 86] DOLLASE W.A., "Correction of intensities for preferred orientation in powder diffractometry: application of the March model", *J. Appl. Cryst.*, vol. 19, p. 267-272, 1986.

[DUM 37] DUMOND J.W.M., "Theory of the use of more than two successive x-ray crystal reflections to obtain increased resolving power", *Phys. Rev.*, vol. 52, p. 872-883, 1937.

[DUN 97] DUNSTAN D.J., "Strain and strain relaxation in semiconductors", *J. Mater. Sci.*, vol. 8, p. 337-375, 1997.

[ELD 69] ELDERTON W.D., JOHNSON N.L., *System of frequency curves*, Cambridge Press, New York, 1969.

[ELT 96] ELTON N.J., SALT P.D., "Particle statistics in quantitative X-ray diffractometry", *Powder Diffraction*, vol. 11, no. 3, p. 218-229, 1996.

[ERG 68] ERGUN S., "Direct method for unfolding convolution products – its application to x-ray scattering intensities", *J. Appl. Cryst.*, vol. 1, p. 19-23, 1968.

[EST 02] ESTERMANN M.A., DAVID W.I.F., "Patterson methods in powder diffraction: maximum entropy and symmetry minimum function techniques" in W.I.F DAVID., K SHANKLAND, L.B MAC CUSKER, Ch. BAERLOCHER (eds.), *Structure determination from powder diffraction data*, Oxford University Press, 2002.

[EVA 93] EVAIN M., DENIARD P., JOUANNEAUX A., BREC R., "Potential of the Inel x-ray position sensitive detector: a general study of the Debye-Scherrer setting", *J. Appl. Cryst.*, vol. 26, p. 563-569, 1993.

[EWA 12] EWALD P.P., Dispersion und Doppelbrechung von Elektronengittern, Inaugural-Dissertation zur Erlangung der Doktorwürde Königl. Ludwigs Maximilians Universität zu München, February 1912.

[EWA 16a] EWALD P.P., "Zur Begrundung der Kristalloptik. Teil I: Dispersionstheorie", *Annalen der Physik*, vol. 49, p. 1-38, 1916.

[EWA 16b] EWALD P.P., "Zur Begrundung der Kristalloptik. Teil II: Theorie der Reflexion und Brechung", *Annalen der Physik*, vol. 49, p. 117-143, 1916.

[EWA 17] EWALD P.P., "Zur Begründung der Kristalloptik. Teil III: die Kristalloptik der Röntgenstrahlen", *Annalen der Physik*, vol. 54, p. 519-597, 1917.

[FED 12] FEDOROW E., "Die Praxis in der krystallochemischen Analyse und die Abfassung der Tabellen für dielselbe", *Zeitsch. Kryst.*, p. 513-575, 1912.

[FEW 01] FEWSTER P.F., *X-ray scattering from semiconductors*, Imperial College Press, 2001.

[FEW 91] FEWSTER P.W., "Multicrystal x-ray diffraction of heteroepitaxial structures", *Appl. Surf. Sci.*, vol. 50, p. 9-18, 1991.

[FEW 93a] FEWSTER P.F., "X-ray diffraction from low dimensional structures", *Semicond. Sci. Technol.*, vol. 8, p. 1915-1934, 1993.

[FEW 93b] FEWSTER P.F., "Characterization of quantum wells by x-ray diffraction", *J. Phys. – D: Appl. Phys.*, vol. 26, p. A142-A145, 1993.

[FEW 95] FEWSTER P.F., ANDREW N.L., "Absolute lattice parameter measurement", *J. Appl. Cryst.*, vol. 28, p. 451-458, 1995.

[FEW 97] FEWSTER P.F., "Reciprocal space mapping", *Critical Review in Solid State and Mater. Sci.*, vol. 22, p. 69-110, 1997.

[FIN 89] FINGER L.W., COX D.E., JEPHCOAT A.P., "A correction for powder diffraction peak asymmetry due to axial divergence", *J. Appl. Cryst*., vol. 27, p. 892-900, 1994.

[FIN 89] FINGER L.W., "Modern powder diffraction", in BISH D.L., POST J.E. (eds.), *Reviews in mineralogy*, vol. 20, Mineralogical Society of America, Washington, 1989.

[FIS 96] FISCHER K., OETTEL H., "Analysis of residual stress gradient in thin films using Seemann-Bohlin x-ray diffraction", *Mater. Sci. Forum*, Trans Tech. Pub., Switzerland, vol. 228-231, p. 301-306, 1996.

[FIT 95] FITCH A.N., "High resolution powder diffraction studies of polycrystalline materials", *Nucl. Instrum. Meth. B*, vol. 97, p. 63-69, 1995.

[FLO 55] FlÖRKE O.W., SADFELD H., "Ein Verfahren zur Herstellung texturfreier Röntgen Pulverpreparate", *Z. Krist.*, vol. 106, p. 460-466, 1955.

[FOM 96] FOMM L., "Die Wellenlänge der Röntgen-strahlen", *Annalen der Physik und Chemie*, vol. 59, p. 350-353, 1896.

[FRE 87] FREVEL L.K., "Profiles of CuKα lines", *Powder Diffraction*, vol. 2, no. 4, p. 237-241, 1987.

[FRI 12] FRIEDRICH W., KNIPPING P., von LAUE M., "Interferenz-Erscheinungen bei Röntgenstrahlen", *Sitzungsberichte der Königlich Bayerischen Akademie der Wissenschaften*, p. 303-322, June 1912, reprinted in "Interferenzerscheinnungen bei Röntgenstrahlen", *Annalen der Physik*, vol. 41, p. 971-990, 1913.

[FUJ 99] FUJINAWA G., TORAYA H., STAUDENMANN L., "Parallel slit analyzer developed for the purpose of lowering tails of diffraction profiles", *J. Appl. Cryst*., vol. 32, p. 1145-1151, 1999.

[GAB 77] GABRIEL A., "Position sensitive x-ray detectors", *Rev. Sci. Instrum.*, vol. 48, no. 10, p. 1303-1305, 1977.

[GAB 78] GABRIEL A., DAUVERGNE F., ROSENBAUM C., "Linear, circular and two dimensional position sensitive detectors", *Nucl. Instrum. Meth.*, vol. 152, p. 191-194, 1978.

[GIA 02] GIACOVAZZO C., *Fundamental of crystallography*, 2nd edition, Oxford University Press, 2002.

[GIA 96] GIACOVAZZO C., "Direct methods and powder data: state of the art and perspective", *Acta Cryst. A*, vol. 52, p. 331-339, 1996.

[GIL 96] GILMORE J.C., "Maximum entropy and Bayesian statistics in crystallography: a review of practical applications", *Acta Cryst. A*, vol. 52, p561-589, 1996.

[GIL 02] GILMORE J.C., SCHANKLAND K., DONG W., "A maximum entropy approach to structure solution", in W.I.F DAVID, K SHANKLAND, L.B MAC CUSKER, Ch. BAERLOCHER, *Structure determination from powder diffraction data*, Oxford University Press, 2002.

[GLA 10] GLASSON J.L., "Secondary Röntgen rays from metallic salts", *Proc. Camb. Phil. Soc.*, vol. 15, p. 437-441, 1910.

[GOL 79] GÖBEL H.E., "A new method for fast XRPD using a position sensitive detector", *Adv. X-ray Anal.*, vol. 22, p. 255-265, 1979.

[GOL 04] GOLSHAN M. LAUNDY D, FEWSTER, P.F., MOORE M, "Three dimensional reciprocal space mapping: application to polycrystalline CVD diamond", in MITTEMEIJER E.J., SCARDI P. (eds.), *Diffraction analysis of the microstructure of materials,* Springer Series in Materials Science, vol. 68, p 527-539, 2004.

[GRE 85] GREAVES C., "Rietveld analysis of powder neutron diffraction data displaying anisotropic crystallite size broadening", *J. Appl. Cryst.*, vol. 18, p. 48-50, 1985.

[GRO 88] GROMA I., UNGAR T., WILKENS M., "Asymmetric x-ray line broadening of plastically deformed crystals. I. Theory." *J. Appl. Cryst.*, vol. 21, p. 47-53, 1988.

[GRO 98a] GROSS M., HAAGA S., FIETZEK H., HERRMANN M., ENGEL W., "Measurements in parallel-beam geometry achiev a Göbel mirror at a laboratory source", *Mater. Sci. Forum*, Trans. Tech. Pub., Switzerland, vol. 278-281, p. 242-247, 1998.

[GRO 98b] GROMA I., "X-ray line broadening due to an inhomogeneous dislocation distribution", *Phys. Rev. B*, vol. 57, no. 13, p. 7535-7542, 1998.

[GUA 96] GUALTIERI A., NORBY P., HANSON J., HRILLAC J., "Rietveld refinement using synchrotron x-ray powder diffraction data collected in transmission geometry using imaging plate detector: application to standard m-ZrO_2", *J. Appl. Cryst.*, vol. 29, p. 707-713, 1996.

[GUI 37] GUINIER A., "Dispositif permettant d'obtenir des diagrammes de diffraction de poudres cristallines très intense avec un rayonnement monochromatique", *Comptes Rendus Acad. Sci.*, vol. 204, p. 1115-1116, 1937.

[GUI 39] GUINIER A., "La diffraction des rayons X aux très petits angles : application à l'étude de phénomènes ultramicroscopiques", *Annalen der Physik*, vol. 12, p. 161-237, 1939.

[GUI 64] GUINIER A., *Théorie et technique de la radiocristallographie*, Dunod, Paris, 1964.

[GUI 95] GUILLOU N., AUFFRÉDIC J.P., LOUËR D., "An unexpected double valence change for cerium during the thermal decomposition of $CeK_2(NO_3)_6$", *J. Solid State Chem.*, vol. 115, p. 295-298, 1995.

[GUI 96] GUINEBRETIERE R., MASSON O., SILVA M.C., FILLION A., SURMONT J.P., DAUGER A., "Diffraction des rayons X en réflexion sous incidence fixe. Mise en œuvre d'un détecteur courbe à localisation (CPS 120 INEL)", *J. Phys. IV*, vol. 6, p. 111-121, 1996.

[GUI 98] GUINEBRETIÈRE R., SOULESTIN B., DAUGER A., "XRD and TEM study of heteroepitaxial growth of zirconia on magnesia single crystal", *Thin Sol. Films*, vol. 319, p. 197-201, 1998.

[GUI 99] GUINEBRETIÈRE R., DAUGER A., MASSON O., SOULESTIN B., "Sol-gel fabrication of heteroepitaxial zirconia films on MgO (001) substrates", *Phil. Mag. A*, vol. 79, no. 7, p. 1517-1531, 1999.

[GUI 05] GUINEBRETIÈRE R., BOULLE A., MASSON O., DAUGER A., "Instrumental aspects in X-ray diffraction on polycrystalline materials", *Powder Diffraction*, vol. 20, no. 4, p. 294-305, 2005.

[HAA 85] HAASE E.L., "The determination of lattice parameters and strains in stressed thin films using X-ray diffraction with Seeman-Bohlin focusing", *Thin Solid Films*, vol. 124, p. 283-291, 1985.

[HAG 03] HAGA H., WIND C.H., "Die Beugung der Röntgenstrahlen", *Annalen der Physik*, vol. 10, p. 305-312, 1903.

[HAG 69] HÄGG G., ERSSON N.O., "An easily adjustable Guinier camera of highest precision", *Acta Cryst. A,* vol. 25, p. S64, 1969.

[HAG 99] HAGA H., WIND C.H., "Die Beugung der Röntgenstrahlen", *Annalen der Physik und Chemie*, vol. 68, p. 884-895, 1899.

[HAL 66] HALDER N.C., WAGNER C.N.J., "Analysis of the broadening of powder pattern peaks using variance, integral breadth, and Fourier coefficients on the line profile", *Adv. X-ray Anal.*, vol. 9, p. 91-102, 1966.

[HAL 77] HALL M.M., VEERARAGHAVAN V.G., RUBIN H., WINCHELL P.G., "The approximation of symmetric x-ray peaks by Pearson type VII distributions", *J. Appl. Cryst.*, vol. 10, p. 66-68, 1977.

[HAN 36] HANAWALT J.D., RINN H.W., "Identification of crystalline materials", *Indust. Eng. Chem. Anal.*, vol. 8, p. 244-247, 1936.

[HAN 38] HANAWALT J.D., RINN H.W., FREVEL L.K., "Chemical analysis by x-ray diffraction. Classification and use of x-ray diffraction patterns", *Indust. Eng. Chem. Anal.*, vol. 10, p. 457-512, 1938.

[HAR 90] HART M., CERNIK R.J., PARRISH W., TORAYA H., "Lattice parameter determination for powders using synchrotron radiation", *J. Appl. Cryst.*, vol. 23, p. 286-291, 1990.

[HAR 93] HÄRTWIG J., HÖLZER G., WOLF J., FÖRSTER E., "Remeasurement of the profile of the characteristic CuKα emission line with high precision and accuracy", *J. Appl. Cryst.*, vol. 26, p. 539-549, 1993.

[HAS 84] HASTING J.B., THOMLINSON W., COX D.E., "Synchrotron x-ray powder diffraction", *J. Appl. Cryst.*, vol. 17, p. 85-95, 1984.

[HE 02] HE B.B., PRECKWINKEL U., "X-ray optics for two dimensional diffraction." *Adv. X-ray Anal.*, vol. 45, p. 332-337, 2002.

[HEI 86] HEIZMANN J.J., LARUELLE C., "Simultaneous measurement of several x-ray pole figures", *J. Appl. Cryst.*, vol. 19, p. 467-472, 1986.

[HEL 98] HELLIWELL J.R., "Synchrotron radiation and crystallography: the first 50 years", *Acta Cryst. A*, vol. 54, p. 738-749, 1998.

[HIL 00] HILLIER S., "Accurate quantitative analysis of clay and other minerals in sandstones by XRD: comparison of a Rietveld and a reference intensity ratio (RIR) method and the importance of sample preparation", *Clay minerals*, vol. 35, p. 291-302, 2000.

[HIL 99] HILLIER S., "Use of an air brush to spray dry samples for x-ray powder diffraction", *Clay minerals*, vol. 34, p. 127-135, 1999.

[HIL 84] HILL R.J., MADSEN I.C., "The effect of profile step counting time on the determination of crystal structure parameters: X-ray Rietveld analysis", *J. Appl. Cryst.*, vol. 17, p. 297-306, 1984.

[HIL 86] HILL R.J., MADSEN I.C., "The effect of profile step width on the determination of crystal structure parameters and estimated standard deviations by X-ray Rietveld analysis", *J. Appl. Cryst.*, vol. 19, p. 10-18, 1986.

[HIL 87] HILL R.J., HOWARD C.J., "Quantitative phase analysis from neutron powder diffraction data using the Rietveld method", *J. Appl. Cryst.*, vol. 20, p. 467-474, 1987.

[HIL 87] HILL R.J., MADSEN I.C., "Data collection strategies for constant wavelength Rietveld analysis", *Powder diffraction*, vol. 2, no. 3, p. 146-162, 1987.

[HIL 92] HILL R.J., "Rietveld refinement round robin. I. Analysis of standard X-ray and neutron data for $PbSO_4$", *J. Appl. Cryst.*, vol. 25, p. 589-610, 1992.

[HIL 94] HILL R.J., CRANSWICK L.M.D., "Rietveld refinement round robin. II. Analysis of monoclinic ZrO_2", *J. Appl. Cryst.*, vol. 27, p. 802-844, 1994.

[HOF 55] HOFFMANN E.G., JAGODZINSKI H., "Eine neue, hochauflösende Röntgenfeinstruktur Anlage mit verbessertem, fokussierendem Monochromator und Feinfokusröhre", *Z. Metallk.,* vol. 46, p. 601-610, 1955.

[HOL 95] HOLY V., DARHUBER A.A., BAUER G., WANG P.D., SONG Y.P., SOTOMAYOR TORRES C.M., HOLLAND M.C., "Elastic strains in GaAs/AlAs quantum dots study high resolution x-ray diffraction", *Phys. Rev. B*, vol. 52, no. 11, p. 8348-8357, 1995.

[HOL 97] HOLY V., GIANNINI C., TAPFER L., MARSCHNER T., STOLZ W., "Diffuse x-ray reflection from multilayers with stepped interfaces", *Phys. Rev. B*, vol. 55, no. 15, p. 9960-9968, 1997.

[HOL 99] HOLY V., PIETSCH U., BAUMBACH T., *High resolution x-ray scattering from thin films and multilayers*, Springer Tracts in Modern Physics, 149, 1999.

[HON 92] HONKIMAKI V., SUORTTI P., "Whole pattern fitting in energy dispersive powder diffraction", *J. Appl. Cryst.*, vol. 25, p. 97-104, 1992.

[HUA 90] HUANG T.C., "Surface and ultra thin film characterization by grazing incidence asymmetric Bragg diffraction", *Ad. X-Ray Anal.*, vol. 33, p. 1-10, 1990.

[HUL 17a] HULL A.W., "The crystal structure of iron", *Phys. Rev.*, vol. 9, p. 84-87, 1917.

[HUL 17b] HULL A.W., "A new method of x-ray crystal analysis", *Phys. Rev.*, vol. 10, no. 6, p. 661-696, 1917.

[HUP 13] HUPKA E., STEINHAUS W., "Systems of lines obtain reflection of x-rays", *Nature*, vol. 91, no. 2262, p. 10, 1913.

[IMB 96] IMBERT A., BERTIN-SANS H., "Diffusion des rayons de Röntgen", *Comptes Rendus Acad. Sci.*, p. 524-525, 1896.

[ISH 99] ISHIZAWA N., MATSUSSHIMA Y., HAYASHI M., UEKI M., "Synchrotron radiation study of yttria stabilized zirconia $Zr_{0.758}Y_{0.242}O_{1.879}$", *Acta Cryst. B*, vol. 55, p. 726-735, 1999.

[IWA] IWASAKI H., YURUGI T., YOSHIMURA Y., "Wavelength modulated diffraction: a new method for phase determination", *Acta Cryst. A*, vol. 55, p. 864-870, 1999.

[JAM 67] JAMES R.W., "The optical principles of the diffraction of x-rays", in BRAGG W.L. (ed.), *The crystalline state*, vol. 2, London, G. Bell & Sons, 1967.

[JAN 98] JANOT C., DUBOIS J.M., *Les quasicristaux, matière à paradoxes*, EDP Science, 1998.

[JAU 22] JAUNCEY G.E.M., "The effect of damping on the width of x-ray spectrum lines", *Phys. Rev.*, vol. 19, p. 64-67, 1922.

[JEN 96] JENKINS R., SNYDER R.L., *Introduction to x-ray powder diffractometry*, J. Wiley & Sons, 1996.

[JIA 02] JIANG L., AL-MOSHEKY Z., GRUPIDO N., "Basic principle and performance characteristics of multilayer beam conditioning optics", *Powder Diffr.*, vol. 17, p. 81-93, 2002.

[JOH 31] JOHAN H.H., "Die Erzeugung lichtstarker Röntgenspektren mit Hilfe von Konkavkristallen", *Z. Phys.*, vol. 69, p. 185-206, 1931.

[JOH 33] JOHANSSON T., "Über ein neuartiges, genau fokussierendes Röntgenspektrometer", *Z. Phys.*, vol. 82, p. 507-528, 1933.

[JON 38] JONES F.W., "The measurement of particle size by x-ray method", *Proc. Roy. Soc. Lond. A.*, vol. 166, p. 16-43, 1938.

[KAL 95] KALCEFF W., ARMSTRONG N., CLINE J.P., "An evaluation of deconvolution techniques in x-ray profile broadening analysis and the application of the maximum entropy method to alumine data", *Adv. X-Ray Anal.*, vol. 38, p. 387-395, 1995.

[KEE 13] KEENE H.B., "The reflection of x-rays", *Nature*, vol. 91, no. 2266, p. 111, 1913.

[KEI 82] de KEIJSER Th.H., LANGFORD J.I., MITTEMEIJER E.J., VOGELS A.B.P., "The use of the Voigt function in a single line method for the analysis of x-ray diffraction line broadening", *J. Appl. Cryst.*, vol. 15, p. 308-314, 1982.

[KEI 83] de KEIJSER Th.H., MITTEMEIJER E.J., ROZENDAL H.C.F., "The determination of crystallite size and lattice strain parameters in conjunction with the profile refinement method for the determination of crystal structure", *J. Appl. Cryst.*, vol. 16, p. 309-316, 1983.

[KID 03] KIDD P., "Investigation of the precision in x-ray diffraction analysis of VCSEL structures", *J. Mater. Sci*, vol. 14, p. 541-550, 2003.

[KIE 73] KIELKOPF J.F., "New approximation to the Voigt function with applications to spectral line profile analysis", *J. Opt. Soc. Am.*, vol. 63, no. 8, p. 987-995, 1973.

[KLI 88] KLIMANEK P., KUZEL R., "X-ray diffraction line broadening due to dislocations in non-cubic materials. I. General considerations and the case of elastic isotropy applied to hexagonal crystals", *J. Appl. Cryst.*, vol. 21, p. 59-66, 1988.

[KLU 74] KLUG H.P., ALEXANDER L.E., *X-ray diffraction procedures*, John Wiley & Sons, New York, 2nd edition, 1974.

[KNA 04] KNAPP M., JOCO V., BAEHTZ C., BRECHT H.H., BERGHAEUSER A., EHRENBERG H., von SEGGERN H., FUESS H., "Position-sensitive detector system OBI for high resolution x-ray powder diffraction using on-site readable image plates", *Nucl. Instrum. Meth.*, vol. 521, p. 565-570, 2004.

[KNI 13] KNIPPING P., "Durchgang von Röntgenstrahlen durch Metalle", *Physik. Zeitsch.,* vol. 14, p. 996-998, 1913.

[KOC 12] KOCH P.P., "Über die Messung der Schwärzung photographischer Platten in sehr schmalen Bereichen. Mit Anwendung auf die Messung der Schwärzungsverteilung in einigen mit Röntgenstrahlen aufgenommenen Spaltphotogrammen von Walter und Pohl", *Annalen der Physik*, vol. 38, p. 507, 1912.

[KRI 63] KRIVOGLAZ M.A., RYBOSHAPKA K.P., "Theory of X-ray scattering by crystals containing dislocations, screw and edge dislocations randomly", *Fiz. Metal. Metalloved.*, vol. 15, p. 18-31, 1963.

[KRI 69] KRIVOGLAZ M.A., "Théorie de la diffraction des rayons X et des neutrons thermiques par des cristaux réels", Masson, Paris 1969.

[LAA 84] van LAAR B., YELON W.B., "The peak in neutron powder diffraction", *J. Appl. Cryst.*, vol. 17, p. 47-54, 1984.

[LAN 78] LANGFORD J.I., "A rapid method for analysing the breadths of diffraction and spectral lines using the Voigt function", *J. Appl. Cryst.*, vol. 11, p. 10-14, 1978.

[LAN 86] LANGFORD J.I., LOUER D., SONNEVELD E.J., VISSER J.W., "Applications of total pattern fitting to a study of crystallite size and strain in zinc oxide powder", *Powder Diffraction*, vol. 1, no. 3, p. 211-221, 1986.

[LAN 92] LANGFORD J.I., "The use of the Voigt function in determining microstructural properties from diffraction data by means of pattern decomposition", *NIST Proceedings of "Accuracy in powder diffraction II",* p. 110-126, 1992.

[LAN 93] LANGFORD J.I., BOULTIF A., AUFFREDIC J.P., LOUER D., "The use of pattern decomposition to study the combined x-ray diffraction effects of crystallite size and stacking faults in ex-oxalate zinc oxide", *J. Appl. Cryst.*, vol. 26, p. 22-33, 1993.

[LAN 96] LANGFORD J.I., LOUËR D., "Powder diffraction", *Rep. Prog. Phys.* vol. 59, p. 131-234, 1996.

[LAU 13a] LAUE M., "Eine quantitative Prüfung der theorie für die Interferenzerscheinungen bei Röntgenstrahlen", *Annalen der Physik*, vol. 41, p. 989-1002, 1913.

[LAU 13b] LAUE M., "Die dreizälig symmetrischen Röntgenstrahlaufnahmen an regulären Kristallen", *Annalen der Physik*, p. 397-414, 1913.

[LAU 26] LAUE M., "Lorentz faktor und Intensitätverteilung in Debye-Scherrer Ringen", *Zeitsch. Krist.*, vol. 64, p. 115-142, 1926.

[LEB 88] LEBAIL A., DUROY H., FOURQUET J.L., "*Ab initio* structure determination of LiSbWO6 by x-ray powder diffraction", *Mater. Res. Bull.,* vol. 23, p. 447-452, 1988.

[LEB 92] LEBAIL A., "Modeling anisotropic crystallite size and microstrain in Rietveld analysis", *NIST Proceedings of "Accuracy in powder diffraction II",* p. 142-152, 1992.

[LEB 97] LEBAIL A., JOUANNEAUX A., "A qualitative account for anisotropic broadening in whole powder diffraction pattern fitting by second rank tensors", *J. Appl. Cryst.*, vol. 30, p. 265-271, 1997.

[LEB 99] LEBAIL A., "Accounting for size and microstrain in whole powder pattern fitting", in SNYDER R.L., FIALA J., BUNGE H.J., *Defect and microstructure analysis by diffraction*, IUCr Monographs on crystallography, no. 10, Oxford University Press, p. 535-555, 1999.

[LEB 05] LEBAIL A., "Whole powder pattern decomposition methods and applications: a retrospective", *Powder Diffraction,* vol. 20, p. 316-326, 2005.

[LEG 99] LEGRAND C., YI J.H., THOMAS P., GUINEBRETIÈRE R., MERCURIO J.P., "Structural characterization of sol-gel deposited $SrBi_2Nb_2O_9$ thin film on (00l) $SrTiO_3$ single crystal", *J. Eur. Ceram. Soc.*, vol. 19, p. 1379-1381, 1999.

[LEN 01] LENORMAND P., Etude de l'évolution microstructurale de précurseurs d'oxyde de zirconium à l'état gel, xérogel, couches minces et aérogel par diffusion de rayons X, PhD Thesis, University of Limoges, 2001.

[LEN 94] LENARD P., "Über Kathodenstrahlen im Gases von atmosphärischen Druck und im äussersten Vacuum", *Annalen der Physik und Chemie*, vol. 51, p. 225-267, 1894.

[LEN 95] LENARD P., "Über die absorption der Kathodenstrahlen", *Annalen der Physik und Chemie*, vol. 56, p. 255-275, 1895.

[LEN 97] LENARD P., "Über die electrische Wirkung der Kathodenstrahlen auf atmosphärische Luft", *Annalen der Physik und Chemie*, vol. 63, p. 253-260, 1897.

[LEO 04] LEONI M., DI MAGGIO R., POLLIZZI S., SCARDI P., "X-ray diffraction methodology for the microstructural analysis of nanocrystalline powder: application to cerium oxide", *J. Am. Ceram. Soc.*, vol. 87, p. 1133-1140, 2004.

[LEV 97] LEVINE L.E., THOMSON R., "X-ray scattering by dislocations in crystal. General theory and application to screw dislocations", *Acta Cryst. A*, vol. 53, p. 590-602, 1997.

[LIG 94] LIGEN Y., HAILIN S., KEWEI X., JIAWEN H., "A correction of the Seemann Bohlin method for stress measurements in thin films", *J. Appl. Cryst.*, vol. 27, p. 863-867, 1994.

[LOD 12] LODGE O., "Becquerel memorial lecture", *J. Chem. Soc. Trans.*, p. 2005-2042, 1912.

[LOU 69a] LOUER D., WEIGEL D., LOUBOUTIN R., "Méthode directe de correction des profils de raies de diffraction des rayons X. I. Méthode numérique de déconvolution", *Acta Cryst. A*, vol. 25, p. 335-338, 1969.

[LOU 69b] LOUER D., WEIGEL D., "Méthode directe de correction des profils de raies de diffraction des rayons X. II. Influence de la fente réceptrice sur l'enregistrement d'un profil de raie de diffraction X", *Acta Cryst. A*, vol. 25, p. 338-350, 1969.

[LOU 69c] LOUBOUTIN R., LOUER D., WEIGEL D., "Méthode directe de correction des profils de raies de diffraction des rayons X. III. Sur la recherche de la solution optimale lors de la déconvolution", *Acta Cryst. A*, vol. 28, p. 396-399, 1972.

[LOU 82] LOUER D., VARGAS R., "Indexation automatique des diagrammes de poudre par dichotomies successives", *J. Appl. Cryst.*, vol. 15, p. 542-545, 1982.

[LOU 88] LOUER D., LANGFORD J.I., "Peak shape and resolution in conventional diffractometry with monochromatic X-rays", *J. Appl. Cryst*., vol. 21, p. 430-437, 1988.

[LOU 92] LOUER D., LOUER M., TOUBOUL M., "Crystal structure determination of lithium diborate hydrate, $LiB_2O_3(Oh).H_2O$, from x-ray powder diffraction data collected with a curved position sensitive detector", *J. Appl. Cryst.*, vol. 25, p. 617-623, 1992.

[LOU 95] LOUER D., LOUER M., DZYABCHENKO V.A., AGAFONOV V.A., CÉLIN R., "Structure of a metastable phase of pirecetam from x-ray powder diffraction using the atom-atom potential method", *Acta Cryst. B*, vol. 51, p. 182-187, 1995.

[LUT 90] LUTTEROTTI L., SCARDI P., "Simultaneous structure and size strain refinement by the Rietveld method", *J. Appl. Cryst.*, vol. 23, p. 246-252, 1990.

[MAC 67] MACK M., PARRISH W., "Seemann-Bohlin X-ray diffractometry. II. Comparison of aberrations and intensity with conventional diffractometer", *Acta Cryst*., vol. 23, p. 693-700, 1967.

[MAR 98] MARY C., GUINEBRETIERE R., TROLLIARD G., SOULESTIN B., VILLECHAIZE P., DAUGER A., "Epitaxial zirconia films on sapphire substrates", *Thin Sol. Films*, vol. 336, p. 156-159, 1998.

[MAR 00] MARY C., LENORMAND P., GUINEBRETIERE R., LECOMTE A., DAUGER A., "Diffraction des rayons X sur couches minces polycristallines ou épitaxiées. Utilisation d'un montage en réflexion asymétrique équipé d'un détecteur courbe à localisation", *J. Phys. IV*, vol. 10, p. 377-386, 2000.

[MAS 96a] MASSON O., GUINEBRETIÈRE R., DAUGER A., "Reflection asymmetric powder diffraction with flat plate sample using a curved position sensitive detector (INEL CPS 120)", *J. Appl. Cryst.*, vol. 29, p. 540-546, 1996.

[MAS 96b] MASCIOCCHI N., ARTIOLI G., "Lattice parameters determination from powder diffraction data: results from a round robin project", *Powder Diffraction*, vol. 11, no. 3, p. 253-258, 1996.

[MAS 96c] MASSON O., RIEUX V., GUINEBRETIÈRE R., DAUGER A., "Size and shape characterization of TiO_2 aerogel nanocrystals", *Nanostructured materials*, vol. 7, no. 7, p. 725-731, 1996.

[MAS 98a] MASSON O., GUINEBRETIÈRE R., DAUGER A., "Profile analysis in asymmetric powder diffraction with parallel beam geometry and curved position sensitive detector", *Mater. Sci. Forum*, Trans. Tech. Pub., Switzerland, vol. 278-281, p. 115-120, 1998.

[MAS 98b] MASSON O., Etude des défauts de structure par diffraction des rayons X sur poudres – utilisation d'un montage en réflexion asymétrique équipé d'un détecteur courbe à localisation, PhD Thesis, University of Limoges, 1998.

[MAS 01] MASSON O., GUINEBRETIÈRE R., DAUGER A., "Modelling of line profile asymmetry cause axial divergence in powder diffraction", *J. Appl. Cryst.*, vol. 34, p. 436-441, 2001.

[MAS 03] MASSON O., DOORYHREE E., FITCH A.N., "Instrument line-profile synthesis in high-resolution synchrotron powder diffraction", *J. Appl. Cryst.*, vol. 36, p. 286-294, 2003.

[MAS 05] MASSON O., BOULLE A., GUINEBRETIÈRE R., LECOMTE A., DAUGER A., "On the use of one dimensional position sensitive detector for x-ray diffraction reciprocal space mapping: data quality and limitations", *Rev. Sci. Instrum.*, vol. 76, p. 063912-1 - 063912-6, 2005.

[MIC 95] MICELI P.F., PALMSTROM C.J., "X-ray scattering from rotational disorder in epitaxial films: an unconventional mosaic crystal", *Phys. Rev. B*, vol. 51, p. 5506-5509, 1995.

[MOR 96] MORAME Ch., ZABEL H., "Metal/Al_2O_3: a new class of x-ray mirrors", *J. Appl. Phys.*, vol. 80, no. 7, p. 3639-3645, 1996.

[MOS 13] MOSELEY H.G.J., DARWIN C.G., "The reflexion of x-rays", *Phil. Mag.*, vol. 26, p. 210-232, 1913.

[MUG 69] MUGHRABI H., UNGAR T., KIENLE W., WILKENS M., "Long range internal stresses and asymmetric x-ray line broadening in tensile deformed [001] oriented copper single crystals", *Phil. Mag. A*, vol. 53, p. 793-813, 1986.

[NAN 78] NANDI R.K., SEN GUPTA S.P., "The analysis of x-ray diffraction profiles from imperfect solids by an application of convolution relations", *J. Appl. Cryst.*, vol. 11 p. 6-9, 1978.

[NAV 25] NAVIAS A.L., "Quantitative determination of the development of mullite in fired clays by an x-ray method", *J. Am. Ceram. Soc.*, vol. 8, p. 296-302, 1925.

[NES 00] NESTERETS Y.I., PUNEGOV V.I., "The statistical kinematical theory of x-ray diffraction as applied to reciprocal-space mapping", *Acta Cryst. A*, vol. 56, p. 540-548, 2000.

[NIS 01] NISHIBORI E., TAKATA M., KATO K., SAKATA M., KUBOTA Y., AOYAGI S., KUROIWA Y., YAMAKATA M., IKEDA N., "The large Debye–Scherrer camera installed at SPring-8 BL02B2 for charge density studies", *J. Phys. Chem. Sol.*, vol. 62, p. 2095-2098, 2001.

[NIST] National Institute of Standard and Technology, US Department of Commerce Bldg. 202, room 204 Gaithersburg, MD 20899 USA.

[NOR 97] NORBY P., "Synchrotron powder diffraction using imaging plate: crystal structure determination and Rietveld refinement", *J. Appl. Cryst.*, vol. 30, p. 21-30, 1997.

[NUT 99] NUTTALL C.J., DAY P., "Modelling stacking faults in the layered molecular based magnets $AM_2Fe(C_2O_4)_3$ {M=Mn, Fe; A=organic cation}", *J. Sol. Stat. Chem.*, vol. 147, p. 3-10, 1999.

[O'CO 97] O'CONNOR B.H., van RIESSEN A., CARTER J., BURTON G.R., COOKSON D.J., GARRETT R.F., "Characterization of ceramic materials with BIGDIFF: a synchrotron radiation Debye-Scherrer powder diffractometer", *J. Am. Ceram. Soc.*, vol. 80, p. 1373-1381, 1997.

[OET 99] OETZEL M., HEGER G., "Laboratory X-ray powder diffraction: a comparison of different geometries with special attention to the usage of the Cu Kα doublet", *J. Appl. Cryst*., vol. 32, p. 799-807, 1999.

[ORT 78] ORTENDAHL D., PEREZ-MENDEZ V., STOKER V., BEYERMANN W., "One dimensional curved wire chamber for powder X-ray crystallography", *Nucl. Instum. Meth.,* vol. 156, p. 53-56, 1978.

[OTT 97] OTTO J.W., "On the peak profile in energy dispersive powder x-ray diffraction with synchrotron radiation", *J. Appl. Cryst.*, vol. 30, p. 1008-1015, 1997.

[PAR 60] PARRISH W., "Results of the IUCr precision lattice parameter project", *Acta Cryst*., vol. 13, p. 838-850, 1960.

[PAR 67] PARRISH W., MACK M., "Seemann-Bohlin X-ray diffractometry. I. Instrumentation", *Acta Cryst*., vol. 23, p. 687-692, 1967.

[PAT 34] PATTERSON A.L., "A Fourier series method for the determination of the components of interatomic distances in crystals", *Phys. Rev.*, vol. 46, p. 372-376, 1934.

[PAT 35] PATTERSON A.L., "A direct method for the determination components of interatomic distances in crystals", *Z. Krist*., vol. 90, p. 517-542, 1935.

[PAW 81] PAWLEY G.S., "Unit cell refinement from powder diffraction scans", *J. Appl. Cryst.*, vol. 14, p. 357-361, 1981.

[PEC 03] PECHARSKY V.K., ZAVALIJ P.Y., *Fundamentals of powder diffraction and structural characterization of materials*, Kluwer Academic Publishing, Norwell, USA, 2003.

[PER 95] PERRIN J., "Nouvelles propriétés des rayons cathodiques", *Comptes Rendus Acad. Sci.*, vol. 121, p. 1130-1134, 1895.

[PES 02] PESCHAR A., ETZ A., JANSEN J., SCHENK H., "Direct methods in powder diffraction – basic concept" in W.I.F. DAVID, K. SHANKLAND, L.B. MAC CUSKER, Ch. BAERLOCHER (eds.), *Structure determination from powder diffraction data*, Oxford University Press, 2002.

[PES 95] PESCHAR R., SCHENK H., CAPKOVA P., "Preferred orientation correction and normalization procedure for ab initio structure determination from powder data", *J. Appl. Cryst.*, vol. 28, p. 127-140, 1995.

[PHI 62] PHILLIPS D.L., "A technique for the numerical solution of certain integral equations of the first kind", *J. Assoc. Comput. Mach.*, vol. 9, p. 854-864, 1962.

[PIE 04] PIETSCH U., HOLÝ V., BAUMBACH T., *High resolution X-ray scattering – from thin films to lateral nanostructures,* 2nd edition, New York: Springer-Verlag, 2004.

[PLA 75] PLANÇON A., TCHOUBAR C., "Study of stacking faults in partially disordered kaolinites. I. Stacking model allowing only translational faults", *J. Appl. Cryst.*, vol. 8, p. 582-588, 1975.

[PLA 76] PLANÇON A., TCHOUBAR C., "Study of stacking faults in partially disordered kaolinites – II. Models of stacking containing rotation faults", *J. Appl. Cryst.*, vol. 9, p. 279-285, 1976.

[PUT 99] PUTZ H., SCHÖN J.C., JANSEN M., "Combined method for *ab initio* structure solution from powder diffraction data", *J. Appl. Cryst.*, vol. 32 p. 864-870, 1999.

[RAB 25] RABINOV I.I., "Note on the diffraction of x-rays by a wedgeshaped slit", *Proc. Nat. Acad. Sci*., vol. 11, p. 222-224, 1925.

[RAC 48] RACHINGER W.A., "A correction for the α_1 α_2 doublet in the measurement of widths of x-ray diffraction lines", *J. Sci. Instrum.*, vol. 25, p. 254-255, 1948.

[REI 02] REISS C.A., "The RTMS technology: dream or reality?", *Newsletter of the Commission on Powder Diffraction of the International Union of Crystallography*, vol. 27, p. 21-23, 2002.

[REN 98] RENAUD G., "Oxide surfaces and metal/oxide interfaces studi grazing incidence x-ray scattering", *Surf. Sci. Reports*, vol. 32, no. 1-2, p. 1-90, 1998.

[RIE 67] RIETVELD H.M., "Line profiles of neutron powder diffraction peaks for structure refinement", *Acta Cryst*., vol. 22, p. 151-152, 1967.

[RIE 69] RIETVELD H.M., "A profile refinement method for nuclear and magnetic structures", *J. Appl. Cryst.*, vol. 2, p. 65-71, 1969.

[RIE 95a] RIELLO P., FAGHERAZZI G., CLEMENTE D., CANTON P., "X-ray Rietveld analysis with a physically based background", *J. Appl. Cryst.*, vol. 28, p. 115-120, 1995.

[RIE 95b] RIELLO P., FAGHERAZZI G., CANTON P., CLEMENTE D., SIGNORETTO M., "Determining the degree of crystallinity in semicrystalline materials by means of the Rietveld analysis", *J. Appl. Cryst.*, vol. 28, p. 121-126, 1995.

[RIE 98] RIELLO P., CANTON P., FAGHERAZZI G., "Quantitative phase analysis in semicrystalline materials using the Rietveld method", *J. Appl. Cryst.*, vol. 31, p. 78-82, 1998.

[RIT 98] RITTER VON GEITLER J., "Über die Verschiedenheit der physikalischen Natur der Kathodesstrahlen und der Röntgenstrahlen", *Annalen der Physik und Chemie*, vol. 66, p. 65-73, 1898.

[ROB 98] ROBERTS M.A., FINNEY J.L., BUSHNELL-WYE G., "Development of curved image-plate techniques for studies of powder diffraction, liquids and amorphous materials", *Mater. Sci. Forum*, Trans. Tech. Pub., Switzerland, vol. 278-281, p. 318-322, 1998.

[ROD 92] RODRIGUEZ CARVAJAL J., Fullprof ILL Program, Grenoble, 1992.

[RON 95] RÖNTGEN W.C., "Über eine neue Art von strahlen", *Sitzungsbericht der Würzburg Physik und Medicin Gesellschaft*, 1895.

[RON 96a] RÖNTGEN W.C., "Eine neue Art von strahlen", *Sitzungsbericht der Würzburg Physik und Medicin Gesellschaft*, 1896.

[RON 96b] *Beiblätter zu den Annalen der Physik und Chemie*, p. 401-406, 1896 (reprinted in [RON 95] and [RON 96a]).

[RON 96c] RÖNTGEN W.C., "On a new kind of x-ray", *Nature*, vol. 53, no. 1369, p. 274-276, 1896.

[RUL 71] RULAND W., "The convergence of the van Citter method of déconvolution", *J. Appl. Cryst.*, vol. 4, p. 328-329, 1971.

[RUT 00] RUTHERFORD E., McCLUNG R.K., "Energy of Röntgen and Becquerel rays and the energy required to produce an ion in gases", *Proc. Roy. Soc. Lond.*, vol. 67, p. 245-250, 1900.

[RUT 97] RUTHERFORD E., "On the electrification of gases exposed to Röntgen rays and the absorption of Röntgen radiation by gazes and vapours", *Phil. Mag.*, vol. 43, p. 241-255, 1897.

[SAB 95] SABINE T.M., KENNEDY B.J., GARETT R.F., FORAN G.J., COOKSON D.J., "The performance of the Australian powder diffractometer at the Photon Factory, Japan", *J. Appl. Cryst.*, vol. 28, p. 513-517, 1995.

[SAD 09] SADLER G.C.A., "Transformations of x-rays", *Phil. Mag.*, vol. 18, p. 107-132, 1909.

[SAG 97a] SAGNAC G., "Sur la transformation des rayons X par les métaux", *Comptes Rendus Acad. Sci.*, vol. 125, p. 942-944, 1897.

[SAG 97b] SAGNAC G., "Sur la transformation des rayons X par les métaux", *Comptes Rendus Acad. Sci.*, vol. 125, p. 230-232, 1897.

[SAG 99] SAGNAC G., "Transformations des rayons X par la matière", *J. Phys.*, vol. 8, p. 65-89, 1899.

[SAN 93] SANKAR G., WRIGHT P.A., NATARAJAN S., THOMAS M.J., GREAVES G.N., DENT A.J., DOBSON B.R., RAMSDALE C.A., JONES R.H., "Combined QuEXAFS-XRD: a new technique in high-temperature materials chemistry; an illustrative in situ study of the zinc oxide-enhanced solid-state production of cordierite from a precursor zeolite", *J. Phys. Chem.*, vol. 97, p. 9550-9554, 1993.

[SAN 97] SANCHEZ BAJO F., CUMBRERA F.L., "The use of the pseudo-Voigt function in the variance method of the X-ray line broadening analysis", *J. Appl. Cryst.*, vol. 30, p. 427-430, 1997.

[SAR 05a] SARRAZIN P., CHIPERA S., BISH D., BLAKE D., VANIMAN D., "Vibrating sample holder for XRD analysis with minimal sample preparation", *Adv. X-ray Anal., v*ol. 48, p. 156-164, 2005.

[SAR 05b] SARRAZIN P., BLAKE D., FELDMAN S., CHIPERA S., VANIMAN D., BISH D., "Field deployment of a portable XRD/XRF instrument on Mars analog terrain", *Adv. X-ray Anal.*, vol. 48, p. 194-203, 2005.

[SCA 93] SCARDI P., LUTTEROTTI L., TOMASI A., "XRD characterization of multilayered systems", *Thin Sol. Films*, vol. 236, p. 130-134, 1993.

[SCA 97] SCARDI P., MATACOTTA F.C., DEDIU V.I., CORRERA L., "X-ray diffraction line broadening effects in $MBa_2Cu_3O_{7-\delta}$ (M=Y, Gd) thin films", *J. Mater. Res.*, vol. 12, no. 1, 28-37, 1997.

[SCA 99] SCARDI P., LEONI M., "Fourier modelling of the anisotropic line broadening of x-ray diffraction profiles due to line and planar lattice defects", *J. Appl. Cryst.*, vol. 32, p. 671-682, 1999.

[SCA 02] SCARDI P., LEONI M., "Line profile analysis: pattern modeling versus profile fitting", *J. Appl. Cryst.*, vol. 39, p. 24-31, 2006.

[SCA 02] SCARDI P., LEONI M., "Whole powder pattern modelling", *Acta Cryst. A*, vol. 58, p. 190-200, 2002.

[SCA 04] SCARDI P., LEONI M., "Whole powder pattern modelling: theory and applications", in MITTEMEIJER E.J., SCARDI P., *Diffraction analysis of the microstructure of materials,* Springer Series in Materials Science, vol. 68, p. 51-91, 2004.

[SCH 18] SCHERRER P., "Bestimmung der Grösse und der inneren Struktur von Kolloiteilchen mittels Röntgenstrahlen", *Nachrichten von der Gesellschaft der Wissenschaften zu Gottingen Mathematisch Physikalische*, vol. 1-2, p. 96-100, 1918.

[SCH 49] SCHWINGER J., "On the classical radiation of accelerated electrons", *Phys. Rev.*, vol. 75, no. 12, p. 1912-1925, 1949.

[SCH 65] SCHOENING F.R.L., "Strain and particles size from x-ray line breaths", *Acta Cryst.*, vol. 18, p. 975-976, 1965.

[SCH 88] SCHUSTER M., MÜLLER L., MAUSER K.E., STRAUB R., "Quantitative X-ray fluorescence analysis of boron in thin films of borophosphosilicate glasses", *Thin Sol. Films*, vol. 157, p. 325-336, 1988.

[SCH 95] SCHUSTER M., GÖBEL H., "Parallel beam coupling into channel-cut monochromators using curved graded multilayers", *J. Phys. D: Appl. Phys.*, vol. 28, p. 270-275, 1995.

[SCH 96] SCHUSTER M., GÖBEL H., "Application of graded multilayer optics in x-ray diffraction", *Adv. X-ray Anal.*, vol. 39, p. 57-71, 1996.

[SCH 97] SCHMID S., THOMPSON J.G., WITHERS R.L., PETRICEK V., ISHIZAWA N., KISHIMOTO S., "Re-refinement of composite modulated $Nb_2Zr_{(x-2)}O_{(2x+1)}$ (x = 8) using synchrotron radiation data", *Acta Cryst. B*, vol. 53, p. 851-860, 1997.

[SEE 19] SEEMANN H., "Eine fokussierende röntgenspektroskopische anornung für Kristallpulver", *Annalen der Physik*, vol. 53, p. 455-464, 1919.

[SHI 86] SHISHIGUCHI S., MINATO I., HASHIZUME H., "Rapid collection of x-ray powder data for pattern analysis by a cylindrical position sensitive detector", *J. Appl. Cryst.*, vol. 19, p. 420-426, 1986.

[SIL 96] SILVA M.C., Influence de l'organisation nanostructurale des précurseurs de zircone sur les processus de cristallisation et transformation de phase, PhD Thesis, University of Limoges, 1996.

[SIL 97] SILVA M.C., TROLLIARD G., MASSON O., GUINEBRETIÈRE R., DAUGER A., LECOMTE A., FRIT B., "Early stages of crystallization in gel derived ZrO_2 precursors", *J. of Sol Gel Sci. and Tech.,* vol. 8, p. 419-424, 1997.

[SMI 79] SMITH G.S., SNYDER R.L., "F_n: a criterion for rating powder diffraction patterns and evaluating the reliability of powder pattern indexing", *J. Appl. Cryst.*, vol. 12, p. 60-65, 1979.

[SMI 79a] SMITH S.T., SNYDER R.L., BROWNELL W.E., "Minimization of preferred orientation in powders by spray drying", *Adv. X-ray Anal.*, vol. 22, p. 77-87, 1979.

[SMR 99] SMRCOK L., MAILING J., "Inorganic crystal structures from powder data – a retrospective", *Powder Diffraction*, vol. 14, no. 1, p. 5-9, 1999.

[SOL 24] SOLLER W., "A new precision x-ray spectrometer", *Phys. Rev.*, vol. 24, p. 158-167, 1924.

[SOM 00a] SOMMERFELD A., "Theoretisches über die Beugung der Röntgenstrahlen", *Phys. Zeitsch.*, vol. 1, p. 105-111, 1900.

[SOM 00b] SOMMERFELD A., "Theoretisches über die Beugung der Röntgenstrahlen", *Phys. Zeitsch.*, vol. 2, p. 55-60, 1900.

[SOM 01] SOMMERFELD A., "Die Beugnung der Röntgenstrahlen unter der Annahme von Ätherstössen", *Phys. Zeitsch.*, vol. 2, p. 88-90, 1901.

[SOM 12] SOMMERFELD A., "Über die Beugung der Röntgenstrahlen", *Annalen der Physik*, vol. 38, p. 715-724, 1912.

[SPE 95] SPERLING Z., "Specimen displacement error in focusing systems", *Powder Diffr.*, vol. 10, p. 278-281, 1995.

[STA 00] STACHS O., GERBER T., PETKOV V., "An image plate chamber for x-ray diffraction experiments in Debye–Scherrer geometry", *Rev. Sci. Instrum.*, vol. 71, p. 4007-4009, 2000.

[STA 92] STAHL K., THOMASSON R., "Using CPS120 curved position sensitive detector covering 120°. Powder diffraction data in Rietveld analysis. The dehydration process in the zeolite Thomsonite", *J. Appl. Cryst.*, vol. 25, p. 251-258, 1992.

[STA 92] STANTON M., PHILIPS W.C., LI Y., KALATA K., "Correcting spatial distorsions and non uniform response in area detectors", *J. Appl. Cryst.*, vol. 25, p. 549-558, 1992.

[STA 94] STAHL K., "The Huber G670 imaging-plate Guinier camera tested on beamline I711 at the MAX II synchrotron", *J. Appl. Cryst.,* vol. 33, p. 394-396, 2000.

[STA 94] STAHL K., HANSON J., "Real time x-ray synchrotron powder diffraction studies of the dehydration processes in scolecite and mesolite", *J. Appl. Cryst.*, vol. 27, p. 543-550, 1994.

[STO 01] STOWIK J., ZIEBA A., "Geometrical equatorial aberrations in a Bragg-Brentano powder diffractometer with a linear position-sensitive detector", *J. Appl. Cryst*., vol. 34, p. 458-464, 2001.

[STO 42] STOKES A.R., WILSON A.J.C., "A method of calculating the integral breaths of Debye-Scherrer lines", *Proc. Camb. Phil. Soc.*, vol. 38, p. 313-322, 1942.

[STO 44] STOKES A.R., WILSON A.J.C., "A method of calculating the integral breaths of Debye-Scherrer lines: generalization to non-cubic crystals", *Proc. Camb. Phil. Soc.*, vol. 40, p. 197-198, 1944.

[STO 48] STOKES A.R., "A numerical Fourier analysis method for the correction of widths and shapes of lines on x-ray powder photographs", *Proc. Phys. Soc.*, vol. 61, p. 382-391, 1948.

[STO 96] STOKES G.G., "On the nature of the Röntgen rays", *Proc. Camb. Phil. Soc.*, vol. 9, no. 4, p. 215-216, 1896.

[STO 97] STÖMMER R., METZER T., SCHUSTER M., GÖBEL H., "Triple axis diffractometry on GaN/Al_2O_3(001) and AlN/Al_2O_3(001) using a parabolically curved graded multilayer as analyser", *Nuovo Cimento*, vol. 19, no. 2-4, p. 465-472, 1997.

[STR 00] STRUTT R.J., "On the behaviour of the Becquerel and Röntgen rays in a magnetic field", *Proc. Roy. Soc. Lond.*, vol. 66, p. 75-79, 1900.

[SUL 94] SULYANOV S.N., POPOV A.N., KHEIDER D.M., "Using of two-dimensional detector for x-ray powder diffractometry", *J. Appl. Cryst.*, vol. 27, p. 934-942, 1994.

[SUT 95] SUTTA P., JACKLIAK Q., TVAROZEK V., NOVOTNY I., "X-ray diffraction line profile analysis of ZnO thin films deposited on Al-SiO_2-si substrates", *Science and technology of electroceramic thin films*, Kluwer Academic Publishing, p. 327-334, 1995.

[SWI 96] SWINTON A.A.C., "Professor Röntgen's discovery", *Nature*, vol. 53, no. 1369, p. 276-277, 1896.

[SYN 99] SNYDER R.L., FIALA J., BUNGE H.J., *Defect and microstructure analysis by diffraction*, IUCr Monographs on crystallography, no. 10, Oxford University Press, 1999.

[TAK 02] TAKATA M., NISHIBORI E., KATO K., KUBOTA Y., KUROIWA Y., SAKATA M., "High resolution Debye-Scherrer camera installed at SPRING-8", *Adv. X-ray Anal.*, vol. 45, p. 377-384, 2002.

[TAK 98] TAKAGI Y., KIMURA M., "Generalized grazing-incidence-angle X-ray diffraction (G-GIXD) using image plates", *J. Synch. Radiat.*, vol. 5, p. 488-490, 1998.

[TAY 91] TAYLOR J.C., "Computer programs for standardless quantitative analysis of minerals using the full powder diffraction profile", *Powder diffraction*, vol. 6, p. 2-9, 1991.

[TER 13] TERADA T., "X-rays and crystal", *Nature*, vol. 91, no. 2270, p. 213, 1913.

[THO 06a] THOMSON J.J., "On the secondary Röntgen radiation", *Proc. Camb. Phil. Soc.*, vol. 13, p. 322-324, 1906.

[THO 06b] THOMSON J.J., "On the secondary Röntgen radiation", *Proc. Camb. Phil. Soc.*, vol. 14, p. 109-114, 1906.

[THO 87a] THOMPSON P., REILLY J.J., HASTINGS J.M., "The accommodation of strain and particle size broadening in Rietveld refinement. Its application to de-deuterided lani alloy", *J. Less Com. Met.*, vol. 129, p. 105-114, 1987.

[THO 87b] THOMPSON P., COX D.E., HASTINGS J.B., "Rietveld refinement of Debye-Scherrer synchrotron x-ray data from Al_2O_3", *J. Appl. Cryst.*, vol. 20, p. 79-83, 1987.

[THO 96a] THOMPSON S.P., "Some experiments with Röntgen's Rays", *Phil. Mag.*, vol. 42, p. 162-167, 1896.

[THO 96b] THOMSON J.J., "Longitudinal electric waves, and Röntgen's X-rays", *Proc. Camb. Phil. Soc.*, vol. 9, no. 1, p. 49-61, 1896.

[THO 96c] THOMSON J.J., RUTHERFORD E., "On the passage of electricity through gases exposed to Röntgen rays", *Phil. Mag.*, vol. 42, p. 392-407, 1896.

[THO 97a] THOMSON J.J., "On the cathode rays", *Proc. Camb. Phil. Soc.*, vol. 9, no. 5, p. 243-244, 1897.

[THO 97b] THOMSON J.J., "Cathode rays", *Phil. Mag.*, vol. 44, p. 293-316, 1897.

[THO 97c] THOMSON J.J., "Note on the Rutherford paper 'On the electrification of gases exposed to Röntgen rays and the absorption of Röntgen radiation by gases and vapours'", *Phil. Mag.*, vol. 43, p. 255, 1897.

[THO 98a] THOMSON J.J., "A theory of the connection between cathode and Röntgen rays", *Phil. Mag.*, vol. 45, p. 172-183, 1898.

[THO 98b] THOMSON J.J., "On the charge of electricity carried by the ions produced by Röntgen rays", *Phil. Mag.*, vol. 46, p. 528-545, 1898.

[THO 98c] THOMSON J.J., "On the connection between the chemical composition of a gas and the ionization produced in it by Röntgen rays", *Proc. Camb. Phil. Soc.*, vol. 10, no. 1, p. 10-14, 1898.

[THO 98d] THOMSON J.J., "On the diffuse reflection of Röntgen rays", *Proc. Camb. Phil. Soc.*, vol. 9, no. 8, p. 393-397, 1898.

[TIK 63] TIKHONOV A.N., "O Reshenii necorrectno nostavtennyh zadach i metode regulraizacii", *Dokl. Akad. Nauk.*, vol. 151, p. 501-504, 1963.

[TIK 77] TIKHONOV A.N., ARSENIN V.Y., *Solution of ill posed problems,* Winston & Sons, Washington DC, 1977.

[TIZ 96] TIZLIOUINE A., BESSIÈRES J., HEIZMANN J.J., BOBO J.F., "Thin film study using low incidence and Bragg-Brentano texture goniometry. Application to mono-and bilayers of Al and Al/Fe", *J. Appl. Cryst.*, vol. 29, p. 531-539, 1996.

[TOR 00] TORAYA H., HIBINO H., "$K\alpha_1$-$K\alpha_2$ characteristic of a parabolic graded multilayer", *J. Appl. Cryst.*, vol. 33, p. 1317-1323, 2000.

[TOR 93] TORAYA H., "Position constrained and unconstrained powder pattern decomposition methods", in YOUNG R.A. (ed.), *The Rietveld method*, IUCr monographs on crystallography, no. 5, Oxford University Press, New York, 1993.

[TOR 94] TORAYA H., OCHIAI T., "Refinement of unit cell parameters by whole powder pattern fitting technique", *Powder Diffraction*, vol. 9, p. 272-279, 1994.

[TOR 99a] TORAYA H., "Quantitative phase analysis of alpha and beta silicon nitrides – I. Estimation of errors", *J. Appl. Cryst.*, vol. 32, p. 704-715, 1999.

[TOR 99b] TORAYA H., HAYASHI S., NAKAYASU T., "Quantitative phase analysis of alpha and beta silicon nitrides. II. Round robins", *J. Appl. Cryst.*, vol. 32, p. 716-729, 1999.

[TOU 56a] TOURMARIE M., "Utilisation du deuxième moment comme critère d'élargissement des raies Debye-Scherrer – elimination de l'effet instrumental", *Comptes Rendus Acad. Sci.*, p. 2016-2018, 1956.

[TOU 56b] TOURMARIE M., "Utilisation du deuxième moment comme critère d'élargissement des raies Debye-Scherrer. Signification physique", *Comptes Rendus Acad. Sci.*, p. 2161-2164, 1956.

[TOW 99] TOWNSEND J.S., "Secondary Röntgen rays", *Proc. Camb. Phil. Soc.*, vol. 10, no. 4, p. 217-226, 1899.

[TRE 91] TREACY M.M.J., NEWSAM J.M., DEEM M.W., "A general recursion method for calculating diffracted intensities from crystals containing planar faults", *Proc. Roy. Soc. Lond. A*, vol. 433, p. 499-520, 1991.

[TUT 12] TUTTON A.E.H., "The crystal space lattice reveal Röntgen rays", *Nature*, vol. 90, no. 2246, p. 306-309, 1912.

[TUT 13a] TUTTON A.E.H., "Great advance in crystallography", *Nature*, vol. 91, no. 2280, p. 490-494, 1913.

[TUT 13b] TUTTON A.E.H., "Great advance in crystallography", *Nature*, vol. 91, no. 2281, p. 518-522, 1913.

[UNG 99] UNGAR T., "The dislocation based model of strain broadening in x-ray line profile analysis", in SNYDER R.L., FIALA J., BUNGE H.J. (eds.), *Defect and microstructure analysis by diffraction*, IUCr Monographs on crystallography, no. 10, Oxford University Press, p. 264-317, 1999.

[UNG 99b] UNGAR T., LEONI M., SCARDI P., "The dislocation model of strain anisotropy in whole pattern fitting: the case of an Li-Mn cubic spinel", *J. Appl. Cryst.,* vol. 32, p. 290-295, 1999.

[UST 99] USTINOV A.I., "Effect of planar defects in crystals on the position and profile of powder diffraction lines", in SNYDER R.L., FIALA J., BUNGE H.J. (eds.), *Defect and microstructure analysis by diffraction*, IUCr Monographs on crystallography, no. 10, Oxford University Press, p. 264-317, 1999.

[UST 04] USTINOV A.I., OLIKHOVSKA L.O., BUDARINA N.M., BERNARD F., "Line profile fitting: the case of fcc crystals containing stacking faults", in MITTEMEIJER E.J., SCARDI P. (eds.), *Diffraction analysis of the microstructure of materials,* Springer Series in Materials Science, vol. 68, p 333-359, 2004.

[VAL 90] VALVODA V., KUZEL R., CERNY R., RAFAJA D., MUSIL J., KADLEC S., PERRY A.J., "Structural analysis of thin films by Seemann-Bohlin X-ray diffraction", *Thin Solid Films*, vol. 193-194, p. 401-408, 1990.

[VOI 12] VOIGT W., "Über das Gesetz der Intensitätsverteilung innerhalb der Linien eines Gasspektrums", *Sitzungsberichte Königliche Bayerische Akademie der Wissenschaften*, vol. 42, p. 603-620, 1912.

[VOS 97] VOSMAER A., ORTT F.L., "Röntgen ray theory", *Nature*, vol. 56, p. 316, 1897.

[WAL 02] WALTER B., "Über die Haga und Windschen Beugungsversuche mit Röntgenstrahlen", *Phys. Zeitsch.*, vol. 3, p. 137-143, 1902.

[WAL 08] WALTER B., POHL R., "Zur Frage der Beugung der Röntgenstrahlen", *Annalen der Physik*, vol. 25, p. 715-724, 1908.

[WAL 09] WALTER B., POHL R., "Weitere Versuche über die Beugung der Röntgenstrahlen", *Annalen der Physik*, vol. 29, p. 331-354, 1909.

[WAL 24a] WALTER B., "Beugungsfransen an Spaltaufnahmen mit Röntgenstrahlen", Annalen der Physik, vol. 74, p. 661-672, 1924.

[WAL 24b] WALTER B., "Beugungsfransen an Spaltaufnahmen mit Röntgenstrahlen – 2. Mitteilung", *Annalen der Physik*, vol. 75, p. 189-194, 1924.

[WAL 98] WALTER B., "Über die Natur der Röntgenstrahlen", *Annalen der Physik und Chemie*, vol. 66, p. 74-82, 1898.

[WAR 50] WARREN B.E., AVERBACH B.L., "The effect of cold work distortion on x-ray patterns", *J. Appl. Phys.*, vol. 21, p. 595-599, 1950.

[WAR 55] WARREN B.E., "A generalized treatment of cold work in powder patterns", *Acta Cryst.*, vol. 8, p. 483-486, 1955.

[WAR 69] WARREN B.E., *X-ray diffraction*, Addison-Wesley, 1969

[WAS 53] WASSERMANN G., WIEWIOROSKY J., "Über ein Geiger-Zählrohr-Goniometer nach dem Seemann-Bohlin prinzip", *Z. Metallk.*, vol. 44, p. 567-570, 1953.

[WER 74] WERTHEIM G.K., BUTLER M.A., WEST K.W., BUCHANAN D.N.E., "Determination of the Gaussian and Lorentzian content of experimental line shape", *Rev. Sci. Instrum.*, vol. 45, p. 1369-1371, 1974.

[WER 85] WERNER P.E., ERIKSSON L., WESTDAHL M., "Treor, a semi exhaustive trial and error powder indexing program for all symmetries", *J. Appl. Cryst.*, vol. 18, p. 367-370, 1985.

[WHI 11] WHIDDINGTON R., "The production of characteristic Röntgen radiations", *Proc. Camb. Phil. Soc.*, vol. 16, p. 150-154, 1911.

[WIE 03] WIEDEMANN H., *Synchrotron radiation*, Springer, 2003.

[WIL 53] WILLIAMSON G.K., HALL W.H., "X-ray line broadening from filed aluminium and wolfram", *Acta Met.*, vol. 1, p. 22-31, 1953.

[WIL 62a] WILSON A.J.C., *X-ray optics – The diffraction of x-rays by finite and imperfect crystals*, Spottiswoode Ballantyne & Co, London, 2nd edition, 1962.

[WIL 62b] WILSON A.J.C., "On variance as a measure on line broadening in diffractometry. General theory and small particle size", *Proc. Phys. Soc.*, vol. 80, p. 286-294, 1962.

[WIL 63] WILSON A.J.C., "On variance as a measure of line broadening in diffractometry – II. Mistakes and strain", *Proc. Phys. Soc.*, vol. 81, p. 41-46, 1963.

[WIL 70] WILKENS M., "The determination of density and distribution of dislocations in deformed single crystals from broadened x-ray diffraction profiles", *Phys. Stat. Sol. A*, vol. 2, p. 359-370, 1970.

[WIL 76] WILKENS M., "Broadening of x-ray diffraction lines of crystals containing dislocation distributions", *Kristall. Tech.*, vol. 11, p. 1159-1169, 1976.

[WIL 97] WILSON C.T.R., "Condensation of water vapour in the presence of dust free air and other gases", *Phil. Trans. A*, p. 265-307, 1897.

[WIN 01] WIND C.H., "Zum Fresnelschen Beugungsbilde eines Spates", *Phys. Zeitsch.*, vol. 2, no. 18, p. 265-267, 1901.

[WIN 99] WIND C.H., "Zur Demonstration einer von E. Mach entdeckten Optischen Tauschung", *Phys. Zeitsch.*, vol. 1, p. 112-113, 1899.

[WOL 48] DE WOLFF P.M., "Multiple Guinier Cameras", *Acta Cryst.*, vol. 1, p. 207-211, 1948.

[WOL 59] DE WOLFF P.M., TAYLOR J.M., PARRISH W. "Experimental study of effect of crystallite size statistics on x-ray diffractometer intensities", *J. Appl. Phys.*, vol. 30, p. 63-69, 1959.

[WOL 68] DE WOLFF P.M., "A simplified criterion for the reliability of a powder pattern indexing", *J. Appl. Cryst.*, vol. 1, p. 108-113, 1968.

[WOL 81] WÖLFEL E.R. "A new method for quantitative X-ray analysis of multiphase mixtures", *J. Appl. Cryst.*, vol. 14, p. 291-296, 1981.

[WOL 83] WÖLFEL E.R., "A novel curved position sensitive proportional counter for x-ray diffractometry", *J. Appl. Cryst.*, vol. 16, p. 341-348, 1983.

[WU 98] WU E., MAC E., GRAY A., KISI E.H., "Modelling dislocation induced anisotropic line broadening in Rietveld refinements using a Voigt function. I. General principles", *J. Appl. Cryst.*, vol. 31, p. 356-362, 1998.

[YAM 92] YAMANAKA T., KAWASAKI S., SHIBATA T., "Time-resolved observations of solid reactions and structure transitions using a PSD, an SSD and computer aided measurement and control", *Adv. X-ray Anal.*, vol. 35, p 415-423, 1992.

[YOU 93] YOUNG R.A., *The Rietveld method*, IUCr monographs on crystallography, no. 5, Oxford University Press, New York, 1993.

[ZAC 48a] ZACHARIASEN W.H., "The crystal structure of the normal orthophosphates of barium and strontium" *Acta Cryst.*, vol. 1, p 263-265, 1948.

[ZAC 48b] ZACHARIASEN W.H., "Crystal chemical studies of the 5*f*-series of elements. I. New structure types", *Acta Cryst.*, vol. 1, p 265-268, 1948.

[ZAC 48c] ZACHARIASEN W.H., "Crystal chemical studies of the 5*f*-series of elements. II The crystal structure of Cs_2PuCI_6", *Acta Cryst.*, vol. 1, p 268-269, 1948.

[ZAC 48d] ZACHARIASEN W.H., "Crystal chemical studies of the 5*f*-series of elements. III. A study of the disorder in the crystal structure of anhydrous uranyl fluoride", *Acta Cryst.*, vol. 1, p 277-281, 1948.

[ZAC 48e] ZACHARIASEN W.H., "Crystal chemical studies of the 5*f*-series of elements. IV. The crystal structure of $Ca(UO_2)O_2$ and $Sr(UO_2)O_2$", *Acta Cryst.*, vol. 1, p 281-285, 1948.

[ZAC 48f] ZACHARIASEN W.H., "Crystal chemical studies of the 5*f*-series of elements. V. The crystal structure of uranium hexachloride", *Acta Cryst.*, vol. 1, p 285-287, 1948.

This page intentionally left blank

Index

H, I, J

L

M

O, P, Q

R

S

T

W